REVIEW

Dopant impurity diffusion from polymer diffusants and its applications in semiconductor device technology. A review

E. G. Guk, A. V. Kamanin, N. M. Shmidt, V. B. Shuman, and T. A. Yurre

A. F. Ioffe Physicotechnical Institute, Russian Academy of Sciences, 194021 St. Petersburg, Russia
(Submitted June 3, 1997; accepted for publication July 6, 1998)
Fiz. Tekh. Poluprovodn. **33**, 257–269 (March 1999)

Aspects of the nontraditional diffusion of various impurities from polymer diffusants into silicon and III-V semiconducting compounds are examined. Data are presented on the application of this method to the technology of semiconductor devices based on silicon and AlGaAs/GaAs and InGaAs(P)/InP heterostructures. © *1999 American Institute of Physics*. [S1063-7826(99)00103-9]

1. INTRODUCTION

Diffusion is one of the oldest methods, successfully used for many decades, in semiconductor device manufacturing technology, including for modern devices, and its development and improvement continue.

One diffusion technique involves the diffusion of dopants from solid-state film diffusants.[1–4] This technique competes successfully with the widespread method of diffusion from a flow of carrier gas, primarily because it does not require complicated equipment for monitoring and maintaining the composition of a gaseous phase, offers a wide variety of diffusants and the possibility of using sources containing several dopant elements, and can produce low surface concentrations ($10^{17}-10^{18}$ cm^{-3}) in a single-stage diffusion process.

The attractiveness of this method should be noted especially for the technology of III–V compounds, since the diffusion process can be carried out in an open system, without taking special measures to maintain a constant pressure of the volatile group V component in order to prevent thermal decomposition of the material.

Polymer diffusants are a relatively new type of solid-state film source that has been used in silicon technology for less than 20 years and in III–V technology for less than 10 years.

Solid-state film sources were first prepared for use in silicon technology in the 1960s. They were obtained from solutions of salts or acids. Later, compositions were created in the form of films consisting of a solution of organic polymer (e.g., cellulose) and solid oxides dispersed in them or other compounds of the dopant element.[5] Since the end of the 1960s silicon-organic compositions based on tetraethoxysilane (TEOS) and chemical compositions of a dopant element have been developed.[1,6,7]

Diffusants based on TEOS[8–10] have so far been used successfully in silicon technology and compete both with diffusion from gas flows and with ion implantation because of their simplicity and low cost. In the 1980s these diffusants came to be widely used in III–V semiconductor technology.[11–13]

When polymer diffusants are used, the process breaks up into two stages: (1) formation of a glassy film of diffusant on the surface from a special emulsion by drying in air at a temperature of 200–300 °C, and (2) diffusion of the dopant impurity from this film into the semiconductor. The main deficiencies of TEOS are low stability of the solution, high mechanical stresses which, in some cases, cause cracking of the diffusant film, and the unavoidable presence of SiO_2 in the film, which produces complicated changes in the concentration profile of the impurity and requires removal of the SiO_2 after diffusion.

A fundamentally new approach to creating film diffusants, which eliminated the deficiencies noted above, was the development of entirely homogeneous polymer diffusion sources which include atoms of the dopant elements in the composition of their element-organic components. This idea was first advanced by researchers at the Physicotechnical Institute and the Leningrad Technological Institute.[14] Later, the use of a polymer matrix was proposed by others,[3,4,15] but the polymer was only used as a binding material, as a solid carrier, in which the element-organic compound or oxide of the dopant element is distributed with a greater or lesser degree of uniformity and homogeneity.

In fact, a uniform distribution of the dopant element in a polymer film can be accomplished by bonding it chemically to the polymer or by its complete solubility in the polymer. A chemical bond may develop as a result of the photostructuring process or preexist when a suitable element-organic polymer is used. Here exact dosing of the dopant becomes possible by varying its concentration in the composition. In addition, the possibility of introducing almost any dopant into the composition of a polymer diffusant, as well as several dopant elements simultaneously, has been demonstrated.

The interesting experimental data that were obtained in the first 6–7 years on compositions of polymer diffusants and their applications in the semiconductor technology of silicon power devices were summarized in a book by Guk *et al.*[2] However, the high level of the results obtained up to

that time has led to continued, intense research on these diffusants, both for developing new devices and for expanding the domain of their applications in the technology of devices based on polycrystalline Si and III–V compounds. These results are discussed in this paper.

The purpose of this review article is to acquaint readers with the possibilities for and features of this type of solid-state film sources, as well as with data obtained over the last decade on the use of these sources in scientific research on and device engineering of devices based on Si and the III–V compounds. We shall also point out the prospects for using polymer diffusants in the fabrication of ultrafine (smaller than 100 nm) diffusion regions in Si and for controlling the lifetime of minority charge carriers.

2. DIFFUSION OF DOPANTS FROM POLYMER DIFFUSANTS INTO SI AND III–V COMPOUNDS

In their work on creating polymer diffusant compositions, El'tsov *et al.*[14] settled on the azide-containing photoresists as the most promising basis for chemical modification of photoresists into polymer diffusion sources. Their main components are the light-sensitive, low-molecular aryl azide and a film forming polymer that can be structured. Ultraviolet irradiation causes photolysis of the aryl azide with formation of some extremely reactive intermediate products, the aryl nitrenes. These compounds cause transverse cross linking of the polymer chains, which leads to formation of a phototopograph with the specified properties. The use of element-organic compounds as either the light sensitive or polymer component of the composition makes it possible to form polymer layers which include dopant atoms directly in the composition of a three-dimensional grid, i.e., chemically bonded and uniformly distributed within it. The use of such polymer layers as diffusion sources makes precise and smooth control of the amount of dopant in them possible.

After formation of a polymer diffusant layer on the wafers by centrifugation, depending on the type of material used, the diffusion process is initiated either immediately after the film is deposited or after preliminary thermal decomposition in an oxidizing atmosphere. Here the organic compounds decompose and oxides of the dopants form a flat, uniform film on the wafer surface. After thermal decomposition, diffusion takes place for the required time at temperatures of 850–1300 °C in Si and 450–700 °C in III–V compounds. The choice of optimum temperature and decomposition time for the different compounds was based on a comprehensive study of the process and has been described in detail elsewhere.[2]

The first successful experiments with polymer diffusants containing B, P, Al, and other dopants in widespread use for silicon technology showed that the scatter in the surface concentration N_s on 60-mm-diam wafers was $\pm 5\%$ for low and $\pm 3\%$ for high surface impurity concentrations in the diffusion layer for arbitrary diffusion conditions. Good reproducibility of these results from wafer to wafer and from batch to batch was obtained.[2] It was shown that for a given diffusion regime for B, P, Sb, and As, the surface concentration N_s is determined only by the amount of impurity introduced into the composition of the polymer diffusant per unit surface area of the wafer. This distinguishes polymer diffusants favorably from diffusants based on TEOS, for which the surface impurity concentration depends nonlinearly on the amount of it in the composition.[1]

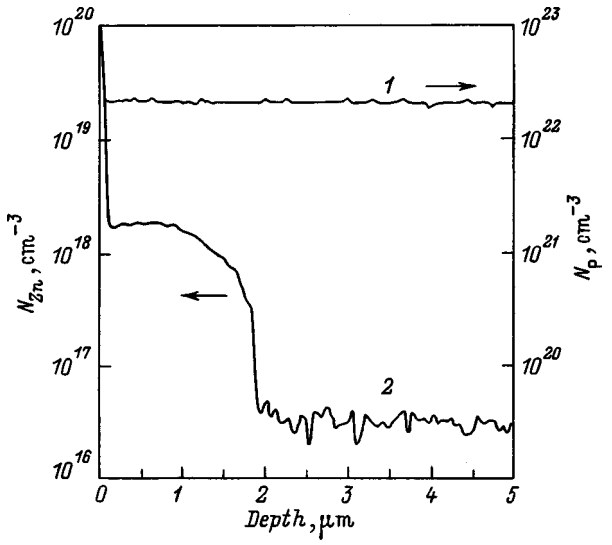

FIG. 1. SIMS profiles of the distribution of phosphorus (*1*) and zinc (*2*) in InP.

Since the diffusion of majority dopants from polymer diffusants into Si has been described in detail in an earlier review article,[2] here we shall discuss the possibilities of this method for silicon technology, which have been established in the last decade, while diffusion into III–V compounds will be described in more detail since this method was developed at the Physicotechnical Institute comparatively recently (in 1990) and has no analogs elsewhere in the world.

2.1. Diffusion of zinc into III–V compounds

As noted above, polymer diffusants are attractive for III–V technology primarily because diffusion is possible in an open system without special efforts to maintain the pressure of the volatile group-V components. Thus, in developing a diffusant, one of the major requirements of the polymer matrix is that it should aid in protecting the semiconductor surface from decomposition. The mechanical transfer of polymer compositions developed for silicon technology is by no means always effective, since they were created for an oxidizing atmosphere and higher temperatures. Oleophilic polymers containing Zn have been used for various III–V compounds. Using InP, the first experiments[16,17] showed that the polymer matrix of the diffusant forms a layer on the semiconductor surface that inhibits decomposition of the substrate; this makes it possible to carry out diffusion of zinc at temperatures up to 650 °C for a few hours. The absence of significant decomposition of the surface after diffusion of Zn into n^0-InP at 500 °C is indicated by the distribution of phosphorus in the diffusion layer of the InP (Fig. 1, curve *1*) measured by secondary-ion mass spectrometry (SIMS). Analogous results have been obtained for GaAs and the solid solutions InGaAs, InGaAsP, AlGaAs, InAlAs, and InGaP.

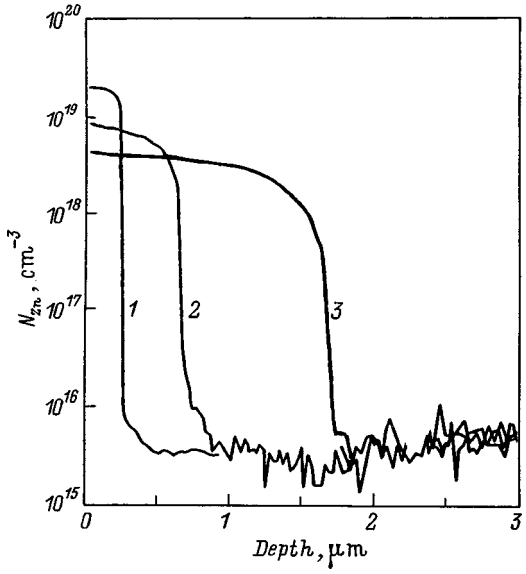

FIG. 2. SIMS profiles of the distribution of Zn in GaAs (*1*), InGaAs (*2*), and InGaAsP (*3*).

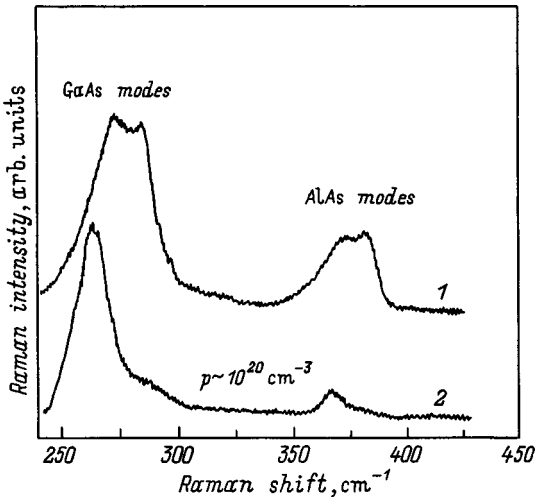

FIG. 3. Raman scattering spectra before (*1*) and after (*2*) diffusion of Zn into $Al_{0.2}Ga_{0.8}As$.

The distribution profiles of Zn (Figs. 1 and 2) have a form similar to that obtained by traditional methods.

Data on the effective diffusion coefficient for InP, InGaAsP, InGaAs, GaAs, InAlAs, and AlGaAs are listed in Table I (prior to diffusion the electron concentration in these materials was $5\times10^{16}-10^{17}$ cm^{-3} (Refs. 18 and 19).

The values of the effective diffusion are close to those obtained for these materials by other methods.[20–22] There is a clear tendency toward a noticeable increase in the diffusion coefficient with an increasing indium content in the indium-containing compounds and aluminum in the aluminum-containing compounds. This tendency indicates that the diffusion of Zn is controlled by the self-diffusion of indium, gallium, and aluminum and proceeds by a ''kick-out'' mechanism. Quantitative estimates are difficult, since the self-diffusion of indium has been determined inaccurately and data on its concentration and temperature dependences are lacking.

Published data[23] imply that the dependence of the depth at which the $p-n$ junction lies (x_j) on the diffusion time (t) has the same form ($x_j^2\propto t$) as when traditional diffusion methods are used.[20,21] The polymer film can be regarded as an unbounded diffusion source for process times less than 2 h and temperatures below 650 °C.

TABLE I. Effective diffusion coefficients of Zn in III–V compounds.

Material*	Diffusion temperature, °C	D_{eff}, 10^{-12} cm^2/s
InP	500	9.4
$In_{0.8}Ga_{0.2}As_{0.39}P_{0.61}$	500	9.4
$In_{0.73}Ga_{0.27}As_{0.63}P_{0.37}$	500	7.3
$In_{0.58}Ga_{0.42}As_{0.9}P_{0.1}$	500	3.6
$In_{0.53}Ga_{0.47}As$	500	2.7
GaAs	650	0.1
$Ga_{0.85}Al_{0.15}As$	650	0.9
$Ga_{0.55}Al_{0.45}As$	650	9.1
$In_{0.5}Al_{0.5}As$	500	9.4

Note: The diffusion time is 30 min.
*The electron concentration prior to diffusion was $5\times10^{16}-10^{17}$ cm^{-3}.

2.1.1. Diffusion of Zn in $Al_xGa_{1-x}As$. Published data on the diffusion of Zn by traditional methods in $Al_xGa_{1-x}As$/GaAs structures are quite contradictory, both in terms of the values of the diffusion coefficient and regarding the solubility limit of Zn.[22,24–29] The contradictions among these data are related to the following factors: nonreproducibility of the diffusion conditions, uncontrolled distribution of the intrinsic defects in the skin layer of the AlGaAs, and uncontrolled composition of the solid solution with regard to Al in the skin layer which differs from the bulk composition.

A study of the diffusion of Zn from polymer diffusants into layers of $Al_xGa_{1-x}As$ ($x=0.05-0.54$)[19] showed that this method can be used to reduce the influence of these factors on the results of the diffusion. Homogenization of the composition of $Al_xGa_{1-x}As$ in the surface region to a depth of up to 0.2 μm has been observed after diffusion of Zn.[30] The effect showed up in Raman scattering spectra of these layers before and after Zn diffusion. Some Raman spectra are shown in Fig. 3. Before diffusion (curve *1*) four bands were observed in the spectra which corresponded to LO-phonons at 273 and 284 cm^{-1} (GaAs phonons) and at 370 and 381 cm^{-1} (AlAs phonons). These bands indicated the existence of two layers with different amounts of Al ($x=0.2$ and $x=0.4$) in the skin layer of the sample. After diffusion of Zn, only two peaks (263 and 360 cm^{-1}) were observed in the spectra, which corresponded to highly doped ($p\sim10^{20}$ cm^{-3}) $Al_{0.2}Ga_{0.8}As$. The presence of a weak shoulder at 295 cm^{-1} in the Raman spectrum showed that a surface layer with a low AlAs content ($x\leqslant0.1$) was formed.

Studies of the Raman spectra from different portions of wafers showed that before diffusion the nonuniformity in the Al content in the surface layer of the solid solution was as high as 200% over the area of a 30×30 mm^2 wafer. After diffusion, the deviation in the Al content for the same wafers was less than 15–20%. Besides homogenization of the com-

position, a drop in the Al content in the surface region was observed to a depth of 0.1–0.2 μm.

For all the compositions that were studied, after diffusion it was possible to obtain hole concentrations in the surface layer in the range from 2×10^{19} to 10^{20} cm^{-3} and the depth of the $p-n$ junction for $x=0.05$ and 0.2 was almost an order of magnitude lower than for $Al_xGa_{1-x}As$ with $x=0.5$.

2.1.2. Diffusion of Zn in InP. In InP it is by no means always possible to attain 100% activation of Zn implanted by traditional diffusion methods.[31,32] The concentration of holes in the doped layer is only 10–20% of the concentration of the implanted Zn.[33] It has been shown[19] that the choice of the concentration of Zn (N_{Zn}) in the skin layer is important from the standpoint of complete activation of the introduced impurity, and that it must not exceed the solubility limit (L_{Zn}) at the diffusion temperature. When polymer diffusants are used, it is easy to attain the optimum N_{Zn} in the polymer solution. Polymer films containing no more than 10% of Zn by volume are the most useful films, as indicated in Ref. 23, for obtaining Zn-doped diffusion layers in InP. In this case, according to SIMS and Raman scattering data, the hole concentration in the diffusion layer corresponds to the concentration of introduced Zn. These data correlate well with the activation energy of the zinc, $Q=0.53$ eV (Ref. 23), obtained from the temperature dependence of the diffusion coefficient D_{eff}. Theoretical estimates[34] for electrically active zinc occupying crystal lattice sites give an activation energy of 0.37 eV, and for neutral interstitial Zn the activation energy is $Q=1.25$ eV. Experiments where Zn has been introduced by other methods have yielded different values, $Q=0.3-0.4$ eV (Refs. 34 and 35) and $Q=1.3-1.6$ eV (Refs. 20, 36, and 37).

In addition to a different degree of activation produced as a result of changing the relationship between N_{Zn} and L_{Zn}, we also see a change in the shape of the Zn distribution profile. Figure 4 shows SIMS profiles of the distribution of Zn atoms in InP after diffusion at 500 °C for 30 min for two source concentrations of Zn (1% and 20%). The profile of curve *1* corresponds to $N_{Zn}<L_{Zn}$ (1% Zn) and its shape is well known from many papers (e.g., Ref. 20). This form of the Zn distribution can be regarded as typical for Zn diffusion into III–V compounds. An anomalous Zn distribution profile shape for $N_{Zn}>L_{Zn}$ (20% Zn, curve *2*) has also been reported in several papers,[38] where it was attributed to rapid defect formation in the diffusion region.

Thus, the data from studies of the steady-state diffusion of Zn into n^0-InP and *i*-InP from polymer film diffusants are in good agreement with data obtained by other diffusion methods. However, in the former case, the data were obtained more simply in an open system without maintaining the vapor pressure of the volatile component of the III–V compound. In addition, the ability to completely activate the introduced Zn without subsequent annealing is an important feature of this method that is not always feasible by other methods.

Carrying out the diffusion process in an open system without maintaining the vapor pressure of the volatile component of the III–V compound makes it easy to investigate the different stages of the diffusion process under identical conditions, which is not always possible with the other methods. These investigations are of interest from the standpoint of studying defect formation, clarifying the behavior of nonequilibrium intrinsic defects and their interactions with doping impurities, and understanding the diffusion mechanism.

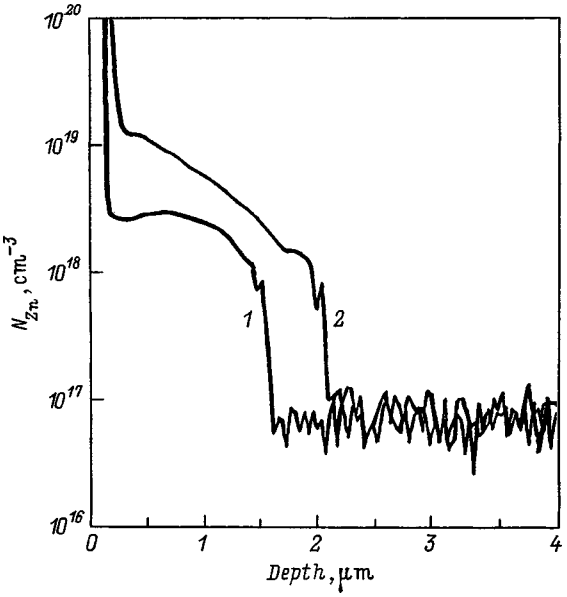

FIG. 4. SIMS profiles of the distribution of Zn in InP after diffusion at 500 °C for 30 min. The Zn concentration in the source is 1% (*1*), 20% (*2*).

Data of this sort have been published for InP.[19,23,39] These studies[23] have revealed a number of interesting features of the initial, furthest from equilibrium and least studied, stage of the diffusion process:

–In the initial stage of diffusion, anomalously rapid diffusion of Zn atoms is observed with $D_{eff}\sim10^{-8}$ cm^2/s at 375 °C, or two to four orders of magnitude higher than D_{eff} for steady-state diffusion.

–The degree of activation of the introduced Zn is low, less than 50%.

–The shape of the Zn profile after the initial state of diffusion at temperatures below 500 °C differs noticeably from that after steady-state diffusion (Fig. 5, curves *1* and *2*). The greatest deviation is observed for $N_{Zn}>L_{Zn}$.

–The shape of the Zn profile in semi-insulating *i*-InP obtained after the initial stage of diffusion is similar to the profiles obtained after steady-state diffusion; i.e., it contains a plateau between two different diffusion fronts.[40]

–The initial stage of diffusion is accompanied by the generation of many microscopic defects.[23,39] Defect formation is greatest for $N_{Zn}>L_{Zn}$. Here the region in which defect formation is observed extends into the volume of the semiconductor to a greater depth than the diffusion front. Comparative studies of the distribution of dislocations and microscopic defects over the depth of the diffusion layers, following the different stages of the diffusion process, have clarified the behavior of the nonequilibrium intrinsic defects[23] and shown that the defect formation and diffusion processes evolve very dynamically with time, and that this

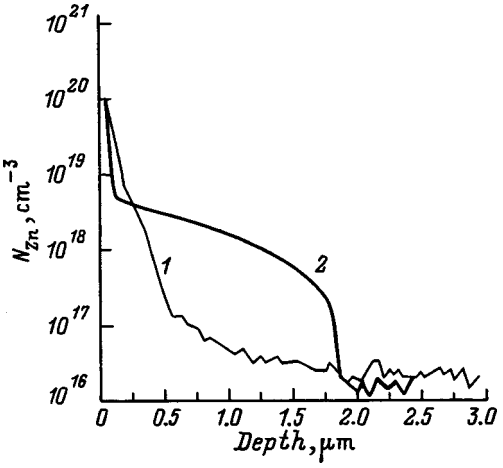

FIG. 5. SIMS profiles of the distribution of Zn in InP after an initial stage of diffusion up to a temperature of 450 °C (*1*) and after stationary diffusion at 450 °C for 30 min (*2*).

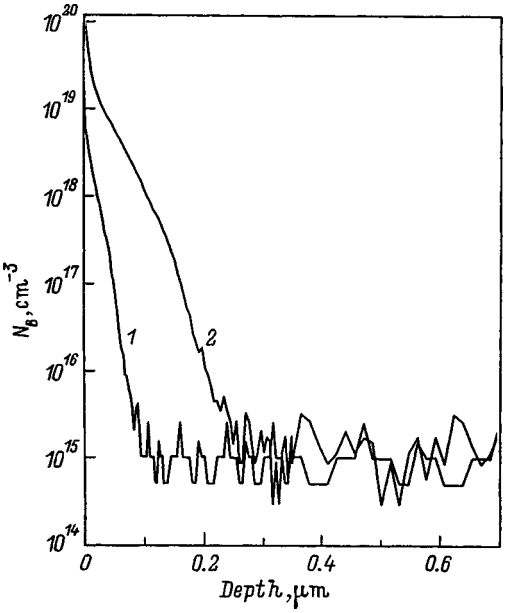

FIG. 6. SIMS profiles of the distribution of B in Si after diffusion at (*1*) 900 °C for 10 min and (*2*) 1000 °C for 10 min.

dynamics has essentially been ignored in theoretical analyses of impurity diffusion.

2.2. New possibilities for this method in silicon technology

In the last decade several possibilities for diffusion from polymer diffusants have been elucidated, including the fabrication of ultrashallow diffusion layers, controlling the lifetime of charge carriers, and using this method effectively in scientific studies. In particular, the use of polymer diffusants has made it possible to conduct direct studies of the effect of sulfur on the parameters of high-voltage devices.

2.2.1. Fabrication of ultrashallow diffusion layers. It is well known that the traditional diffusion methods do not ensure the reproducible production of shallow (less than 100 nm) doped and lightly doped (less than 10^{18} cm^{-3}) regions in Si and this has been the reason for a switch from diffusion technologies to ion implantation for the production of silicon MOS structures and integrated circuits.

The studies reported in Ref. 4 showed that the use of polymer diffusants as a source of dopant impurities yields extremely encouraging results. By changing the concentration of the dopant in a polymer diffusant it is possible to reproducibly vary the impurity concentration in the skin layer from 5×10^{17} to 10^{21} cm^{-3}, and by choosing the temperature and time regime, it is possible to achieve complete activation of the introduced impurity and obtain doped regions with dimensions less than 100 nm. Figure 6 shows SIMS profiles of the distribution of boron.

2.2.2. Controlling the lifetime of minority charge carriers. Developers of semiconductor devices face various problems: a material with a short minority carrier lifetime is preferable for fast-response devices, while a material with a long minority carrier lifetime is preferable for high-voltage diodes and solar cells. These polar opposite problems can be solved using polymer diffusants for controlling the lifetime in the active region of the device. To obtain a long lifetime during high-temperature heat treatments, it is common practice to use methods which prevent the penetration of undesired impurities and Schottky defects from the wafer surface into its volume[42,43] or methods which make it possible to remove undesired impurities from the bulk, such as liquid-phase gettering[44] or gettering followed by prolonged annealing at temperatures where the solubility of recombination centers is low and the diffusion coefficients are large (700–900 °C).[45] It has been shown[46] that by using polymer diffusion sources it is possible to obtain long hole and electron lifetimes (τ_p and τ_n) in silicon $p-i-n$ structures even when high-temperature heat treatment is done in air. The best results ($\tau_p, \tau_n = 150-300\ \mu$s) are close to those for the original single crystals.

In order to obtain a material with a short minority charge carrier lifetime by the traditional method for creating high-power, high-frequency diodes, a silicon structure with $p-n$ junctions is usually formed and then at a higher temperature (800–900 °C) atoms of Au or Pt are introduced to create the required concentration of recombination centers in the base. The development of polymer diffusion sources including gold element-organic compounds in their compositions has made it possible for the first time to propose a method for diffusion of deep impurities from a bounded source. As a result, a high uniformity of the gold concentration was obtained in the bulk of the wafer; the concentration profile of N_{Au} did not have a U-shape. Layer-by-layer measurements of the gold concentration showed that the scatter in N_{Au} was less than 5% over the depth and over the area of the wafer. This method made it possible to obtain reproducible results, regardless of the history of the sample; the density of dislocations and the concentration of the shallow impurity had essentially no effect on the results. It was possible to obtain N_{Au} of $10^{13}-10^{15}$ cm^{-3} with good reproducibility and carry out this process at the high temperatures (900–1200 °C) typical of the diffusion of shallow impurities.[2]

The feasibility of the combined diffusion of boron and platinum has been investigated.[47] This was done on ground and polished wafers of *n*-Si with $\rho_0 = 5\,\Omega\cdot$cm. After a film of

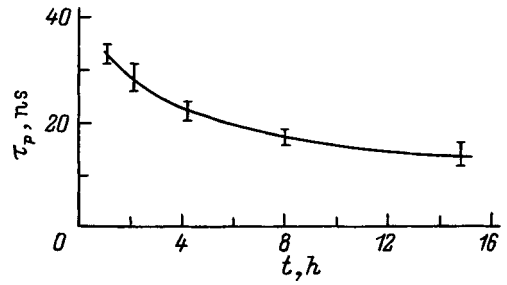

FIG. 7. Hole lifetime as a function of the time for combined diffusion of Pt and B.

the polymer diffusant was formed, it was decomposed at 450 °C for 30 min and diffusion was carried out in air in the specified regime.

The concentration and the uniformity of the distribution of Pt were estimated from the magnitude and uniformity of τ_p in the base of the diode structures. For otherwise equal conditions (for example, with diffusion for an hour at 1200 °C), τ_p in the wafers with a ground surface is 3–4 times smaller than in the polished wafers. Because of the instability of the Pt-Si solid solution, the rate of cooling after diffusion also affects the results of the diffusion. Thus, for example, cooling to 800 °C at a rate of 1 °C/min increases τ_p by several factors. Therefore, air quenching (cooling the wafers to room temperature in a few seconds) was used. When the diffusion time is increased, τ_p falls (Fig. 7). The rise in the Pt concentration with increased diffusion time may have an effect on the diffusion mechanism, which is limited by the influx of vacancies that diffuse from the surface and form in the bulk of the material. This mechanism was observed previously[48] during the diffusion of gold into silicon. Judging from the minimal value of τ_p that was obtained, as well as from the degree of compensation of the resistivity of the base, the maximum solubility of platinum ($\sim 10^{16}$ cm^{-3}) was not obtained in Ref. 47. Increasing the diffusion temperature from 1100 to 1200 °C noticeably increases the uniformity and reproducibility of the results, as well as the platinum concentration.

These experiments[47] were done with sources that contain both an excess of Pt and a low Pt concentration, which provided for diffusion from unbounded and bounded sources and made it possible to vary the lifetime from 10 ns to 10 μs.

2.2.3. Effect of sulfur on the parameters of high-voltage devices. Introducing sulfur into silicon by any conventional method such as in a sealed cell,[49] inevitably causes surface erosion. This circumstance has prevented direct investigation of the effect of sulfur on the parameters of semiconductor devices. Sulfur creates donor levels in silicon with energies $E_d = 0.18$ and 0.37 eV and has a diffusion coefficient that is three orders of magnitude greater than that of Al.[49] The diffusion of sulfur into silicon high-voltage structures from polymer diffusants has been studied.[50] Use of a polymer diffusion source made it possible to control the amount of sulfur per unit wafer area over a wide range, which ensured the complete absence of erosion on the silicon surface. A high surface quality was retained even with the maximum amount of diffusant ($\sim 10^{17}$ cm^{-2}), when the sulfur concentration in the diffusion layer was close to the maximum solubility. A polymer film containing an organic sulfur compound was deposited onto high-voltage diode structures on either *n*-type ($\rho_0 = 20-200\ \Omega\cdot$cm) or *p*-type silicon wafers ($\rho_0 = 10-700\ \Omega\cdot$cm). During diffusion of S, initial thermal decomposition of the polymer film was not carried out because of the extremely high volatility of SO_2. Diffusion was carried out in air at temperatures of 1000–1200 °C and the processing time was varied from 15 min to several hours. After the surface layer was removed, the concentration of electrically active sulfur was monitored.

These studies showed that the diffusion of sulfur into *p*-type Si causes a change in the type of conductivity of the material, while that into *n*-type Si reduces the resistivity ρ. The scatter in the value of ρ over the wafer area is $<5\%$. The concentration of sulfur was essentially independent of the cooling rate, of the concentration of dislocations (in the range $0-2\times10^4$ cm^{-2}), of the type of conductivity, and ρ_0. The S concentration was affected by the surface treatment of the initial wafers, other conditions being the same: in polished silicon it is roughly an order of magnitude higher than in etched silicon. This indicates that sulfur is trapped by a silicon surface only in the initial stage of thermal processing (as in the case of Al diffusion in an oxidizing atmosphere). In other words, we can assume that S diffused from a bounded source. Sulfur penetrates relatively freely through a p^+-layer, while an n^+-layer retards sulfur. Gettering of sulfur introduced into silicon by subsequent diffusion of phosphorus is inefficient. Thus, after diffusion of phosphorus for 4 hours at 1230 °C, the concentration of S in a 0.35-mm-thick wafer was only lowered by a factor of 3. At the same time, prolonged annealing of wafers with imbedded sulfur at 800 °C reduced its concentration only slightly. In the latter case, gettering as a result of the decomposition of the solid solution proceeded slowly, since the diffusion coefficient of sulfur at 800 °C is too low ($<10^{-10}$ cm$^2\cdot$s^{-1}). The breakdown voltages ($U_{\rm br}$) of the diode structures were lower after introduction of sulfur and were consistent with the resistivity of the base. It should be noted that the low gettering efficiency for sulfur is a positive factor during the deliberate introduction of this element into silicon in the course of device fabrication. However, this also implies that it is necessary to carefully avoid even traces of sulfur in the production sequence for fabrication of high-voltage devices, since sulfur is a cause of lowered breakdown voltages in Si-devices and of thermal instability in Si.[50]

2.2.4. Conclusion of Sec. 2.2. Studies have shown that polymer diffusants greatly extend the set of dopant impurities and their combinations compared to the standard film diffusants and other diffusion methods because of the multiplicity of monomer and polymer element-organic compounds. These features have made it possible for the first time to achieve diffusion of the impurities which create deep levels from organic sources, along with the joint diffusion of these impurities with shallow impurities. As a result, it seemed possible to control the minority charge carrier lifetime in the active region of silicon devices over a range from 10 ns to 10 μs.

Polymer diffusants make it possible to introduce essen-

tially all the required impurities into Si, and to regulate the surface concentration of impurities (N_s) precisely and smoothly over several orders of magnitude, with a high uniformity. In a number of cases (such as the diffusion of sulfur) this method is the only way of avoiding surface erosion. The scatter in N_s across 60-mm-diam wafers is $\pm 5\%$ for low and $\pm 3\%$ for high N_s in the diffusion layer for arbitrary diffusion regimes. These results are as good as those obtained by the conventional methods: diffusion in a gas flow, diffusion from TEOS sources, and ion implantation, but have been obtained by a simpler, more convenient, and cheaper method.

In the technology of semiconducting III–V compounds, the use of polymer diffusants makes it possible to carry out the process in an open system, without special measures to maintain the vapor pressure of the volatile group-V components, in contrast with cell diffusion and diffusion in a carrier-gas flow. In addition, as opposed to the other solid-state film sources, here it is possible to avoid excess mechanical stresses in the surface region of the semiconductor and to ensure complete activation of the dopant impurity.

These prospects and features have predetermined the efficiency of this method in scientific studies, as well as its applications in semiconductor device technology.

3. APPLICATIONS OF POLYMER DIFFUSANTS IN SEMICONDUCTOR DEVICE TECHNOLOGY

The results cited above have made it possible to use polymer diffusants in the technology of high-power silicon semiconducting devices: high-voltage diodes and thyristors, and modulator thyristors comparable in speed with high-power hydrogen thyratrons. It should be noted that the uniformity of the diffusion layers is decisive for the production of modulator thyristors. Increasing this uniformity through the use of polymer diffusants has made it possible to obtain modulator thyristors that have pulse powers of 10^6 W and risetimes of 15–30 ns.[51–55] Polymer diffusants are used for industrial production of the type KU-102 and KU-108 thyristors at the Svetlana Company.

Polymer diffusants have been used for the production of various types of solar cells and high-power silicon devices, as well as for creating subcontact layers in AlGaAs/GaAs light-emitting diode structures and $p-n$ junctions in InGaAs/InP photodetector structures for fiber optics communications.

3.1. Clipper diodes

One application of polymer compositions, which ensure a maximum surface concentration of boron, is the creation of high-power, fast diodes with a response time of 10^{-11} s for protection from momentary overvoltages. A study[56,57] has been made of the properties of silicon clipper diodes fabricated using polymer diffusion sources. The measurements showed that in some of the diodes there is no microplasma, even for diodes with areas exceeding 1 cm^2, while in the remainder the breakdown voltages for the first microplasma are very close to the breakdown voltage in the main area of the $p-n$-junction. This kind of breakdown can be regarded as quasiuniform. The magnitude of the differential resistance in the linear segment of the reverse branch of the pulsed current-voltage characteristic of the diodes served as a measure of the uniformity of the diode breakdown. As the experiments and calculations showed, the major factor determining the magnitude of the differential resistance for pulses lasting on the order of or more than 10^{-5} s is heating avalanche multiplication region by the flowing current. A more uniform breakdown corresponds to more uniform heat release over the diode surface area and, therefore, to a smaller differential resistance. Because of the uniformity of the diffusion layer, diode structures with surface areas of 1–5 cm^2 were obtained. During a breakdown of these structures the avalanche current flows over almost the entire area of the $p-n$ junction, even when the reverse current density is 10 A/cm^2 (for further rises in the current the differential resistance remains constant).

3.2. Solar cells

Shallow $p-n$ junctions in silicon are usually produced either by diffusion from the gaseous phase or by ion implantation. However, it has been shown[58] that polymer diffusants can be used to fabricate shallow diffusion layers (0.3–1 μm) with low scatter in the surface concentration on large area wafers. Boron and phosphorus containing diffusants have been used to make solar cells from commercial single crystal silicon intended for operation with solar concentrators. Their characteristics were similar to those obtained by diffusion from the gaseous phase[59] or by ion implantation.[60] The high filling factor of the current-voltage characteristics (0.82–0.83) provided evidence of a low spread resistance of the frontal emitter layer, and that it might be possible to optimize the layer resistance in conformity with a chosen contact grid. The scatter in the characteristics (short-circuit current 33–35 mA/cm^2 for extraatmospheric (space) solar irradiation, open-circuit voltage 590 mV) of solar cells obtained from a single 60-mm-diam wafer no greater than $\pm 2\%$ for an element size of 4.6×4.6 mm^2.

Profiled polycrystalline silicon is a promising material for solar cell manufacture. Its major disadvantage is a low minority carrier lifetime and, therefore, low solar cell efficiency. One feature of polycrystalline silicon is a rather high density of dislocations, which can also vary over wide limits from grain to grain. This parameter has a strong effect on the electrical characteristics of polycrystalline silicon, including on the minority carrier lifetime. A study has been made[61] of a high-temperature gettering process for profiled polycrystalline silicon produced by the Stepanov method and intended for the manufacture of large area solar cells. The gettering efficiency was studied as a function of the density of dislocations in the original material. Within the confines of a grain the density of dislocations oscillated about certain constant values which are different for different grains (from 10^2 to 10^8 cm^{-2}). Diode mesostructures were formed on polycrystalline grains with a certain density of dislocations.

The gettering efficiency was estimated from the magnitude of the electron lifetime τ_n at a high injection level measured by a method described by Lax and Neustadter.[62] The

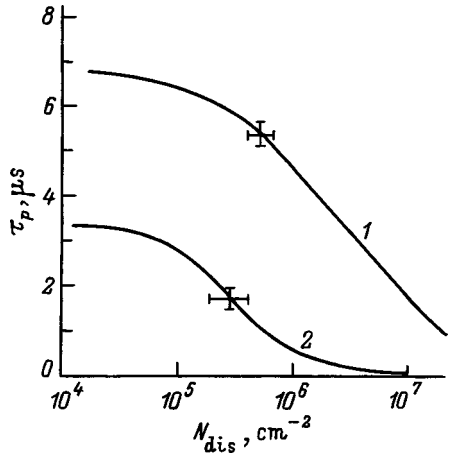

FIG. 8. The lifetime of minority charge carriers (τ_n) as a function of the density of dislocations (N_{dis}) in polycrystalline silicon wafers: (*1*) subjected to high-temperature gettering by a phosphorus containing polymer diffusant followed by low-temperature annealing and (*2*) control samples subjected only to low-temperature annealing.

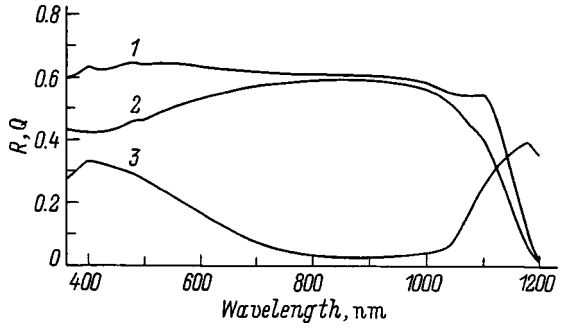

FIG. 9. Spectral characteristics of concentrator solar cells: (*1*) effective internal collection coefficient $[Q/(1-R)]$, (*2*) external collection coefficient (Q), and (*3*) reflectivity of the front side (R).

data on the density of dislocations and τ_n were averaged over a large number of samples. A phosphorus containing polymer source was used as a getter. High-temperature gettering was performed for two hours at 1200 °C. The surface concentration of phosphorus in the diffusion layer was 10^{21} cm^{-3}. Subsequent low-temperature annealing (700 °C) was performed in order to enhance the extraction of metallic impurities. After removal of the n^+-layer a shallow n^+-p junction was formed on the wafers at 850 °C with a surface concentration on the order of 10^{20} cm^{-3}. A high-efficiency of high-temperature gettering, which made it possible to raise τ_n by several factors, was demonstrated. The gettering efficiency depends on the number of dislocations in the polycrystalline silicon. Figure 8 implies that a greater gettering effect is attained in regions with low and medium densities of dislocations. For densities of dislocations of 10^2-10^3 cm^{-2}, on isolated mesostructures τ_n was as high as 20 μs. For densities of dislocations greater than 10^7 cm^{-2}, τ_n remains small, at less than 1 μs. As a result of high-temperature gettering, the excess loss currents in the n^+-p junctions caused by metallic precipitates in the space charge region were reduced to 10^{-7} A/cm^2 and the diffusion currents were reduced to 10^{-11} A/cm^2, while the ideality coefficient of the current-voltage characteristics approached unity.

3.3. Multijunction silicon concentrator solar cells

Solar cells intended for converting concentrated solar radiation have been under development for many years.[63,64] The most important problem that arises when solar radiation is highly concentrated is to obtain a series resistance of the concentrator solar cell of no more than $R_s=10^{-2}-10^{-3}$ Ω·cm^2. In the course of developing the traditional structures with $p-n$ junctions, whose area is perpendicular to the incident solar flux, some mutually contradictory requirements inevitably arise for the layer resistance of the emitter, the spectral sensitivity, the shadowing created by the contact grid, etc. In this design for concentrator solar cells it is therefore not possible to obtain small R_s and the efficiency of these cells rises as the illumination intensity is raised to 60–80 suns and then falls. Besides the traditional structures with ''horizontal'' $p-n$-junctions, multijunction concentrator solar cell structures have also been made with vertical $p-n$ junctions,[63] which meet the requirements imposed on concentrator solar cells very much better.

Collector solar cells have been fabricated using *p*-type silicon wafers (KDB-12 brand) with diameters of 40–60 mm and thicknesses of 300 μm upon which a p^+-p-n^+ structure was deposited by gradual diffusion of boron and phosphorus from polymer sources.[2] The thickness of the diffusion layers was 1 μm. After the phosphorus diffusion, the wafers were annealed for 15 hours at 720 °C to getter the deep-level impurities. This technique gives an electron lifetime (measured by the Lax method) of 45–55 μs; i.e., the electron diffusion length exceeded the base thickness.[65,66]

The spectral dependence of the reflectivity (R) of one of the samples is shown in Fig. 9 (curve *3*). Compared to a single-layer coating, a two-layer antireflection coating gives a wider spectral region for small values of the reflectivity; R is less than 5% for $\lambda=710-1010$ nm. The spectral dependence of the carrier collector coefficient (Q) for the same sample is shown as curve *2* in Fig. 9, and that of the effective collection coefficient, $Q/(1-R)$, as curve *1*. As can be seen from these data, these multijunction collector solar cells have a high sensitivity in both the infrared (IR) and ultraviolet (UV). In the IR, the high (rate of) collection of minority carriers is the result of a reduced distance (compared to a planar structure) covered by the carriers before they are separated by the vertical $p-n$ junctions. In the UV, we see a high rate of carrier collection, because the UV radiation is absorbed, not in the heavily doped emitter, but directly in the lightly doped base, which has a long diffusion length and low rate of surface recombination. Thus, the effective carrier collection coefficient is essentially independent of wavelength in a wide range of wavelengths (340–1080 nm).

The short-circuit current (I_{sc}) per photoactive surface of a single structure was 27.5–30 mA/cm^2 (AM0, 25 °C). A characteristic of one of the samples for a concentration $K=22$ of the solar radiation is shown in Fig. 10. The open-circuit voltage (U_{oc}) across this concentrator solar cell reached 2350 mV, $I_{sc}=8$ mA, and the filling factor (FF) was 0.8. The large value of FF is evidence of a low series

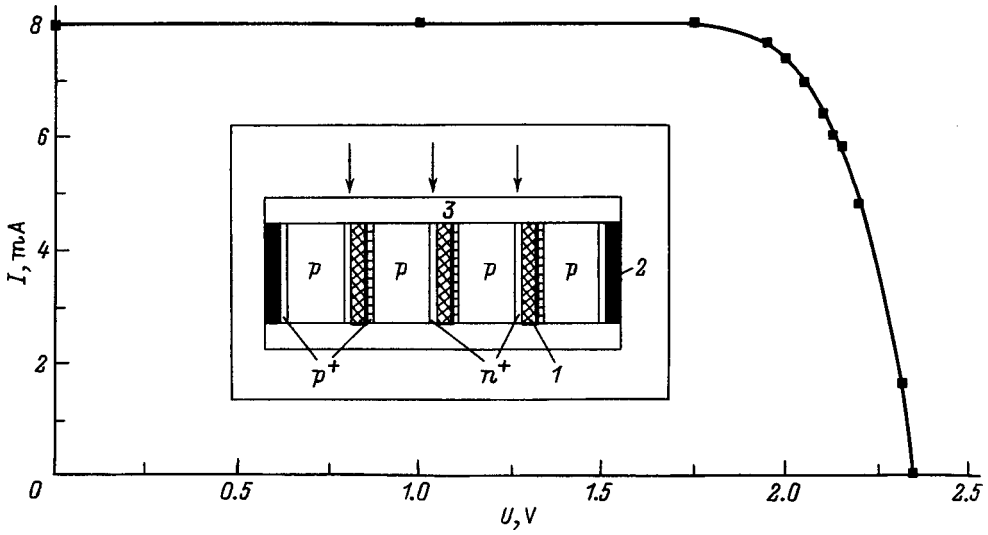

FIG. 10. Load characteristic of a concentrator solar cell containing four series-connected $p-n$ junctions for an illumination intensity of 22 suns. The inset shows the structure of the collector solar cell: (*1*) silumin, (*2*) electrode, (*3*) antireflecting coating.

resistance ($\sim 10^{-2}\ \Omega\cdot\mathrm{cm}^2$) per structure, which has been attained as a result of the continuous metallization of the heavily doped p^+- and n^+-layers. The radiative conversion efficiency (η) for an irradiation power of 22 suns exceeds 11% (AM1.5).

Therefore, this technology has made it possible, for the first time, the fabrication, from commercial silicon, of concentrator solar cells with vertical $p-n$ junctions that have entirely satisfactory characteristics. Their high sensitivity in the UV means that these structures can be used as sensors in this region of the spectrum.

3.4. Photodetectors

The diffusion of Zn from polymer films has been used to create p^+-regions and $p-n$ junctions in $In_{0.53}Ga_{0.47}As/InP$, $p-i-n$-photodiodes intended for operation in fiber optics communication lines. The design of the $p-i-n$-photodiode is shown in the inset in Fig. 11 (Ref. 67). The structure was grown by liquid-phase epitaxy on an InP substrate. An original method for growing pure (with concentrations below 10^{16} cm^{-3}) layers of solid solutions, which is based on gettering of background impurities by a solution-alloy doped with rare-earth elements, was used to obtain the *i*-layer. The *i*-layer in the photodetector structures had a concentration on the order of 10^{15} cm^{-3} and a mobility of $(1.0-1.5)\times 10^4$ $\mathrm{cm}^2/(\mathrm{V}\cdot\mathrm{s})$ at 300 K.[67] Diffusion was carried out in a window of an SiO_2 mask shaped by photolithography. The same mask served to protect the periphery of the $p-n$ junction. The important feature of these photodetectors is the combination, in a single device, of high-response time ($\lesssim$100 ns), sensitivity, and low dark currents.

Figure 11 shows current-voltage characteristics of InP and InGaAs $p-i-n$-photodiodes obtained under various diffusion conditions. These studies made it possible to find the optimum conditions for producing local $p-n$ junctions with dark-current densities of 5×10^{-7} $\mathrm{A/cm}^2$ for a reverse bias of 5 V. It should be noted that these values match those for their best known equivalents.[68]

This method also can be used to raise the yield percent of suitable $p-n$ junctions with low dark currents (Fig. 12, histogram 1) compared to cell diffusion (Fig. 12, histogram

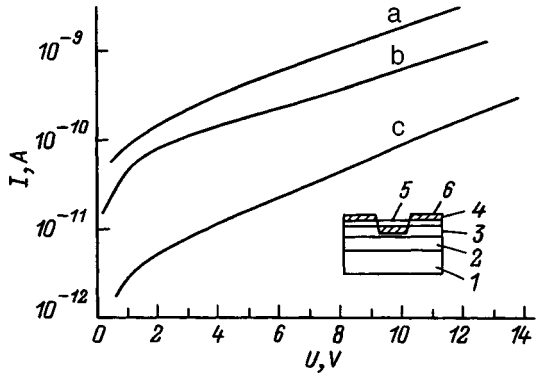

FIG. 11. The reverse branches of current-voltage characteristics ($T=300$ K) of $p-n$ junctions obtained under the following diffusion conditions: (a) $T=550$ °C, 30 min, $N_{Zn}>L_{Zn}$; (b) $T=550$ °C, 30 min, $N_{Zn}<L_{Zn}$; (c) $T=450$ °C, 30 min, $N_{Zn}<L_{Zn}$. The inset is a sketch of the design of a $p-i-n$ photodiode structure: (*1*) *n*-InP:Sn; (*2*) n^0-InP buffer layer; (*3*) narrow-band *n*-InGaAs (InGaAsP) layer with a wide gap $E_g=0.73(0.8)$ eV; (*4*) SiO_2; (*5*) *p*-InGaAs (InGaAsP); (*6*) *n*-InGaAsP with $E_g\simeq 1.0$ eV.

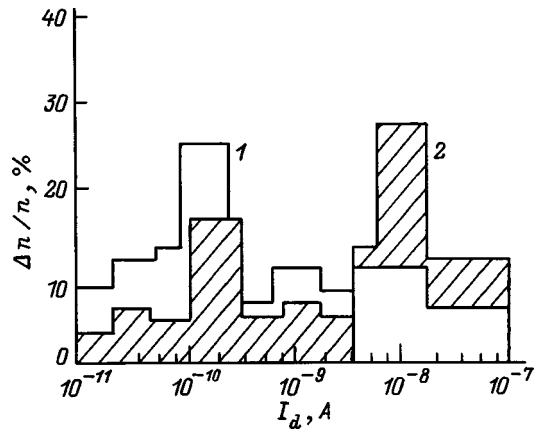

FIG. 12. Histograms of the distribution over a wafer of the dark current I_d for a reverse bias voltage $U=5$ V across $p-n$ junctions obtained by diffusion from polymer diffusants (histogram 1) and by cell diffusion (histogram 2).

2) and, most importantly, to increase substantially the reproducibility of the results from one process batch to the next. It also saves the preparer from having to perform such operations as pumpdown, sealing and unsealing quartz cells, and weighing the suspensions that form the diffusion source.

3.5. Light-emitting diodes

The technology developed here has been used to create heavily doped subcontact layers for $Al_xGa_{1-x}As$/GaAs light-emitting diode structures for the purpose of reducing the contact resistance.[22] Prior to diffusion the structures had cutoff voltages of 1.7 and 2.0 V for light-emitting diodes at $\lambda = 0.80$ and $\lambda = 0.66\ \mu$m, respectively. The layers of $Al_xGa_{1-x}As$ into which the Zn was diffused had the following composition: $x = 0.14-0.15$, $0.20-0.22$, and $0.52-0.54$ for light-emitting diodes with emission wavelengths $\lambda = 0.87$, 0.80, and 0.66 μm, respectively. Diffusion was carried out in the upper layer using the method described in Ref. 19.

In all the samples the concentration of holes in the surface layer after diffusion ranged from 2×10^{19} to 10^{20} cm^{-3} with the depth of the $p-n$ junction for the compositions with $x = 0.05$ and $x = 0.2$ almost an order of magnitude smaller than for $Al_xGa_{1-x}As$ with $x = 0.5$. In addition, after diffusion the skin layer of the structures was homogeneous in terms of its Al content. The deviations in the composition were less than 15–20% over the wafer area.

Comparative studies of light-emitting diode structures with emission wavelengths $\lambda = 0.8$ and 0.66 μm before and after diffusion demonstrated an effective reduction in the contact resistance. Because of the formation of a doped layer, the threshold voltages were lowered from 1.7 to 1.5 V for light-emitting diodes with $\lambda = 0.8\ \mu$m and from 2.0 to 1.8 V for those with $\lambda = 0.66\ \mu$m for a forward current of 10 mA.

4. CONCLUSIONS

It has been shown that polymer diffusants have the following advantages over other solid state film sources: a more uniform distribution of a dopant impurity over the semiconductor surface, the possibility of precise and smooth regulation of the dopant concentration beginning at 10^{17} cm^{-3} for shallow-level impurities and at 10^{13} cm^{-3} for deep-level impurities, the simultaneous inclusion of several dopant impurities in the diffusant, and other advantages. It is possible to avoid nonlinear dependences of the dopant impurity concentration at the semiconductor surface on its concentration in the diffusant, excess mechanical stresses at the surface, and incomplete activation of an introduced impurity. In addition, it is possible to fabricate local doped regions by creating a microprofile using photosensitive polymers as a photolithography base, as well as by diffusion through an SiO_2 mask. These advantages have made it possible to obtain an entire series of semiconductor devices with unique characteristics.

[1] A. I. Borisenko, V. V. Novikov, N. E. Prikhid'ko, I. M. Mitnikova, and L. F. Chepik, *Thin Inorganic Films in Microelectronics* [in Russian], Nauka, Leningrad (1972).
[2] E. G. Guk, A. V. El'tsov, T. A. Yurre, and V. B. Shuman, *Photoresist-diffusants in Semiconductor Technology* [in Russian], Nauka, Leningrad (1984).
[3] K. D. Beyer, J. Electrochem. Soc. **123**, 1556 (1976).
[4] K. D. Beyer, J. Electrochem. Soc. **124**, 630 (1977).
[5] A. B. Lyubashevskaya, L. A. Kataeva, and L. A. Bobrov, Voprosy radioélektroniki, ser. OT, No. 9, 17 (1968).
[6] N. E. Prikhikd'ko, A. I. Borisenko, L. F. Chepik, V. V. Novikov, and I. M. Mitnikova, Voprosy radioélektroniki, ser. TPO, No. 1, 20 (1970).
[7] D. B. Zee, Solid-State Electron. **10**, 623 (1967).
[8] V. Ramamurthy, ASTM. Special Technicial Publication. *Fourth International Symp. on Semicond. Processing* (San. Jose, CA, USA, 1987), p. 95.
[9] S. T. Ten and D. G. S. Chuan, Sol. Energy Mater. **19**, 237 (1989).
[10] B. Unger, U. Schade, M. Hannert *et al.*, Proc. SPIE **1128**, 17 (1990).
[11] N. Arnold, R. Schmitt, and K. Heime, J. Phys. D, Appl. Phys. **17**, 443 (1984).
[12] H. Albrecht and Ch. Lauterbach, Jpn. J. Appl. Phys. **25**, Part 2, L589 (1986).
[13] D. L. Murrell, Semicond. Sci. Technol. **5**, 414 (1990).
[14] A. V. El'tsov, E. G. Guk, and T. A. Yurre, Pis'ma Zh. Tekh. Fiz. **1**, 257 (1975) [Sov. Tech. Phys. Lett. **1**, 123 (1975)].
[15] Pat. USA (1993) No. 5094976.
[16] S. V. Belyakov, L. A. Busygina, A. T. Gorelenok, A. V. Kamanin, V. A. Kukatov, A. V. Merkulov, I. A. Mokina, N. M. Shmidt, and T. A. Yurre, Pis'ma Zh. Tekh. Fiz. **18**, 35 (1992) [Sov. Tech. Phys. Lett. **18**, 486 (1992)].
[17] B. Ya. Ber, L. A. Busygina, A. T. Gorelenok, A. V. Kamanin, A. V. Merkulov, I. A. Mokina, N. M. Shmidt, I. Yu. Yakimenko, and T. A. Yurre, in *Proceedings of the 17th Conference on Defects in Semicond.* (Gmünden, Austria) [Mater. Sci. Forum **143–147**, 1415 (1994)].
[18] A. V. Kamanin, A. V. Merkulov, A. M. Mintairov, I. A. Mokina, N. M. Shmidt, L. A. Busygina, and T. A. Yurre, in *Proceedings of CAS'95 Int. Semicond. Conf.* (Sinaia, Romania, 1995), p. 293.
[19] A. V. Kamanin, I. A. Mokina, N. M. Shmidt, L. A. Busygina, and T. A. Yurre, in *Proceedings of the 8th International Conference on* InP *and Related Compounds* (Schwäbisch Gmünd, Germany, 1996), p. 334.
[20] B. Tuck and A. Hooper, J. Phys. D, Appl. Phys. **8**, 1806 (1975).
[21] M. Glade, J. Hergeth, D. Grützmacher, K. Masseli, and P. Balk, J. Cryst. Growth **108**, 449 (1991).
[22] B. I. Boltax, T. D. Dzhafarov, Yu. P. Demakov, and I. E. Moronchuk, Fiz. Tekh. Poluprovodn. **9**, 825 (1975) [Sov. Phys. Semicond. **9**, 494 (1975)].
[23] A. V. Kamanin, I. A. Mokina, and N. M. Shmidt, Solid-State Electron. **39**, 1441 (1996).
[24] D. R. Campbell and K. K. Shih, Appl. Phys. Lett. **19**, 330 (1971).
[25] C. P. Lee, S. Margalit, and A. Yariv, Solid-State Electron. **21**, 905 (1978).
[26] Y.-R. Yuan, K. Eda, G. A. Vawter, and J. L. Merz, J. Appl. Phys. **54**, 6044 (1983).
[27] V. M. Andreev and O. V. Sulima, Zh. Tekh. Fiz. **54**, 1320 (1984) [Sov. Phys. Tech. Phys. **29**, 761 (1984)].
[28] S. E. Blum, M. B. Small, and D. Gupta, Appl. Phys. Lett. **42**, 108 (1983).
[29] S. K. Ageno, R. J. Roedel, N. Mellen, and J. S. Escher, Appl. Phys. Lett. **47**, 1193 (1985).
[30] B. Ya. Ber, A. T. Gorelenok, A. V. Kamanin, A. V. Merkulov, A. M. Mintairov, I. A. Mokina, N. M. Shmidt, and I. Yu. Yakimenko, in *Proceedings of the 23rd International Symposium Compound Semiconductors* (St. Petersburg, Russia, 1996) [Inst. Phys. Conf. Ser. **155**, 965 (1997)].
[31] R. M. Kundukhov, S. G. Metreveli, and N. V. Siukaev, Fiz. Tekh. Poluprovodn. **1**, 924 (1967) [Sov. Phys. Semicond. **1**, 479 (1967)].
[32] A. Hooper, B. Tuck, and A. J. Baker, Solid-State Electron. **17**, 531 (1974).
[33] G. J. van Gurp, T. van Dongen, G. M. Fontijn, J. M. Jacobs, and D. L. Tjaden, J. Appl. Phys. **65**, 553 (1989).
[34] K. Kazmierski, A. M. Huber, G. Morillot, and B. de Cremoux, Jpn. J. Appl. Phys. **23**, Part 1, 628 (1984).
[35] Y. Matsumoto, Jpn. J. Appl. Phys. **22**, 1699 (1983).
[36] G. J. van Gurp, P. R. Boudewijn, M. N. C. Kempeners, and D. L. Tjaden, J. Appl. Phys. **61**, 1846 (1987).
[37] U. Schade and P. Enders, Semicond. Sci. Technol. **7**, 752 (1992).
[38] T. Y. Tan, S. Yu, and U. Gösele, Opt. Quantum Electron. **23**, S863 (1991).
[39] N. N. Faleev, A. T. Gorelenok, A. V. Kamanin, I. A. Mokina, A. V. Merkulov, E. L. Obukhova, and N. M. Shmidt, in *Proceedings of the 7th International Conference on* InP *and Related Compounds* (Sapporo, Japan, 1995), p. 105.

[40] A. T. Gorelenok, N. N. Faleev, A. V. Kamanin, A. V. Merkulov, I. A. Mokina, E. L. Obukhova, and N. M. Shmidt, in *Proceedings of the 8th Conference on Semi-Insulat.* III–V *Mater.* (Warsaw, Poland) [*Semi-insulating* III–V *Materials*, edited by M. Godlewski (Singapore, World Scientific Co. Pte. Ltd., 1994), p. 279].
[41] B. Ya. Ber, E. G. Guk, A. V. Kamanin, Yu. A. Kudryavtsev, I. A. Mokina, N. M. Shmidt, V. B. Shuman, L. A. Busygina, and T. A. Yurre, J. Vac. Sci. Technol. B **16**, 426 (1998).
[42] H. Shiraki, Jpn. J. Appl. Phys. **14**, 747 (1975).
[43] G. A. Rozgonui, P. M. Petroff, and M. H. Read, J. Electrochem. Soc. **122**, 1725 (1975).
[44] S. J. Silverman and J. B. Singleton, J. Electrochem. Soc. **105**, 591 (1958).
[45] R. V. Konakova and V. B. Shuman, Élektron. tekhn., ser. 2, No. 5, 66 (1970).
[46] E. G. Guk and V. B. Shuman, Voprosy radioélektroniki, ser. TPO, No. 3, 23 (1981).
[47] E. G. Guk, V. B. Shuman, and T. A. Yurre, in *Proceedings Conf. on Technology of HIgh-power Semiconductor Devices* [in Russian], Valgus, Tallin (1987), p. 43.
[48] W. M. Bullis, Solid-State Electron. **9**, 143 (1966).
[49] R. O. Carlson, R. N. Hall, and E. M. Pell, J. Phys. Chem. Sol. **8**, 81 (1959).
[50] E. G. Guk, A. V. El'tsov, S. F. Luizova, V. B. Shuman, and T. A. Yurre, Pis'ma Zh. Tekh. Fiz. **11**, 227 (1985) [Sov. Tech. Phys. Lett. **11**, 93 (1985)].
[51] M. M. Akhmedova, A. F. Kardo-Sysoev, I. G. Chashnikov, and V. B. Shuman, Fiz. Tekh. Poluprovodn. **9**, 817 (1975) [Sov. Phys. Semicond. **9**, 485 (1975)].
[52] V. P. Reshetin and V. B. Shuman, Radiotekh. Elektron. **25**, 436 (1980).
[53] V. B. Shuman, Radiotekh. Elektron. **25**, 1560 (1980).
[54] A. F. Kardo-Sysoev, V. P. Reshetin, and V. B. Shuman, Radiotekh. Elektron. **20**, 1484 (1975).
[55] A. F. Kardo-Sysoev, V. P. Reshetin, and V. B. Shuman, Radiotekh. Elektron. **20**, 1768 (1975).
[56] A. S. Zubrilov and V. B. Shuman, Zh. Tekh. Fiz. **57**, 1843 (1987) [Sov. Phys. Tech. Phys. **32**, 1105 (1987)].
[57] A. S. Zubrilov, O. A. Kotin, and V. B. Shuman, Fiz. Tekh. Poluprovodn. **23**, 607 (1989) [Sov. Phys. Semicond. **23**, 380 (1989)].
[58] E. G. Guk, V. B. Shuman, and M. Z. Shvarts, Pis'ma Zh. Tekh. Fiz. **21**, 40 (1995) [Tech. Phys. Lett. **21**, 258 (1995)].
[59] R. D. Nasby, C. M. Garner, F. W. Sexton, J. L. Rodriguez, B. H. Rose, and H. T. Weaver, Sol. Cells **6**, 49 (1982).
[60] A. R. Kirkpatrick, J. Minnucci, and A. C. Greenwald, IEEE Trans. Electron Devices **ED-24**, 429 (1977).
[61] I. Yu. Volchek, E. G. Guk, V. B. Shuman, and D. V. Tarkhin, Geliotekhnika, No. 4, 26 (1991).
[62] B. Lax and S. F. Neustadter, J. Appl. Phys. **25**, 1148 (1954).
[63] A. Farenbruch and R. Bube, *Fundamentals of Solar Cells*, Academic Press, N.Y. (1987).
[64] M. M. Koltun, *Optics and Metrology of Solar Cells* [in Russian], Nauka, Moscow (1985).
[65] E. G. Guk, N. S. Zimogorova, M. Z. Shvarts, and V. B. Shuman, Zh. Tekh. Fiz. **67**, 129 (1997) [Tech. Phys. **42**, 238 (1997)].
[66] E. G. Guk, T. A. Nalet, M. Z. Shvarts, and V. B. Shuman, Fiz. Tekh. Poluprovodn. **31**, 855 (1997) [Semiconductors **31**, 851 (1997)].
[67] V. M. Andreev, A. T. Gorelenok, M. Z. Zhingarev, L. E. Klyachkin, V. V. Mamutin, N. M. Saradzhishvili, V. I. Skopina, O. V. Sulima, and N. M. Shmidt, Fiz. Tekh. Poluprovodn. **19**, 668 (1985) [Sov. Phys. Semicond. tors **19**, 411 (1985)].
[68] A. J. Moseley, M. Q. Kearley, R. C. Morris, J. Urquhart, M. J. Goodwin, and G. Harris, Electron. Lett. **27**, 1566 (1991).

Translated by D. H. McNeill

ELECTRONIC AND OPTICAL PROPERTIES OF SEMICONDUCTORS

Dielectric peroperties of the semiconducting compounds $Cd_{1-x}Fe_xTe$

P. V. Żukowski, J. Partyka, and P. Węgierek

Technical University of Lublin, Lublin, Poland

J. W. Sidorenko and J. A. Szostak

Belorussian State University, Minsk, Belarus

A. Rodzik

Jagellonion University, Krakow, Poland

(Submitted June 29, 1998; accepted for publication July 1, 1998)
Fiz. Tekh. Poluprovodn. **33**, 270–272 (March 1999)

The dielectric permittivity and conductivity of $Cd_{1-x}Fe_xTe$ compounds ($0<x\leqslant 0.03$) are measured as functions of temperature and frequency. It is found that the Fe atoms are distributed in a correlated fashion in the Cd sublattice. © *1999 American Institute of Physics.* [S1063-7826(99)00203-3]

In a previous paper[1] we studied the permittivity and resistance of $Cd_{1-x}Mn_xTe$ ($0<x\leqslant 0.7$) for alternating currents with frequencies of 100 Hz–10 kHz. There we also presented a model of the experimentally observed, thermally activated growth of the permittivity based on jump charge transfer between neutral defects which brings deep levels into the band gap of semiconductor materials. It turned out that this phenomenon, first observed in silicon bombarded by neutrons from a high-flux beam reactor,[2] is typical of a broad class of semiconductor materials.

We have studied the optical and electrical properties of $Cd_{1-x}Fe_xTe$ compounds.[3,4] It was found that these materials are compensated, semi-insulating semiconductors, and that iron atoms bring deep levels into the band gap. These properties are a prerequisite for the appearance of the additional polarization which is attributable to the jump charge transfer.[1]

In this paper we present the results of an experimental study of the dielectric properties of the semiconductor compounds $Cd_{1-x}Fe_xTe$ ($0<x\leqslant 0.03$). Capacitors with a plate area of about 20 mm^2 were made of 0.45-mm-thick semiconductor wafers with different compositions by depositing silver paste on them for the permittivity measurements. The capacitance and resistance measurements were made using E7-14 (frequencies 0.1, 1, and 10 kHz) and E7-12 (1 MHz) digital impedance meters.

Figures 1 and 2 show plots of the permittivity of $Cd_{1-x}Fe_xTe$ materials for different measurement temperatures and concentrations of iron. The figures show that at low temperatures the permittivity of the samples with different values of x is about 10. As the temperature is raised, ε increases and the increase in ε is delayed as the measurement frequency is increased. The slope of the curves remains constant for a given sample at the different measurement frequencies (see Fig. 1).

The activation energies for jump charge transfer of the defects which cause the rise in ε were estimated from the temperature curves obtained here using the model of Ref. 1.

Figure 3 shows the frequency dependences of the permittivity and conductivity obtained using a VM-507 impedance meter (50 kHz–500 kHz) and a VM-560 Q-factor measurement system (50 kHz–35 MHz). It is clear from this figure that ε for the material $Cd_{0.9965}Fe_{0.0035}Te$ at 77 K is constant over the entire measured frequency range. The permittivity at 300 K is about 10^3 for low frequencies and it

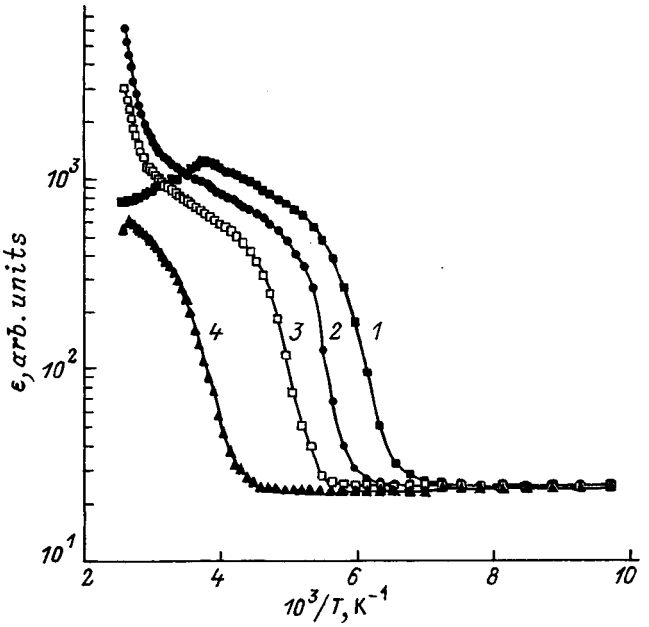

FIG. 1. The permittivity of $Cd_{0.9965}Fe_{0.0035}Te$ as a function of temperature for measurement frequencies of 0.1 kHz (*1*), 1 kHz (*2*), 10 kHz (*3*), and 1 MHz (*4*).

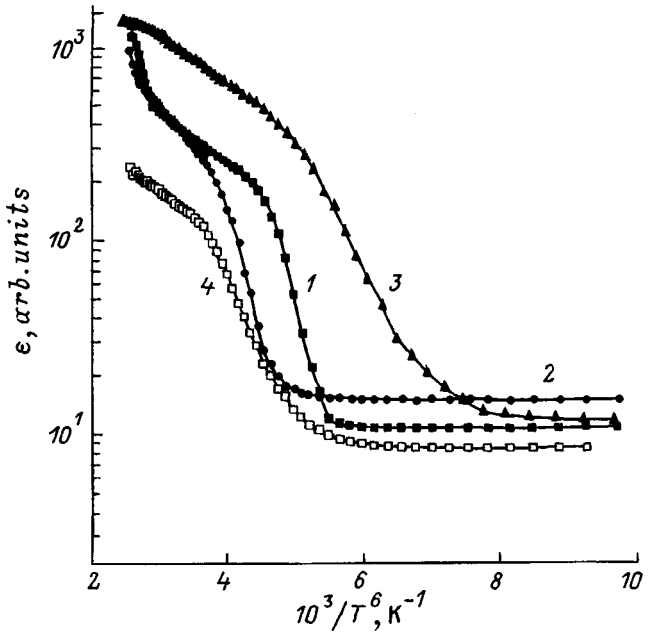

FIG. 2. The permittivity of $Cd_{1-x}Fe_xTe$ compounds as a function of temperature for different compositions $x=0.0035$ (*1*), 0.01 (*2*), 0.02 (*3*), and 0.03 (*4*). The measurement frequency is 10 kHz.

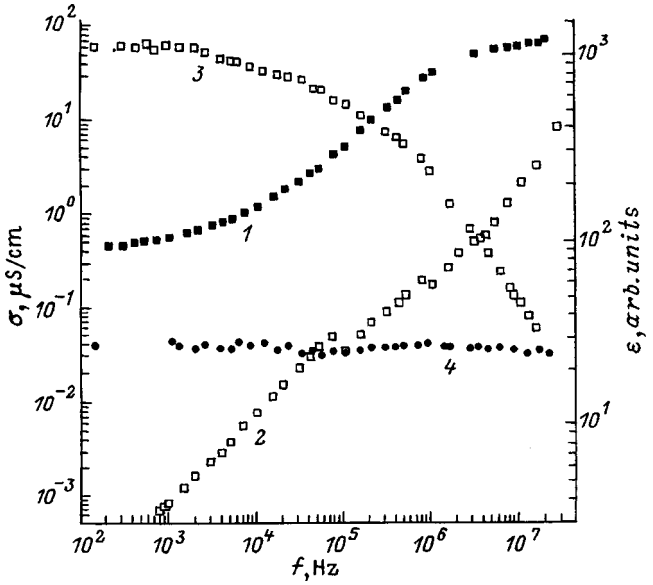

FIG. 3. The permittivity (*3*, *4*) and conductivity (*1*,*2*) as functions of measurement frequency. Measurement temperature: 300 K (*1*,*3*) and 77 K (*2*,*4*).

decreases slowly, approaching the value of ε obtained at 77 K at a frequency of about 20 MHz. The frequency dependence of the conductivity for $T=300$ K in curve 1 of Fig. 3 shows that σ increases to a frequency of about 1 MHz and for $f>1$ MHz there is a further increase with a tendency to saturate.

The observed temperature and frequency dependences of ε are fully consistent with the model proposed in Ref. 1, according to which dipoles develop as a result of jump charge transfer of electrons between neighboring neutral defects in the crystal and produce an additional polarization of the crystal. Electrons which move in jumps should also produce a hopping conductivity, which increases along with the measurement frequency in an alternating field.[5] It is clear from the $\sigma(f)$ curves in Fig. 3 that the conductivity of these materials also varies the way it should for materials with a hopping conductivity mechanism.

On the basis of an analysis of data from a study of ε in $Cd_{1-x}Mn_xTe$ materials, in Ref. 1 we proposed a defect model in which jump charge transfer between the defects causes a rise in ε. These defects are defects of the Te sublattice, whose nearest surroundings contain one, two, three, and four Mn atoms as x is raised gradually from 0 to 0.70. Each of these configurations corresponds to a unique activation energy ΔE_i, where i is the number of nearest-neighbor Mn atoms of a defect. In $Cd_{1-x}Fe_xTe$ materials, the changes in the activation energy for jump charge transfer between defects occur at much smaller values of x than in $Cd_{1-x}Mn_xTe$.

The activation energy for pure CdTe ($x=0$) was found[1] to be $\Delta E_0 \leqslant 0.12$ eV. As the Fe concentration is increased to $x=0.0035$, the activation energy rises to $\Delta E_1=0.38$ eV and remains constant until $x=0.01$. As x is increased further to $0.02 \leqslant x \leqslant 0.03$, $\Delta E_2=0.14$ eV (see Fig. 2.)

By analogy with the $Cd_{1-x}Mn_xTe$ materials, we assume that the defects with an activation energy of $\Delta E_1=0.38$ eV contain a single Fe atom, while those with $\Delta E_2=0.14$ eV contain two Fe atoms.

In the $Cd_{1-x}Mn_xTe$ materials, the displacement of Mn atoms in the Cd sublattice is close to random. Thus, defects which contain two Mn atoms are predominant for $x \sim 0.50$. For $x=0.02$ their probability of formation is smaller by more than a factor of 100.

In the $Cd_{1-x}Fe_xTe$ compounds, the change in the number of Fe atoms included in the defects takes place much more rapidly than in $Cd_{1-x}Mn_xTe$. This may mean that the Fe atoms move in a correlated fashion in the Cd sublattice, and that even for small values of x, $x \geqslant 0.02$, the dominant defects are those containing two Fe atoms.

The tendency of Fe atoms to have a correlated disposition in the CdTe crystal lattice observed in the above studies of ΔE may explain the low solubility of Fe atoms in $Cd_{1-x}Fe_xTe$ materials, for which a single phase solid solution exists only up to $x \leqslant 0.05$ (Ref. 6).

[1] P. W. Żukowski, A. Rodzik, and J. A. Szostak, Fiz. Tekh. Poluprovodn **31**, 714 (1997) [Semiconductors **31**, 610 (1997)].
[2] P. W. Żukowski, S. B. Kantorow, K. Kiszczak, D. Mączka, A. Rodzik, V. F. Stelmakh, and E. Czarnecka-Such, Phys. Status Solidi A **128**, 117 (1991).
[3] A. Holda, A. Rodzik, A. A. Melnikov, and P. Żukowski, Acta Phys. Pol. **87**, 357 (1995).
[4] A. Holda, A. Rodzik, A. A. Melnikow, and P. Żukowski, Phys. Status Solidi B **189**, 543 (1995).
[5] N. F. Mott and E. A. Davis, *Electronic Processes in Non-crystalline Materials*, Oxford (1971).
[6] J. Furdyna and J. Kossuth (Eds.), *Semimagnetic Semiconductors* (Mir, Moscow, 1992).

Translated by D. H. McNeill

Current-illumination characteristics of CdHgTe crystals with photoactive inclusions

A. I. Vlasenko and Z. K. Vlasenko

Institute of Semiconductor Physics, National Academy of Sciences of Ukraine, 252028 Kiev, Ukraine
(Submitted May 27, 1998; accepted for publication July 28, 1998)
Fiz. Tekh. Poluprovodn. **33**, 273–276 (March 1999)

The current-illumination characteristics of CdHgTe crystals with photoactive inclusions are studied. It is shown that the specific features of the current-illumination characteristics in these crystals, including experimentally observed superlinear segments, may be determined by switching of the dominant recombination channels, the removal of recombination barriers, and decreasing effective geometric dimensions of the inclusions associated with a reduction in the diffusion displacement length as the nonequilibrium carrier lifetime is lowered. Experimental data are presented, along with calculations based on a model of recombination fluxes in different channels. © *1999 American Institute of Physics.* [S1063-7826(99)00303-8]

The shape of the current-illumination characteristics of photoconductors is determined mainly by the dominant mechanism for recombination and the parameters of the driving pulse (the intensity I and time t_{imp}).[1–3] However, that the ''ideal'' current-illumination characteristics for particular dominant recombination mechanisms are not always observed experimentally. This applies, in particular, to crystals and layers of $Cd_xHg_{1-x}Te$ ($x=0.2$), where deviations from the dependence with an exponent of 0.3 characteristic of interband collisional recombination are often observed at high excitation levels:[4,5] segments with other exponents, saturation regions, superlinear segments, etc.[5,6] This may be related to the influence of fluctuations in the composition, inclusions of a second phase, grain boundaries, etc.[7] This paper is devoted to an experimental study and analysis of the current-illumination characteristics of homogeneous and inhomogeneous CdHgTe crystals.

EXPERIMENTAL RESULTS AND DISCUSSION

We have studied CdHgTe crystals ($x\approx0.2$) with equilibrium carrier concentrations $n_0\approx10^{14}-10^{16}$ cm^{-3} excited by pulses from an Nd laser (wavelength $\lambda\approx1.06\mu$m, $t_{\rm imp}\approx2\times10^{-8}$ s) at a temperature $T=77$ K. The nonequilibrium charge carrier lifetime τ was determined from the photoconductivity relaxation kinetics. The composition of the crystals was monitored using an electron-probe x-ray spectral microanalyzer (Camebax), as well as the long wavelength edge of the photoabsorption spectra. A typical distribution of the composition in inhomogeneous CdHgTe crystals is given in Ref. 7.

Figure 1 shows experimental current-illumination characteristics for homogeneous CdHgTe crystals with different values of n_0. They typically have several segments: linear (with a slope of ~1), sublinear (a transition region with a nearly linear slope of 0.3), and saturation. The steady-state continuity equation for the interband collisional recombination which predominates in crystalline CdHgTe ($x=0.2$), disregarding the diffusion and drift terms, is:

$$J=\frac{\Delta n}{\tau};\quad \tau=\frac{2\tau_{Ai}}{v^2+1},\quad v=v_n+\gamma=\frac{n_0}{n_i}+\frac{\Delta n}{n_i},\qquad (1a)$$

where $J\propto I$ is the generation rate, τ_{Ai} is τ in the intrinsic material, n_i is the intrinsic carrier concentration, γ is the injection level, and v_n is the doping level. For $n_0>(1-3)\times10^{14}$ cm^{-3} and $v_n\gg1$, we have

$$J=\frac{n_i}{2\tau_{Ai}}\gamma(v_n^2+2v_n\gamma+\gamma^2).\qquad (1b)$$

When $t_{\rm imp}>\tau_0$ (τ_0 is the lifetime for a nonequilibrium charge carrier concentration $\Delta n\ll n_0$), a stationary regime exists for arbitrary levels of excitation. When $\gamma<1$, the second and third terms in Eq. (1b) are small and the initial segment of the current-illumination characteristic has a linear dependence of the form $\log\Delta n\propto\log\tau_0+\log I$, which is displaced relative to the coordinate origin by an amount $\log\tau_0$. As the parameters of the material (x, n_0) or the temperature

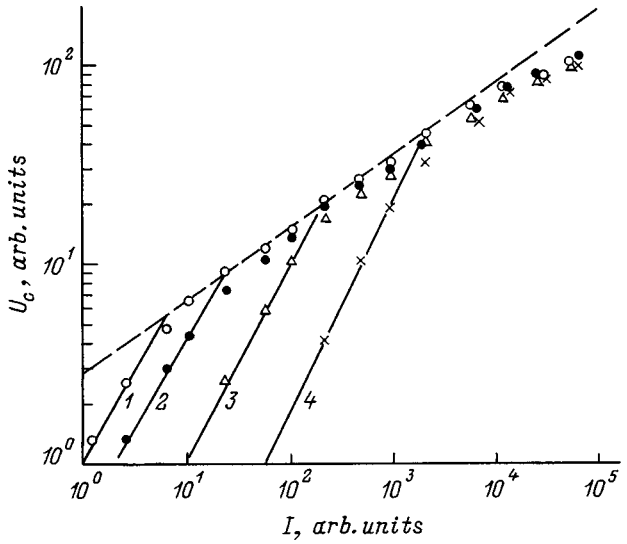

FIG. 1. Current-illumination characteristics of homogeneous CdHgTe crystals ($x\approx0.2$). n_0 (10^{15} cm^{-3}): 0.33 (*1*), 0.62 (*2*), 1.2 (*3*), and 2.7 (*4*). U_c is the photoconductivity signal.

T are varied, τ_0 changes accordingly and in the initial segment of the current-illumination characteristic a family of parallel straight lines displaced with respect to one another, with the same slope, will be observed (Fig. 1) (here the recombination is linear). For medium levels of excitation ($v_n > \gamma > 1$) the effect of the second term in Eq. (1b) becomes greater. For $\gamma > (1/2)v_n$, τ decreases with increasing Δn ($\tau \propto \Delta n^{-1}$), and the current-illumination characteristic enters a sublinear, nearly quadratic, segment (for $\gamma \leqslant v_n$ the partial contribution of the third term in Eq. (1b) is less than 25%). As the level of excitation is raised, the third term in Eq. (1b) becomes predominant, the slope of the current-illumination characteristic decreases and, for high excitation levels ($\gamma > 2v_n$), we have $\tau \propto \Delta n^{-2}$ and $J \propto \Delta n^{-3}$. Evidently, the length on the I axis of the segments of the current-illumination characteristic with different slopes is determined by the relationship between γ and v_n. The slope is ~ 1 for $\gamma < (1/2)v_n$, in a transition region (slope close to 0.5) for $(1/2)v_n < \gamma < 2v_n$, and ~ 0.3 for $\gamma > 2v_n$. With increasing v_n (and, therefore, decreasing τ_0), the transition region into the sublinear segment is shifted toward higher intensities.

Linear generation occurs for $t_{\text{imp}} \ll \tau_0$; i.e., in the initial segment of the current-illumination characteristic a linear dependence of $\Delta n(I)$ develops ($\log \Delta n \propto \log t_{\text{imp}} + \log I$) and its displacement with respect to the origin is determined only by t_{imp}. Note that the current-illumination characteristic can retain its linearity even for $\Delta n > n_0$, as long as $\tau(\Delta n)$ remains greater than t_{imp} and with further increases in Δn, τ becomes shorter than t_{imp}; i.e, a stationary regime sets in and the current-illumination characteristic enters a sublinear phase.

At very high excitation levels the current-illumination characteristic saturates, perhaps as a result of a bolometric effect, i.e., a reduction in the thickness of the layer in which recombination takes place as the surface diffusion length L_s becomes shorter with increasing Δn.[5]

Segments with other slopes of the current-illumination characteristic are observed in some crystals and layers of CdHgTe, including superlinear segments (Fig. 2) which may result from other dominant recombination mechanisms or the effect of photoactive inclusions on the formation of the current-illumination characteristic.

When Shockley–Read recombination predominates (in the compensated or wider band ($x > 0.23$) crystals,[8–10]) the current-illumination characteristic can be described using a model with recombination centers of two types r and s which are asymmetric in the capture coefficients for holes $C_{p(r,s)}$ and electrons $C_{n(r,s)}$.[2] In the initial segment, while Δn still does not change the electron N_{r0} and hole P_{r0} concentrations at the r centers significantly, recombination is monomolecular and the current-illumination characteristic is linear, $\tau_n \propto (C_{nr}P_{r0})^{-1}$. For medium excitation levels, when P_r is comparable to Δn with $N_r \approx \text{const}$, recombination is bimolecular and the current-illumination characteristic enters a segment with a slope of 0.5, where $\tau_n \propto (C_{nr}\Delta n)^{-1}$. At high excitation levels, when N_r decreases and hole filling of the s-centers is significant, the contribution g_r of the recombination flux through the r-centers becomes smaller and the yield

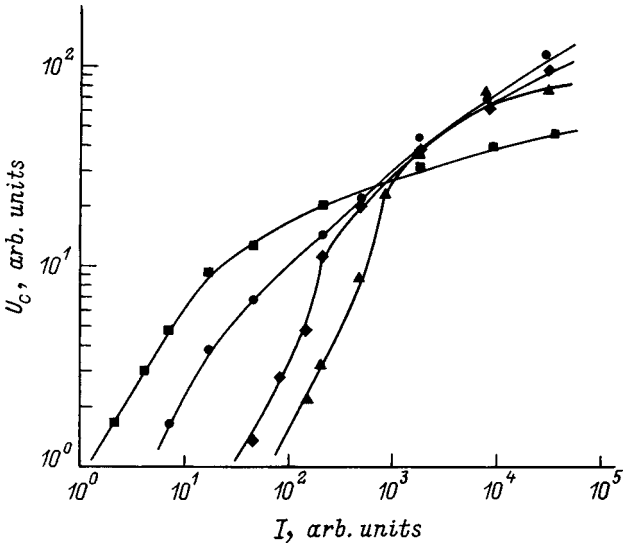

FIG. 2. Current-illumination characteristics of CdHgTe crystals ($x \approx 0.2$) with photoactive inclusions. The different curves correspond to different samples. U_c is the photoconductivity signal.

g_s through the s-centers increases; the current-illumination characteristic enters saturation (so-called optical charge exchange takes place), τ_n falls, and the photoconductivity saturates with increasing I. For further increases in I, when $g_s > g_r a_n^{-1}$ ($a_n = C_{nr}/C_{ns} \ll 1$), the recombination flux is controlled by the s-centers and is bimolecular (for high concentrations of s-centers they are increasingly filling by holes until the condition $\tau_n = \tau_p$ is satisfied and the photoconductivity is bipolar).

The current-illumination characteristics of CdHgTe crystals with photoactive inclusions must be analyzed taking into account the dominant recombination processes in the matrix (v) and inclusions (i), as well as the possibility of their switching from one to the other at certain excitation levels (for example, taking into account the growth, as the concentration of collisionally interacting carriers n increases, in the probability of an interband collisional *eeh*-process from Shockley–Read for low concentrations of r- and s-centers to interband collisional). Here for each mechanism a segment with a characteristic variation $\Delta n(I)$ may be realized. It is also necessary to take into account the dependence on Δn of the ratios τ_i/τ_v of the lifetimes in the matrix and in the inclusions, the recombination barriers E_{rec},[11] the diffusion displacement length L_D, and other parameters, which can change the partial contributions of the recombination fluxes in the matrix and inclusions to the effective lifetime τ_{eff} of nonequilibrium charge carriers as Δn increases.

Let us assume that in the matrix and inclusions recombination is determined by a single dominant mechanism, interband collisional, but with different rates for this process, which are attributable, for example, in the case of recombinationally active inclusions, to a narrowing of the band gap E_g or (and) an elevated concentration n_0.

In the case of inclusions with $E_{gi} < E_{gv}$, τ_{eff} is determined by the sum of the recombination fluxes in the matrix and the inclusions,

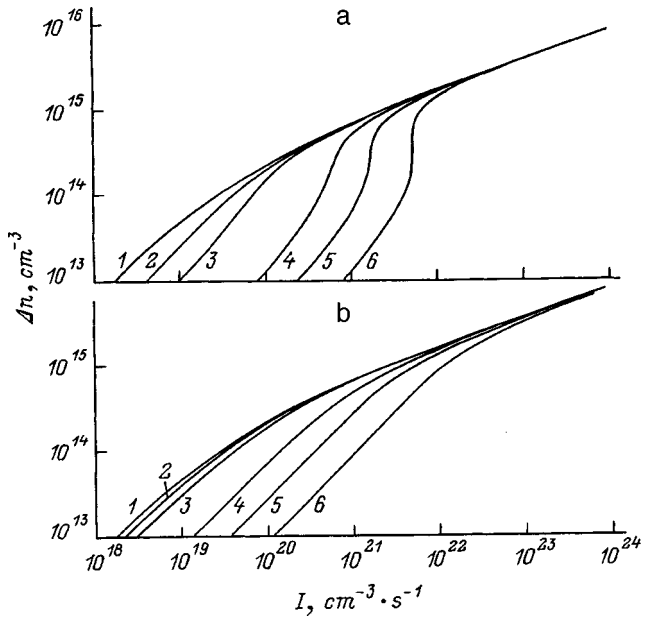

FIG. 3. Calculated current-illumination characteristics for CdHgTe crystals ($x\approx 0.2$) with $n_0=3\times10^{14}$ cm^{-3} for concentrations N_i (cm^{-3}) of inclusions: 0 (*1*), 10^3 (*2*), 10^4 (*3*), 10^5 (*4*), 3×10^5 (*5*), 10^6 (*6*). Explanations are in the text.

$$\tau_{\text{eff}}=\left\{V_iN_i\frac{1}{\tau_i}+V_DN_i\frac{1}{\tau_D}+\frac{1}{\tau_v}[1-(V_i+V_D)N_i]\right\}^{-1}, \tag{2}$$

where V_i and V_D are the volumes of the inclusions and of the diffusion regions associated with them, respectively. For spherical inclusions $V_i=(4/3)\pi r_c^3$ and $V_D\approx 4\pi(r_c+L/2)^2L$, where r_c is the average radius of the inclusions; N_i is the concentration of inclusions; $L\approx L_D=(D\tau)^{1/2}$ for $r_c>L_D$ and $L=(r_cL_D)^{1/2}$ for $r_c<L_D$,[12] where D is the diffusion coefficient (~ 4 cm^2/s), and $\tau_D\approx\tau_i$.

Figure 3a shows families of current-illumination characteristics calculated using Eq. (2) for CdHgTe crystals with inclusions that have $E_{gi}<E_{gv}$ and concentrations $N_i=0-10^6$ cm^{-3} for $n_0=3\times10^{14}$ cm^{-3}, $r_c=10^{-3}$ cm, and $\tau_i=10^{-8}$ s. While Δn is small, τ_v and therefore L_D are independent of Δn and the current-illumination characteristic is linear with a slope of 1. As Δn increases, τ_v and L_D and, therefore, the effective volume V_i+V_D of the inclusions decrease (the second term in Eq. (2) approaches zero), the crystal becomes ''light sensitive,'' and the current-illumination characteristic enters a superlinear segment. With further increases in Δn, the ratio of the volumes of the matrix and inclusions stabilizes and the current-illumination characteristic enters a segment with a slope of 1/3. Note that with increasing Δn, $\tau_v\to\tau_i$, but for inclusions with $x_i<x_v$ and for large Δn, the inequality $\tau_i<\tau_v$ is maintained[7,8] and the inclusions remain recombinationally active. For a more exact analysis, in Eq. (2) it is necessary to take into account the quasielectric ''constricting'' field of the variable-gap regions (which can be done by replacing L_D with the diffusion-drift lengths L^+, L^-),[1] as well as the different doping levels in the host and inclusions.

In the case of inclusions with $n_{0i}>n_{0v}$, the lifetimes in the host and inclusions satisfy the conditions $\tau_v\propto n_v^{-2}$ and $\tau_i\propto n_i^{-2}$, respectively. In the diffusion regions at the matrix-inclusion boundaries, recombination barriers[11] E_{rec} participate in recombination. Although these barriers increase τ_D compared to τ_i, calculations show that they leave these regions recombinationally with respect to the host. In this case,

$$\tau_{\text{eff}}=\left\{V_iN_i\frac{1}{\tau_i}+V_DN_i\frac{1}{\tau_i\exp(E_{\text{rec}}/kT)}+\frac{1}{\tau_v}[1-(V_i+V_D)N_i]\right\}^{-1}, \tag{3}$$

where $|E_{\text{rec}}|=kT\ln(n_i/n_v)=kT\ln\{(n_{0i}+\Delta n)/(n_{0v}+\Delta n)\}$ and $E_{\text{rec}}\to 0$ with increasing Δn.

Figure 3b shows families of current-illumination characteristics calculated using Eq. (3) for CdHgTe crystals with these kinds of inclusions at concentrations $N_i=0-10^6$ cm^{-3} for the following parameters: $n_{0v}=3\times10^{14}$ cm^{-3}, $r_c=10^{-3}$ cm, and $n_{0i}=3\times10^{16}$ cm^{-3}. There is no superlinear segment of the current-illumination characteristics in this case, since the reduction in L_D with increasing Δn is compensated by a reduction in, and then the complete elimination of, the recombination barriers. The carrier concentration in the matrix equilibrates and N_i also decreases, primarily because of inclusions with small deviations of n_{0i} from n_{0v}. For $\Delta n\approx n_{0i}\approx n_{0v}$ and $E_{\text{rec}}=0$, it turns out that $\tau_v=\tau_i$ and the crystal becomes recombinationally homogeneous with an exponent of ~ 0.3 in the current-illumination characteristic. These inclusions affect the current-illumination characteristic only in the impurity conduction region; as T is increased and a transition into the intrinsic conduction region takes place, the concentration of free carriers equilibrates over the sample, the inclusions disappear, and the current-illumination characteristic takes a form similar to that shown in Fig. 1.

The picture becomes more complicated when both types of inclusions are present, as well as when there are different mechanisms for recombination in the matrix and in the inclusions, such as Shockley–Read recombination with several types of recombination levels and interband recombination, collisional or (and) radiative, as is typical of most wide-band semiconductors.[2] In this case, their partial contribution to the overall recombination process in the crystal as Δn increases (and, accordingly, L_D and E_{rec} decrease) may change within certain ranges of I, and the shape of the current-illumination characteristic will be determined by the exponents that are characteristic of these mechanisms; this is often observed in inhomogeneous and polycrystalline semiconductors.[5,7,13,14]

[1] S. M. Ryvkin, *Photoelectric Phenomena in Semiconductors* [in Russian], Nauka, Moscow (1963).
[2] V. E. Lashkarev, A. V. Lyubchenko, and M. S. Sheĭnkman, *Nonequilibrium Processes in Photoconductors* [in Russian], Nauk. dumka, Kiev (1981).
[3] V. A. Zuev, V. G. Litovchenko, and G. A. Sukach, Fiz. Tekh. Poluprovodn. **9**, 1641 (1975) [Sov. Phys. Semicond. **9**, 970 (1975)].
[4] F. Bartoli, R. Allen, L. Esterowitz *et al.*, J. Appl. Phys. **45**, 2150 (1974).
[5] A. I. Vlasenko, K. R. Kurbanov, A. V. Lyubchenko, and E. A. Sal'kov, Ukr. Fiz. Zh. **27**, 1392 (1982).

[6] A. I. Vlasenko, V. A. Gnatyuk, P. E. Mozol' *et al.*, Izv. RAN. Neorg. mater. **31**, 1335 (1995).
[7] A. I. Vlasenko, Yu. N. Gavrilyuk, V. Z. Latuta, A. V. Lyubchenko, and E. A. Sal'kov, Pis'ma Zh. Tekh. Fiz. **5**, 1013 (1979) [Sov. Tech. Phys. Lett. **5**, 423 (1979)].
[8] A. D. Vlasenko, Ukr. Fiz. Zh. **42**, 856 (1997).
[9] D. L. Polla and C. E. Jones, J. Appl. Phys. **52**, 5119 (1981).
[10] A. I. Vlasenko, Z. K. Vlasenko, and A. V. Lyubchenko, Fiz. Tekh. Poluprovodn. **31**, 1323 (1997) [Semiconductors **31**, 1140 (1997)].
[11] M. S. Sheĭnkman and A. Ya. Shik, Fiz. Tekh. Poluprovodn. **10**, 209 (1976) [Sov. Phys. Semicond. **10**, 128 (1976)].
[12] N. N. Grigor'ev, L. A. Karachevtseva, K. R. Kurbanov, and A. V. Lyubchenko, Fiz. Tekh. Poluprovodn. **25**, 464 (1991) [Sov. Phys. Semicond. **25**, 280 (1991)].
[13] A. Baĭdullaeva, B. K. Dauletmuratov, A. I. Vlasenko, V. A. Gnatyuk, and P. E. Mozol', Fiz. Tekh. Poluprovodn. **27**, 56 (1993) [Semiconductors **27**, 29 (1993)].
[14] V. N. Babentsov, A.I. Vlasenko, P. E. Mozol, and E. P. Kopishinskaya, Proc. SPIE **2648**, 369 (1995).

Translated by D. H. McNeill

Temperature dependences of the photoconducitivty of CdHgTe crystals with photoactive inclusions

A. I. Vlasenko and Z. K. Vlasenko

Institute of Semiconductor Physics, National Academy of Sciences of Ukraine, 252028 Kiev, Ukraine
(Submitted May 27, 1998; accepted for publication July 28, 1998)
Fiz. Tekh. Poluprovodn. **33**, 277–281 (March 1999)

The temperature dependences of the lifetime and photoconductivity spectral characteristics of $Cd_xHg_{1-x}Te$ ($x=0.2$) crystals with photoactive inclusions have been studied. It is shown that the *N*-shaped temperature variation in the effective lifetime in inhomogeneous crystals, in particular, its sharp temperature activation in the region of the transition from impurity to intrinsic conductivity, is determined by an interband collisional process with recombinationally active regions whose effective geometric sizes change as the temperature is raised, rather than by a Shockley-Read mechanism. The smoothing out of the nonmonotonicity in the photoconductivity spectral characteristics in the fundamental absorption region during heating is explained in terms of this model. Calculations in qualitative agreement with the experimental data are presented. © *1999 American Institute of Physics.* [S1063-7826(99)00403-2]

The functional parameters of semiconducting materials are extremely sensitive to their degree of structural perfection. This is true to a great extent for semiconducting solid solutions characterized by a developed system of point and extended defects, in particular, $Cd_xHg_{1-x}Te$. It has been shown[1–4] that fluctuations in the composition, inclusions of a second phase (especially Te), and small angle walls lower the photosensitivity and affect the electrical properties of the crystals.[5–7] Nevertheless, a number of questions relating to the behavior of the photoconductivity in inhomogeneous $Cd_xHg_{1-x}Te$ crystals, in particular, its temperature characteristics, require further experimental study and theoretical analysis. This paper is devoted to a study of the temperature dependence of the photoconductivity in these crystals.

EXPERIMENTAL RESULTS AND DISCUSSION

We have studied CdHgTe crystals with $x\approx 0.19-0.21$ and equilibrium carrier concentrations $n_0\approx 3\times 10^{14}-6\times 10^{15}$ cm^{-3}. The concentration and mobility (μ_H) were measured by the Hall method in weak magnetic fields. The spectral dependences of the photoconductivity in the steady state were studied for wavelengths $\lambda=2-15\,\mu$m. The effective nonequilibrium charge carrier lifetime τ_{eff} was estimated from the photoconductivity relaxation curves (according to the segments with the largest partial amplitude) excited by CO_2 laser pulses ($\lambda=10.6\,\mu$m) (at temperatures where the band gap $E_g<0.117$ eV) and GaAs laser pulses ($\lambda=0.9\,\mu$m) (at temperatures where the crystal becomes transparent and insensitive to CO_2 laser light; the correctness of the attribution of the τ_{eff} measured in this way to the bulk lifetimes has been discussed elsewhere.[8,9] The measurements were made at temperatures $T=77-300$ K. The amounts of the principal components (Cd, Hg, Te) in the crystals and their deviations from the matrix proportions were monitored by electron-probe x-ray microanalysis (Camebax), as well as from the long-wavelength peak of the spectral photoconductivity characteristics. We have published typical spatial distributions of the compositions of the components of these crystals elsewhere.[1,2] The measurement samples were prepared by traditional methods.[8]

Figure 1 shows the temperature curves $\tau_{\text{eff}}(T)$ for crystals ($x\approx 0.2$, $n_0\approx 1\times 10^{15}$ cm^{-3}) with narrow-gap inclusions. Also shown here are the calculated lifetime $\tau(T)$ for interband collisional recombination (dashed curve) and experimental data for a uniform crystal (1*A*). Most crystals of this type are characterized by a nonexponential dependence or one with several exponents, including long-lived components (up to 500 μs) in a number of cases, in the photoconductivity relaxation curves, a substantial reduction in τ_{eff}, and a deviation of their temperature and concentration dependences from the theoretical curves (for the interband collisional recombination mechanism that predominates in these crystals). This behavior may be indicative of the presence of effective recombination sinks in the host that getter nonequilibrium charge carriers from the volume of the host.[1] In the $\tau_{\text{eff}}(T)$ curves with increasing *T* there is typically a reduction in the lifetime in the impurity conduction region, activation in the transition region, and then a sharp drop in the intrinsic conduction region (curves *1–4*). In some crystals, in the impurity conduction region only a smooth fall in the lifetime is observed (curve *5*). In the intrinsic conduction region a deviation of the $\tau_{\text{eff}}(T)$ curve from the theory is often observed for this matrix composition.

Figure 2 shows the spectral dependence of the photoconductivty of sample 4 at several fixed temperatures in the interval $T=77-300$ K. The absence of a distinct intrinsic photoconductivity peak and the spreading out of the long-wavelength edge are, as a rule, characteristic of crystals with narrow-gap inclusions, and the peaks in the fundamental absorption region at $\lambda=3-5\,\mu$m and the sharp increase in

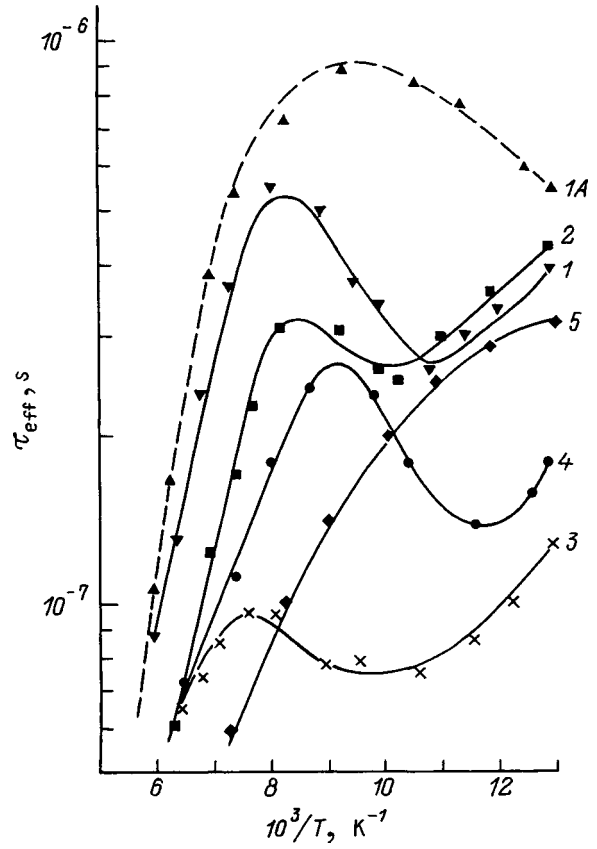

FIG. 1. The effective nonequilibrium charge carrier lifetime τ_{eff} as a function of temperature for $Cd_xHg_{1-x}Te$ crystals: (1A) uniform sample with $n_0=1\times10^{15}$ cm^{-3}; (*1*–*5*) samples with narrow band inclusions with $n_0=(10^{15}$ cm$^{-3})$ 0.8 (*1*), 1.0 (*2*), 1.2 (*3*), 2.0 (*4*), 1.4 (*5*). The dashed curve is $\tau_v(T)$ calculated using Eq. (2) for interband collisional recombination with $n_0=1\times10^{15}$ cm^{-3}. The numbers on the curves correspond to the sample numbers.

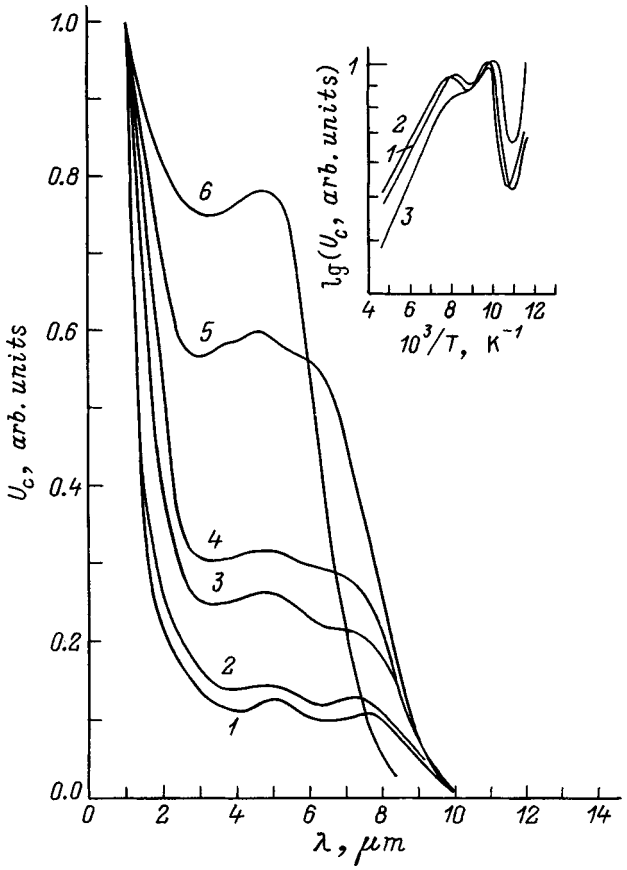

FIG. 2. Spectral characteristics of the photoconductivity of sample 4 (see Fig. 1). Temperature T (K): 85 (*1*), 100 (*2*), 115 (*3*), 130 (*4*), 185 (*5*), 300 (*6*). The inset shows the temperature variations in the photoconductivity U_c for light with $\lambda=8$ (*1*), 5.3 (*2*), 1.5 μm (*3*).

photoconductivity for $\lambda<2\,\mu$m are caused by the presence in this crystal of Te inclusions and of regions in the $Cd_xHg_{1-x}Te$ which are enriched in CdTe, as confirmed by x-ray spectral analysis data.

The inset in Fig. 2 shows the temperature variation in the steady-state photoconductivity signal (U_c) for this crystal for fixed excitation wavelengths. Note the qualitative correlation between the $\tau_{\text{eff}}(T)$ (Fig. 1, curve *4*) and $U_c(T)$ $\propto\tau(T)\mu_H(T)$ curves. The retention of the characteristic features of $U_c(T)$ and, accordingly, $\tau(T)$ [considering the almost linear dependence[2] of $\mu_H(T)$ for these T] during illumination at different wavelengths and, therefore, for different thicknesses $b\approx1/k+L_D$ (where k is the absorption coefficient) of the photoactive layer, is significant. For $\lambda\approx1.5\,\mu$m the depth at which nonequilibrium charge carriers are generated is $k^{-1}\approx1\,\mu$m, for $\lambda=5.3\,\mu$m, $k^{-1}\approx10\,\mu$m, and for $\lambda=8\,\mu$m, $k^{-1}\approx30-100\,\mu$m.[11] Since the diffusion displacement length $L_D=(D\tau)^{1/2}$ (where D is the diffusion coefficient for the nonequilibrium charge carriers) is less than 10 μm for these crystals [note that for surface excitation ($\lambda=1.5\,\mu$m), the effective diffusion length $L_s<L_D$ (Ref. 10)], we may conclude that the generation-recombination processes in the different layers of the crystal are the same in nature. The small difference between $U_c(T)$ for surface excitation ($\lambda=1.5\,\mu$m) (the inset in Fig. 3, curve *3*) and the volume curves (curves *1* and *2*) may be indicative of somewhat different parameters for interband Auger recombination in the skin layer of the sample.[9,10]

The influence of inclusions on the photosensitivity of the crystal is determined by their concentration N_i and size r_c, as well as by the types of nonequilibrium charge carrier generation ($G_{v,i}$) and recombination ($\tau_{v,i}^{-1}$) (the subscripts i and v refer to the inclusions and host). The more the ratio of the concentrations of nonequilibrium charge carriers in the inclusions and the matrix, $G_i\tau_i/G_v\tau_v$, differs from unity, the more the inclusions will affect the photosensitivity.

For calculating the effect of photoactive regions on τ_{eff} in a crystal we shall use the combined rates of recombination in the host and inclusions,

$$\tau_{\text{eff}}=\left[\sum_k V_{ik}N_{ik}(\tau_{ik}^{-1}-\tau_v^{-1})-\tau_v^{-1}\right]^{-1}, \tag{1}$$

where V_i is the volume of an inclusion [for spherical inclusions $V_{ik}=(4/3)\pi(r_{ck}+L_{\text{eff}})^3$], the subscript k characterizes a set of inclusions with the same parameters r_{ck}, τ_{ik}, and N_{ik}; $L_{\text{eff}}\approx L_D$ for $r_c>L_D$ and $L_{\text{eff}}=\sqrt{r_cL_D}$ for $r_c<L_D$ (Ref. 3).

We analyze the $\tau_{\text{eff}}(T)$ curves further in the approximation of spherical island narrow-band inclusions with $\tau_i<\tau_v$. We note the following circumstance: from the stand-

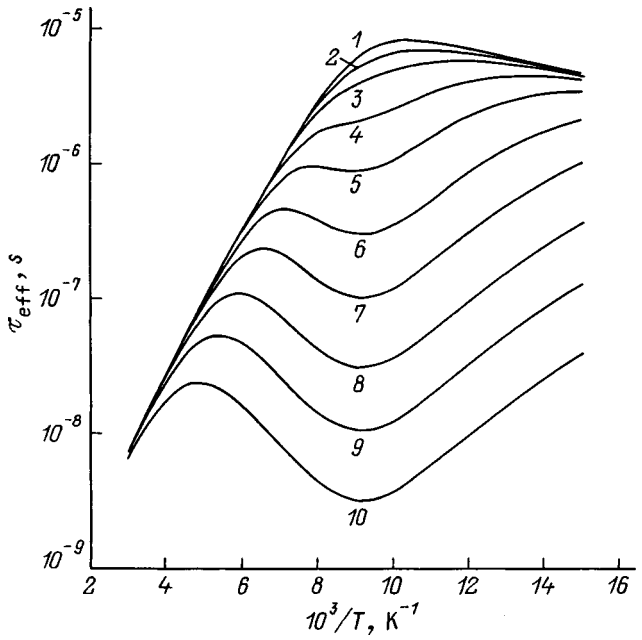

FIG. 3. τ_{eff} calculated using Eq. (1) for crystals with recombinationally active inclusions. The computational parameters of the matrix and inclusions are $x_v=0.21$, $n_0=3\times10^{14}$ cm^{-3}, $x_i=0.16$, and $r_c=10^{-3}$ cm. N_i (cm^{-3}): 0 (*1*), 10^2 (*2*), 3×10^2 (*3*), 10^3 (*4*), 3×10^3 (*5*), 10^4 (*6*), 3×10^4 (*7*), 10^5 (*8*), 3×10^5 (*9*), 10^6 (*10*).

point of its effect on the photosensitivity of an inhomogeneous crystal, the lifetime τ_v plays a double role. When it increases, on one hand, the photosensitivity of the matrix material rises and, on the other, $L_D=\sqrt{D\tau_v}$ and, therefore, the effective geometric sizes of the inclusions increase, but for recombinationally active inclusions this acts in the opposite direction, i.e., toward reducing the photosensitivity (1) of the sample. When τ_v decreases, conversely, the photosensitivity of the material drops, but recombinationally active inclusions have a greater effect on it, which may, on the whole, cause ''photosensitizing'' of the sample. In the $U_c(T)$ and $\tau_{\text{eff}}(T)$ curves in the impurity conduction region, this leads to features associated with the specific $\tau_v(T)$ dependences for the interband collisional recombination which predominates in $Cd_xHg_{1-x}Te$ with $x=0.2$. To this recombination we must first attribute the activation of τ_v with increasing T in the impurity conduction region associated with a positive temperature coefficient α for the variation in E_g for $x\leqslant0.5$ and, therefore, with a drop in the rate of the Auger process for a constant n_0.[8] The expression for τ_v in an *n*-type material can be written in the form

$$\tau_v=\frac{2\tau_{Ai}}{\nu_n^2+1},\qquad \nu_n=\frac{n_0}{n_i}>1, \tag{2}$$

where τ_{Ai} is the lifetime in the intrinsic material, n_i is the intrinsic carrier concentration, and ν_n reflects the level of doping of the material.

In the impurity conduction region ($n_0\approx$ const), $\tau_v(T)\propto n_i^2\tau_{Ai}$, and after substituting the functions $\tau_{Ai}(T)$ (Ref. 8) and $n_i(T)$ (Ref. 12) for τ_v and L_D, we obtain

$$\tau_v\propto T^{3/2}E_g^2=T^{3/2}(E_{g0}+\alpha T)^2, \tag{3a}$$

and

$$L_D\sim[(kT/e)\mu_D\tau_v]^{1/2}\sim T^{5/4}(E_{g0}+\alpha T), \tag{3b}$$

where E_{g0} is the value of E_g as $T\to0$, and μ_D is the bipolar diffusion mobility.

For *n*-type material, the ratio of the electron and hole mobilities, $b=\mu_n/\mu_p\gg1$ (in CdHgTe with $x\approx0.2$ and $b\approx100$) in the impurity and intrinsic conductivity regions and $\mu_D=(1+\nu_n^{-2})\mu_p$. Thus, the temperature dependence of μ_D is weak for $\nu_n\gg1$ (impurity conductivity) and down to $\nu_n=1$ (intrinsic conductivity) μ_D varies in the range $(1-2)\mu_p$ [according to different data, $\mu_p=300-1000$ cm^2/ (V·s)].

Equation (3) implies that τ_v increases with rising T with a power-law dependence $\tau\propto T^l$ ($l>3/2$). As the temperature is raised, the $\tau_v(T)$ for different n_0 approach the dependence $\tau_{Ai}(T)$, since $\nu_n\to1$ [(Eq. (2)]. Here the transition to the $\tau_{Ai}(T)$ curve shifts to higher temperatures with increasing n_0. The dependence $L_D(T)$ is weaker, but, since $\tau_{\text{eff}}\propto V_i^{-1}\propto(L_D)^{-3}$ [for $\tau_i\ll\tau_v$, see Eq. (1)] in a crystal with recombinationally active inclusions, for the temperature dependence of the photosensitivity in crystals with large concentrations or dimensions we have

$$\tau_{\text{eff}}(T)\propto\tau_v(T)T^{-5.25}(E_{g0}+\alpha T)^{-5}\propto T^{-3.75}(E_{g0}+\alpha T)^{-3}. \tag{4}$$

Therefore, a strong temperature dependence of the effective dimensions of the inclusions is imposed on the temperature variation $\tau_v(T)$ and, despite an increase in τ_v in this region, τ_{eff} and, therefore, the sensitivity of the crystal may decrease. Experimentally, this is confirmed by the curves $\tau_{\text{eff}}(T)$ and $U_c(T)$ shown in Fig. 1 and in the inset in Fig. 2 (in the temperature range $T=77-90$ K). We emphasize that τ_{eff} in Eq. (4) has been calculated for $\tau_i\ll\tau_v$ and for large inclusion sizes ($r_c>L_D$). For $r_c<L_D$, as noted above, the quantum effect for L_{eff} must be taken into account, so that the temperature variation is as $\tau_{\text{eff}}(T)\propto T^{-3.4}(E_{g0}+\alpha T)^{-3.5}$. For the cases of other inclusions with other geometries (characteristic of dislocations, low angle walls, etc.), these dependences are different. The geometry of the recombinationally active regions can apparently be judged from the character of these dependences. With further increases in T in the transition region $\upsilon_n\to1$, τ_v decreases and approaches τ_{Ai}, L_D decreases and τ_{eff} increases [see Fig. 1 (curves *1–4*) and the inset in Fig. 2 ($T=90-110$ K)]. It should be noted that the power-law dependences for $\tau_{\text{eff}}(T)$ can be treated as exponential with different characteristic activation energies E_a within this narrow temperature interval and interpreted as the participation of a Shockley-Read channel in recombination through local centers at depth E_a. This evidently is the cause of the wide scatter in published estimates of the depth of the recombination levels determined from the activation energy for the lifetime in this region.

If the inclusions are associated with fluctuations in the doping, then their sizes and concentration decrease with rising T, since the concentration of the majority carriers flattens out over the volume. Regions with elevated n_{0i} lose the recombinational activity relative to the host ($\tau\propto n_0^{-2}$). According to Eq. (1), $\tau_{\text{eff}}\to\tau_v$ not only because of a reduction in L_D

and the recombination barriers $E_{\rm rec}$ that are available in this case,[13] but also because of a reduction in the concentration N_i of the inclusions themselves, primarily through inclusions with small deviations in doping level from the host. Here $\tau_{\rm eff}(T)$ becomes even steeper. With further increases in T and the transition into the intrinsic conductivity region, τ_v approaches τ_{Ai} and decreases sharply, i.e., $\tau_{\rm eff}\to\tau_v\to\tau_{Ai}$ [see Fig. 1 and the inset in Fig. 2 ($T>130$ K)]. It should be noted that for certain concentrations (above critical) and sizes of the inclusions, which are attributablle to fluctuations in composition, the $\tau_{vAi}(T)$ and $\tau_{\rm eff}(T)$ curves may not coincide in this region and $\tau_{\rm eff}$ will be determined by the recombination parameters of the inclusions, rather than those of the host.

These remarks make clear the relative smoothing out, as a rule, of the nonmonotonic spectral characteristics of the photoconductivity in the strong absorption region during heating (Fig. 2). In fact, if variable gaps are absent, we have

$$\frac{\tau_v}{\tau_i}=\frac{v_{ni}^2+1}{v_{nv}^2+1}=1+\frac{v_{ni}^2-v_{nv}^2}{v_{nv}^2+1};\quad v_{ni}=\frac{n_{0i}}{n_i}. \tag{5}$$

With increasing T and the transition into the intrinsic conductivity region ($v_{ni},v_{nv}\to 1$), the quantities τ_v and τ_i approach one another, which causes a relative sensitizing at short wavelengths during heating. Small fluctuations in the spectral characteristics are preserved if the inclusions are associated with fluctuations in the composition, e.g., $x_i\gtrless x_v$ and their lifetime differs from the host value in the intrinsic conductivity region, as well. Note that the spectral shift of the peaks in the fundamental absorption region varies with T in a slightly different way than the main peak because of the different temperature coefficients α for the host and because of the various inclusions.

Figure 3 shows the temperature dependences $\tau_{\rm eff}(T)$ calculated using Eq. (1) for $Cd_xHg_{1-x}Te$ crystals ($x=0.21$) with $n_0=3\times10^{14}$ cm^{-3} and different concentrations of inclusions, N_i ($r_c=10^{-3}$ cm and $x_i=0.16$), including the temperature variations of τ_v, τ_i, $L_{\rm eff}$, and μ_D. As N_i increases, the degree to which the inclusions affect $\tau_{\rm eff}$ and the nonmonotonic N-shaped character of $\tau_{\rm eff}(T)$ become greater. We note the satisfactory agreement between the calculations and the experimental data, which may support the validity of our model for the temperature dependence of the photoconductivity of crystals with photoactive inclusions.

[1] A. I. Vlasenko, Yu. N. Gavrilyuk, V. Z. Latuta, A. V. Lyubchenko, and E. A. Sal'kov, Pis'ma Zh. Tekh. Fiz. **5**, 1013 (1979) [Sov. Tech. Phys. Lett. **5**, 423 (1979)].
[2] A. I. Vlasenko, A. V. Lyubchenko, and E. A. Sal'kov, Ukr. Fiz. Zh. **25**, 1317 (1980).
[3] N. N. Grigor'ev, L. A. Karachevtseva, K. R. Kurbanov, and A. V. Lyubchenko, Fiz. Tekh. Poluprovodn. **25**, 464 (1991) [Sov. Phys. Semicond. **25**, 280 (1991)].
[4] A. I. Vlasenko, A. V. Lyubchenko, and V. G. Chalaya, Fiz. Tekh. Poluprovodn. **30**, 377 (1996) [Sov. Phys. Semicond. **30**, 209 (1996)].
[5] Yu. A. Kontsevoĭ, Fiz. Tekh. Poluprovodn. **4**, 1184 (1970) [Sov. Phys. Semicond. **4**, 662 (1970)].
[6] V. A. Artem'ev, V. V. Mikhnovich, and S. G. Titarenko, Fiz. Tekh. Poluprovodn. **22**, 150 (1988) [Sov. Phys. Semicond. **22**, 93 (1988)].
[7] N. N. Grigor'ev, A. V. Lyubchenko, and E. A. Sal'kov, Ukr. Fiz. Zh. **34**, 1088 (1989).
[8] A. I. Vlasenko, Yu. N. Gavrilyuk, A. V. Lyubchenko, and E. A. Sal'kov, Fiz. Tekh. Poluprovodn. **13**, 2180 (1979) [Sov. Phys. Semicond. **13**, 1274 (1979)].
[9] A. I. Vlasenko, K. R. Kurbanov, A. V. Lyubchenko, and E. A. Sal'kov, Ukr. Fiz. Zh. **27**, 1392 (1982).
[10] A. I. Vlasenko, A. V. Lyubchenko, and E. A. Sal'kov, Ukr. Fiz. Zh. **25**, 434 (1980).
[11] M. D. Blue, Phys. Rev. **134**, 226 (1964).
[12] J. L. Shmit, J. Appl. Phys. **42**, 803 (1971).
[13] M. S. Sheĭnkman and A. Ya. Shik, Fiz. Tekh. Poluprovodn. **10**, 209 (1976) [Sov. Phys. Semicond. **10**, 128 (1976)].

Translated by D. H. McNeill

Raman scattering spectroscopy of $Zn_{1-x}Cd_xSe$ films grown on GaAs substrates by molecular-beam epitaxy

L. K. Vodop'yanov, N. N. Mel'nik, and Yu. G. Sadof'ev

P. N. Lebedev Physics Institute, Russian Academy of Sciences, 117924 Moscow, Russia
(Submitted July 15, 1998; accepted for publication July 18, 1998)
Fiz. Tekh. Poluprovodn. **33**, 282–284 (March 1999)

Data from the first measurements of the Raman scattering spectra of $Zn_{1-x}Cd_xSe$ ($x=0-0.55$) films grown on GaAs substrates by molecular-beam epitaxy are presented. An analysis of the experimental spectra shows that in the $Zn_{1-x}Cd_xSe$ system studied here there is a single-mode realignment of the vibrational spectrum with composition. © *1999 American Institute of Physics.* [S1063-7826(99)00503-7]

The recently renewed interest in semiconductor solid solutions (alloys) is attributable to their widespread use in creating quantum-well structures and microelectronic devices. Special attention has been focused on the study of alloys in the form of thin epitaxial layers which form the basis of quantum wells and superlattices. Here the problem arises of whether it is correct to transfer the properties of a bulk material, especially an alloy, to thin layers. Usually it is assumed, without any special justification, that these properties are identical. It has been shown, however,[1] that the rearrangement of the phonon spectrum in CdZnTe films as the concentrations of the components are varied is different from the realignment in such bulk crystals.

Modern applications associated with the creation of integrated optoelectronic devices require the growth of films of II-VI compounds on a suitable material, such as GaAs, for this type of integration. In this case, however, a mismatch of the lattice parameters gives rise to elastic stresses which change the physical properties of the film.

There is some interest in studying the dynamics of the crystal lattice of $Zn_{1-x}Cd_xSe$ films. Structures with quantum wells[2] and quantum dots[3,4] have been created and studied using thin films of this alloy. Efficient emitters of blue light based on structures of this type can be created. However, the properties of this alloy (in contrast with other alloys of II-VI compounds that have been studied extensively) have not been studied adequately. There is a paper by Brafman[5] on the Raman scattering spectra of bulk ZnCdSe crystals in which it was proposed that this system exhibits single-mode behavior.

As far as we know, there are no published papers on the optical Raman scattering spectrum of epitaxial ZnCdSe films. In this paper we present the first data on measurements of Raman scattering on phonons for epitaxial films of $Zn_{1-x}Cd_xSe$ ($0\leqslant x\leqslant 0.55$) which we have grown by molecular-beam epitaxy on GaAs substrates. The analyzed shape of the Raman scattering lines confirms the high degree of crystallinity of these films. Brafman's hypothesis[5] that this is a single-mode system is confirmed.

Heteroepitaxial layers of ZnCdSe on GaAs were obtained by molecular-beam epitaxy on a Katun' system supplemented by an ion pressure gauge for monitoring the intensity of the molecular beams and an electron Auger spectrometer. The base pressure in the apparatus was 10^{-8} Pa. An installed fast electron diffractometer was used to monitor the cleanliness of the substrate before epitaxy and the nucleation and growth of the epitaxial film.

Epitaxy was carried out on chromium compensated substrates of (111)-oriented gallium arsenide with a 3° disorientation to the {110} direction by evaporating special high-purity (6N) Zn, Cd, and Se from individual molecular sources. The substrate surface was cleaned of the natural oxides by heating in vacuum at 580° in the absence of selenium or zinc vapor.

The samples were grown at a substrate temperature of 280–320 °C with a ratio of the equivalent pressures of the molecular selenium beam to the total pressure of the zinc and cadmium molecular beams close to 2. This ensures the appearance on the surface of a superstructure consisting of a mixture of (1×2) and $c(2\times 2)$ reconstructions and growth under close to stoichiometric conditions. Here the epitaxy temperature was lowered in the range indicated above as the cadmium content of the grown films increased. The thickness of the grown films was 1–2 μm. The rate of growth of the films was held at 1 μm/h. The composition of the grown epitaxial films was monitored using the ratio of the intensities of the *LMM*-lines of the Auger transitions of Zn and Se, as well as using cathodoluminescence spectra.

Optical Raman scattering spectra were taken on a U-1000 spectrometer in a backscatter geometry with excitation by several lines of Kr and Ar^{2+} lasers. The resolution was 1 cm^{-1}.

Some typical Raman scattering spectra for epitaxial $Zn_{1-x}Cd_xSe$ films grown on GaAs substrates, taken in a backscatter geometry with excitation by the 4880-Å line at room temperature, are shown in Fig. 1. For $x=0$, i.e., for pure ZnSe, the spectrum contains three scattering lines. The high-frequency line at 293 cm^{-1} is associated with an LO-mode of GaAs. It appears because the zinc selenide film is partially transparent to the probe light. This line can still be seen for a composition with $x=0.09$, but at higher Cd concentrations ($x=0.39$), when the gap is narrower, and the film is therefore less transparent, it vanishes. The highest

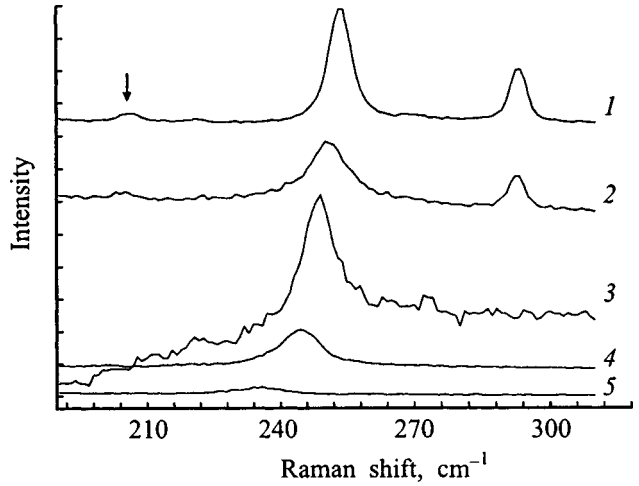

FIG. 1. First-order Raman scattering spectra for $Zn_{1-x}Cd_xSe$ films excited by the 4880-Å line. x: 0 (*1*), 0.09 (*2*), 0.14 (*3*), 0.38 (*4*), and 0.55 (*5*).

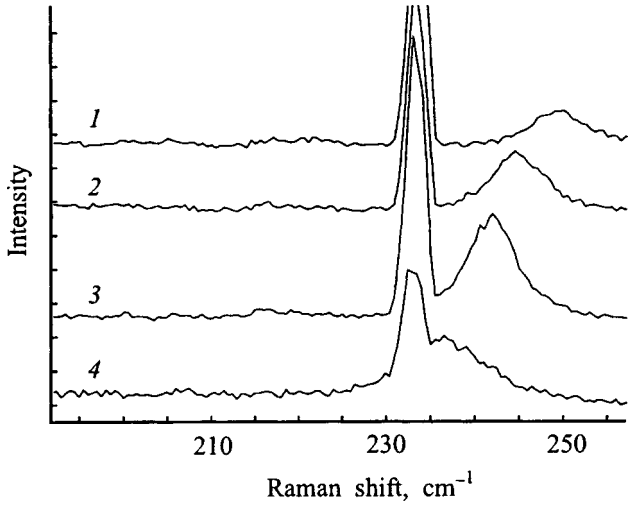

FIG. 2. Raman scattering spectra of $Zn_{1-x}Cd_xSe$ films excited by the 6471-Å line. x: 0.11 (*1*), 0.22 (*2*), 0.32 (*3*), and 0.55 (*4*). The intense lines near 233 cm^{-1} belong to the gas-discharge plasma of the Kr laser.

intensity in the spectrum for $x=0$ is the line at 253.5 cm^{-1} due to scattering on LO-vibrations of ZnSe. The weak band at 206 cm^{-1} is apparently associated with the TO-mode of ZnSe. The observed frequencies of the LO- and TO-modes are the same as those obtained for bulk crystals of ZnSe. This indicates that there are no noticeable elastic stresses, which would change the phonon frequencies. It should be noted that the observation of the TO-mode in the back-scattering spectrum from the (100) surface of the ZnSe film contradicts the selection rules which predict the appearance of only LO-modes. Clearly, the TO-mode is activated because of a violation of the selection rules due to the distortion of the crystal structure at the film-substrate interface. This can also explain the disappearance of the TO-band because of the use of narrower-band compositions when the film is opaque for the probe laser line and the interface is no longer a factor.

As Fig. 1 shows, when the Cd content of the alloy is increased, the intensity of the Raman scattering bands decreases, probably because of a reduction in the effective thickness of the excited layer. Thus, in order to increase the intensity of the scattered lines we took spectra of films enriched in Cd using the red 6471-Å line of a krypton laser (Fig. 2). The LO-bands clearly show up more distinctly. In addition, narrow lines of a gaseous plasma can be seen in the spectra; this circumstance facilitates a more accurate determination of the frequency shifts of the phonons as functions of the alloy composition.

An analysis of these spectra for films of alloys with $0\leqslant x\leqslant 0.55$ (Figs. 1 and 2) shows that the frequency of the LO-mode shifts smoothly to lower energies as x is increased, going to 237 cm^{-1} for $x=0.55$. We did not observe splitting of the LO-band into two peaks localized near ZnSe- and CdSe-like vibrations for any of the compositions. This indicates that the crystal lattice dynamics of $Zn_{1-x}Cd_xSe$ films is characterized by a single-mode realignment of the phonon spectrum. This conclusion becomes even more evident if we consider the plot of the frequency of the LO-phonons as a function of x, shown in Fig. 3.

We have also analyzed the shape of the optical Raman phonon scattering lines using a computer program. This analysis showed that the LO-phonon Raman scattering bands have a mostly Lorentz shape, and that the half-width of the bands is less than 10–12 cm^{-1}. This last point indicates that the films which we grew had a high degree of crystallinity.

The single-mode behavior which we have observed in the epitaxial layers of ZnCdSe is extremely unusual for semiconducting alloys of II-VI compounds. From the standpoint of the existing criteria, the character of the realignment in this system is ambiguous. Thus, the classical criterion[6] predicts single-mode behavior for this system. A more modern criterion based on the discussion by Chang and Mitra[7] and reformulated for phonons in substitution solid solutions[8] predicts a two-mode realignment for the ZnCdSe system. According to this criterion, two-mode realignment occurs in (AB)C alloys when the vibrational perturbation energy produced as a result of replacing an A atom by a B atom is greater than the vibrational energy of the interactions of the atoms in the AC lattice. In other words, the following in-

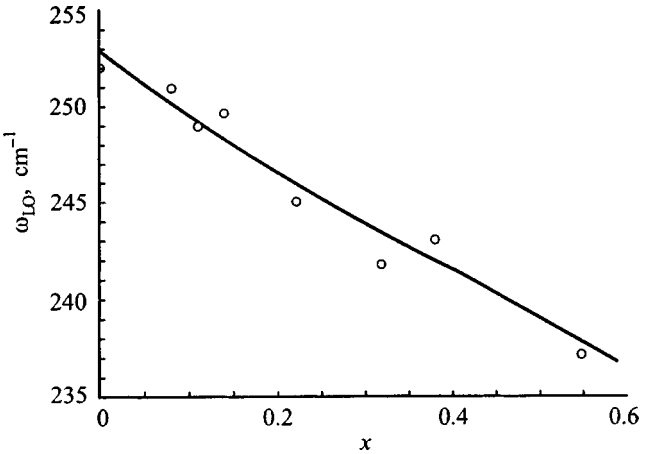

FIG. 3. The frequency ω_{LO} of LO-phonons plotted as a function of the Cd content x in $Zn_{1-x}Cd_xSe$ films.

equality must be satisfied: $\Delta m\Omega^3 > K$, where Δm is the mass defect, Ω is the frequency of the local mode, and K – the strength constant – can be determined from the formula $K=(2\omega_{TO}^2+2\omega_{LO}^2)M/3$, where M is the reduced mass. We can then express the criterion for a two-mode realignment as follows:

$$P \equiv \frac{\Delta m}{M}\frac{3\Omega}{2\omega_{TO}^2+\omega_{LO}^2} \geqslant 1. \quad (1)$$

Substituting into Eq. (1) the masses of the Zn, Cd, and Se atoms and the frequencies of the TO- and LO-phonons for CdSe, $\omega_{TO}=169\ \mathrm{cm}^{-1}$ and $\omega_{LO}=211\ \mathrm{cm}^{-1}$, and assuming the frequency of the local vibrations to be equal to the maximum frequency of the allowed phonon spectrum, $\Omega=\omega_{LO}$ (the local mode of Zn in CdSe was not observed), we obtain $P=1.368>1$, which indicates a two-mode realignment and contradicts our observations. This may be explained by the fact that the changes in the strength constants resulting from substitution in the alloy have been disregarded in deriving the criterion. Therefore, this criterion is an approximation.

This work was supported by the Russian Fund for Fundamental Research (RFFI) (Project No. 97-02-16791) and the Russian MNTP for the Physics of Solid State Nanostructures (Projects 97-1047 and 97-2019).

[1] D. Olegro, P. Raccah, and J. Faurie, Phys. Rev. B **33**, 3819 (1986).
[2] P. Gingo, M. De Vittorio, R. Rinald, and R. Cingolani, Phys. Rev. B **54**, 16 934 (1996).
[3] M. Strassberg, V. Kutzer, U. Pohl, A. Hoffman, I. Broser, N. N. Ledentzov, D. Bimberg, A. Rosenauer, U. Fischer, D. Gerthsen, I. L. Krestikov, M. V. Maximov, P. S. Kop'ev, and Zh. I. Alferov, Appl. Phys. Lett. **72**, 942 (1998).
[4] B. Zhang, W. Wang, T. Uasuda, Y. Segava, K. Edamatsu, and T. Itoh, Appl. Phys. Lett. **71**, 3370 (1997).
[5] O. Brafman, Solid State Commun. **11**, 447 (1972).
[6] I. Chang and S. Mitra, Adv. Phys. **20**, 359 (1971).
[7] Y. Onodera and Y. Toyozawa, J. Phys. Soc. Jpn. **24**, 341 (1968).
[8] J. Dow, W. Packard, H. Blackstead, and D. Jenkins, *Dynamical properties of solids*, V. 7: *Phonon physics*, edited by G. Hortoy (1995) p. 349.

Translated by D. H. McNeill

Optical and photoelectric properties of $Zn_{1-x}Fe_xTe$ crystals

Yu. P. Gnatenko* and I. A. Farina

Institute of Physics, National Academy of Sciences of Ukraine, 252650 Kiev, Ukraine

R. V. Gamernyk

Lviv State University, 290005 Lviv, Ukraine

(Submitted July 21, 1998; accepted for publication July 18, 1998)
Fiz. Tekh. Poluprovodn. **33**, 285–288 (March 1999)

The optical and photoelectric properties of the new van Fleck semimagnetic semiconductors $Zn_{1-x}Fe_xTe$ ($x \leqslant 0.046$) are studied for the first time. The structure of the long-wavelength absorption edge and of the photovoltaic current spectrum is found to be caused by photoionization transitions involving various charge states of Fe (Fe^+, Fe^{2+}, and Fe^{3+}). The concentration dependence of the free exciton energy is determined, as well as the locations of the ground states of the Fe^{2+} ($E_v+0.44$ eV) and Fe^+ ($E_c-0.28$ eV) ions. It is noted that the maximum solubility of Fe atoms in ZnTe is determined by FeTe cluster formation.
 [S1063-7826(99)00603-1]

Substitution solid solutions, one component of which is the magnetic Fe^{2+} ion, are van Fleck semimagnetic semiconductors. In the case of the semiconducting II–VI compounds, Fe atoms displace cation sites. It should be noted that, compared to semimagnetic semiconductors, in which Mn^{2+} ions are the magnetic component, the solubility of Fe atoms is substantially lower in the above group of semiconductors. Thus, in the case of the selenides, it is about 15% and for the tellurides, no more than 5%.[1] Thus far, $Cd_{1-x}Fe_xSe$ crystals have been studied most extensively. As for the tellurides, only a few papers on various physical properties of the semimagnetic semiconductor $Cd_{1-x}Fe_xTe$ have been published.[2–4] Of these Ref. 3 is the most complete from the standpoint of studies of the physical properties. As far as we know, only one paper has been published on $Zn_{1-x}Fe_xTe$ crystals and it dealt with their magnetic properties.[5]

Our goal in this study was to use data on the optical and photoelectric properties of the semimagnetic semiconductors $Zn_{1-x}Fe_xTe$ in order to obtain information on the introduction of Fe atoms into the ZnTe crystal lattice, on the formation of substitution solid solutions, on how Fe atoms affect the energy structure of ZnTe, and, primarily, on the positions of the Fe^{2+} and Fe^+ ions relative to the energy bands of the crystal.

The $Zn_{1-x}Fe_xTe$ ($x \leqslant 0.046$) crystals studied here were grown by the Bridgman method. The concentration of Fe atoms was determined more accurately using an MS-46 x-ray microanalyzer.

The optical spectra were studied using a KSVU-6 spectral system. The measurements at low temperatures were conducted using an UTREKS system, which makes it possible to stabilize the temperature within ± 0.01 K.

The photovoltaic current measurements were made with a V7-30 voltmeter-electrometer. Samples in the form of plane-parallel slabs with thicknesses of 3–5 mm were used for these measurements. Annular contacts were deposited by soldering indium on the natural cleavage surfaces of the crystals and tested for resistance by measuring their current-voltage characteristics. Prior to the photovoltaic current measurements the samples were heated to a temperature of 350 K and slowly (over 2 h) cooled in darkness while shorted out. The photovoltaic current spectra were normalized to the same amount of incident photons.

Information on the band (energy) structure of the semiconductors and its variation as a result of the formation of substitution solid solutions can be obtained from low-temperature measurements of the exciton reflection and absorption spectra in the neighborhood of the intrinsic absorption edge, since these spectra are extremely sensitive to various defects in the crystal lattice (disordering, impurities, intrinsic defects).

The data on the exciton reflection spectra indicate the existence of shift to shorter wavelengths in the energies of the characteristic bands which is associated with the formation of $Zn_{1-x}Fe_xTe$ substitution solid solutions and has been observed previously for crystalline $Cd_{1-x}Fe_xTe$.[2] Figure 1 shows a plot of the energy of the exciton reflection band (E_{exc}) of $Zn_{1-x}Fe_xTe$ as a function of the Fe concentration (x). The experimental points are well fit by the straight line

$$E_{exc}(x) = E(0) + 1.0x \text{ (eV)}, \tag{1}$$

where $E(0)$ gives the location of the exciton reflection band of ZnTe that was not specially doped. The observed scatter in the points is caused by a nonuniform distribution of Fe atoms over the crystal ingot, especially at high concentrations (about 4%), which is apparently close to the maximum solubility of Fe in crystalline ZnTe. This is also indicated by a substantial broadening of the exciton reflection bands: for $x=0.008$ the half-width of the exciton band is twice that for pure ZnTe, while for $x=0.046$ the width has increased by more than a factor of 4. This broadening is related to the nonuniform distribution of the Fe atoms and to the formation of clusters involving Fe. Thus, for crystals with $x=0.046$,

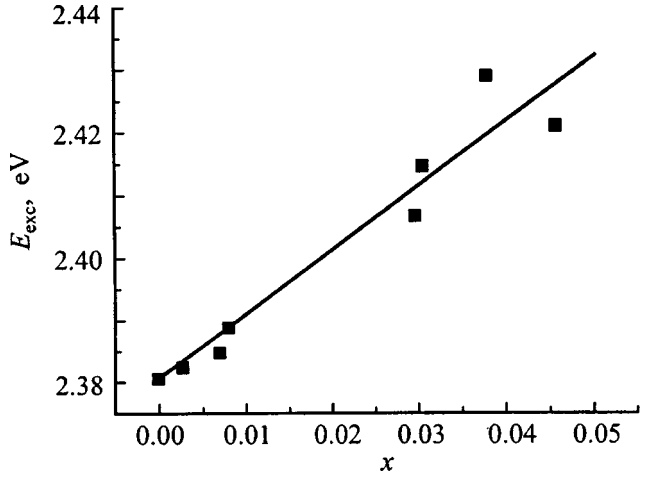

FIG. 1. Energy location of the exciton reflection band, E_{exc}, as a function of the Fe concentration in $Zn_{1-x}Fe_xTe$ crystals at $T=4.2$ K. The straight line corresponds to Eq. (1).

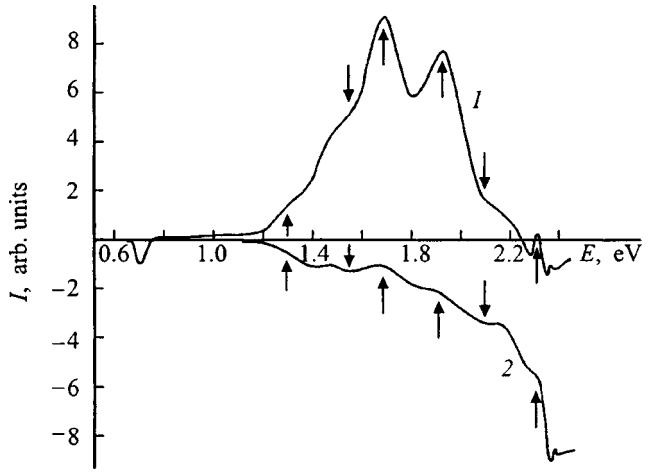

FIG. 3. Photovoltaic current (I) spectra of $Zn_{1-x}Fe_xTe$ crystals at $T=77$ K. Curves *1* and *2* correspond to $x=0.0027$ and 0.008.

x-ray microprobe analysis (area $2\times3\mu m^3$) revealed cluster formations involving Fe and Te atoms with dimensions of $150\times50\mu$m. In these inclusions the Fe atom content was about 30 wt. %, which may indicate that FeTe clusters have developed. Evidently, the formation of clusters of this type limits the maximum solubility of Fe atoms in the group II–VI tellurides.

Figure 2 shows absorption spectra of $Zn_{1-x}Fe_xTe$ crystals with different concentrations of Fe measured at $T=4.2$ K. Besides the absorption edge, which in the range of measured absorption coefficients ($k<250$ cm^{-1}) shifts to longer wavelengths as the Fe atom concentration is raised, an impurity absorption band can be seen with an energy peak at $E=1.31$ eV. The intensity of this band increases as the Fe concentration is raised. An analogous band has been observed previously for $Cd_{1-x}Fe_xTe$ crystals.[2] This band corresponds[6] to intracenter transitions between the ground $^5E(^5D)$ state and the $^3T_1(^3H)$ excited state of Fe^{2+} ions. The structure observed at the long wavelength edge of the band is caused by an electronic-vibrational interaction involving vibrations with different energies (frequencies of 35 and 125 cm^{-1}). Vibrations at these frequencies have been observed before in studies of intracenter absorption by Co^{2+} ions[7] and Mn^{2+} ions[8] in crystalline ZnTe. The shape of these bands is indicative of the presence of a strong electronic-vibrational interaction for these intracenter transitions, and also indicates that the excited $^3T_1(^3H)$ state lies in the band gap of the crystal, in contrast with the semimagnetic semiconductor $Cd_{1-x}Fe_xTe$.[2]

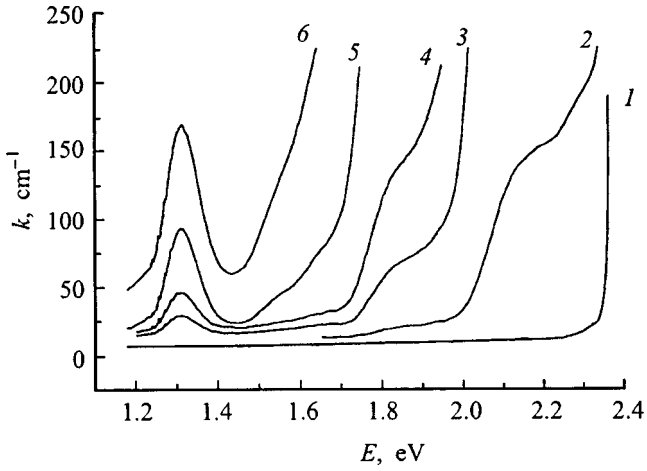

FIG. 2. Optical absorption spectra of $Zn_{1-x}Fe_xTe$ crystals at $T=4.2$ K. Curves *1-6* correspond to $x=0$, 0.001, 0.0027, 0.008, 0.030, and 0.046.

The long-wavelength shift of the absorption edge in the measured range of absorption coefficients (Fig. 2), as well as the fact that structure has the form of steps whose intensity increases as the Fe atom concentration is raised, indicate that this absorption involves Fe ions. The shape of the absorption spectra suggests that it may originate from photoionization. In order to establish the nature of the observed absorption, we have measured photovoltaic current spectra, some examples of which are shown in Fig. 3 for $Zn_{1-x}Fe_xTe$ with different concentrations of Fe. At the lower concentration ($x=0.0027$, curve *1*) the photovoltaic current spectrum contains two intense bands of positive polarity located at $E_1=1.94$ eV and $E_2=1.70$ eV. It should be noted that the polarity of the photovoltaic current was determined by the sign of the charge in the front (illuminated) surface of the test sample and was opposite to the sign of the excited carriers. Thus, it should be assumed that the shorter wavelength photovoltaic current band corresponds to a photoionization transition from the ground $^5E(^5D)$-state of the Fe^{2+} ion into the conduction band. This hypothesis is in fairly good agreement with the location of the levels of these ions in II–VI group semiconductors in terms of a diagram showing the location of the energy bands of different crystals with respect to the vacuum level.[9] In fact, in such a diagram the locations of the valence bands for CdTe and ZnTe crystals are the same. Thus, the difference in the location of the ground state of the Fe^{2+} ion relative to the conduction band should correspond roughly to the difference in the gap widths of crystalline CdTe and ZnTe. Since the donor photoionization energy of Fe^{2+} ions is 1.08 eV for $Cd_{1-x}Fe_xTe$ crystals, the value obtained here for $Zn_{1-x}Fe_xTe$ ($E_1=1.94$ eV) is in

fairly good agreement with that expected according to this scheme. Thus, the positive polarity band with its energy $E_1 = 1.94$ eV can be attributed to the following photoionization transition:

$$Fe^{2+}[^5E(^5D)] + \hbar\omega \rightarrow Fe^{3+} + e, \quad (2)$$

where $\hbar\omega = 1.94$ eV. Thus, the ground state of Fe^{2+} lies in the gap of crystalline ZnTe at $E_v + 0.44$ eV. The photovoltaic current band with energy $E_2 = 1.70$ eV may correspond to a photoionization transition from the excited $^5T_2(^5D)$-state, consistent with the energy location of this level with respect to the ground $^5E(^5D)$-state. Therefore, for CdTe:Fe crystals, it is ~ 0.25 eV (Ref. 10); i.e., the following photoionization transition takes place:

$$Fe^{2+}[^5T_2(^5D)] + \hbar\omega \rightarrow Fe^{3+} + e, \quad (3)$$

where $\hbar\omega = 1.70$ eV. It should be noted that the population of the excited $^5T_2(^5D)$-state is the result of acceptor photoionization of Fe^{3+} ions with their transfer into this excited state; this is confirmed by the observation of a negatively polarized band with energy $E_3 = 0.7$ eV in the photovoltaic current spectrum.

In the short-wavelength wing of the band at $E_1 = 1.94$ eV there is a feature near 2.10 eV in the form of an inflection which, as measured photovoltaic current spectra for crystalline $Zn_{1-x}Fe_xTe$ ($x = 0.008$) show, are obviously associated with the appearance of a negatively polarized band (in Fig. 3 the location of this band is indicated by an arrow). This band may develop because of photoionization transitions of the type

$$Fe^{2+} + \hbar\omega \rightarrow Fe^{+} + h, \quad (4)$$

where $\hbar\omega = 2.10$ eV. Fe^{3+} and Fe^{+} charge states have been observed previously in electron spin resonance (ESR) spectra of ZnTe crystals.[11] In the case of Fe^{+} the photosensitive ESR signal was found to increase at an energy of 2.25 eV. Thus, the energy we have obtained for the acceptor photoionization of Fe^{2+} ions is consistent with the data of Ref. 11 and indicates that the Fe^{+} level in ZnTe crystals lies at $E_c - 0.28$ eV. An approximation of the position of this level in other II–VI group crystals using a diagram of their energy levels relative to the vacuum level[9] indicates that for all the other crystals in this group the Fe^{+} level is at resonance with the conduction band. It must be assumed that this is why no Fe^{+} ion level has yet been observed in the band gap of the other II–VI crystals.

In the long-wavelength wing of the 1.70-eV band, there are also two features in the form of inflections, one of which, at 1.57 eV, may be caused by acceptor photoionization of Fe^{3+} ions with their transfer into the Fe^{2+} charge state in the excited $^3T_1(^3H)$-state, i.e.,

$$Fe^{3+} + \hbar\omega \rightarrow Fe^{2+}[^3T_1(^3H)] + h, \quad (5)$$

where $\hbar\omega = 1.57$ eV. The other feature, at about 1.3 eV, is related to the deformation of the photovoltaic current spectrum by a rather intense intracenter absorption band of the Fe^{2+} ions.

In the shortest-wavelength portion of the photovoltaic current spectrum for $x = 0.0027$ one can see a positively polarized band at 2.32 eV, as well as a negatively polarized band at 2.36 eV. The first band is caused by photoionization of singly charged zinc vacancies, i.e., by a transition from an acceptor level $E_c + 0.05$ eV into the conduction band, and the second, by dissociation of excitons. The segment of the photovoltaic current spectrum observed on the short wavelength side of the exciton band is associated with band-band transitions.

The measured photovoltaic current spectra for crystalline $Zn_{1-x}Fe_xTe$ with higher Fe concentrations (Fig. 3, curve *2*) have a similar structure; i.e., positively and negatively polarized bands are observed at the energies marked by the arrows in Fig. 2. The difference in the spectra for $Zn_{1-x}Fe_xTe$ with different Fe concentrations is that, in the region 1.2–2.2 eV, *n*-type conductivity is observed when the concentration is lower, while for higher Fe atom concentrations, *p*-type conductivity occurs in the entire spectral range that was studied, along with a slight shift in the exciton line to shorter wavelengths. The observed hole conductivity of $Zn_{1-x}Fe_xTe$ ($x = 0.008$) crystals over a wide spectral range is primarily caused by strong (compared to the *n*-type impurity conductivity) hole conductivity in the band-band transition region. This is because, for a high concentration of Fe atoms ($x = 0.008$) the substitution of Zn vacancies by impurity atoms greatly reduces the number of the singly charged Zn vacancies which determine the electron conductivity of ZnTe crystals in the band-band transition region. Furthermore, impurity Fe^{2+} centers begin to trap free electrons efficiently and this favors an increase in the amount of Fe^{+} ions. We have observed an analogous phenomenon before in ZnTe crystals doped with Cr.[12]

An analysis of photovoltaic current spectra therefore shows that the observed long-wavelength shift in the absorption edge of $Zn_{1-x}Fe_xTe$ crystals in the region of relatively low absorption coefficients ($k < 250$ cm^{-1}) and its step-like structure are related to photoionization processes involving various charge states of Fe (Fe^{+}, Fe^{2+}, and Fe^{3+}). In the case of Fe^{2+} ions, we have observed photoionization transitions involving the ground state and excited states of the impurity ions. Energy locations of Fe^{+} and Fe^{2+} ions in the band gap of $Zn_{1-x}Fe_xTe$ crystals have been determined.

*E-mail: gnatenko@iop.kiev.ua; Fax: 380 (44) 265-30-33

[1] A. Mycielski, Acta Phys. Pol. A **73**, 839 (1988).
[2] Yu. P. Gnatenko, I. A. Farina, R. V. Gamernik, A. S. Krochuk, and P. I. Babyi, Fiz. Tekh. Poluprovodn. **27**, 1639 (1993) [Semiconductors **27**, 906 (1993)].
[3] C. Testelin, A. Mauger, C. Rigaux, M. Gnillot, and A. Mycielski, Solid State Commun. **71**, 923 (1989).
[4] A. Saren, B.A. Orlowski, and S. Kuzminski, Acta Phys. Pol. A **79**, 183 (1991).
[5] V. G. Abramishvili, A. V. Komarov, S. M. Ryabchenko, and V. I. Pogorelyi, Fiz. Tekh. Poluprovodn. **23**, 575 (1989) [Sov. Phys. Semicond. **23**, 360 (1989)].
[6] B. M. Vul, V. S. Ivanov, V. A. Rukavishnikov *et al.*, Fiz. Tekh. Poluprovodn. **6**, 1264 (1972) [Sov. Phys. Semicond. **6**, 751 (1972)].
[7] Yu. P. Gnatenko, A. I. Zhmurko, and I. A. Farina, Ukr. Fiz. Zh. **33**, 24 (1988).

[8] Yu. P. Gnatenko and A. I. Zhmurko, Ukr. Fiz. Zh. **30**, 843 (1985).
[9] Yu. P. Gnatenko, Author's abstract of candidate's dissertation, Institute of Physics, National Academy of Sciences of Ukraine, Kiev (1992).
[10] G. A. Slack, F. S. Ham, and R. M. Chrenko, Phys. Rev. **152**, 376 (1966).
[11] T. L. Estle and W. C. Holton, Phys. Rev. **150**, 159 (1966).
[12] V. S. Blazhkiv, R. V. Gamernik, Yu. P. Gnatenko, A. S. Krochuk, and E. V. Smishko, Ukr. Fiz. Zh. **33**, 714 (1988).

Translated by D. H. McNeill

Calculating the band structure of $InSb_{1-x}Bi_x$ solid solutions

V. G. Deĭbuk,* Ya. I. Viklyuk, and I. M. Rarenko

Yu. Fedkovich Chernovtsy State University, 274012 Chernovtsy, Ukraine
(Submitted April 10, 1998; accepted for publication September 15, 1998)
Fiz. Tekh. Poluprovodn. **33**, 289–292 (March 1999)

The empirical pseudopotential method including the spin-orbit interaction is used to calculate the band structure of the substitution solid solution $InSb_{1-x}Bi_x$. This makes it possible to study the dependence of the band gap on the temperature and composition of the alloy in the virtual-crystal approximation. The calculations are in good agreement with the available experimental data. © *1999 American Institute of Physics.* [S1063-7826(99)00703-6]

The narrow-gap substitution solid solutions based on III–V compounds are promising materials for solid-state electronics. Interest in these materials has recently increased markedly in connection with multicomponent alloys, which are potentially very important materials for creating infrared (IR) detectors, low-noise filters for communications systems, and continuously tuneable lasers.[1,2] Today, the most accessible semiconductor materials for fabricating far-IR devices (wavelengths $\lambda > 8\mu$m) are CdHgTe alloys. The properties of these crystals, however, depend to a substantial degree on the manufacturing process, which is not so highly developed as that for the III–V compounds. Many unpredictable factors have a major effect on the band gap, and degradation processes cause instability in the physical and ecological characteristics.[3]

The conventional III–V alloys do not offer the possibility of extending the wavelength range beyond a limit of $\lambda = 7.5\mu$m (InAsSb). Thus, there are now two alternative ways of solving this problem. The first is to produce new, multicomponent materials base on III–V. The second basically involves changing the band gap through the stresses which develop in the corresponding superlattices and heterostructures.[4] Both the first and second approaches have their strong and weak points.

Experimental studies of the InSb–InBi system began about 30 years ago with the classical papers of Jean-Louis.[5–7] Production difficulties in growing these substitution solid solutions have thus far delayed their wide introduction into practice. However, recent advances in this area[8,9] have opened up new possibilities for obtaining and using them. Because of this circumstance, there is increasing interest in their fundamental properties, such as the electronic band structure and the dependence of the band gap on the alloy composition and temperature, and, therefore, in the optical and photoelectric characteristics of these materials.

The fact that InBi crystallizes into a tetragonal ($B10$) structure and is a semimetal, which is not typical of most III–V compounds (they are cubic semiconductors), has stimulated research on the interrelation between its anomalous crystalline structure and its physical properties.[10] The ratio of the lattice constants in InBi is $c/a = 0.9545$.[9] The physical properties of the solid solution $InSb_{1-x}Bi_x$ ($x < 3\%$) have been studied in a number of papers and it has been shown that in this range of variation in the composition, a substitution solid solution with a sphalerite structure and a straight band gap is formed. The first computational estimates of the band structure of $InSb_{1-x}Bi_x$ used three methods: Herman's relativistic corrections method, the empirical pseudopotential (EPP) method, and the van Vechten semiconductor model.[7] They could not quantitatively explain the concentration and temperature dependences of the band gap width and, therefore, of the optical properties. Although the electrical and optical properties of this solid solution are of great practical interest, detailed calculations of the electronic band structure have not been done until now. In this paper we calculate the electronic energy spectrum of $InSb_{1-x}Bi_x$ by the empirical pseudopotential method including the spin-orbit interaction in the approximation of a virtual crystal and investigate the concentration and temperature dependences of the band gap width theoretically.

To calculate the electronic band structure it is necessary to solve the Schrödinger equation, for which the one-electron pseudopotential Hamiltonian in atomic units has the form

$$H = -\nabla^2 + V_p(\mathbf{r}), \tag{1}$$

where

$$V_p(\mathbf{r}) = V(\mathbf{r}) + \sum_t (E - E_t)|b_t\rangle\langle b_t| \tag{2}$$

is the crystal potential, $V_p(\mathbf{r})$ is the true crystal potential, and $|b_t\rangle$ is the wave function of the ground state with energy E_t. Disregarding its nonlocal part, we write the Fourier transform of the pseudopotential $V_p(\mathbf{r})$ as

$$V_p(\mathbf{r}) = \sum_{\mathbf{G}} V_L(\mathbf{G}) \exp[i(\mathbf{G}\cdot\mathbf{r})], \tag{3}$$

where

$$V_L(\mathbf{G}) = \sum_\alpha S_\alpha(\mathbf{G}) \nu_\alpha(\mathbf{G}), \tag{4}$$

$$S_\alpha(\mathbf{G}) = \frac{1}{N_\alpha} \sum_j \exp[-i(\mathbf{G}\cdot\mathbf{R}_\mathbf{j}^\alpha)], \tag{5}$$

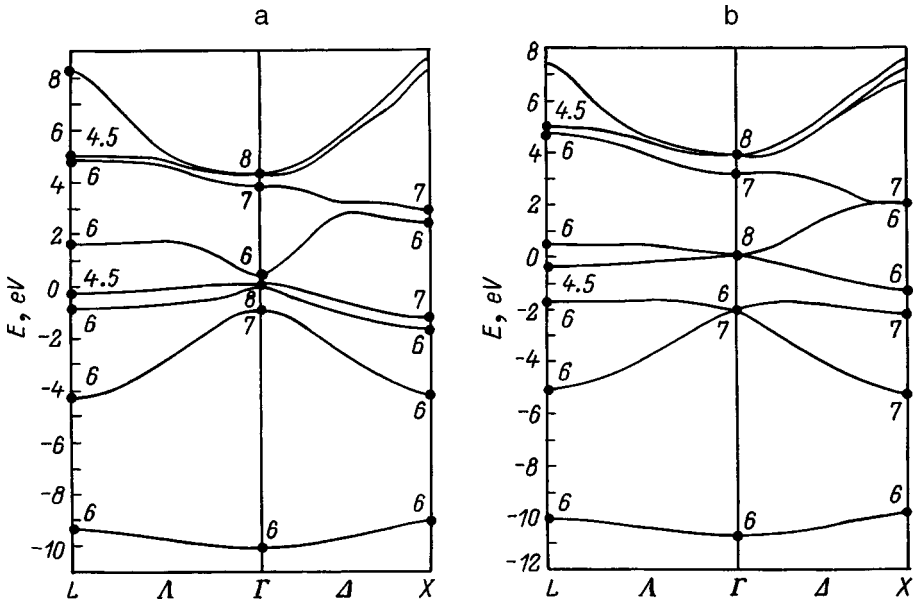

FIG. 1. The band structure of InSb (a) and InBi (b).

where **G** are the reciprocal lattice vectors, $\nu_\alpha(G)$ are the atomic pseudopotential form factors, N_α is the number of atoms of type α in a unit cell, and $\mathbf{R}_j^\alpha$ determines the position of the jth atom of type α. For the case of N-(8-N) compounds with a zincblende structure, on choosing the coordinate origin as the midpoint of the line joining the nearest A and B atoms, these equations can be reduced to the form

$$V_L(\mathbf{G}) = v^S(\mathbf{G})\cos(\mathbf{G}\cdot\boldsymbol{\tau}) + iv^A(\mathbf{G})\sin(\mathbf{G}\cdot\boldsymbol{\tau}), \tag{6}$$

where

$$v^S(G) = [v_{\mathrm{A}}(G) + v_{\mathrm{B}}(G)]/2,$$
$$v^A(G) = [v_{\mathrm{A}}(G) - v_{\mathrm{B}}(G)]/2, \tag{7}$$

where $\boldsymbol{\tau} = (a/8)\cdot(1,1,1)$, and a is the lattice constant.

In the empirical pseudopotential method we only consider the first four terms, which can be justified by the cutoff of the strong core potential. The band structure of $\mathrm{InSb}_{1-x}\mathrm{Bi}_x$ can be found by solving the secular equation

$$\det\left|\{K^2 - E_n(\mathbf{k})\}\delta_{\mathbf{GG}'}\delta_{ss'} + V_L(\mathbf{G}-\mathbf{G}')\delta_{ss'} + V_{so}^{ss'}(\mathbf{K},\mathbf{K}')\right| = 0. \tag{8}$$

The spin-orbit term is

$$V_{so}^{ss'}(\mathbf{K},\mathbf{K}') = (\mathbf{K}\times\mathbf{K}')\sigma_{ss'} \times\{-i\lambda^S\cos(\mathbf{K}-\mathbf{K}')\cdot\tau + \lambda^A\sin(\mathbf{K}-\mathbf{K}')\cdot\tau\}. \tag{9}$$

Here s and s' are the spin states, the σ are the Pauli matrices, $\mathbf{K} = \mathbf{k} + \mathbf{G}$, and λ^A and λ^S are regarded as fit parameters for the spin-orbit splitting of the upper valence band. According to the virtual-crystal approximation (VCA) and Vegard's law, the lattice constants and pseudopotential form factors for the substitution solid solution $\mathrm{InSb}_{1-x}\mathrm{Bi}_x$ can be constructed in the form of the linear combinations

$$a_{ss} = a_{\mathrm{InBi}}x + a_{\mathrm{InSb}}(1-x),$$
$$V_{ss} = V_{\mathrm{InBi}}x + V_{\mathrm{InSb}}(1-x), \tag{10}$$

where a_{ss} and V_{ss} are the lattice constant and form factor of the substitution solid solution.

Numerical calculations have been done along the principal directions of symmetry of the Brillouin zone in a basis of 137 plane waves (the secular determinant including the spin states had a dimensionality of 274×274). Figure 1 shows the band structures of InSb and InBi calculated using the

TABLE I. Pseudopotential parameters used in the calculations.

Model parameters	InSb		InBi	
	Data from Ref. 11	Our data	Data from Ref. 7	Our data
$\nu^S(3)$	−0.2547	−0.2285	−0.22	−0.285
$\nu^S(8)$	0.0188	0	−0.03	−0.0035
$\nu^S(11)$	0.0452	0.0405	0.02	0.0145
$\nu^A(3)$	0.0302	0.06	0.08	0.049
$\nu^A(4)$	0.0012	0.05	0.05	0.035
$\nu^A(11)$	0.0329	0.01	0.02	0.005
λ^S	0.00231	0.00230	⋯	0.001693
λ^A	0.00028	0.00028	⋯	0.003443

TABLE II. Interband separations (in eV) at several symmetry points of the Brillouin zone.

Brillouin zone point	InSb			InBi	
	EPP[11]	Our calculations	Expt.[12]	EPP[10]	Our calculations
$\Gamma_{8v}-\Gamma_{6c}$	0.26	0.247	0.2357	1.9	1.97
$\Gamma_{7v}-\Gamma_{6c}$	1.05	1.23	1.216	0	0
$\Gamma_{8v}-\Gamma_{7c}$	3.65	3.6	⋯	2.56	3.1
$\Gamma_{8v}-\Gamma_{8c}$	3.68	4.21	⋯	3.10	3.83
$L_{4,5v}-L_{6c}$	2.03	1.89	1.9	1.25	1.18
$L_{6v}-L_{6c}$	2.60	2.48	⋯	1.75	2.11
$L_{4,5v}-L_{6c}$	5.3	5.71	⋯	4.12	4.87
$X_{7v}-X_{6c}$	3.95	3.73	⋯	0.75	0.77
Δ_{so}	0.82	0.99	0.98	1.9	1.97

theoretical parameters listed in Table I and compared with the parameters of other papers.[7,11] In the limiting cases of $x=0$ (InSb) and $x=1$ (InBi) the calculated energy separations between the electronic levels in the high symmetry points are in satisfactory agreement with published experimental data and pseudopotential calculations by others (Table II). As opposed to InSb, in InBi the *s*-band of In falls below the *p*-band of Bi at the point Γ by almost 2 eV, which was noted in Refs. 7 and 10.

The effect of temperature on the band structure of these solid solutions can be taken into account using the Brooks-Yu theory.[13] While at zero temperature the electronic energies are calculated as functions of the atomic pseudopotential form factors

$$E(\mathbf{k})=E(\mathbf{k},\{V_j(\mathbf{G})\}), \tag{11}$$

at finite temperatures each Fourier component of the jth atomic pseudopotential is corrected with the help of the Debye-Waller factor $M_j(\mathbf{G},T)$,

$$E(\mathbf{k},T)=E(\mathbf{k},\{V_j(\mathbf{G})\exp[-M_j(\mathbf{G},T)]\}). \tag{12}$$

For cubic crystals the Debye-Waller factor is given by

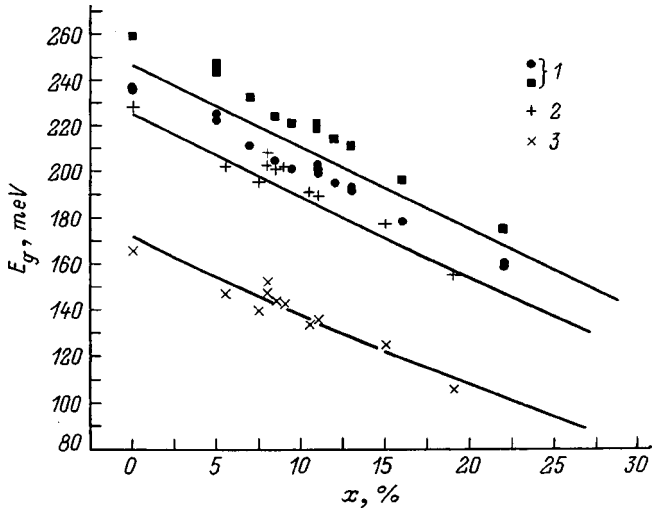

FIG. 2. The variation in the band gap E_g with composition for $InSb_{1-x}Bi_x$. The smooth curves are calculated and the points are experimental data.[6] $T=0$ (*1*), 77 (*2*), 300 K (*3*).

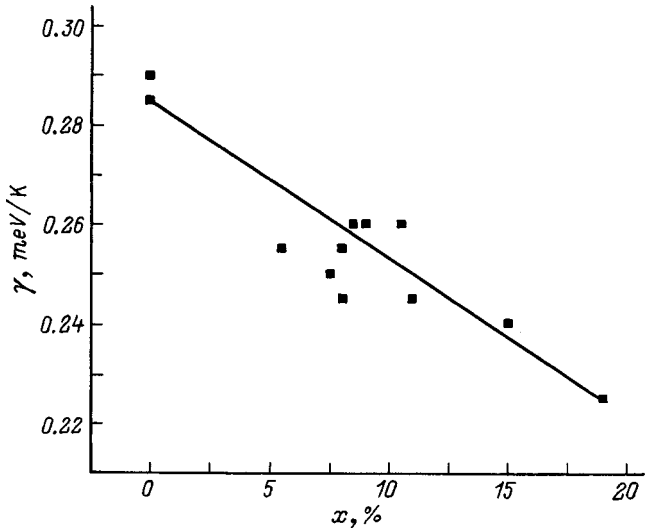

FIG. 3. The band gap temperature coefficient $\gamma=-\Delta E_g/\Delta T$ as a function of the Bi content. The points are experimental data.[6]

$$M_j(\mathbf{G},T)=\frac{|\mathbf{G}|^2}{6}\langle U_j^2(T)\rangle, \tag{13}$$

where the mean square displacement $\langle U_j^2\rangle$ of the jth atom obeys the Debye equation

$$\langle U_j^2(T)\rangle=\frac{3\hbar^2}{m_j k_B}\frac{T}{\Theta_j^2}\left[\Phi\left(\frac{\Theta_j}{T}\right)+\frac{1}{4}\frac{\Theta_j}{T}\right], \tag{14}$$

where the m_j are the ion masses, Θ_j are the Debye temperatures of each type of atom, and Φ_j is the Debye integral of the first kind. In our calculations the Debye temperatures for In, Bi, and Sb were assumed to be $\Theta_{In}=112$ K, $\Theta_{Bi}=120$ K, and $\Theta_{Sb}=220$ K.[14] The effect of the thermal expansion of the lattice was taken into account in the appropriate formulas for the temperature dependence of the lattice constants. Figure 2 shows a comparison of the calculated temperature and concentration dependences of the band gap E_g of semiconducting $InSb_{1-x}Bi_x$ solid solutions with experimental data from optical absorption experiments.[6] The variation in the coefficient $\gamma=-\Delta E_g/\Delta T$ with x calculated on the basis of this band structure is shown in Fig. 3.

The satisfactory agreement between the experimental and theoretical curves justifies the hope that this model gives a correct description of the energy band structure of these ternary semiconductor solid solutions. It can serve as a basis for further study and prediction of their optical properties and for a correct approach to solving the technological problems of obtaining more perfect material with the required band gap.

*E-mail: vdei@chsu.cv.ua

[1] A. Rogalski, *New ternary alloy systems for infrared detectors* (Bellingham, Washington, SPIE Press, 1994).
[2] T. I. Voronina, B. E. Dzhurtanov, T. S. Lagunova, M. A. Sipovskaya, V. V. Sherstnev, and Yu. P. Yakovlev, Fiz. Tekh. Poluprovodn. **32**, 278 (1998) [Semiconductors **32**, 250 (1998)].
[3] J. Furdyna, J. Appl. Phys. **64**, 29 (1988).

[4] Z. I. Alfërov, Fiz. Tekh. Poluprovodn. **32**, 1 (1998) [Semiconductors **32**, 1 (1998)].
[5] A. M. Jean-Louis and C. Hamon, Phys. Status Solidi **34**, 329 (1969).
[6] A. M. Jean-Louis, B. Ayrault, and J. Vargas, Phys. Status Solidi **34**, 341 (1969).
[7] A. M. Jean-Louis and G. Duraffourg, Phys. Status Solidi B **59**, 495 (1973).
[8] R. Kh. Akchurin and T. V. Sakharova, Zh. Tekh. Fiz. **62**, 16 (1992) [Sov. Phys. Tech. Phys. **37**, 895 (1992)].
[9] R. Kh. Akchurin, V. G. Zinov'ev, T. M. Kuz'micheva, and V. B. Ufimtsev, Kristallografiya **27**, 561 (1982).
[10] J. E. Schierber and J. P. Van Dyke, Phys. Rev. B **15**, 890 (1977).
[11] C. V. Alvarez, J. P. Walter, R. W. Boyd, and M. L. Cohen, J. Phys. Chem. Solids **34**, 337 (1973).
[12] V. I. Gavrilenko, A. M. Grekhov, D. V. Korbutyak, and V. G. Litovchenko, *Optical Properties of Semiconductors. A Handbook* [in Russian], Naukova Dumka, Kiev (1987).
[13] M. L. Cohen and J. R. Chelikowsky. *Electronic structure and optical properties of semiconductors*, Springer-Verlag, Berlin (1988).
[14] I. S. Grigor'ev and E. Z. Mikhaĭlova, Eds., *Physical Quantitites. A Handbook* [in Russian], Énergoatomizdat, Moscow (1991).

Translated by D. H. McNeill

SEMICONDUCTOR STRUCTURES, INTERFACES AND STRUCTURES

Effective charge carrier lifetime in CdHgTe variable-gap structures

V. M. Osadchiĭ, A. O. Suslyakov, V. V. Vasil'ev, and S. A. Dvoretsky

Institute of Semiconductor Physics, Siberian Branch of the Russian Academy of Sciences, 630090 Novosibirsk, Russia

(Submitted May 5, 1998; accepted for publication June 29, 1998)
Fiz. Tekh. Poluprovodn. **33**, 293–296 (March 1999)

The effective charge carrier lifetime in *n*-type CdHgTe variable-gap structures is calculated with allowance for Auger recombination and recombination at dislocations. It is shown that introducing wide, variable-gap layers can eliminate the effect of surface recombination and yield long effective lifetimes, even for high densities of dislocations (above 10^7 cm^{-2}). The calculated charge carrier lifetimes are in agreement with measurements on variable-gap structures grown by molecular-beam epitaxy. © *1999 American Institute of Physics.* [S1063-7826(99)00803-0]

INTRODUCTION

The photoelectric characteristics of photoconductors based on cadmium-mercury-tellurium compounds are determined by the minority charge carrier lifetime, which depends on both the structural perfection of the material and the surface recombination rate.

There are a number of ways to passivate the surface: using insulating layers[1] or *in situ* growing of wide band-gap[2] or variable-gap[3] layers. Only the first two cases have been examined theoretically.[1,2,4]

In order to improve the structural perfection in epitaxial growth techniques it is customary to use substrates whose lattice parameter matches the epitaxial CdHgTe layer. Thus, in CdHgTe epitaxial structures grown by molecular-beam epitaxy (MBE)[5,6] on substrates of CdZnTe that are matched in terms of the lattice parameter, a dislocation density of $\sim 3\times 10^5 - 3\times 10^6$ cm^{-2} is observed. At the same time, in CdHgTe structures grown on GaAs substrates with CdTe buffer layers,[6,7] a higher density of dislocations, $\sim 2\times 10^6 - 5\times 10^7$ cm^{-2}, is observed.

It is known that dislocations can manifest electrical activity,[8] by, for example, making a dominant contribution to carrier recombination and determining the minority charge carrier lifetime. It has been shown from surface potential measurements[9] that at an interface with an oxide, the lifetime in bulk CdHgTe (with a cadmium content $x_{\mathrm{Ca}}=0.3$) at the surface layer depends on the density of dislocations, n_d. For $n_d < 2\times 10^5$ cm^{-2}, the lifetime saturates and no longer depends on the dislocation density. Evidently, there are other recombination centers which limit the lifetime. An empirical formula for the lifetime as a function of dislocation density was proposed. At the same time, photoconductivity measurements, which yielded the lifetime for the structure as a whole, showed that the lifetime is twice that measured in the skin layer for the same dislocation density. We believe that this difference may be related to recombination at the oxide-CdHgTe interface and to a dependence of the surface recombination rate on the density of dislocations emerging at the CdHgTe surface.

The dependence of the lifetime on the dislocation density has been studied[6] in CdHgTe structures grown on CdZnTe and GaAs substrates. It was stated that observed lifetimes may be related to charge carrier recombination at dislocations in the bulk of the CdHgTe, as in Ref. 9. It was shown that for dislocation densities greater than 2×10^6 cm^{-2} in CdHgTe structures on GaAs the lifetimes fall sharply from 200 to 20 ns. Since the short lifetimes in Ref. 9 were observed near the surface, however, it is possible that those in Ref. 6 are also affected by surface recombination.

It is known that introducing a nonuniform potential well into the structure of a photoconductor increases the lifetime.[10] We have developed a technique for growing epitaxial CdHgTe structures by MBE with real-time measurements of the composition of the growing layer.[3] This technique makes it possible to grow CdHgTe layers with arbitrary prespecified profiles of the CdHgTe composition over the thickness of the film. For passivation, epitaxial layers were grown with wide, graded-gap layers at the film-substrate interface and on the surface of the CdHgTe film.

In this paper we use numerical methods to study the effect of graded-gap layers on the effective charge carrier lifetime in *n*-type CdHgTe photoconductors with composition profiles close to the actual ones and compare the theoretical and experimentally measured effective charge carrier lifetimes in CdHgTe heterostructures grown on GaAs substrates by MBE.

MODEL

The calculations were done for photoconductors based on a CdHgTe film with variable-gap layers (Fig. 1a, curve *1*) grown on GaAs substrates with a CdTe buffer layer (Fig. 1b). The profile of the Cd content over the depth of the film is close to the profiles in real structures. Here the band gap

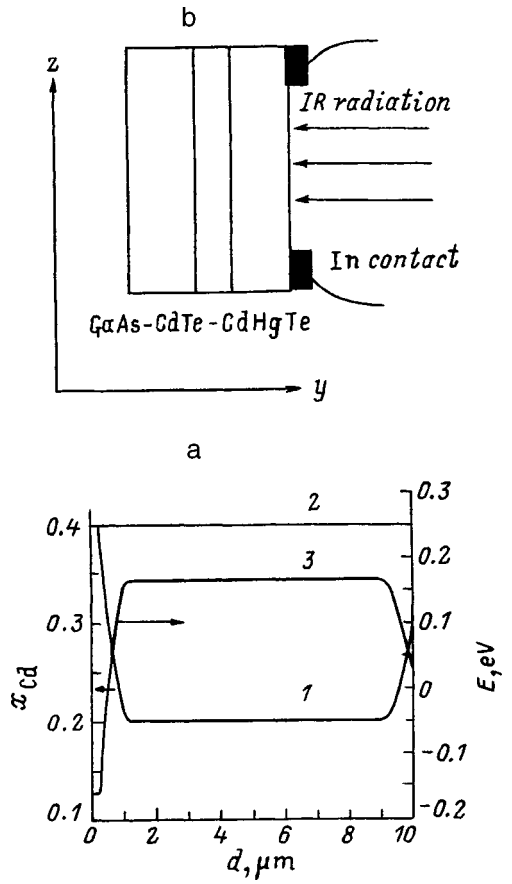

FIG. 1. (a) (*1*) The profile of the cadmium content in the model structure, (*2*) the profile of the edge of the conduction band, and (*3*) the profile of the edge of the valence band. (b) A sketch of the model structure.

increases toward the film surface and toward the interface with the buffer (Fig. 1a; the difference between curves *2* and *3*).

The distribution of nonequilibrium charge carriers in a photoconductor can be determined by solving a one-dimensional diffusion equation that includes recombination and photogeneration of charge carriers and an imbedded field that develops because of the position dependence of the parameters of the band structure. The hole current j_p as a function of the depth y in the structure in an n-type semiconductor is given by[11]

$$j_p(y)=\mu_p(y)p(y)k_BT\frac{d}{dy}\ln n_i^2(y)-\mu_p(y)k_BT\frac{d}{dy}p(y), \tag{1}$$

where μ_p is the hole mobility, p is the hole concentration, n_i is the intrinsic charge carrier concentration, T is the temperature, and k_B is Boltzmann's constant. This expression was obtained in the approximation of a low level of excitation for uniform doping in the y direction. Note that since it contains no dependence on electron affinity, the location of the conduction band is independent of the coordinate y (Fig. 1a, curve *2*).[11] In the calculations an expression for n_i was taken from Hansen and Schmidt,[12] and that for E_g was taken from Finkman and Shachman.[13] It is assumed that $\mu_p=0.01\mu_n$ and the formula for the electron mobility μ_n was taken from Rosbeck *et al.*[14]

The diffusion equation for nonequilibrium holes in n-type CdHgTe is

$$\frac{k_BT}{e}\frac{d}{dy}j_p(y)-G(y)+\frac{p(y)-p_0(y)}{\tau(y)}=0. \tag{2}$$

Here e is the electronic charge, p_0 is the equilibrium hole concentration in the absence of radiation, G is the carrier photogeneration function, given by

$$G(y)=\alpha(y)\,\Phi\exp\left(-\int_0^y\alpha(y')\,dy'\right), \tag{3}$$

where Φ incident radiation flux, α is the calculated absorption coefficient,[15] and τ is the charge carrier recombination time. In n-CdHgTe that is uniform in composition, this time is determined by the $A1$ Auger process[16] and can be found using an equation from Beattie and Landsberg.[17] We introduce the notation τ_A for this quantity below.

Since a calculation of the recombination time at dislocations on a microscopic level is extremely complicated, we have used an empirical model[8] in which the recombination time τ_d at a dislocation is given in terms of the dislocation density n_d by

$$\tau_d=\frac{C_d}{n_d}. \tag{4}$$

The total recombination time in Eq. (2) is given by

$$\frac{1}{\tau}=\frac{1}{\tau_A}+\frac{1}{\tau_d}. \tag{5}$$

In the calculations we took into account recombination channels and just Auger recombination. The parameter C_d in Eq. (4) was varied.

Equation (2) should be supplemented by the boundary conditions[11]

$$j_p(0)=-es_0[p(0)-p_0(0)],$$

$$j_p(L)=es_L[p(L)-p_0(L)], \tag{6}$$

where L is the thickness of the CdHgTe film, and s_0 and s_L are the surface recombination rates at $y=0$, the interface with the buffer, and at $y=L$, the CdHgTe film surface.

In Eq. (2) it is convenient to replace the unknown function by $\nu(y)$ through the substitution $p=n_i^2\nu$. It is then reduced to a quasiharmonic form (like the heat conduction equation), for which a stable difference system has been reported in the literature.[18] Equation (2) was solved using this difference scheme and then we found the effective lifetime τ_{eff}, determined from the condition that the number of photogenerated carriers over time τ_{eff} should equal the number of nonequilibrium carriers in the structure,

$$\tau_{\text{eff}}\int_0^L G(y)dy=\int_0^L\Delta p(y)dy. \tag{7}$$

RESULTS

We have studied CdHgTe structures grown by MBE on (103) GaAs substrates with a CdTe buffer layer. The growth of the CdHgTe layers was begun by growing a layer of constant composition $x_{Cd}=0.3-0.4$ with a thickness of up to 0.2–0.3 μm. We then grew a layer of CdHgTe, in which the composition was varied to the concentrations required for the operating wavelengths of a photodetector device, usually in the range $x^b_{Cd}=0.2-0.24$. The thickness of these layers varied between 1 and 3 μm, depending on the growth rate. Another layer with a constant composition and a thickness of 5–10 μm was grown. Finally, a variable-gap layer with a thickness of 0.5–1 μm and composition ranging from 0.1–0.5 was grown on the surface.

Calculations were done for model structures with composition profiles close to real structures (Fig. 1a). The CdHgTe film thickness was $L=10\mu$m, the thickness of the variable-gap layers was 1 μm on each side, and the cadmium content on the surface, x^s_{Cd} was varied. The electron concentration was 4×10^{14} cm^{-3} and the lattice temperature was 77 K. The surface recombination rate on the left was $s_0=10^5$ cm/s and that on the right, s, was varied from 0 to 10^7 cm/s.

The calculations of the effective lifetime showed that introducing variable-gap layers, naturally, reduces the influence of surface recombination, since the imbedded field repels minority carriers from the surface (Fig. 1a, curve *3*). For complete cutoff of surface recombination it is sufficient to have $\Delta x_{Cd}=x^s_{Cd}-x^b_{Cd}=0.05$, when only Auger recombination is included and when both recombination channels are included. This value for the difference in compositions is close to that calculated[2] for a structure with a sharp heterojunction near the resistor surface and with allowance for only the Auger recombination.

The problem of choosing the coefficient C_d in Eq. (4) arises when calculating the effective lifetime with allowance for the Auger recombination and recombination at dislocations using the empirical model described above. The x-ray swing curves and lifetimes were measured for two samples. An estimate from the half-width of the swing curves shows that our dislocation densities were $(4-6)\times10^7$ cm^{-2} and the lifetimes were 0.4–0.8 μs. A calculation of the lifetime according to our model with allowance for these data yields $C_d=40-80$ s/cm^2.

We have also compared the calculated lifetimes with those measured from photoconductivity relaxation in a number of variable-gap structures whose composition profiles are shown in Fig. 2. In the calculations we took into account the times of Auger recombination and of recombination at dislocations. Table I lists the measured and calculated lifetimes for a temperature of 77 K. We chose $n_d=4\times10^7$ cm^{-2} since it lies in the range determined from the swing curves. There is good agreement between the calculated and measured lifetimes, while the lifetimes for Auger recombination alone differ by an order of magnitude from the experimental values.

These results show that when wide, variable-gap layers are introduced, lifetimes in excess of 1 μs can be obtained even when the dislocation density exceeds 10^7 cm^{-2}. These values are almost two orders of magnitude greater than the lifetimes reported[6] for CdHgTe layers with a similar dislocation density but without variable-gap layers.

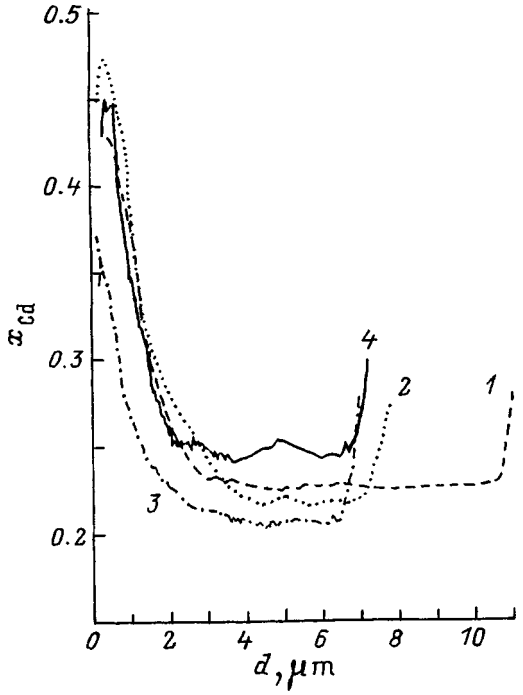

FIG. 2. The composition profiles of structures *1*, *2*, *3*, and *4*.

It is evident that better agreement between the experimental and theoretical times can hardly be obtained in the framework of the simple empirical model of Eq. (4). The recombination rate at dislocations can also have a different dependence on their density, since they might be capture centers, as well as recombination centers.[8] Further comparisons will have to be done with layer-by-layer etching of the CdHgTe layers and measurements of the charge carrier lifetime and dislocation density.

CONCLUSIONS

We have calculated the effective lifetime of charge carriers in *n*-type CdHgTe photoconductors with variable-gap layers. Auger recombination and recombination at dislocations have been taken into account in the calculations. The latter was taken into account through the empirical model of

TABLE I.

Sample number	n, 10^{14} cm^{-3}	τ^A_{calc}, μs	τ_{exp}, μs	τ_{calc}, μs	n_d^{opt}, 10^7 cm^{-2}
1	3.8	24	1.4	1.4	4
2	2.5	40	1.1	1.4	5.3
3	8.6	2.2	1.2	0.9	2.3
4	1.3	370	0.75	1.5	8

Note: τ^A_{calc} is the calculated lifetime determined solely by Auger recombination, τ_{exp} is the measured lifetime, τ_{calc} is the calculated lifetime determined by Auger recombination and recombination at dislocations with $C_d=60$ s/cm^2 and $n_d=4\times10^7$ cm^{-2}, and n_d^{opt} is the density of dislocations at which the measured and calculated lifetimes are equal.

Eq. (4) and the coupling coefficient C_d between the recombination time at dislocations and their density was determined.

It has been shown that the presence of variable-gap layers in a photoconductor leads to a substantial increase in the effective charge carrier lifetime. A difference of 0.05 between the cadmium contents at the surface and in the bulk is sufficient to eliminate the effect of surface recombination on the carrier lifetime, which is then determined solely by volume processes. Introducing variable-gap layers makes it possible to obtain rather high effective lifetimes, despite a high dislocation density (above 10^7 cm^{-2}). Satisfactory agreement was obtained between the measured and calculated effective charge carrier lifetimes in variable-gap structures grown by MBE when recombination at dislocations was taken into account and the relaxation time at dislocations was related to the dislocation density in Eq. (4) with $C_d = 40 - 80$ s/cm^2.

We wish to thank L. D. Burdin, V. S. Varavin, M. V. Yakushev, and N. N. Mikhaĭlov for their participation in growing the CdHgTe epitaxial structures. We also thank V. N. Ovsyuk and Yu. G. Sidorov for a discussion of the results of this study.

[1] R. Pal, R. K. Bhan, K. C. Chhabra, and O. P. Agnihotri, Semicond. Sci. Technol. **11**, 231 (1996).
[2] C. A. Musca, J. F. Siliquini, K. A. Fynn, B. D. Nener, L. Faraone, and S. J. C. Irvine, Semicond. Sci. Technol. **11**, 1912 (1996).
[3] V. N. Ovsyuk, A. O. Suslyakov, T. I. Zakharyash, S. A. Studenikin, V. V. Vasilyev, Yu. G. Sidorov, S. A. Dvoretsky, V. S. Varavin, N. N. Mikhailov, and V. I. Liberman, Proc. SPIE **2746**, 277 (1996).
[4] D. K. Arch, R. A. Wood, and D. L. Smith, J. Appl. Phys. **58**, 2360 (1985).
[5] R. D. Rajavel, D. M. Jamba, O. K. Wu, J. E. Jensen, J. A. Wilson, E. A. Patten, K. Kosai, P. Goetz, G. R. Chapman, and W. A. Radford, J. Cryst. Growth **175/176**, 653 (1997).
[6] S. H. Shin, J. M. Arias, M. Zandian, J. G. Pasko, and R. E. DeWames, Appl. Phys. Lett. **59**, 2718 (1991).
[7] L. He, J. R. Yang, S. L. Wang, S. P. Guo, M. F. Yu, X. Q. Chen, W. Z. Fang, V. M. Qiao, Q. Y. Zhang, R. J. Ding, and T. L. Xin, J. Cryst. Growth **175/176**, 677 (1997).
[8] H. F. Matare, *Defect Electronics in Semiconductors* (Wiley, N.Y.–London, 1971).
[9] T. Yamamoto, Y. Miyamoto, and K. Tanikawa, J. Cryst. Growth **72**, 270 (1985).
[10] V. N. Davydov, E. A. Loskutova, and I. I. Fefelova, Mikroelektronika **15**, 455 (1986).
[11] O. V. Konstantinov and G. V. Tsarenkov, Fiz. Tekh. Poluprovodn. **10**, 720 (1976) [Semiconductors **10**, 427 (1976)].
[12] G. L. Hansen and J. L. Schmidt, J. Appl. Phys. **54**, 1639 (1983).
[13] E. Finkman and S. E. Shachman, J. Appl. Phys. **56**, 2896 (1984).
[14] J. P. Rosbeck, R. E. Starr, S. L. Price, and K. J. Riley, J. Appl. Phys. **53**, 6430 (1982).
[15] W. W. Anderson, Infrared Phys. **20**, 363 (1980).
[16] A. Rogalski and J. Piotrowski, Prog. Quantum Electron. **12**, 87 (1988).
[17] A. R. Beattie and P. T. Landsberg, Proceedings Royal Soc. **A249**, 16 (1959).
[18] A. A. Samarskiĭ and A. V. Gulin, *Numerical Methods* [in Russian], Nauka, Moscow (1989).

Translated by D. H. McNeill

Polarization photosensitivity of GaN/Si heterojunctions

V. M. Botnaruk and S. D. Raevsky

Moldova State University, MD 20009 Kishinev, Moldova

V. V. Belkov, Yu. V. Zhilyaev, Yu. V. Rud, and L. M. Fedorov

A. F. Ioffe Physicotechnical Institute, Russian Academy of Sciences, 194021 St. Petersburg, Russia

V. Yu. Rud

St. Petersburg State Technical University, 195251 St. Petersburg, Russia
(Submitted July 20, 1998; accepted for publication July 28, 1998)
Fiz. Tekh. Poluprovodn. **33**, 297–301 (March 1999)

A technique for fabricating *n*-GaN/Si heterojunctions, which includes chemical deposition of GaN layers with thicknesses of up to 20 μm on a Si substrate in an open gas-transport system, is developed. The photoelectric properties of isotypic and anisotypic heterojunctions are studied in natural and linearly polarized light. A polarization photosensitivity is observed when linearly polarized light is obliquely incident on the surface of the GaN layers. The induced photopleochroism increases quadratically with the angle of incidence θ and reaches 20% for $\theta \cong 75°$. GaN/Si heterojunctions may be useable as broad-band photoanalyzers of linearly polarized light. © *1999 American Institute of Physics.* [S1063-7826(99)00903-5]

Gallium nitride is one of the several types of semiconducting materials which are currently being vigorously studied. Because of substantial progress in the technology of this wide-gap semiconductor ($E_G \cong 3.4$ eV at $T = 300$ K), it may be used in short-wavelength and high-temperature optoelectronics, photoconverters, and other devices.[1–4] There is also special interest in solving the problem of integrating GaN and Si, which may open up possibilities for using silicon, not only for growing large area GaN wafers, but also for combining the unique functional capabilities of these materials. In this paper we focus attention on this topic and report the results of the first study of the photoelectric phenomena for linearly polarized light in heterojunctions created by forming layers of GaN layers on silicon substrates.

1. The GaN layers were obtained by chemical vapor deposition in an open H_2–HCl–NH_3–Ga gas-transport system. Slabs of *n*- and *p*-type silicon with a free charge carrier density $\cong 10^{16}$ cm^{-3} at $T = 300$ K and a thickness $\cong 0.3$ mm were used as the substrate material. Immediately prior to deposition of the layers, the substrate surfaces were subjected to careful cleaning: degreasing in toluene, treatment in boiling isopropyl alcohol (up to 10 min), etching in a $1HF:5H_2O$ solution (up to 1 min), washing in deionized water, and drying in heated isopropyl alcohol vapor. The layers were grown in a reactor with Ga source zone temperatures $T_s \cong 850$ °C and deposition temperatures $T_0 \cong 890-910$ °C. According to a set of physical and technological studies, in order to obtain the most perfect layers it was first necessary to form a thin buffer layer of GaN ($d_B \cong 0.5\mu$m) on the silicon surface. This growth took place at $T_0 \cong 550-565$ °C for $\cong 2$ min. Subsequent growth was at a higher deposition temperature $T_0 \cong 890-910$ °C and over deposition times $t_3 \cong 20-30$ min, GaN layers with thicknesses $d_l \cong 10-20\mu$m were reproducibly formed. The resulting GaN layers have a fine crystalline structure with lattice constants corresponding to published values.[5] X-ray studies showed that the widths of the swing curve in the best of the layers we made are $\theta \cong 5-6°$ for $d_l \cong 20\mu$m, which is comparable to typical values of θ for GaN layers obtained by other methods, including molecular-beam epitaxy, but for $d_l \leqslant 1\mu$m.[6] The GaN layers produced on Si substrates oriented in the (111) and (100) planes generally had high adhesion and continuity. The GaN layers had a uniform tint which varied from black to light-yellow, depending on their thickness, and the outer surface usually has a relief whose structure is determined by the deposition conditions. All the GaN layers had electron conductivity and were characterized by a free electron density $\cong 10^{19}$ cm^{-3}, and a Hall mobility $\cong 10$ cm^2/(V·s) at $T \cong 300$ K.

These technologies yielded anisotypic *n*-GaN/*p*-Si and isotypic *n*-GaN/*n*-Si heterojunctions. The GaN layers were deposited on the (100) and (111) planes of silicon with the natural oxide (several monolayers), as well as with a special coating of SiO_2 to a thickness $d_0 \cong 0.6-0.8\mu$m. These experiments showed that the change in the crystallographic orientation and the presence of an SiO_2 layer on the Si did not show up in a significant way in the structures of the resulting GaN layers.

This method allowed us to obtain heterojunctions with areas of up to 50×50 mm^2, without any fundamental limits on the size. In order to study their photoelectric characteristics, the heterojunctions were attached to a Fedorov table, which is used to control the angle of incidence θ of light on the receiver surface to within $30'$. The heterojunctions were illuminated on the side of the wide-gap GaN layer by linearly polarized light with a degree of polarization of up to 100% over the entire photosensitive area.

2. These heterojunctions have rectification properties. A

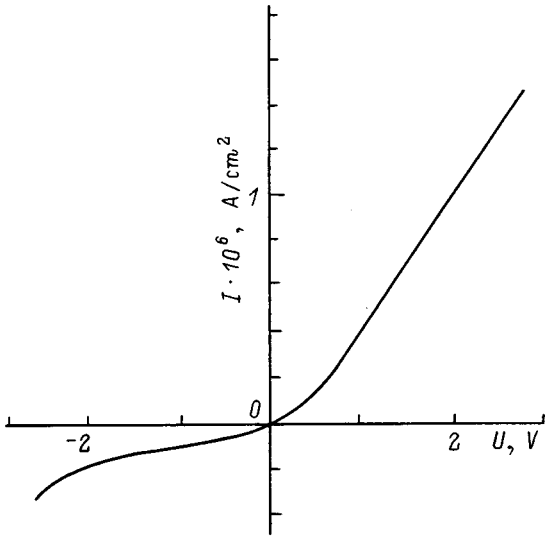

FIG. 1. Steady-state current-voltage characteristic of an *n*-GaN/*p*-Si heterojunction at $T=300$ K. (Sample No. 59.1.1. The forward direction corresponds to a positively polarized external bias voltage on the Si.

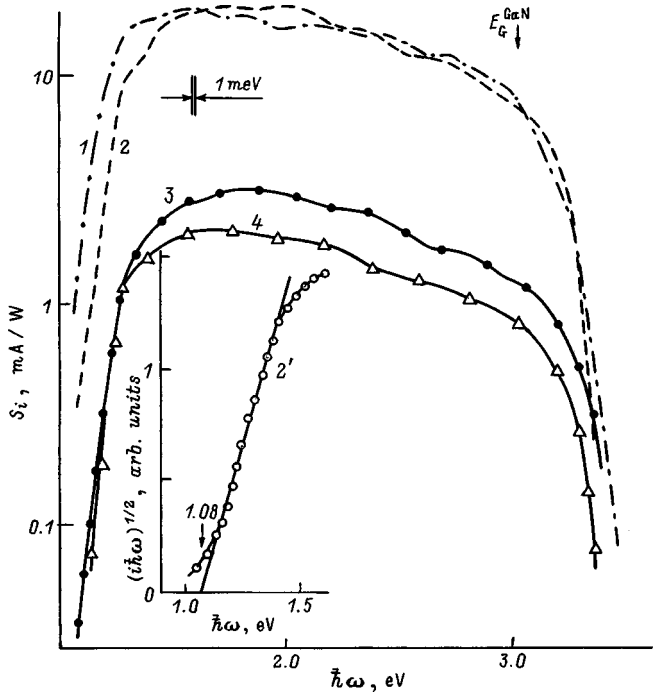

FIG. 2. Spectral variation in the photosensitivity of *n*GaN/*p*-Si heterojunctions at $T=300$ K in natural light. (Sample Nos. 60.1.2 (*1*), 59.1.1 (*2*, *2′*), 59.2.1 (*3*), 60.2.2 (*4*). The heterojunctions are illuminated along a normal to the plane of the GaN.

typical current-voltage characteristic for one of the anisotypic heterojunctions is shown in Fig. 1. Forward rectification in these heterojunctions corresponds to a negative polarity of the external bias at the *n*-GaN layer, while in the isotypic samples it occurs with a positive potential across the GaN. It should also be noted that rectification in isotypic structures is, as a rule, considerably inferior to that in anisotypic ones. The reverse branches of the current-voltage characteristics of the heterojunctions at low voltages have a powe-law dependence that is close to linear, which is evidence of imperfections in the heterojunctions produced here.

3. The isotypic and anisotypic heterojunctions exhibit a photovoltaic effect, whose sign is independent of the incident photon energy in the entire photosensitive spectral range and independent of changes in the localization of the probe light (diameter $\cong 0.2\mu$m) along the surface of the structure. This means that we can assume that photogenerated pairs are separated by the only active region in heterojunctions of this type, which develops as a result of the formation of a contact between the GaN and the *n*- or *p*-type Si substrate.

The photosensitivity of all our heterojunctions is dominant when they are illuminated from the side of the wide-gap layer. In this case, the spectral dependences of the photosensitivity of the isotypic and anisotypic heterojunctions are, as a rule, wide-gap dependences. Figure 2 shows typical spectral variations in the current photosensitivity of Si for several heterojunctions at $T=300$ K in natural light. These curves clearly show the ''window effect,'' in which a high photosensitivity occurs in the range between the band gaps of the materials in contact, and which is characteristic of sharp, ideal heterojunctions.[7] The long-wavelength photosensitivity limit corresponds to the onset of interband absorption in the substrate material of these heterojunctions. In the $(i\hbar\omega)^{1/2},(h\omega)$ plane (where i is the current; curve *2′* in Fig. 2) this part of the curve is straight and extrapolation to $\hbar\omega=0$ is consistent with the band gap of Si, while the short-wavelength photosensitivity limit of these heterojunctions is caused by absorption in the GaN layers.[5] The onset of the short-wavelength drop for Si, as can be seen in Fig. 2, begins at photon energies of 1.8–2.4 eV for the different heterojunctions and is controlled mainly by the thickness of the GaN layers. Furthermore, near the peak S_i in the photosensitivity spectral curves for a number of the heterojunctions we see a slight modulation in the photoresponse (Fig. 2, curves *1-3*). This modulation, however, is not deep enough to determine reliably the locations of the maxima and minima in S_i and, thereby, evaluate their relationship to possible interference of light within the wide-gap layers.

An analysis of the interrelation between the photoelectric parameters of the heterojunctions and the conditions under which they were produced yields the following conclusions. The growth technique developed for use here reproducibly provides heterojunctions with maximum voltage and current photosensitivities of $S_u \cong 20$ V/W and $S_i=150$ mA/W, respectively, at $T=300$ K when GaN layers are deposited on *n*- and *p*-type Si wafers oriented in the (111) plane. The use of slabs with a (100) orientation generally reduces the photosensitivity by two to four orders of magnitude compared to those with a (111) orientation; this indicates that the quality of the interface region depends on the orientation of the substrate. At the same time, it should be noted that the parameters of the heterojunctions did not manifest an explicit dependence on the thickness of the oxide layer on the Si wafers. The total half-width $\delta_{1/2}$ of the photosensitivity spectra for the best structures is $\cong 1.8$ eV, when they are illuminated on the GaN side and tends to decrease as the layer thickness d_l is increased in the range $10-20\mu$m.

When the heterojunctions are illuminated on the sub-

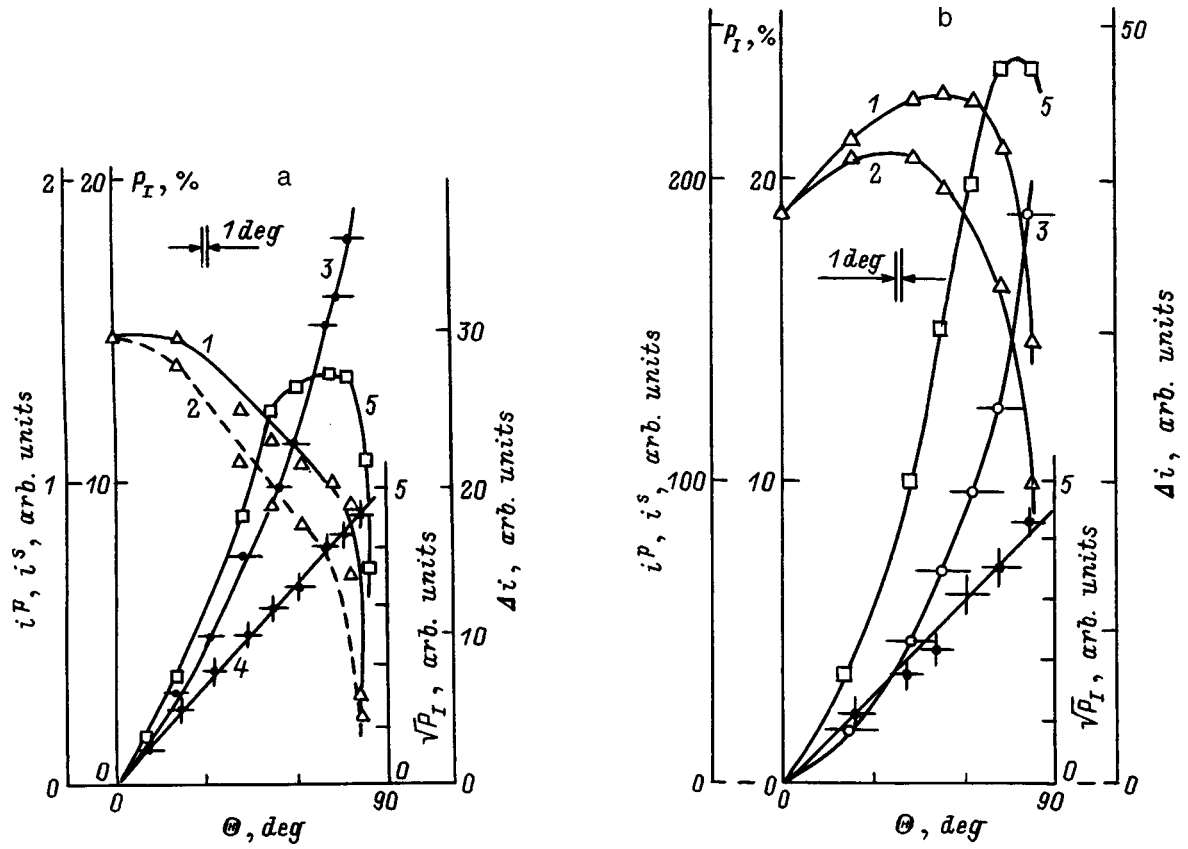

FIG. 3. Short-circuit currents (*1*, *2*), induced photopleochroism P_I (*3*, *4*), and polarization difference in the photocurrents (*5*) as functions of the angle of incidence of linearly polarized light on the plane of GaN/Si heterojunctions at $T=300$ K. (a) Sample No. 59.1.1, $\hbar\omega=1.97$ eV; (b) sample No. 60.1.2.1, $\hbar\omega=2.34$ eV.

strate side, the S_i spectra become narrow-gap spectra ($\delta_{1/2} \cong 0.1-0.2$ eV), reflecting the behavior of optical absorption in Si.

4. Polarization measurements of the photosensitivity of the GaN/Si heterojunctions for normal incidence on either the layer or substrate side did not reveal any dependence of the short-circuit photocurrent i on the azimuthal angle φ, which determines the position of the electric vector **E** of the light wave with respect to the crystallographic axes in the Si substrates. This result is a consequence of the polycrystallinity of the GaN layers and the isotropic nature of photoactive absorption in S. On going to oblique incidence for linear polarized light on the GaN layer surface at angles of incidence $\theta>0°$, the photocurrent i_φ depends periodically on the azimuth of the polarization of the linearly polarized light. The short-circuit photocurrent for $\theta>0°$ in all these heterojunctions was higher when the polarization plane of the radiation coincided with the incidence plane (IP), i.e., when $\mathbf{E}\|$PI, than when $\mathbf{E}\perp$ PI; in other words, $i^p>i^s$. This inequality is satisfied over the entire photosensitive range of the heterojunctions studied here. Typical plots of the short-circuit photocurrent as a function of angle of incidence, $i^p(\theta)$ and $i^s(\theta)$, for these heterojunctions are shown in Fig. 3. For a heterojunction with a rough outer surface of the GaN layers (Fig. 3a), the photocurrents begin to fall off immediately with increasing angle of incidence $\theta>0°$, although the polarization inequality $i^p>i^s$ still holds. Similar behavior has been observed before in GaP/Si heterostructures and explained in terms of imperfections in the surface layers of GaP.[8]

Another type of angular variation in $i^p(\theta)$ and $i^s(\theta)$ is shown in Fig. 3b. For these heterostructures the outer surface of the GaN layers is of much better quality. Figure 3b shows that for both polarizations, for $\theta>0°$ in these heterojunctions the photocurrents initially increase, pass through a maximum, and only then drop off. This behavior of the angular dependences of the photocurrents i^p and i^s suggests that for both polarizations an increase in the angle of incidence causes a reduction in the reflection losses so that i^p and i^s can increase. A simultaneous rise in i^p and i^s may indicate[9,10] interference of the incident radiation in the rather perfect GaN layers. Thus, polarization changes in the photosensitivity may find an application in rapid diagnostics of the quality of GaN layers in fabricated heterojunctions.

The experimental angular dependences of the induced photopleochroism P_I in GaN/Si heterojunctions (Fig. 3) show that increasing the angle of incidence causes a quadratic rise in the polarization photosensitivity, $P_I \propto \theta^2$. It is important to note that with all the heterojunctions $P_I=0$ for $\theta=0°$ over the entire photosensitive range. This suggests that the natural anisotropy of photoactive absorption in GaN is masked by the polycrystallinity of these layers.

The polarization difference $\Delta i=i^p-i^s$ in the photocurrents for these heterojunctions, as can be seen from Fig. 3

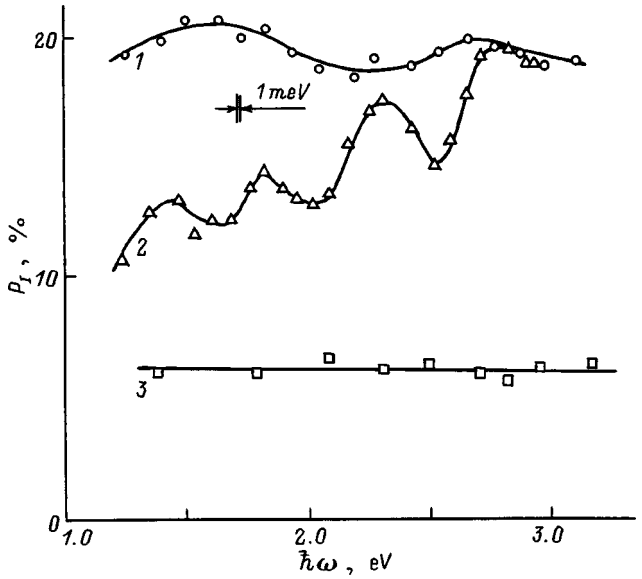

FIG. 4. Spectral variations in the induced photopleochroism of GaN/Si heterojunctions for obliquely incident, linearly polarized light on the GaN collecting face at $T=300$ K. $\theta=75°$. (*1*) Sample No. 59.1.1, (*2*) sample No. 60.1.2.1, (*3*) sample No. 60.1.2.

(curves *5*), becomes greater with increasing θ and reaches a maximum near 70–75°. This parameter is regarded as important for estimating the maximum polarization photosensitivity of heterojunctions and, therefore, determines the range of angles of incidence for which a photodetector will have the greatest sensitivity to linearly polarized light.

The spectral variations in i^p and i^s for obliquely incident, linearly polarized light are similar. Only the gap between the i^p and i^s curves increases for larger θ. Figure 4 shows spectral dependences of P_I for several heterojunctions. These curves show that for oblique incidence of linearly polarized light on the GaN side of these heterojunctions, the induced photopleochroism becomes different from zero, so that they become polarization sensitive. According to theoretical calculations, the induced photopleochroism for a given angle of incidence is determined by the refractive index.[11] Persuant to these estimates, the induced photopleochroism in these heterojunctions should reach $\cong 35°$ when they are illuminated on the GaN side at $\theta \cong 75°$. Our studies show that P_I varies from sample to sample and for the structures studied here ranged from 5–20% (Fig. 4). In a number of heterojunctions the photopleochroism undergoes oscillations and, therefore, depends on the incident photon energy. Such behavior has been observed before in other structures and attributed to a reduction in reflection losses due to interference.[9,10] It may be assumed that such phenomena can occur in our heterojunctions because of variations in the production conditions, and that they cause a reduction in the experimental values of P_I compared to the expected $P_I \cong 35\%$ when interference is absent. It is also possible that this reduction in P_I is caused by changes in the surface structure of the GaN layers.

In conclusion, we point out that the observed induced photopleochroism of these GaN/Si heterostructures suggests that they might be used as broad-band (1.2–3.4 eV) photoanalyzers for linearly polarized light with a maximum azimuthal photosensitivity $\Phi_I \cong 8-10$ mA/W·deg at $T=300$ K, while the observed dependence of P_I on the conditions under which the layers are fabricated might be used as a rapid diagnostic of the quality of GaN layers and, therefore, for optimizing the technology.

[1] X. H. Yang, T. J. Schmidt, W. Shan, J. J. Song, and B. Goldeudery, Appl. Phys. Lett. **66**, 1 (1995).
[2] S. J. Pearton and C. Kuo, MRS Bulletin (February, 1997), p. 17.
[3] S. Nakamura, MRS Bulletin (February, 1997), p. 29.
[4] M. S. Shur and M. A. Khun, MRS Bulletin (February, 1997), p. 44.
[5] *Physical and Chemical Properties of Semiconductors. A Handbook* [in Russian], Nauka, Moscow (1979).
[6] G. A. Martin, B. N. Sverdlov, A. Botchkarev, N. Markoc, D. J. Smith, S. Y. Then, W. N. Thompson, and M. H. Nayfez, Mater. Res. Soc. Symp. Proc. **395**, 67 (1996).
[7] A. Milnes and D. Voight, *Heterojunctions and metal-semiconductor junctions* (Moscow, 1975).
[8] Yu. V. Zilyaev, N. Nazarov, V. Yu. Rud', Yu. V. Rud', and L. M. Nazarov, Fiz. Tekh. Poluprovodn. **27**, 162 (1993) [Semiconductors **27**, 86 (1993)].
[9] V. Yu. Rud', Yu. V. Rud', T. Walter, and H.W. Schock, in Inst. Phys. Conf. Ser. No 152, IOP Publishing Ltd. (1998), p. 971.
[10] V. Yu. Rud' and Yu. V. Rud', Fiz. Tekh. Poluprovodn. **31**, 243 (1997) [Semiconductors **31**, 139 (1997)].
[11] G. A. Medvedkin and Y. V. Rud', Phys. Status Solidi A **67**, 333 (1981).

Translated by D. H. McNeill

Mechanism for heavy Fe doping of epitaxial GaAs/AlGaAs heterostructures

I. Ya. Gerlovin, Yu. K. Dolgikh, S. A. Eliseev, Yu. P. Efimov,* I. A. Nodokus, V. V. Ovsyankin, and V. V. Petrov

Scientific-research Institute of Physics, St. Petersburg State University, 198904 Petrodvorets, Russia

B. Ya. Ber

A. F. Ioffe Physicotechnical Institute, Russian Academy of Sciences, 194021 St. Petersburg, Russia
(Submitted July 28, 1998; accepted for publication August 5, 1998)
Fiz. Tekh. Poluprovodn. **33**, 302–305 (March 1999)

Heterostructures which are maximally doped with iron and which contain bulk layers of GaAs and $Al_xGa_{1-x}As$, as well as GaAs/AlGaAs superlattices are grown on an ÉP-1302 molecular-beam epitaxy system. An analysis of secondary-ion mass spectrometry profiles of the iron penetration shows that during growth on substrates oriented in the [100] plane, the maximum concentrations of iron in the GaAs layers, as well as in the GaAs/AlGaAs superlattices, are two orders of magnitude below those for the ternary solution AlGaAs. A radical enhancement in the maximum Fe concentration (up to 5×10^{18} cm^{-3}) in GaAs/AlGaAs superlattices can be attained by growing them on substrates cut with a 3° deviation from the [100] plane. It is important that at these high doping levels the low-temperature (10 K) absorption and photoluminescence spectra of the superlattices still contain narrow exciton lines. Possible mechanisms for the selective implantation of iron in GaAs/AlGaAs hetrostructures are analyzed. © *1999 American Institute of Physics.* [S1063-7826(99)01003-0]

The doping of epitaxial GaAs heterostructures with iron to very high concentrations (on the order of 10^{19} cm^{-3}) is accompanied by the formation of iron-rich clusters.[1] The presence of clusters of this sort greatly modifies the relaxation characteristics of the heterostructures, making them suitable for use in ultrafast nonlinear optical components.[2] It has been found, however, that the standard technological approaches (combined deposition and δ-doping) for creating iron-rich clusters in bulk layers of GaAs and AlGaAs do not provide heavy doping of GaAs/AlGaAs superlattices.[1] This substantially limits the possible applications for these structures. (A low maximum doping level for epitaxial superlattices has been observed in other studies.[3]) In this paper we present the results of an experimental study aimed at searching for epitaxial growth conditions that offer the possibility of raising the maximum level of iron implantation in GaAs/AlGaAs heterostructures.

The structures were grown on an ÉP-1302 molecular-beam epitaxy system equipped with standard Ga and Al molecular sources and boron nitride crucibles. A sapphire crucible was used for the Fe molecular source, since at the source operating temperature of 840–1080 °C iron reacts chemically with boron nitride. The epitaxial structures were grown on semi-insulating substrates of AGChP-8 grade GaAs(100). The typical growth rate was 0.8–1.1 μm/h.

The distribution of the major constituents and the doping impurity in the grown structures were studied by secondary ion mass spectrometry (SIMS) in a CAMECA IMS4F ion microprobe. The depth of the ion etching crater was measured on a DEKTAK mechanical profilometer. The exact values of the concentration of iron atoms in the GaAs and GaAlAs were determined using calibrated samples obtained by implantation of iron atoms in the corresponding crystals.

In order to determine the maximum level of entry of Fe into the GaAs, test doping was done with different intensities of the iron molecular beam. For this purpose, during continuous epitaxial growth of the GaAs layer, the Fe molecular beam was turned on for a relatively short time (10 min) with a constant source temperature. After the beam was shut off, the Fe source temperature was raised to the next fixed value. In this time the doped layer grew as a pure GaAs layer. The Fe beam was then turned on for a short time, etc. Accordingly, the temperature interval 840–1080 °C was covered in stepwise fashion. The quality of the epitaxial layer during growth was monitored from the fast electron diffraction pattern. For iron source temperatures above 1080 °C it was found that epitaxial growth fails, as revealed in the appearance of images characteristic of three-dimensional growth in the diffraction pattern.

A profile of the Fe concentration in a doped sample is shown in Fig. 1a. As can be seen from the figure, two regions can be distinguished in the sample with substantially different implantation of the dopant: bulk and surface. The first clearly shows distinct doped layers, within which the iron concentration is constant. The doped layers have sharp boundaries and the positions of the boundaries correspond precisely to the times the molecular Fe source is turned on and off. This doping profile shape is evidence of the absence of dopant diffusion. The iron concentrations were nearly the same in all the doped layers, although the density of the molecular beams differ by three orders of magnitude in the extreme points. This means that the observed concentration $(5\pm2)\times10^{16}$ cm^{-3} corresponds to the maximum level of stable iron implantation into GaAs layers under these growth

conditions. Further experiments showed that the maximum Fe concentration remains fixed as the growth temperature is varied in the range 450–550 °C and the crystallographic orientation of the substrate is varied over deviations of 0–3° from the (100) plane.

The Fe concentration profile looks quite different in an initially undoped surface layer. Near the surface the Fe concentration exceeds 10^{20} cm^{-3} and falls off smoothly into the depth of the crystal. The bulk of the Fe impurity introduced during the doping process actually lies in the skin layer of thickness 100–200 nm.

For samples containing bulk layers of the ternary solution AlGaAs the maximum level of stable iron doping was at least two orders of magnitude greater than for pure GaAs. This amount depends weakly on the growth temperature and crystallographic orientation of the substrate.

As the subsequent investigations showed, the doping behavior for multilayer heterostructures is substantially different. Figures 1b and 1c show the doping profiles of samples 151 and 153, both of which contained a GaAs/AlGaAs superlattice (30–35 periods of 7-nm GaAs/7-nm $Al_{0.3}Ga_{0.7}As$) enclosed between thick (400-nm) layers of the ternary solution $Al_{0.3}Ga_{0.7}As$. Iron doping was carried out continuously, beginning at the middle of the first layer of ternary solution and ending at the middle of the second. The density of the molecular Fe beam corresponded to an extremely high level of doping of the ternary solution; the iron source temperature for both structures was 1010 °C. As Figure 1b shows, in sample 151, which was grown on a substrate oriented strictly in the (100) plane, the first layer of ternary solution is uniformly doped with iron to a concentration of 5×10^{18} cm^{-3}. At the boundary with the superlattice the Fe concentration falls rapidly to 2×10^{16} cm^{-3}. This value remains constant almost throughout the entire superlattice, but near the boundary with the second layer of ternary solution it begins to rise. Immediately at the boundary the Fe concentration reaches 10^{20} cm^{-3} and then falls to an equilibrium value of 5×10^{18} cm^{-3} in the interior of the ternary solution. The low maximum level of doping of the GaAs/AlGaAs superlattice seen in this sample agrees well with published data.[1,3]

The Fe concentration profile of sample 153, which was grown on a substrate which deviated from the crystallographic (100) plane by 3° in the (110) direction differs strikingly from the profile of sample 151. (The nominal dimensional parameters, as well as the growth and doping conditions, for samples 151 and 153 were almost the same.) As Fig. 1c shows, the Fe concentration in sample 153 is constant in the entire doping region, without significant jumps at the boundary between the superlattice and the ternary solution. The average Fe concentration here is 3×10^{18} cm^{-3}. A comparison of Figs. 1c and 1b shows that using a substrate that deviates by 3° makes it possible to enhance the maximum Fe doping level in a GaAs/AlGaAs superlattice radically (by more than a factor of 100).

Despite the very high level of iron doping, the degree of structural perfection of the superlattice in sample 153 was rather high. This conclusion was based on a study of the luminescence and absorption spectra of the doped samples in

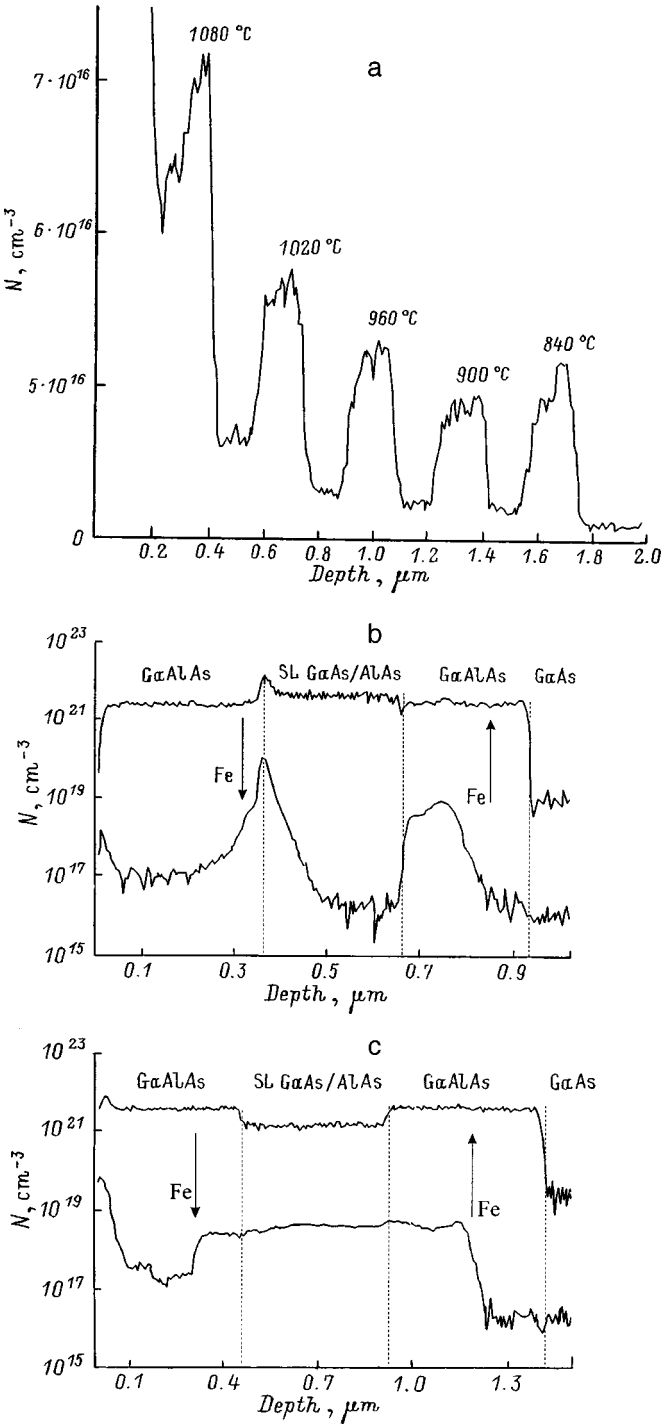

FIG. 1. Heterostructure doping profiles. (a) Sample 73 (a thick layer of GaAs); (b) sample 151 [superlattice on a substrate with orientation (100)]; (c) sample 153 (superlattice on a substrate with a deviation of 3° from the (100) orientation).

the neighborhood of the exciton transitions in the superlattice. Spectra of the undoped control sample 136, with the same structure, were recorded for comparison. Before the absorption spectra were recorded, the opaque GaAs substrate was selectively etched using the method described in Ref. 4. The luminescence was excited by a He-Ne laser and recorded using a DFS-24 spectrometer. An analysis of the resulting spectra (Fig. 2) shows that the introduction of Fe into

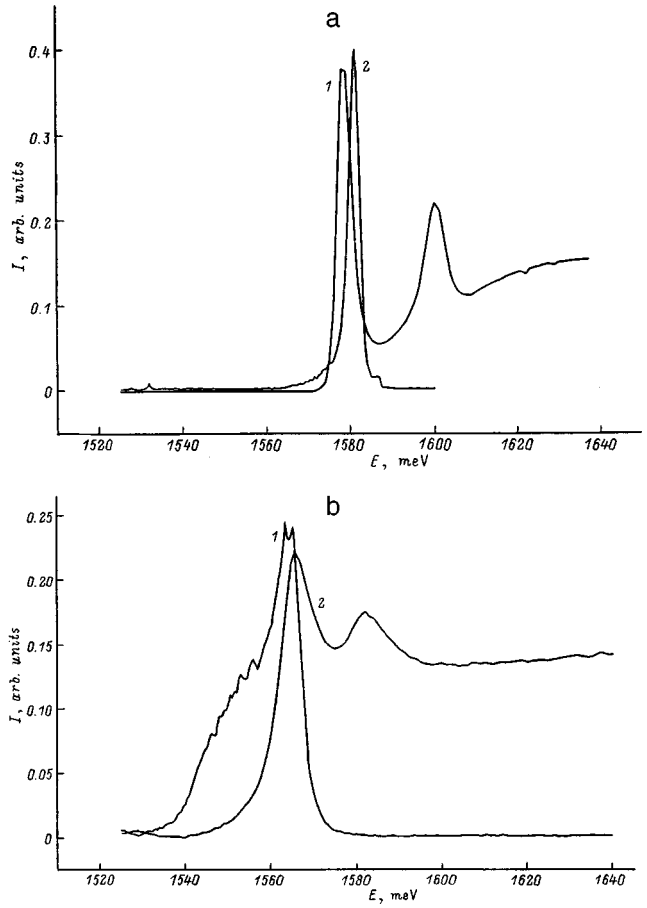

FIG. 2. Absorption (*1*) and exciton luminescence (*2*) spectra of superlattices. (a) Sample 136 (undoped), (b) sample 153.

the superlattice is not accompanied by a sharp deterioration in its quality. The absorption and luminescence spectra of sample 153 contain distinct peaks at locations corresponding to the superlattice excitons. The widths of the exciton peaks and the Stokes shift are only 1.5 times the corresponding widths for the control sample. The widths of the exciton peaks of sample 151, which essentially contains no iron in the superlattice according to the SIMS data, are at least as large as the corresponding values for sample 153. This means that the main reason for the broadening is an overall increase in the level of defects in the heterostructures associated with doping, and not an interaction of the superlattice excitons with iron atoms.

These experimental data yield certain conclusions about the mechanisms leading to formation of the iron doping profile of the GaAs/AlGaAs heterostructures. The most understandable is the process whereby Fe enters the bulk layers of pure GaAs and the ternary solution. The Fe ions, which have a smaller ionic radius than Ga and a different coordination symmetry, are a nonisostructural impurity for crystalline GaAs. Given this circumstance, we might expect that iron, as a dopant impurity, would predominantly enter a site that had lost its structural perfection, i.e., near structural defects and other impurities. Apparently precisely the concentration of these defects determines the maximum level of stable doping of Fe in epitaxial GaAs layers. The strong coupling with defects inhibits diffusion of the dopant ions, which accounts for the presence of the sharp boundaries in the doping profile of Fig. 1a. The excess iron ions which are not bound during the growth process accumulate at the growth surface and partially diffuse into the depth of the material. These ions form the iron-enriched skin layer of the doped samples.

A ternary AlGaAs solution differs from pure GaAs in having an elevated impurity oxygen content at concentrations[4] that can exceed 10^{17} cm^{-3}. In addition, in the ternary solution fluctuations in the composition can play the role of defects that couple Fe ions. It is entirely reasonable to assume that the combined effect of these factors also leads to the sharp increase in the maximum doping level in AlGaAs.

Unfortunately, this simple model cannot explain the observed iron doping behavior in GaAs/AlGaAs superlattices. Here we have, first of all, to refer to the extremely low maximum doping level for growth at a 0° substrate (Fig. 1b). Starting with the quantitative amount of ternary solution in the superlattice, we might expect a reduction by roughly a factor of 2 in the Fe concentration compared to that in a thick layer of AlGaAs, while the concentration is actually more than two orders of magnitude lower. In addition, this model does not explain the radical increase in the maximum doping level of the superlattices when the crystallographic orientation of the substrate deviates from the (100) plane (Figs. 1b and 1c). The main consequence of this deviation is a change in the form of the growth surface (terrace formation) and heterojunctions. This implies that the very existence of alternating heterojunctions and their form have a radical influence on the doping of GaAs/AlGaAs heterostructures with iron. The available experimental data are clearly insufficient for identifying the mechanism for this influence. It can only be assumed that this mechanism is related to the conditions for surface diffusion of the dopant impurity atoms during epitaxial growth. Identifying the specific processes which determine the maximum doping level in GaAs/AlGaAs heterostructures requires further study.

This work was supported by the Russian Fund for Fundamental Research (Grants No. 97-02-18163 and 97-02-18339).

*E-mail: efimov@snoopy.phys.spb.ru; Fax: (812) 428-72-40

[1] M. W. Bench, C. B. Carter, F. Wang, and P. I. Cohen, Appl. Phys. Lett. **66**, 2400 (1995).
[2] D. R. Dykar, D. J. Eaglesham, U. D. Keil, B. I. Greene, P. N. Saete, I. N. Pfeiffer, R. F. Kopf, S. B. Darac, and K. W. West, Mater. Res. Soc. Symp. Proc. **241**, 245 (1992).
[3] M. R. Melloch, C. I. Chang, N. Otsuka, K. Mahalingam, J. M. Woodal, and P. D. Kirchner, J. Cryst. Growth **127**, 499 (1993).
[4] J. J. LePore, J. Appl. Phys. **51**, 6441 (1980).

Translated by D. H. McNeill

Ion neutralization effects at a semiconductor-insulator interface produced as a result of space-charge thermal depolarization of MOS structures

E. I. Goldman, A. G. Zhdan, and N. F. Kukharskaya

Institute of Radio Engineering and Electronics, Russian Academy of Sciences, 141120 Fryazino, Russia
(Submitted July 2, 1998; accepted for publication July 7, 1998)
Fiz. Tekh. Poluprovodn. **33**, 306–310 (March 1999)

Numerical simulation is used to analyze the contributions of ion traps, ion neutralization effects, and minority charge carrier generation near the insulator-semiconductor interface to the temperature dependences of the current $J(T)$ and high-frequency capacitance $C_s(T)$ during thermally stimulated depolarization of MOS structures. In general, even when the insulator contains only one type of mobile ion, the $J(T)$ curves can have three peaks due to the depletion of ion capture centers, the decay of neutral ion+electron associates, and minority charge carrier generation. The temperature sequence of these peaks, and their number (down to one), are determined by the relationships among the activation energies for the corresponding processes and the initial band bending U_0 in the semiconductor. Cases in which the individual peaks merge, with accompanying broadening and symmetrization, can be mistakenly interpreted in terms of the emergence of ion traps with an energy distribution. An analysis of the families of $J(T,U_0,n_0)$ and $C_s(T,U_0,n_0)$ curves (n_0 is the initial density of particles, ions, and neutral associates localized in the insulator at the interface with the semiconductor) makes it possible to distinguish the purely ion phenomena from the electronic, as well as to identify the contributions to the current from ion traps and neutralization effects, and, in principle, to explain the observed evolution of the thermally stimulated depolarization peaks with varying U_0 and n_0, which has not yet received an adequate physical interpretation. © *1999 American Institute of Physics.* [S1063-7826(99)01103-5]

The observed features of ion transport in an insulating layer on a semiconductor surface indicate that electron-ion reactions in the boundary region play an important role, causing neutralization of ions through capture of electrons from the semiconductor into localized states formed by the ions and their dielectric medium.[1] On the other hand, the interpretation of transient ion depolarization processes, especially under thermal stimulation, is usually based either on the idea that ''classical'' ion capture centers exist at the semiconductor-insulator interfaces such that capture of an ion into them does not affect the electronic subsystem of the semiconductor,[2–4] or on volume ion transport mechanisms through the dielectric layer such that the ion-electron interaction has no effect on the interfaces.[5,6] In this regard, it is interesting to trace the qualitative and quantitative effects of ion neutralization and ion traps on the thermally stimulated depolarization characteristics of MOS structures.

Let mobile, for concreteness positive, singly charged, ions be present in a dielectric layer on the surface of an *n*-type semiconductor. Under equilibrium conditions, in polarizing fields they will all be concentrated at the semiconductor-insulator interface, captured in traps, and neutralized (the last is caused by the rather high enrichment of the surface region of the semiconductor). After the depolarizing field is turned off, the equilibrium in the system breaks down and ions can migrate from the interface. We assume that the depolarizing field causes majority charge depletion of the semiconductor surface, that the time of flight of the ions through the insulating layer is short compared to their lifetime in the capture centers (these conditions are clearly realized in sufficiently strong depolarizing fields), and that within the temperature range of concern, ion +electron neutral associates always remain bound at capture centers. In other words, neutral associates or ions are found at the interface in localized states and only an ion can leave a capture center. Depolarization will therefore be limited by two processes, the release of ions from traps and the decay of neutral associates, either through transitions of electrons into the conduction band of the semiconductor or through their recombination with holes, which is more important for large band bending. The depolarization kinetics is described by the equations

$$\frac{dn}{dt} = -\frac{n_i}{\tau_i} e^{-E_i/T}, \tag{1}$$

$$\frac{dn_i}{dt} = -n_i\left\{\frac{e^{-E_i/T}}{\tau_i} + \frac{1}{\tau_C}\left[\frac{N_d}{N_C} e^{-U/T} + e^{-E_0/T}\right] + \frac{1}{\tau_V}\left[e^{-(E_g-E_0)/T} + \frac{p}{N_V}\right]\right\} + n\left[\frac{1}{\tau_C} e^{-E_0/T} + \frac{1}{\tau_V}\frac{p}{N_V}\right], \tag{2}$$

and

$$\frac{dp_s}{dt}=\frac{1}{\tau_V}\left\{n_i\left[\mathrm{e}^{-(E_g-E_0)/T}+\frac{p}{N_V}\right]-\frac{np}{N_V}\right\}+\frac{N_D(z_2-z_1)}{\tau_{DC}}\mathrm{e}^{-E_D/T}\left[1-\mathrm{e}^{(E_g-U)/T}\frac{N_d p}{N_C N_V}\right]. \quad (3)$$

Here n, n_i, and p_s are the surface densities of ions captured by ion capture centers plus neutral associates (n), of ions (n_i), and of holes (p_s); N_d and p are the volume concentrations of donors in the semiconductor and of holes immediately at its interface with the insulator; t is the time; E_i, E_0, and E_D are the activation energies for the ion traps, for ejection of electrons from neutral associates, and hole generation through a volume center in a semiconductor with concentration $N_{D'}$, E_g is the band gap of the semiconductor, U is the surface (depleted) band bending in the semiconductor; T is the temperature in energy units; $\tau_{i,C,DC,V,DV}^{-1}$ are the frequency factors for the probabilities of emptying ion traps (τ_i^{-1}), of electronic transitions from a neutral associate (τ_C^{-1}) and from a volume hole generation center (τ_{DC}^{-1}) into the conduction band of the semiconductor, from the valence band of the semiconductor into a neutral associate (τ_V^{-1}) and into a volume center (τ_{DV}^{-1}); z_1 and z_2 are the coordinates of the volume hole generation region in the surface depletion layer of the semiconductor with width W; N_c and N_v are the densities of states in the conduction and valence bands; and t is time. In accordance with Refs. 7 and 8, z_1 and z_2 are given by

$$\frac{U}{T}=\frac{(W-z_1)^2}{2L_d^2}+\ln\left(\frac{p\,\mathrm{e}^{(E_g-E_D)/T}}{N_V}+1\right),$$

$$\frac{(W-z_2)^2}{2L_d^2}=\left(\frac{E_g-E_D-F}{T}\right)+\ln\theta, \quad (4)$$

where $L_d=(\kappa_s T/4\pi q^2 N_d)^{1/2}$ is the Debye shielding length, κ_s is the dielectric constant of the semiconductor, q is the unit charge, $F=T\ln(N_C/N_d)$ is the Fermi energy in the bulk of the semiconductor, and $\theta=\tau_{DV}/\tau_{DC}$. The relationship between p, p_s, W, and U is found from an empirical approximation to a solution of the Poisson equation expressed in quadrature form[7,8]

$$p=2\pi q^2/(\kappa_s T)(p_s^2+2p_s N_d W),$$

$$\frac{U}{T}=\frac{W^2}{2L_d^2}+2\ln\left(\frac{p_s}{W}+1\right). \quad (5)$$

Equations (1)–(5) must be supplemented by the equation of electrical neutrality,

$$qV_g=U+4\pi q^2 h/\kappa_i(n_i+p_s+N_d W), \quad (6)$$

where $V_g=\mathrm{const}$ is the potential of the field electrode, and h and κ_i are the thickness and dielectric constant of the insulating layer. (The condition $V_g=\mathrm{const}$ is fundamental during the intense generation of minority charge carriers corresponding to heavy nonequilibrium depletion, since when the high frequency capacitance of the MOS structure is held constant, i.e., $W=\mathrm{const}$, it is impossible to obtain an equilibrium state of the system.[6])

The relaxation signals which show up in experiments (the current density J and specific rf capacitance C of the MOS structure) are given by

$$J=\frac{qn_i\,\mathrm{e}^{-E_i/T}}{\tau_i}+q\frac{d}{dt}(n_i+p_s+N_d W)$$

$$C^{-1}=C_i^{-1}+C_s^{-1},\quad C_i=\kappa_i/4\pi h,\quad C_s=\kappa_s/4\pi W.$$

Let us examine the dependences $J(T,U)$ and $C(T,U)$ for a linear temperature scan (thermally stimulated depolarization with $T=T_0+k\beta t$, where T_0 is the initial temperature, k is Boltzmann's constant, and $\beta=\mathrm{const}$ is the rate of heating) obtained by numerical solution of the system of equations (1)–(6) for an MOS structure on Si with the following typical parameters: $h=10^{-5}$ cm, $\kappa_i=3.9$, $N_d=10^{15}$ cm^{-3}, $\kappa_s=11.9$, $E_g=1.12$ eV, $N_C=2.8\times10^{19}(T/300k)^{3/2}$ cm^{-3}, $N_V=1.04\times10^{19}(T/300k)^{3/2}$ cm^{-3}, and $N_D=10^{15}$ cm^{-3}. The calculations were done for $T_0/k=100$ K in the system of dimensionless variables t/τ_i, n/n_0, n_i/n_0, p_s/n_0, $W/n_0N_d^{-1}$, $z_1/n_0N_d^{-1}$, and $z_2/n_0N_d^{-1}$, where n_0 is the initial ($t=0$) total surface density of the ions and neutral associates. The the values of the current and capacitance given below have therefore been orthonormalized: $\tilde{J}\Rightarrow J/(qn_0\tau_i^{-1})$ and $\tilde{C}_s\Rightarrow C_s/(\kappa_s/4\pi n_0 N_d^{-1})$. All the preexponential factors were assumed to be equal ($\tau_i=\tau_C=\tau_{DC}=\tau_V=\tau_{DV}$), since it was assumed that the ion lifetime at the traps and the decay lifetime of the neutral associates, as well as the volume rate of hole generation, are determined mainly by the activation energies E_i, E_0, and E_D. The value $\beta=4.46\times10^{-10}/\tau_i$ (deg/s) corresponded to thermally stimulated depolarization conditions for all the activation energies which appear in the calculations.

Qualitatively, depending on the relationship between the activation energies for the ion traps (E_i) and for the decay of the neutral associates ($\tilde{E}_0$), two situations occur. [Clearly, if the volume mechanism for hole generation predominates, then $\tilde{E}_0=E_0$ ($E_0<E_D$) and $\tilde{E}_0=E_D$ ($E_0>E_D$).] If $E_i-\tilde{E}_0\gg T$, then initially the neutral associates break up and the ions produced by this breakup are then freed from the traps. Accordingly, two current peaks should be observed in the thermally stimulated depolarization curve: a low-temperature electron peak (decay of the neutral associates, peak A) and a high-temperature ion peak (emptying of the ion traps, peak B). If $\tilde{E}_0-E_i\gg T$, then the limiting stage of thermally stimulated depolarization is the breakup of the neutral associates and the thermally stimulated depolarization curves should contain only one peak with both electron and ion components. In principle, in both these cases a current peak that is unrelated to ion transport can appear as a result of the generation of holes which can accumulate after the breakup of neutral associates.

Figure 1 shows thermally stimulated depolarization curves $\tilde{J}(T)$ for $n_0=10^{11}$ cm^{-2}, $E_i-\tilde{E}_0\gg T$, and various values of the initial band bending U_0 in the semiconductor. The thermally stimulated depolarization current has two

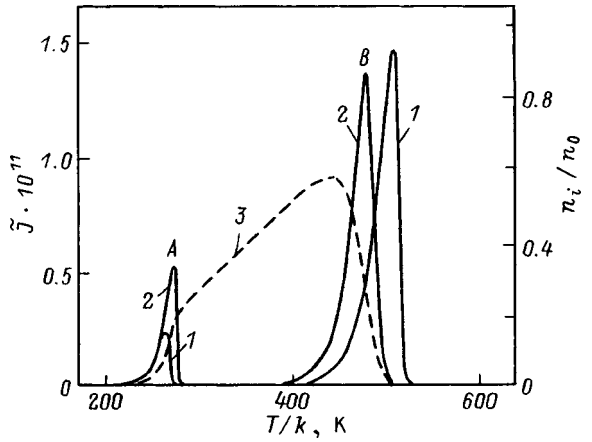

FIG. 1. Thermally stimulated depolarization curves $\tilde{J}(T)$ for different initial band bendings U_0 and a typical temperature dependence of the ion density n_i at the interface. The computational parameters are $n_0=1\times10^{11}$ cm^{-2}, $E_i/300k=38$ (0.98 eV), $E_0/300k=23$ (0.59 eV), $E_D/300k=30.3$ (0.78 eV) (these activation energies are typical for an n-Si/SiO_2 system[3,4,7]); $U_0/300k$ (U_0, eV): 15 (0.39) (curves *1* and *3*), 60 (1.55 (curve *2*).

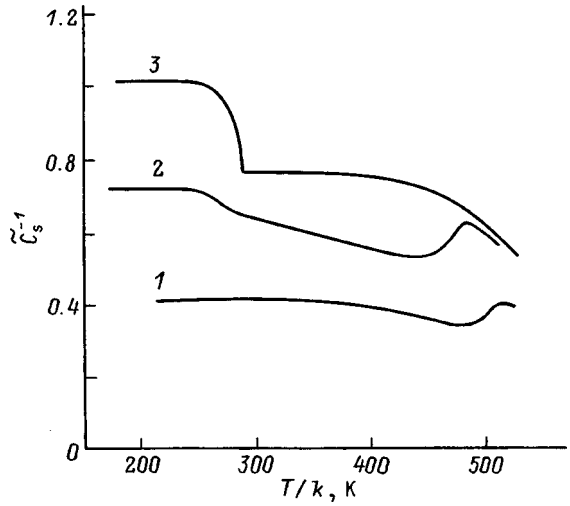

FIG. 2. Temperature variation of the reciprocal $\tilde{C}_s^{-1}$ of the capacitance of the depletion layer of the semiconductor. $U_0/300k$ (U_0 eV): 5 (0.13) (curve *1*), 15 (0.39) (curve *2*), 30 (0.77) (curve *3*). n_0, E_i, E_0 and E_D are as in Fig. 1.

peaks, *A* (due to breakup of neutral associates), whose amplitude rises as U_0 increases and *B* (due to emptying of ion traps), whose amplitude depends only weakly on U_0. The behavior of these peaks as U_0 changes is different: with increasing U_0 peak *A* shifts toward higher temperatures and becomes progressively more asymmetric and peak *B* moves toward lower temperatures and becomes ever more symmetric. The basis for this behavior is the following: for low U_0, neutral associates in the neighborhood of peak *A* do not break up completely because a quasiequilibrium develops in the electron subsystem at the interface due to a reduction in the band bending caused by an increase in the ion charge density. In particular, for $U_0/300k=15$, 20% of the neutral associates break up [Figure 1, the function $n_i(T)$, curve *3*]. With increasing U_0, a quasiequilibrium is attained at gradually increasing temperatures and densities of the ions formed by breakup of the neutral associates (for $U_0/300k=60$, all the neutral associates have already broken up). Therefore, the increase in the amplitude of peak *A* is related to an increase in the number of neutral associates that break up, and its shift is related to an ever later approach of the system to quasiequilibrium. For the largest band bendings, the quasiequilibrium sets in after complete breakup of the neutral associates, so that peak *A* acquires the asymmetric shape characteristic of the kinetics of first-order, thermally stimulated depolarization.[9] Peak *B* develops because of the emptying of the ion traps. Thus, for low U_0 the loss of an ion from the interface stimulates increased band bending and, thereby, a shift of the quasiequilibrium of the electronic subsystem toward more rapid breakup of the neutral associates, which causes filling of the emptied ion traps. This shows up as a ''delay'' in the emptying of the traps, which is less when the initial band bending U_0 is greater. As a result, with increasing U_0, peak *B* shifts toward lower temperatures. For large U_0, hole generation under quasiequilibrium conditions is important. (Since $E_i-E_D\gg T$, the hole generation time is much shorter than the ion lifetime in the traps.) The emptying of the ion traps causes increased band bending and, thereby, additional hole generation, so that the symmetrization of peak *B* with increasing U_0 is related to the contribution of holes to the thermally stimulated depolarization current, which is more important in the decaying side of the peak.

Figure 2 shows plots of $\tilde{C}_s^{-1}(T)$, i.e., of the temperature dependence of the width of the depletion layer of the semiconductor. For low U_0, when hole generation is unimportant, the initial and final charge states of the interface are essentially the same: the hole charge on the interface prior to thermally stimulated depolarization is zero and close to that after it is complete. Thus, the initial and final states of $\tilde{C}_s$ are close. For higher U_0, the role of hole generation increases substantially, especially at high temperatures. As a result, even for relatively low U_0, a maximum appears in the $\tilde{C}_s^{-1}(T)$ curves because the hole generation rate exceeds the rate of loss of the ions from the interface. For still higher initial band bending, this maximum vanishes.

Changing n_0 in the volume does not lead to any fundamental modifications in this behavior. With increasing n_0, the process of establishing a quasiequilibrium in the electronic system at the interface has a stronger effect on the characteristics $\tilde{J}(T)$ and $\tilde{C}_s^{-1}(T)$, while hole generation is less important. Thus, the quasiequilibrium corresponds to a certain number of charged particles (ions, formed as a result of the breakup of neutral associates), which depends weakly on n_0. Thus, when n_0 increases from 10^{11} to 10^{12} cm^{-2} (band bending $U_0/300k=15$), the fraction of the neutral associates which break up in the neighborhood of peak *A* decreases (from 20 to 3%), while the ratio of the amplitudes of peak *A* and peak *B* drops sharply (Fig. 3), so that under actual experimental conditions peak *A* may seem unresolvable against the background of peak *B*. For equal initial band bending, the final (after completion of thermally stimulated depolarization) densities of holes are the same, and the effect of hole generation on the rising side of the $\tilde{C}_s^{-1}(T)$ curve

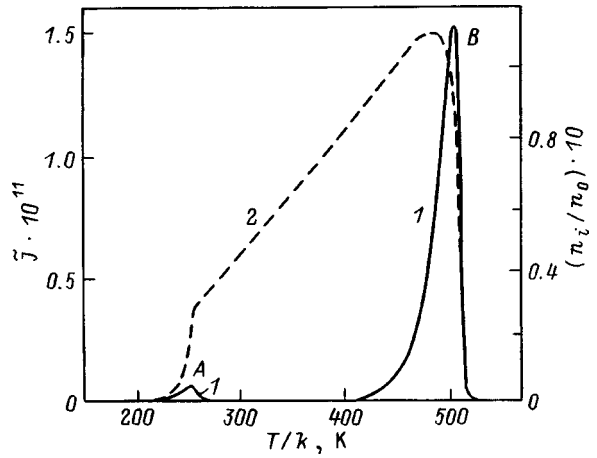

FIG. 3. Temperature dependences of $\tilde{J}$ (*1*) and n_i (*2*) for $n_0=10^{12}$ cm^{-2}, $U_0/300k=15$ (0.39 eV). E_i, E_0, and E_D are as in Figs. 1 and 2.

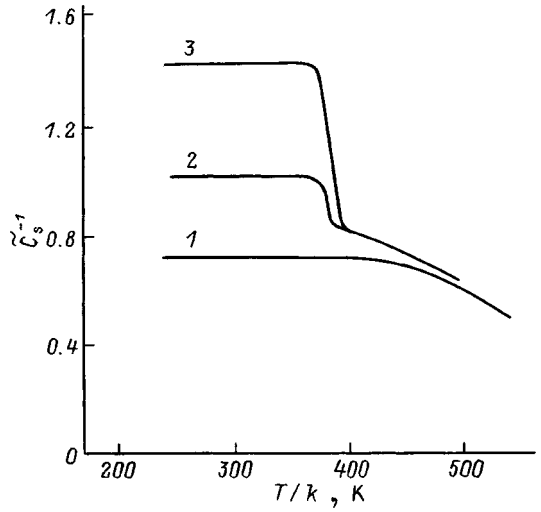

FIG. 5. Temperature dependence of the reciprocal $\tilde{C}_s^{-1}(T)$ of the capacitance of the depletion layer of the semiconductor. $U_0/300k$ (U_0, eV): 15 (0.39) (curve *1*), 30 (0.77) (curve *2*), 60 (1.55) (curve *3*). n_0, E_i, E_0 and E_D are as in Fig. 4.

diminishes. In particular, for $U_0/300k=30$ ($n_0=10^{12}$ cm^{-2}), this side still exists, while by $n_0=10^{11}$ cm^{-2} it has vanished (Fig. 2).

In the case of $\tilde{E}_0-E_i \gg T$, there is a single peak in $\tilde{J}(T)$. Since it was assumed in the calculations that $E_0-E_D \gg T$, thermally stimulated depolarization proceeds under quasi-equilibrium conditions at the interface of both the electron and hole subsystems, and the amplitude of the current peak increases as U_0 rises (Fig. 4). Under these conditions the neutral associates break up mainly through recombination with holes, which are able to accumulate near the interface only after the almost complete breakup of the neutral associates. The thermally stimulated depolarization current is then limited solely by the hole generation rate, which is determined by E_D. Therefore, the activation energy for the ion current on the rising side of the thermally stimulated depolarization curves is equal precisely to E_D (and not E_i or E_0), i.e., to an activation energy that has no direct connection with ion processes. Here a situation which is not typical of thermally stimulated depolarization arises – the rising side of the current peak is determined exclusively by an increase in the ion density n_i, which depends on the balance between the breakup of the neutral associates (through recombination of trapped electrons with holes) and the ejection of ions from traps, and not by a reduction in the ion lifetime in the traps as T increases. There is no significant accumulation of ions in the traps and the thermally stimulated depolarization current is essentially proportional to n_i (Fig. 4, curve *4*).

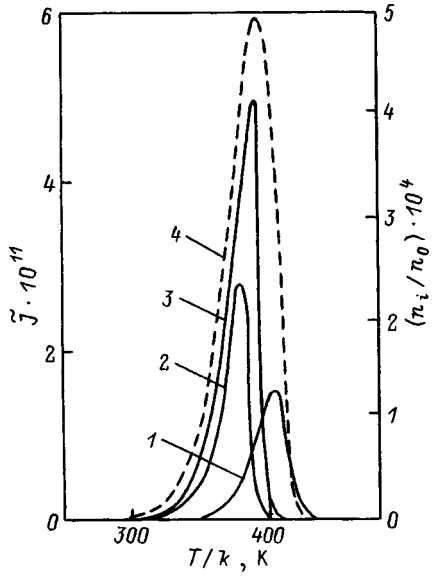

FIG. 4. A family of thermally stimulated depolarization curves $\tilde{J}(T)$ for different initial band bendings U_0 and a typical temperature dependence of the ion density $n_i(T)$ at the interface. The computational parameters are $n_0=10^{11}$ cm^{-2}, $E_i/300k=23$ (0.59 eV), $E_0/300k=38$ (0.98 eV), $E_D/300k=30.3$ (0.78 eV), and $U_0/300k$ (U_0, eV): 15 (0.39) (curves *1* and *4*), 30 (0.77) (curve *2*), and 60 (1.55) (curve *3*).

Figure 5 shows the series of corresponding $\tilde{C}_s^{-1}(T)$ curves. In contrast with the previous case (Fig. 2), they have no rising side, which is as it should be because under quasi-equilibrium conditions the place of an ion that has left the interface is almost instantly filled by a hole. In other words, these curves reflect the accumulation of holes at the interface and, as n_0 increases, the transition from a plateau to the falling side is shifted to higher temperatures and the shape of the current peak changes: its fall becomes ever sharper, since the equilibrium of the system sets in only when an equilibrium hole density has been attained and at a higher rate for higher n_0 and U_0.[7,10] With increasing U_0, the drop in the $\tilde{C}_s^{-1}(T)$ curves becomes steeper due to an increase in the hole generation rate which is proportional to the width of the depletion layer.

Therefore, in the most general case, even when only one type of mobile ion is present in the insulator, three current peaks can appear in the thermally stimulated depolarization curves due to the breakup of neutral associates (activation energy E_0), emptying of ion traps (activation energy E_i), and the generation of holes, the minority charge carriers (activation energy E_D). Depending on the relationships among the values of E_D, E_i, and E_0, the ''hole'' peak can either

precede, follow, or merge with the peak that is associated with purely ionic effects.[1] Merging (with corresponding broadening) of two or three peaks may be erroneously interpreted as caused by the presence of ion traps with an energy distribution on the semiconductor-insulator interface, but, as these calculations have made clear, an analysis of the families of $\tilde{J}(T,U_0,n_0)$ and $\tilde{C}_s(T,U_0,n_0)$ curves can be used to separate the purely ionic and electronic phenomena, establish (even from the qualitative shape of the thermally stimulated depolarization curves) the contributions of ion traps and neutralization effects to the current, and determine the activation energies of the corresponding processes. Here it is useful to employ several well-known and extremely effective experimental techniques (initial heating, factional ''purification,'' varying β, etc.) which, unfortunately, have hardly been used for studying thermally stimulated depolarization in Si MOS structures. If a single peak appears in the thermally stimulated depolarization curves, this may mean that $\tilde{E}_0 - E_i \geqslant T$.[2] Then, if $E_0 > E_D$, the thermally stimulated depolarization current is limited solely by the hole generation rate, which is determined by the activation energy E_D, while the amplitude of the current peak is doubled, since the loss of an ion from the interface takes place simultaneously with the arrival of a hole, i.e., at the same time as the electron leaves in a direction opposite to the displacement of a positive ion. In this case, relaxation experiments cannot be used to determine the activation energy for ion depolarization.

We have examined the case of discrete activation energies E_0 and E_i for greater physical clarity, assuming that, in a polarized insulator, the ions and neutral associates are situated right at the interface. In reality, traps and, therefore, ions and neutral associates, can be distributed over the volume of the insulator near its interface with the semiconductor.[1,11] The thermally stimulated depolarization peaks will then be broadened because of the probability distribution for electron-ion tunneling exchange between the semiconductor and the insulator. Broadening of the thermally stimulated depolarization peaks can also be caused by the dispersive character of ion transport in the volume of the oxide.[12] Formally, this type of broadening can be attributed to the presence of ion capture centers with an energy distribution near the interface. Therefore, the general pattern of the behavior of $\tilde{J}(T)$ and $\tilde{C}_s(T)$ may turn out to be more complicated and then, without the ideas developed here and in Ref. 1, it is impossible to successfully ''decipher'' it and, in principle, to explain the observed evolution of the thermally stimulated depolarization peaks with varying U_0 and n_0,[4,5] which has not yet received an adequate physical interpretation.

[1)]Isolated hole peaks are not shown in the $\tilde{J}(T,U_0,n_0)$ curves presented here, since their appearance in the temperature range corresponding to E_D is physically obvious and has been discussed in detail elsewhere.[7] Here we have analyzed the more interesting intermediate cases in which holes make a direct contribution to the thermally stimulated depolarization peaks.

[2)]The qualitative criteria for this regime are evident from Fig. 4 and the corresponding text.

[1] E. I. Gol'dman, A. G. Zhdan, and G. V. Chucheva, Fiz. Tekh. Poluprovodn. **31**, 1468 (1997) [Semiconductors **31**, 1309 (1997)].
[2] T. W. Hickmott, J. Appl. Phys. **46**, 2583 (1975).
[3] M. R. Boudry and J. P. Stagg, J. Appl. Phys. **50**, 942 (1979).
[4] M. R. Boudry and J. P. Stagg, J. Appl. Phys. **52**, 885 (1981).
[5] T. Hino and K. Yamashita, J. Appl. Phys. **50**, 4879 (1979).
[6] K. Yamashita, M. Iwamoto, and T. Hino, Jpn. J. Appl. Phys. **20**, 1429 (1981).
[7] E. I. Gol'dman, A. G. Zhdan, and A. M. Sumaroka, Fiz. Tekh. Poluprovodn. **26**, 2048 (1992) [Sov. Phys. Semicond. **26**, 1152 (1992)].
[8] E. I. Gol'dman and A. G. Zhdan, Mikroelektronika **23**, 3 (1994).
[9] Yu. A. Gorokhovatskiĭ and G. A. Bordovskiĭ, *Thermally Activated Current Spectroscopy of High-resistance Semiconductors and Dielectrics* [in Russian], Nauka, Moscow (1991), p. 248.
[10] J. G. Simmons and H. A. Mar, Phys. Rev. B **8**, 3865 (1973).
[11] D. J. DiMaria, J. Appl. Phys. **52**, 7251 (1981).
[12] W. Tomaszewiez, J. Rybicki, and P. Grygiel, J. Non-Cryst. Solids **221**, 84 (1997).

Translated by D. H. McNeill

LOW-DIMENSIONAL SYSTEMS

Selective doping in hydride epitaxy and the electrical properties of quantum-well Ge/GeSi:B heterostructures

L. K. Orlov, R. A. Rubtsova, and N. L. Orlova

N. I. Lobachevskiĭ Physics and Engineering Research Institute, 603600 Nizhny Novgorod, Russia
(Submitted July 6, 1998; accepted for publication July 7, 1998)
Fiz. Tekh. Poluprovodn. **33**, 311–315 (March 1999)

The transport properties of different groups of charge carriers in the conducting channels of periodic Ge–$Ge_{1-x}Si_x$ heterosystems grown by hydride epitaxy on germanium are studied as functions of the structural parameters. The results are used to discuss the problem of selective doping of nanometer layers during hydride epitaxy. © *1999 American Institute of Physics.* [S1063-7826(99)01203-X]

Stressed quantum-well heterocompositions based on the elementary semiconductors Si and Ge and their solid solutions are of great interest because of their possible use in modern silicon electronic devices. Especially noteworthy progress has been observed in microelectronics, where comparatively recently Ge–Si heterostructures grown by molecular-beam epitaxy (MBE) have been used to create high-speed heterobipolar transistors[1,2] with switching times close to those for the best GaAs devices. There is also some interest in the possibility of creating field-effect transistors with high electron and hole mobilities based on selectively doped *n*-type $Si/Si_{1-x}Ge_x$ heterostructures with a two-dimensional charge carrier gas in the transport channels. Advances in this area with *n*-type $Si/Si_{1-x}Ge_x$ heterostructures have been discussed by Kuznetsov *et al.*[3] An attempt has been made to obtain the maximum hole mobility for germanium-silicon compositions based on a $Ge/Si_{1-x}Ge_x$ system with the possibility of creating a field-effect transistor with two-dimensional holes.[4]

In the last decade considerable effort has been expended in studying the transport properties, subject to the quantum Hall effect, of two dimensional holes in selectively doped $Ge/Ge_{1-x}Si_x$ heterosystems grown on germanium. Studies are currently under way in the far infrared on the microwave properties of these structures when the charge carrier gas is heated by a pulsed electric field.[7–9] The efforts in this area aimed at creating thin-film lasers based on hot, two-dimensional holes require more attention to the transport characteristics of systems in low fields in order to understand the details of the current flow channels and to refine our understanding of the scattering of charge carriers in them.

On the other hand, until now hydride epitaxy at atmospheric pressure in a reactor[10] has mainly been used to grow $Ge/Ge_{1-x}Si_x$ structures. For a number of objective reasons, this method does not allow fabrication of structures with a sharp compositional profile. (The spreading out of the heterojunctions in this system is as large as 3–4 nm.[11]) The transition from MLE to gaseous phase epitaxy techniques is a necessary step on the way to industrial manufacture of these structures. In this regard, the clarification of all, including the not particularly attractive, features of heterostructures grown by gaseous phase techniques, along with their causes, is an important aspect of the development and improvement of the technology.

Based on previously published studies, including some by electrical methods, in an earlier paper[11] we showed what kind of limits may be imposed on studies of the electron-hole states in layers of $Ge/Ge_{1-x}Si_x$ structures grown by hydride epitaxy as a result of the spreading of the compositional profile over the superlattice period. Our purpose in this study was to investigate the dependence of the hole mobility in the Ge layers of these heterostructures on the impurity concentration level in the barrier layers and to estimate the degree of spreading of a selectively doped δ-layer over the superlattice period. Experimental Hall effect studies were carried out on samples of selectively boron-doped superlattices ($Ge/Ge_{1-x}Si_x$: B) grown by hydride epitaxy at atmospheric pressure.[5–10] The maximum concentration of boron atoms in the solid solution layers was varied over $10^{17}-10^{19}$ cm^{-3}. Tables I and II list the parameters of the structures: the Si content in the layers (x), the superlattice period (d_{SL}) and number of periods (N), the Hall mobility (μ_H), and the surface concentration (p_s). The experimental results are compared with the results of a theoretical analysis.

The theoretical analysis includes a calculation of the

TABLE I. Structural parameters of the first series.

Sample number	x, at.%	N	d_{SL}, nm	μ_H, $cm^2/(V\cdot s)$ ($T=77$ K)	p_s, 10^{10} cm^{-2}
1256	6.0	72	45.5	15000	8.4
1261	7.4	72	53	20580	7.9
1263	7.0	72	70	14160	14.5
1264	10	81	39	10670	12.2
1265	6.0	81	44.5	9560	5.5
1266	6.6	64	50	11590	3.8
1274	8.0	81	59.5	10490	39
1275	6.5	81	57	8090	44

TABLE II. Structural parameters of the second series.

Sample number	x, at.%	N	d_{SL}, nm	μ_H, cm^2/(V·s) (T=77 K)	p_s, 10^{11} cm^{-2}
1121	3.5	1	45	2330	30.7
1122	3.5	5	45	5360	4.31
1123	3.9	15	41.6	7480	2.34
1124	4.7	27	40.3	7840	2.5
1125	4.8	35	36.5	8830	2.3

concentrations of the different charge carrier groups in the conducting channels of the superlattice period including the shape of the potential, followed by a calculation of their mobilities. The shape of the potential $\phi(x)$ was calculated over the period of the structure by numerically solving the Poisson equation for sharp heterojunctions in the system,

$$\frac{d^2\phi}{dz^2}=\frac{4\pi e}{\varepsilon_i}\left\{N_{ci}F_{0.5}\left(\frac{E_F-E_g-e\phi}{kT}\right)-N_{li}F_{0.5}\left(\frac{e\phi-E_F}{kT}\right)-N_{hi}F_{0.5}\left(\frac{e\phi-E_F}{kT}\right)+N_{ai}\right\}. \quad (1)$$

Here $F_{0.5}(e\phi)$ is the Fermi integral, E_F is the Fermi constant, N_{ci} is the density of states of the electrons in the ith layer of the conduction band, N_{li} and N_{hi} are the densities of states of the light (l) and heavy (H) holes in the valence band of the ith layer, and N_{ai} is the acceptor concentration in the ith layer. The splitting of the hole subbands in the germanium layers was estimated using the method described by Orlov *et al.*[12] The characteristic shape of the potential over the period of the structure is plotted in Fig. 1 as a function of the dopant impurity concentration for samples from the first series (Table I) and at two temperatures for sample 1125 from the second series (Table II).

The hole concentrations $p^i_{l,h}$ in the individual layers were determined by integrating over the thickness d_i of the ith layer of the heterostructure,

$$p^i_{l,h}=(1/d_i)\int_{d_i}p_{l,h}(z)dz. \quad (2)$$

The calculated variations in the concentrations of the different kinds of holes with the doping level in the layers are shown in Fig. 2a. The characteristic temperature dependences of the hole concentrations for sample 1125 are shown in Fig. 2b. A stepwise doping profile of the Ge and $Ge_{1-x}Si_x$ layers is assumed.

The mobilities of the jth group of holes in the layers of the structure were calculated, for simplicity, using the formulas

$$\mu_j=1/(1\mu_{1j}+1/\mu_{2j}+1/\mu_{3j}+1/\mu_{4j}), \quad (3)$$

where

$$\mu_{1j}=e\tau/m_j=2000[m_h(\mathrm{Ge})/m_j](T/300)^{-2.3} \quad (4)$$

is the component of the mobility associated with scattering on acoustic and optical phonons,[13]

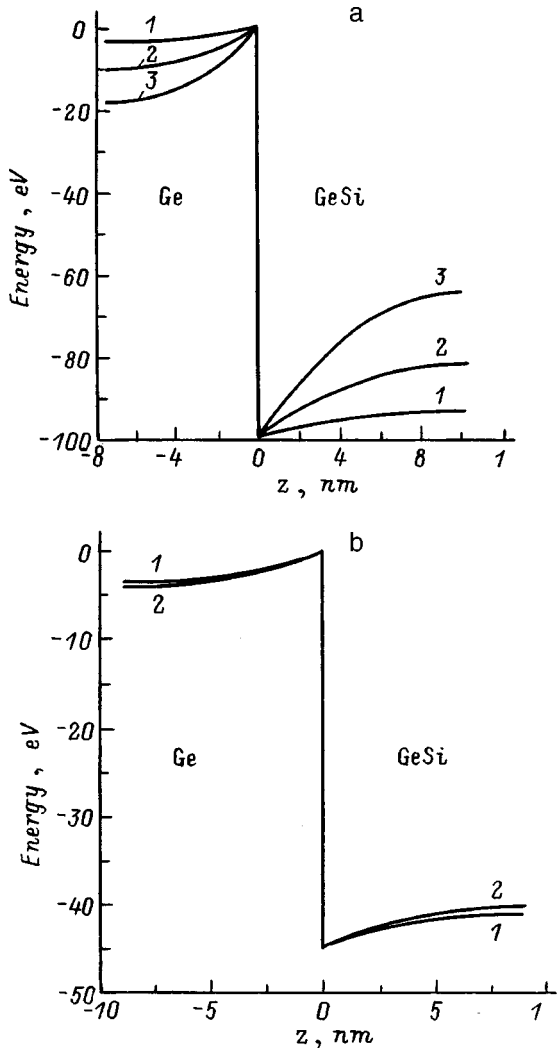

FIG. 1. The shape of the potential over a period of the superlattice. (a) Calculation for the samples from Table I for T=77 K and N_a(GeSi) (10^{17} cm^{-3}): 1 (*1*), 3 (*2*), 6 (*3*); (b) calculation for sample 1125 from Table II at T=4 K (*2*) and 200 K (*1*)

$$\mu_{2j}=(5.166\times10^{14})/(N_{aj}^{0.64})(T/300)^{0.625} \quad (5)$$

is the component associated with scattering on the ionized impurity (the Brooks–Herring formula),[14]

$$\mu_{3j}=e^3m_j/20\varepsilon_j h^3N_0 \quad (6)$$

is the component associated with scattering on neutral impurities with concentration N_0,[15] and

$$\mu_{4j}=\alpha T^{-0.5}/x(1-x) \quad (7)$$

is the component associated with fluctuations in the composition.[15]

Attainment of the highest possible charge carrier mobilities in the system is, to a great extent, the basis of its possible use in practical microelectronics devices.

In a $Ge/Ge_{1-x}Si_x$ structure with ideally sharp changes in the compositional profile and in the concentration of the dopant impurity, one might expect a substantial rise in the mobility of two-dimensional holes, both with the increase in the depth of the quantum wells as the percent content of silicon in the solid solution layers is increased[11] and with the in-

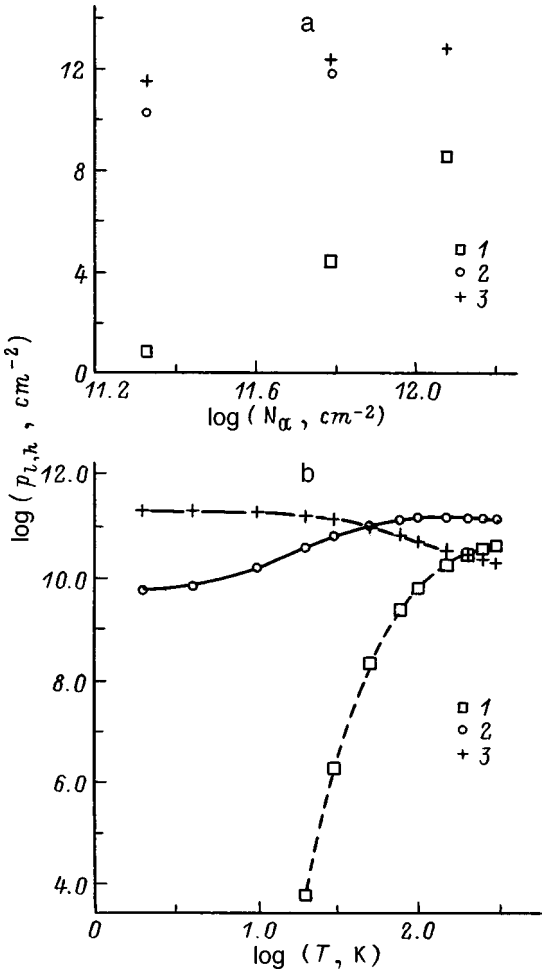

FIG. 2. Concentrations of heavy holes in layers of $Ge_{1-x}Si_x$ (*1*) and Ge (*2*) and of light holes in Ge layers (*3*), calculated for samples in series 1 (Table I) as functions of the doping level of the $Ge_{1-x}Si_x$ layers for $T=77$ K (a) and for sample 1125 (Table II) as a function of temperature (b).

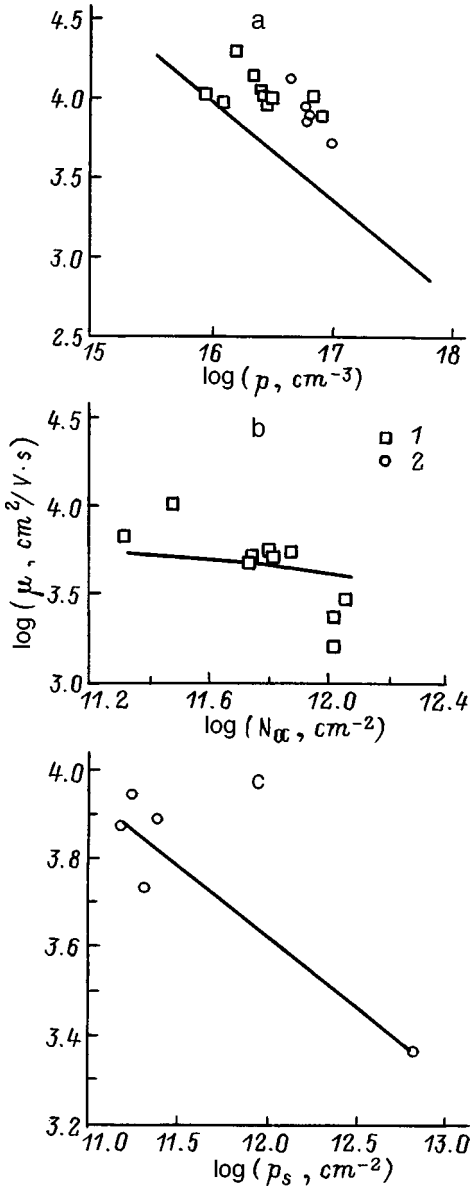

FIG. 3. The hole mobility μ in $Ge/Ge_{1-x}Si_x$ structures as a function of concentration. Experimental data (points): (*1*) samples from series 1 (Table I), (*2*) samples from series 2 (Table II). Solid curves: (a) experimental dependence on the volume hole concentration p for bulk Ge;[16] (b and c) calculated at 77 and 4 K, respectively.

crease in their concentration in the transport channels due to screening of the background scattering centers and a reduction in their effective scattering cross section.

In the periodic $Ge/Ge_{1-x}Si_x$ heterostructures under discussion here, however, the experimentally observed dependence of the Hall mobility of the holes, μ_H, on their surface concentration p_s is different. Most often (Fig. 3) a drop in the mobilities of the holes in the superlattice is observed as their concentration in the germanium layers increases, although throughout the doped region their mobility exceeds the hole mobility in the bulk germanium (solid curve in Fig. 3; Ref. 16). That the hole mobilities in $Ge/Ge_{1-x}Si_x$ superlattices[17] and homogeneous germanium[16] decrease in the same fashion suggests that scattering on impurity centers predominates in both cases.

Figures 3b and 3c show our experimental data which illustrate the way the hole mobility depends on their total concentration in the conducting channels at $T=77$ K (4.2 K) for the samples listed in Tables I and II. The structures in the first series (Table I) were grown under approximately the same conditions, and only a flux of diborane was used in making them, which resulted in a different level N_a of selective doping. The second series of structures, listed in Table II, differs in the total number of periods in the superlattice. In this case, the hole concentration p_s in the superlattice varied because of surface band bending. The hole concentration rose especially strongly when the number of superlattice periods was reduced to unity, simultaneously sharply lowering the mobility of the holes in the channel (Fig. 3c), perhaps because of scattering on a random surface potential.

Studies in high magnetic fields[5,6] of the transport properties of $Ge/Ge_{1-x}Si_x$ structures grown by hydride epitaxy show that, despite the spreading out of the profile, the holes in these systems are two dimensional. Thus, the observed drop in hole mobility in the conducting channels of germanium in a multilayer heterostructure as the dopant impurity concentration is raised can be related both to a rise in the number of heavy holes in the channels (Fig. 2a) (the Fermi

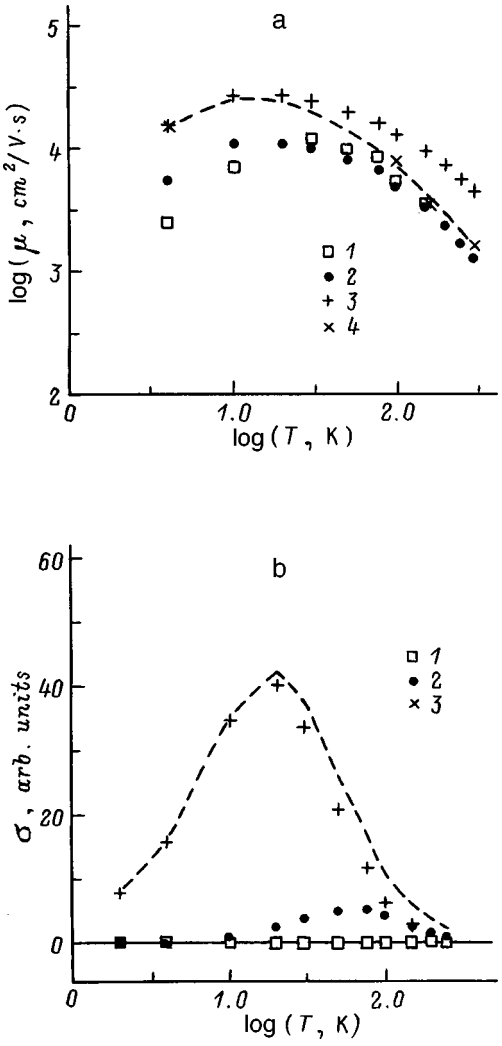

FIG. 4. Calculated temperature dependences of the mobility μ (a) and conductivity σ (b). Calculations for (*1*) heavy holes in $Ge_{1-x}Si_x$ layers, (*2*) heavy holes in Ge layers, and (*3*) light holes in Ge layers; the dashed curve is the sum for all carrier groups; (*4*) experiment.

level in the Ge layer is raised and fills the upper *h*-subband with carriers) and to their more effective scattering on structural defects. The solid curve in Fig. 3b was calculated for the case of lightly doped germanium layers. (The background doping level of the germanium layers is independent of the doping level in the layers of solid solution and remains rather low at $\sim 1\times 10^{16}$ cm^{-3}.) It is clear that allowance for only the mechanism associated with a redistribution of the holes among the subbands does not guarantee the experimentally observed drop in mobility. More likely, by analogy with silane,[11] the pulse of diborane spreads out in the continuous flow of germanium, which accounts not only for the finite width of the δ-layerbut also for the additional impurity background in the germanium layers of the superlattice. Increasing the diborane flux causes a rise in the doping level of the $Ge_{1-x}Si_x$ layers and, accordingly, in the background impurity level in the Ge layers; this in turn causes a rather substantial drop in the mobility of the two dimensional holes.

In the conventional continuous growth regime, therefore, the leading edges of the pulsed diborane flux spread out, causing underdoping of the spacers and the Ge conducting channels. A comparison of our data with the corresponding curves observed in uniformly doped germanium single crystals (Fig. 3a) indicates that the background impurity concentration level in the Ge layers is roughly an order of magnitude lower than the concentration of free holes in them (i.e., lower than the concentration of the dopant impurity in the $Ge_{1-x}Si_x$ layer). Therefore, the characteristic magnitude of the spread of the impurity over the period of the structure (the distance over which the doping level drops by a factor of 3) is roughly 3-4 nm (the spacer thickness), in agreement with an earlier estimate[11] of the spread of silicon.

Allowance for this factor, along with the calculated concentrations of the various groups of holes, makes it possible to compute a temperature dependence (Fig. 4a) of the mobility, consistent with the experimental data, and to evaluate the contributions of the different scattering mechanisms over the entire temperature range that was studied. A numerical simulation for a large number of samples showed that at low temperatures the scattering of holes in the germanium layers is the main factor limiting their mobility.

In conclusion, we note the temperature dependence of the conductivity at low temperatures. It is clear that here it has a distinct maximum. The rise in the conductivity $\sigma(T)$ in the initial segment is related to the increased mobility of the light holes due to a reduction in the role of impurity scattering (Fig. 4a). The drop at higher temperatures is caused by a redistribution of the charge carriers among the subbands in the germanium layer (the concentration of heavy holes in the upper subband increases; see Fig. 2b). Since at temperatures below 50 K the lattice separation is unimportant, the lattice temperature T in Fig. 4b can be replaced by the electron temperature T_e, which is proportional to the effective electric field E. We can then consider this curve as the current-voltage characteristic of the structure and the mechanisms responsible for its shape account for the oscillations in the rf current observed experimentally by Aleshkin *et al.*[18]

We wish to thank the Russian Research (Grant No. 96-02-19278) and INTAS (Grant No. 96-0580) for supporting this work.

[1] T. C. Chen, E. Ganin, H. Stark *et al.* IEEE Trans. Electron Devices **38**, 941 (1991).
[2] A. Gruhle and A. Schuppen, Thin Solid Films **294**, 246 (1997).
[3] V. I. Kuznetsov, K. Werner, S. Redelaar, and J. W. Metselaar, Thin Solid Films **294**, 263 (1997).
[4] Y. H. Xie, E. A. Fitzgerald, D. Monroe, P. J. Silverman, and G. P. Watson, J. Appl. Phys. **73**, 8364 (1993).
[5] B. A. Aronzon, N. K. Chumakov, J. Leotin, J. Galiber, L. Essaleh, A. L. Chernov, O. A. Kuznetsov, L. K. Orlov, R. A. Rubtsova, and O. A. Mironov, Superlattices Microstruct. **13**, 159 (1993).
[6] Yu. G. Arapov, N. A. Gorodilov, O. A. Kuznetsov, V. N. Neverov, L. K. Orlov, R. A. Rubtsova, G. I. Kharus, A. L. Chernov, N. G. Shelushinina, and G. L. Shtrapenin, Fiz. Tekh. Poluprovodn. **27**, 1165 (1993) [Semiconductors **27**, 642 (1993)].
[7] L. K. Orlov, Zh. Leoten, Fu Hua Yang, and N. L. Orlova, Fiz. Tverd. Tela **39**, 2096 (1997) [Phys. Solid State **39**, 1120 (1997)].
[8] L. E. Vorob'ev, L. E. Golub, D. V. Donetskii, E. A. Zibik, Yu. V. Kochegarov, D. A. Firsov, V. A. Schalygin, V. Ya. Aleshkin, O. A. Kuznetsov, L. K. Orlov, E. Towe, I. I. Saydashev, T. S. Cheng, and C. T. Foxon, in *Proceedings of the 23rd International Symposium on Compound Semiconductors* (St. Petersburg, 1996) (1997), p. 153.

[9] V. Ya. Aleshkin, A. A. Andronov, A. V. Antonov, N. A. Bekin, I. V. Erofeeva, V. I. Gavrilenko, O. A. Kuznetsov, E. R. Lin'kova, I. G. Malkina, M. Moldavskaya, D. G. Revin, E. A. Uskova, and B. N. Zvonkov, in *Proceedings of the 23rd International Symposium on Compound Semiconductors* (St. Petersburg, 1996) (1997), p. 61.
[10] M. G. Mil'vidskii, V. I. Vdovin, L. K. Orlov, O. A. Kuznetsov, and V. M. Vorotynsev, in *Growth of Crystals*, edited by E. I. Givargizov and A. M. Melnikova, Consultants Bureau, N. Y.–London (1996), V. 20, p. 13.
[11] L. K. Orlov, R. A. Rubtsova, N. L. Orlova, and V. I. Vdovin, in *Proceedings Conference on the Si–Ge System* [in Russian], IFM RAN, Nizhny Novgorod (1998), p. 127.
[12] L. K. Orlov, V. Ya. Aleshkin, N. G. Kalugin, N. A. Bekin, O. A. Kuznetsov, B. Dietrich, G. Bacquet, J. Leotin, M. Brousseau, and F. Hassen, J. Appl. Phys. **80**, 415 (1996).
[13] V. I. Fistul', *Heavily Doped Semiconductors* [in Russian], Nauka, Moscow (1967), pp. 116 and 97.
[14] V. L. Bonch-Bruevich and S. G. Kalashnikov, *Physics of Semiconductors*, Nauka, Moscow (1990), pp. 116 and 671.
[15] N. A. Agaev and G. Kh. Azhdarov, in *Proceedings Conf. on ''The Study and Appliations of Germanium-silicon Solid Solutions''* [in Russian], Baku-Elm (1990), p. 56.
[16] O. A. Golikova, B. Ya. Moĭzhes, and M. S. Stil'bans, Fiz. Tverd. Tela **3**, 3105 (1961) [Phys. Solid State **3**, 2259 (1961)].
[17] L. K. Orlov, A. V. Potapov, R. A. Rubtsova, Yu. G. Arapov, N. A. Gorodilov, N. G. Shelushinina, Fu Hua Yang, J. Leotin, and M. Goiran, Thin Solid Films **294**, 208 (1997).
[18] V. Ya. Aleshkin, N. A. Bekin, I. V. Erofeeva, V. I. Gavrilenko, Z. F. Krasil'nik, O. A. Kuznetsov, M. D. Moldavskaya, V. V. Nikonorov, and V. M. Tsvetkov, Lith. Phys. J. **35**, 368 (1995).

Translated by D. H. McNeill

Photoluminescence and transport properties of multilayer InAs/GaAs structures with quantum dots

V. A. Kul'bachinskiĭ, V. G. Kytin, R. A. Lunin, A. V. Golikov, I. G. Malkina, B. N. Zvonkov, and Yu. N. Saf'yanov

M. V. Lomonosov Moscow State University, 119899 Moscow, Russia
(Submitted April 15, 1998; accepted for publication July 28, 1998)
Fiz. Tekh. Poluprovodn. **33**, 316–321 (March 1999)

The transport and optical properties of InAs/GaAs structures with quantum dots on a vicinal surface have been investigated as a function of InAs content. It was found that the quantum dots form two-dimensional hole or electron layers, from which the Shubnikov–de Haas effect was observed. The temperature dependence of the resistance was measured in the [110] and [$\bar{1}$10] directions in the temperature range 4.2–300 K, and the anisotropy of the conductivity was found. Strong localization occurs when electrons are trapped in InAs dots. The spectra of in-plane photoluminescence showed strong polarization of the quantum-dot radiation.
 [S1063-7826(99)01303-4]

1. INTRODUCTION

The properties of electrons in one-dimensional structures (quantum filaments) and zero-dimensional structures (quantum dots) are attracting great interest because of possible applications,[1,2] and because interesting fundamental problems are associated with them.[3,4] An effective means of obtaining quantum dots, in which the electron and hole motion is quantized along all three directions, is to allow homogeneous islands of InAs to be formed by elastic stresses in the process of heteroepitaxial growth on a GaAs surface.[5–8] The optical properties of such structures with quantum dots are being studied extensively because they can be used in devices.[1,2] The transport properties of these structures have been less thoroughly studied. In this paper we present the results of an experimental study of the low-temperature transport properties and the photoluminescence spectrum along the plane of layers of InAs/GaAs quantum dots.

2. MEASUREMENT PROCEDURE AND SAMPLES

The structures were grown by organometallic–hydride epitaxy at temperatures in the range 600–650 °C in an atmospheric-pressure reactor from trimethyl indium, trimethyl gallium, and arsenic on semi-insulating GaAs substrates inclined at an angle of 3° from the (001) plane toward the [110] direction. The samples contained from ten to twenty layers of InAs quantum dots, separated by GaAs barriers 0.1 μm thick. The *n*-type samples were not especially doped, and the *p*-type samples contained a delta-layer of carbon in the barriers. The thickness of the spacer was 5–6 nm. The structures were covered from above by a GaAs layer 0.1 μm thick. Certain parameters of the samples are shown in Table I. The quantum dots begin to form when the amount of InAs on the growth surface exceeds 0.8 of a monolayer.[9] The photoluminescence spectra were measured at temperatures $T=300$ and 77 K with excitation by a He–Ne laser. The excitation level was 10^{21} photon/cm^{2}sec. The transport measurements were made on square samples with sides along the [110] and [$\bar{1}$10] directions and on samples in the form of double Hall bridges of two different orientations. The temperature dependences of the resistance were measured in the temperature range 1.6–300 K, and the Shubnikov–de Haas effect, the magnetoresistance $\Delta\rho(B)$, and the Hall coefficient R_H were measured in magnetic fields B up to 10 T, created by a superconducting solenoid.

3. RESULTS OF THE MEASUREMENTS AND DISCUSSION

3.1. Optical properties of the structures

The size of the quantum dots, 5–7 nm, was determined from the maximum of the photoluminescence spectrum, using the theory developed in Refs. 3 and 8. The photoluminescence spectra in these papers were calculated for an empty isolated dot. In the test samples, the states at the dots were filled with charge carriers, and therefore the quoted sizes are only a rough estimate. The interaction of adjacent dots can be reduced to the broadening of the levels and the formation of a two-dimensional zone. In the tight-binding model, the broadening equals $2NI$, where N is the number of nearest neighbors, $I=\int\varphi^*(\mathbf{r}+\mathbf{h})V(\mathbf{r})\varphi(\mathbf{r})d\mathbf{r}$ is the overlap integral, φ is the electron (hole) wave function of a single quantum dot, and $\mathbf{h}$ is a translation vector.[10] To estimate overlap integral I, $V(r)$ can be replaced with the value of the discontinuity of the conduction band ΔE_c for electrons and of the valence band ΔE_v for holes. For two tangential bases of the quantum dots, the overlap of the electron wave functions is less than 2%, and that of the hole wave functions is less than 1.5%.[8] The overlap integral is thus less than $0.02\Delta E_c$ for electrons and less than $0.015\Delta E_v$ for holes. The level broadenings are hence 138 meV for electrons and 30 meV for holes; i.e., the maximum of the photoluminescence spectrum does not shift by more than 90 meV, which is comparable to the experimentally observed value. The shift of photoluminescence spectra is even less because of the Coulomb interaction, since the electron and hole levels shift

TABLE I. Parameters of the samples.

Sample number	Type of conductivity	N_p	$h\nu_{max}$, eV	Quantity of InAs in the layer, ML	N_{QD}, 10^{11} cm^{-2}	$\rho_\perp$, $\Omega/\square$	$\rho_\perp/\rho_\parallel$	n_H, 10^{11} cm^{-2}	n_{SH}, 10^{11} cm^{-2}
1		12	1.38	2.35	7.4	⋯	⋯	0.58	⋯
2	*p*	10	1.36	2.5	6.8	1270	2.18	2.7	⋯
3		20	1.34	4.6	30	954	⋯	2.4	2.6
4		10	1.415	2.25	10	1057	1.19	5.3	4.8
5		20	1.345	4.3	39	41000	1.5	0.30	⋯
6		12	1.41	2.1	8.3	8290	1.89	0.36	⋯
7	*n*	10	1.37	3.0	10	2120	6.87	1.08	1.9
8		10	1.41	2.4	9.5	385	2.08	1.20	1.5
9		15	1.28	4.7	11	7800	5.3	1.60	2.2
10		10	1.38	2.3	7.3	574	3.42	1.91	2.6

Note: N_p is the number of periods in the structures, $h\nu_{max}$ is the energy of the maximum in the photoluminescence spectrum at $T=77$ K, ML$=0.325$ nm is the thickness of a monolayer of InAs, N_{QD} is the concentration of quantum dots per layer, $\rho_\perp$ and $\rho_\parallel$ are the resistivities in the [110] and [$1\bar{1}0$] directions at $T=4.2$ K; n_H is the Hall concentration of current carriers per layer, n_{SH} is the concentration of current carriers, determined from the Shubnikov–de Haas effect.

in the same direction in doped structures. The estimate of the size of the quantum dots made at the beginning of the paragraph is thus quite acceptable. The same size of the quantum dots and their ordering along the terraces are obtained on the test structures by directly measuring them with a tunneling atomic-force microscope.[1)]

The width of a terrace on a vicinal surface with a disorientation angle of 3° is theoretically $d=5.6$ nm in the case of GaAs. In practice, there is a distribution over width which was studied in Refs. 11 and 12 as a function of the disorientation angle. There are always larger terraces in the samples, and this causes quantum dots with a size greater than the theoretical value of d to appear.

Figure 1a shows the setup for measuring the photoluminescence. To compare the radiation of the quantum dots with that of a quantum well, an $In_{0.2}Ga_{0.8}As$ quantum well with a width $W=5$ nm was added to one of the samples. The photoluminescence spectrum of this sample is shown in Fig. 1b. As can be seen from the figure, the radiation of the quantum dots and that of the quantum wells are well separated. No polarization of the photoluminescence from the quantum well is observed, whereas the photoluminescence of the layer of quantum dots is strongly polarized in the plane of the structures (no photoluminescence polarization is observed from an individual quantum dot). This fact is unexpected, since recombination with the participation of heavy hole states, giving radiation polarized in the plane of the structure, is identically inherent to quantum wells and quantum dots. The observed phenomenon can probably be explained by the difference in the degrees of mixing of the heavy hole states at the heteroboundaries in layers with a different structure.[13,14]

Figure 2 shows the photoluminescence spectra at 77 K for *p*-type samples 1, 2, and 4 (Fig. 2a), and for *n*-type samples 7, 9, and 10 (Fig. 2b). The solid curves show the intensity of the emitted light in the plane of the structures in the [110] direction with polarization $\mathbf{E}\perp[001]$, and the dashed curves show the intensity of the emitted light in the same direction but with polarization $\mathbf{E}\|[001]$. The light emitted in the [001] direction is not polarized (the dot–dashed curve for sample 9). The photoluminescence intensity I_{pl} on the right-hand side of the peaks is proportional to $\exp(-h\nu/kT)$, which corresponds to a Boltzmann distribution. The half-width of the photoluminescence spectra, amounting to 20–60 meV, is evidence that the sizes of the quantum dots are scattered and it is independent of tempera-

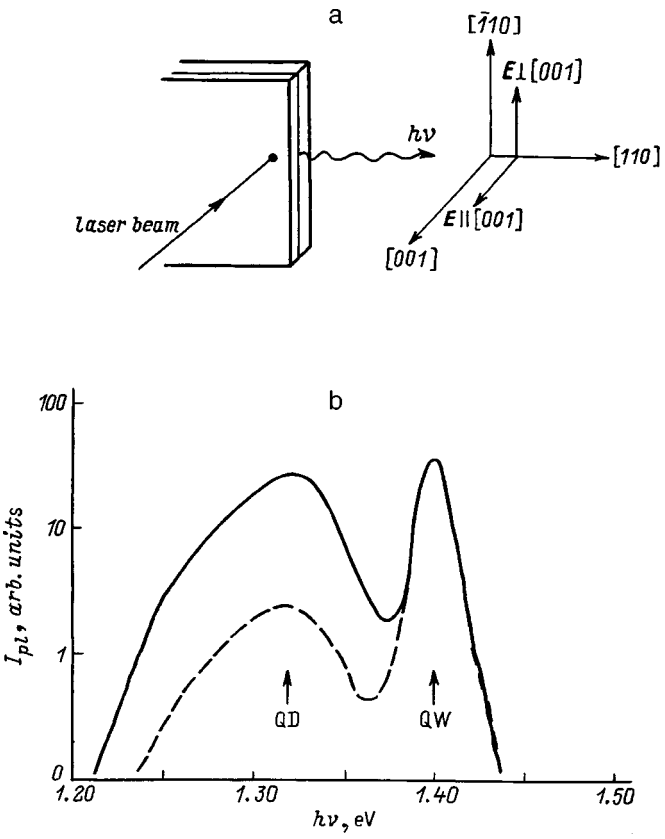

FIG. 1. (a) Layout for measuring the photoluminescence spectra; (b) dependence of photoluminescence intensity I_{pl} at $T=77$ K on photon energy $h\nu$ in a structure with a quantum well $In_{0.2}Ga_{0.8}As$ with width $W=5$ nm and a layer of quantum dots with an effective thickness of three InAs monolayers. The solid curve shows the light intensity in the [110] direction with polarization $\mathbf{E}\perp[001]$, and the dashed curve shows that for $\mathbf{E}\|[001]$. The arrows indicate the emission energies of the quantum dots (QD) and quantum well (QW).

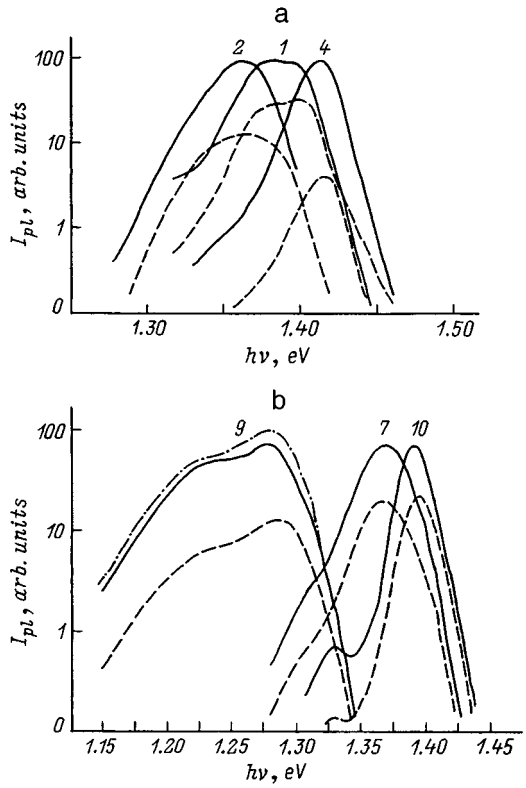

FIG. 2. Photoluminescence spectra at 77 K for (a) *p*-type samples, (b) *n*-type samples. The solid curves show the light intensity emitted in the [110] direction, with polarization $\mathbf{E}\perp[001]$, and the dashed curves show that with $\mathbf{E}\|[001]$. The light emitted in the [001] direction is not polarized (the dot-dashed curve for sample 9). The numbers on the curves correspond to the sample numbers in Table I.

ture in the range 77–300 K for all samples other than sample 1. In sample 1, the half-width increases with increasing temperature. This behavior is probably attributable to the fact that all the zero-dimensional electron states in it are filled because of high carrier concentration. The resulting energies of the photoluminescence peaks equal 1.34–1.41 eV for the *p*-type samples and 1.28–1.41 eV for the *n*-type samples.

The structures were also studied by means of x-ray diffraction, and data for the amount of indium in the layer of quantum dots were obtained (see Table I). The concentration of quantum dots is estimated as $(6.8–30)\times10^{11}\,\mathrm{cm}^{-2}$ for various samples. For such concentrations of the quantum dots, the distance between them is comparable with the size of a quantum dot, and the size of the quantum dots in turn is close to the width of a step on the disoriented substrate.

3.2. Transport properties of the structures

All the samples can be divided into two groups, depending on the current-carrier concentration at room temperature, obtained from the Hall effect in weak fields. In samples with a hole concentration less than $0.6\times10^{11}\,\mathrm{cm}^{-2}$ at room temperature or with an electron concentration less than $0.3\times10^{11}\,\mathrm{cm}^{-2}$, the resistance increased by several orders of magnitude as the temperature was lowered, and they became nonconducting (samples *1* and *5*) even at liquid-nitrogen temperature. There is thus a critical concentration at room temperature less than $10^{11}\,\mathrm{cm}^{-2}$, below which all the urrent carriers are localized as temperature decreases both in *p*-type samples and in *n*-type samples. This concentration does not correlate with the concentration of quantum dots (see Table I), since the localization occurs not only in quantum dots but also in a larger-scale potential well, as will be seen from the subsequent results.

In samples with a larger initial hole or electron concentration, resistance ρ decreases as temperature decreases to about 50 K and then increases, as shown in Fig. 3 for sample 6. Measurements of resistance ρ showed anisotropy in both types of samples, depending on temperature T: ρ is a factor of 3–12 greater in the [110] direction than in the $[\bar{1}10]$ direction; this can be explained by the formation of quantum dots into chains in the $[\bar{1}10]$ direction along the steps. The formation of chains of InAs quantum dots on a faceted GaAs surface was observed by means of a tunnelling microscope in such structures in Ref. 15. The temperature dependences of the resistance of sample 6 in the [110] direction (curve *1*)

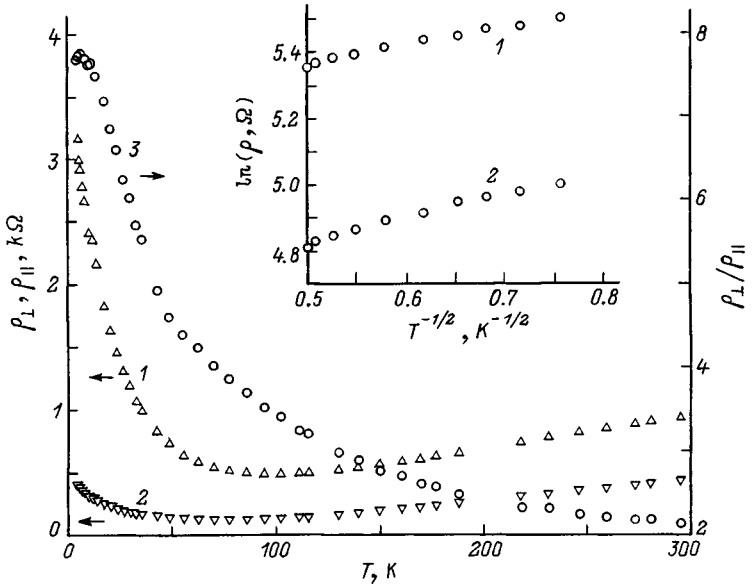

FIG. 3. Temperature dependences of resistance $\rho_\perp$ in the [110] direction (curve *1*), $\rho_\parallel$ in the $[\bar{1}10]$ direction (*2*), and resistance anisotropy $\rho_\perp/\rho_\parallel$ (*3*) for sample 6. The inset shows the dependence of the resistance ρ on $1/T^{1/2}$ for sample 4, measured along [110] (*1*) and along $[\bar{1}10]$ (*2*).

and in the $[\bar{1}10]$ direction (curve *2*) are shown in Fig. 3. The same figure shows the temperature dependence of the resistance anisotropy (curve *3*). Starting from these results, it can be assumed that the dots were aligned along the steps in the test samples. In this case, the resistance across the steps will be greater than the resistance along the steps. Such resistance anisotropy was observed in GaAs structures delta-doped with tin on the vicinal surface,[16–18] where the tin was distributed predominantly along the steps because of segregation, causing the conductivity to be anisotropic. It is possible that the dots are located not at the center of the terraces but adhere to the edges of the steps, as is experimentally observed for Ge dots on the vicinal surface of GaAs.[19]

In the temperature region $1.6<T<4.2$ K, the dependence of the logarithm of ρ is approximately linear in $T^{-1/2}$. As an example, the inset in Fig. 3 shows the logarithm of the resistance vs $T^{-1/2}$, measured in two directions, for sample 4. These experimental facts are evidence that the current carriers are localized.[20] The conductivity for interacting two-dimensional electrons is $\sigma_{xx}\sim\exp(-T_0/T)^{1/2}$. From the experimental data, we have $T_0\simeq 0.3$ K for sample *4* and $T_0=3.7$ K for sample 2. Such localization is possible when electrons are trapped by potential-energy fluctuations that appear as the structures grow.

Negative magnetoresistance was observed in weak magnetic fields for all the samples at liquid-helium temperature. The magnetic-field dependence of the negative magnetoresistance varied from quadratic to logarithmic. The absolute value of the negative magnetoresistance in weak fields increases as the temperature decreases from 4.2 to 1.6 K. The negative magnetoresistance with its characteristic dependence on magnetic field and temperature can be explained by quantum corrections to the conductivity for the two-dimensional case.[21,22]

Quantum oscillations of the magnetoresistance are observed in stronger magnetic fields. Figure 4a shows as an example the magnetoresistance oscillations in sample 7 at $T=1.6$ K. The variation of the oscillation frequency in an oblique magnetic field (see the inset in Fig. 4a) showed that the oscillations are determined by two-dimensional current carriers formed by a layer of quantum dots incorporated into the growing layer of GaAs. This is also evidenced by the observation of the quantum Hall effect in the test structures (Fig. 4b). The presence of two-dimensional electrons can be explained by the overlap of the electronic wave functions from separate quantum dots, since the density of the dots is high in the test samples. The oscillation amplitude increases as temperature decreases from 4.2 to 1.6 K. The period of the Shubnikov–de Haas oscillations can be used to compute the concentrations of the two-dimensional current carriers, which are somewhat greater than the Hall concentrations calculated for one layer (see Table I). The concentrations of current carriers calculated for one layer are less than the estimated concentration of quantum dots.

The magnetoresistance in strong magnetic fields is different for *p*-type and *n*-type samples. In *n*-type samples, after initial negative magnetoresistance in weak magnetic fields and Shubnikov–de Haas oscillations in intermediate fields, a sharp increase of the resistance was observed in strong magnetic fields. The resistance in a fixed magnetic field increasedproportionally to $T^{-1/2}$ as temperature decreased. As an example, Fig. 5 shows the magnetic-field dependences of

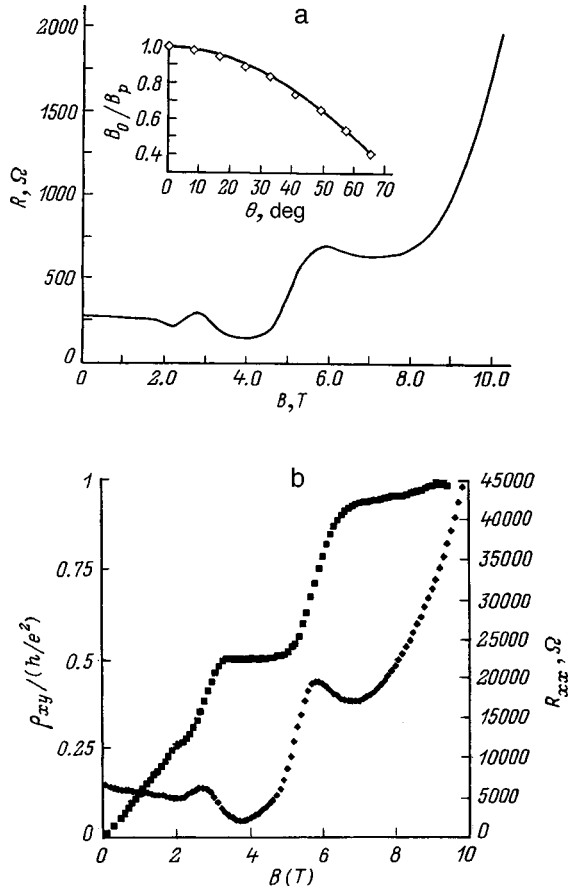

FIG. 4. Quantum oscillations of the magnetoresistance ρ_{xx} of sample 7 at $T=1.6$ K (a) and the quantum Hall effect in sample 10 at $T=4.2$ K (b). The inset shows the dependence of the ratio of the magnetic field B_0 corresponding to one of the maxima of the oscillations in a perpendicular field to the magnetic field B_p corresponding to the same maximum in a tilted magnetic field vs the angle θ of the tilt of the field direction from the vertical. The points show the experimental data, and the solid curve shows $\cos\theta$.

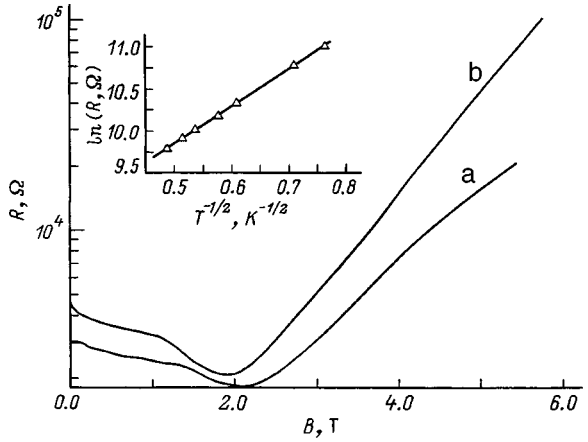

FIG. 5. Magnetoresistance of sample 6 at two temperatures *T*, K: 4.2 (a) and 1.7 (b). The inset shows the logarithm of the resistance vs $T^{-1/2}$ in a fixed magnetic field of $B=6$ T.

the resistance at two temperatures for sample 6, while the inset shows the $T^{-1/2}$ dependence of the resistance for the same sample at a fixed magnetic field of 6 T. The observed dependences are evidence of a metal–insulator transition in a magnetic field. No such transition is observed in *p*-type samples: In magnetic fields up to 10 T, the magnetoresistance remains positive and of moderate size.

4. CONCLUSIONS

In this paper we have discussed the optical and transport properties of multilayer InAs/GaAs structures with quantum dots, grown on substrates with a small disorientation angle relative to the [001] direction. A region with increased polarization is observed in the photoluminescence spectra in the plane of the layers.

It has been found that InAs quantum dots in GaAs form two-dimensional electron or hole layers for which the Shubnikov–de Haas effect is observed. The low-temperature conductivity of the structures possess anisotropy: The conductivity along the $[\bar{1}10]$ direction, i.e., along the steps, is greater than the conductivity in the perpendicular [110] direction. All these data are evidence that the dots are formed on a profiled surface predominantly along the steps. A strong localization of two-dimensional current carriers is detected at reduced temperature. As the magnetic field increases, a metal–insulator transition is observed in *n*-type samples at liquid-helium temperature.

This work was supported by the program ''The physics of solid-state nanostructures,'' Grant No. 97-1089, and by the Russian Fund for Fundamental Research, Grant No. 96-15-96500.

[1)]Measurements made by D. O. Filatov.

[1] H. Sakaki, G. Yusa, T. Someya, Y. Ohno, T. Noda, H. Akiyama, Y. Kadoya, and H. Noge, Appl. Phys. Lett. **67**, 3444 (1995).
[2] K. Imamura, Y. Sugiyama, Y. Nakata, S. Muto, and N. Yokoyama, Jpn. J. Appl. Phys. **34**, L1445 (1995).
[3] J.-Y. Marzin, J.-M. Gerard, A. Izrael, and D. Barrier, Phys. Rev. Lett. **73**, 716 (1994).
[4] H. Drexler, D. Leonard, W. Hansen, J. P. Kotthaus, and P. M. Petroff, Phys. Rev. Lett. **73**, 2252 (1994).
[5] T. Noda, M. R. Fahy, T. Matsusue, B. A. Joyce, and H. Sakaki, J. Cryst. Growth **127**, 783 (1993).
[6] D. Leonard, M. Krishnamurthy, C. M. Reaves, S. P. Den-Baars, and P. M. Petroff, Appl. Phys. Lett. **63**, 3203 (1993).
[7] D. Leonard, K. Pond, and P. M. Petroff, Phys. Rev. B **50**, 11 687 (1994).
[8] M. Grundmann, O. Stier, and D. Bimberg, Phys. Rev. B **52**, 11 969 (1995).
[9] B. N. Zvonkov, E. R. Lin'kova, I. G. Malkina, D. O. Filatov, and F. L. Chernov, JETP Lett. **63**, 439 (1996).
[10] J. M. Ziman, *Principles of the Theory of Solids* (Cambridge University Press, London, 1972).
[11] J. Ahopello, M. Sopanen, H. Lipsanen *et al.*, in Abstracts of the Second International Conference on Low Dimensional Structures and Devices, Lisbon, Portugal, 1997, O21.
[12] F. Lelarge, Z. Z. Wang, A. Cavanna, F. Laruelle, and B. Etienne, Europhys. Lett. **39**, 97 (1997).
[13] E. L. Ivchenko, A. Yu. Kaminskii, and U. Rossler, Phys. Rev. B **54**, 5852 (1996).
[14] I. G. Malkina, V. Ya. Aleshkin, B. N. Zvonkov, and Yu. N. Saf'anov, Phys. Low-Dim. Struct. **1/2**, 61 (1997).
[15] Y. Arakawa, in *Proceedings of the Twenty-Third International Conference on the Physics of Semiconductors*, Berlin, 1996, p. 1349.
[16] A. D. Visser, V. I. Kadushkin, V. A. Kul'bachinskiĭ, V. G. Kytin, A. P. Senichkin, and E. L. Shangina, JETP Lett. **59**, 363 (1994).
[17] V. A. Kul'bachinskiĭ, V. G. Kytin, V. I. Kadushkin, and A. P. Senichkin, Fiz. Tverd. Tela **37**, 2693 (1995) [Phys. Solid State **37**, 1481 (1995)].
[18] V. A. Kulbachinskii, N. B. Brandt, V. G. Kytin, V. I. Kadushkin, A. P. Senichkin, and E. L. Shangina, Phys. Low-Dim. Struct. **12**, 237 (1995).
[19] Y.-N. Yang, Y. S. Luo, and J. H. Weaver, Phys. Rev. B **46**, 15 387 (1992).
[20] I. P. Zvyagin, Phys. Status Solidi B **120**, 503 (1983).
[21] B. L. Altshuler and A. G. Aronov, in *Modern Problems in Condensed Matter Physics*, edited by A. L. Efros and M. Pollak (Elsevier, 1985), p. 1.
[22] P. A. Lee and T. V. Ramakrishnan, Rev. Mod. Phys. **57**, 287 (1985).

Translated by W. J. Manthey

AMORPHOUS, GLASSY AND POROUS SEMICONDUCTORS

Comparative study of the optical properties of porous silicon and the oxides SiO and SiO_2

A. N. Obraztsov and V. Yu. Timoshenko

M. V. Lomonosov Moscow State University, 119899 Moscow, Russia

H. Okushi and H. Watanabe

Electrotechnical Laboratory, Tsukuba, Ibaraki 305, Japan
(Submitted June 8, 1998; accepted for publication July 1, 1998)
Fiz. Tekh. Poluprovodn. **33**, 322–326 (March 1999)

The results of a comparative study of the optical absorption and photoluminescence in layers of porous silicon, silicon oxides (SiO and SiO_2), and powdered silicon are presented. It is found that the position of the absorption-band edge, determined from the data of photoacoustic spectroscopy and from photoluminescence spectra, correlates with the degree of oxidation of the silicon. Differences are detected in the frequency dependences of the photoacoustic signal for the porous silicon samples, depending on the quantum energy of the exciting light.
 [S1063-7826(99)01403-9]

INTRODUCTION

Despite the large number of publications (see, for example, the review article by Gullis *et al.*[1]) dealing with porous silicon (PS), the question of the nature of its optical properties is still imortant because of the extremely complex structure of this material. Since porous silicon is characterized by an enormous inner surface[2] (up to 600 m^2/cm^3), its optical properties depend not only on the parameters of the nanostructures but also on the composition of their surface coating.[3–5] In this connection, it is very important to determine the role of the various oxides that enter into the composition of this material. We have accordingly conducted a comparative study of the optical absorption and photoluminescence (PL) in samples of porous silicon films and powdered Si, SiO, and SiO_2. Here the light absorption was studied by a method based on the photoacoustic (PA) effect, which has demonstrated that it is highly effective for porous and powdered materials.[6–8]

EXPERIMENTAL PROCEDURE

In this study we have investigated layers of porous silicon formed on the surface of single-crystal *p*-type silicon wafers with a resistivity of 10 $\Omega\cdot$cm and a surface orientation of (100). An anodization process in an HF (50%) : $C_2H_5OH = 1:1$ solution with a current density of 30 mA/cm^2 for 5 min was used to obtain the porous silicon. After electrochemical processing, the samples were rinsed in ethanol and dried in air. The measurements were made after holding the samples in air for several weeks. The thickness of the porous layer, measured with an optical microscope on a transversely sheared surface, was about 15 μm. The porosity, determined by gravimetric measurements, was about 80%. Visually the porous silicon was a mirror-smooth, uniformly colored film on the surface of the silicon wafer.

We also used powdered Si (99.99%, produced by the firm f-Chemical), SiO (99.9%, produced by Nacalai Tesque Inc.), and SiO_2 (99.995%, produced by Aldrich Chemical Co.).

The photoluminescence was measured at room temperature, with excitation by the radiation of a He–Ne laser (633 nm), using a Renishaw spectrometer.

As was already pointed out, the photroacoustic (PA) effect was used to obtain the optical absorption spectra; this causes a PA signal to appear with an amplitude proportional to the absorption coefficient of the light.[6] A fundamental feature of this method, which makes it especially effective for studying porous layers, is that it makes it possible to obtain the absorption spectrum without separating the porous-silicon film from the opaque silicon substrate. A modernized PA spectrometer made by Princeton Applied Research Corp. (Model 6001) was used for the measurements. They were made at room temperature in the spectral range from 200 to 1500 nm, with a step of 2 nm. A mechanical interrupter was used to modulate the light beam in the frequency range from 20 to 5000 Hz. To allow for the spectral distribution of the radiation of the light source (a superhigh-pressure xenon lamp with a grating monochromator), the spectral dependences of the PA signal amplitude, recorded at the chosen modulation frequency of the light, were normalized to the PA spectrum obtained at the same frequency for a sample of carbon black. The absorption spectrum of the latter can be considered to coincide with that of an absolute blackbody.[6]

Bearing in mind that the logarithm of the PA signal amplitude depends linearly on the logarithm of the modulation

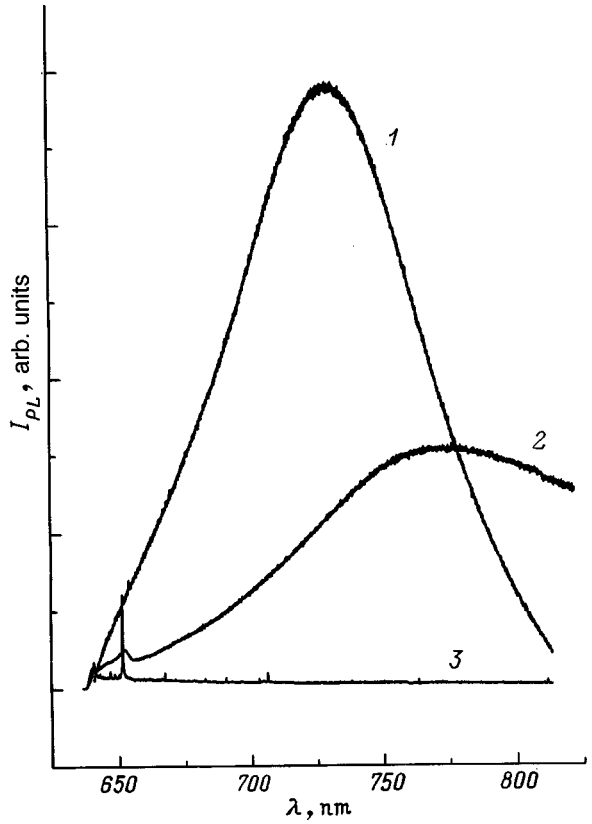

FIG. 1. Photoluminescence spectra $I_{PL}(\lambda)$ for porous silicon (*1*) and the oxide SiO (*2*), along with the spectrum of silicon dioxide SiO_2 (*3*), recorded under the same conditions.

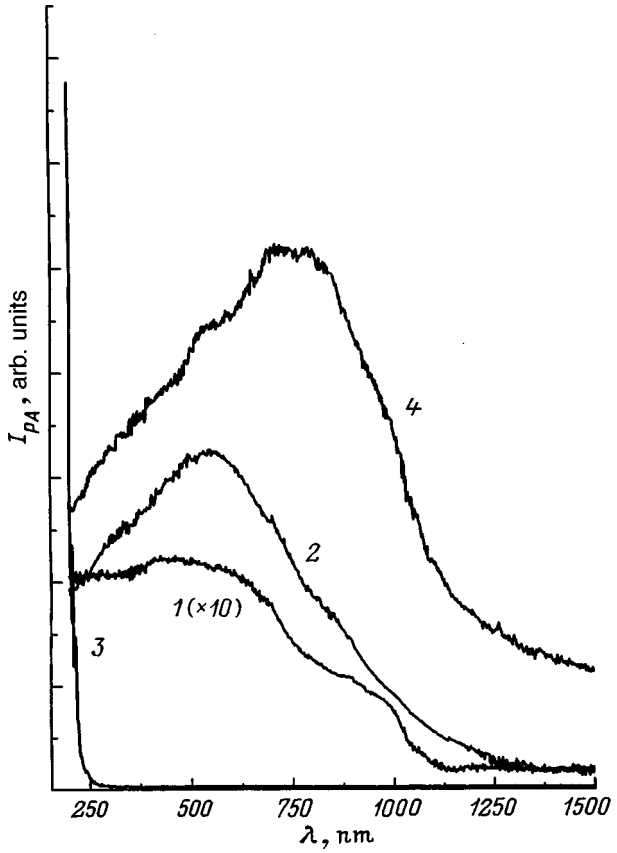

FIG. 2. Spectral dependences of the PA signal amplitude $I_{PA}(\lambda)$ for porous silicon (*1*) and the oxides SiO (*2*) and SiO_2 (*3*), as well as for powdered Si (*4*), recorded with the light modulated at 90 Hz.

frequency with high accuracy for carbon black,[6] the frequency characteristics were determined for the recording system, including a sensitive microphone and suitable amplifiers. The frequency characteristics thus obtained were used to normalize the experimental dependences of the PA signal amplitude on the modulation frequency.

RESULTS AND DISCUSSION

Appreciable PL from all the test objects was recorded for layers of PS and for the oxide SiO. The corresponding spectra are shown in Fig. 1, along with the spectrum recorded for SiO_2 powder. The maximum PL intensity was at about 730 nm for PS and about 770 nm for SiO. Moreover, there is a relatively weak line in the region of 650 nm in the spectrum of the SiO powder (Fig. 1, curve *2*); this is the 480-cm^{-1} Raman line characteristic of Si–O–Si bonds and of Si–Si bonds in amorphous silicon.[9] A line with a similar spectral position was also recorded for the SiO_2 powder (Fig. 1, curve *3*).

The similarity of the PL spectra for the PS layers and the SiO samples, in our opinion, is evidence that the optical properties of these materials are interrelated. For example, this can be because silicon clusters of nanometer dimensions are present in both materials. Such clusters, as is well known,[1] are characteristic of high-porosity PS. For the SiO samples, the silicon clusters can most likely be associated with regions of disturbed stoichiometry. Such regions can be regarded as defect-localization sites in the mobility gap of the amorphous material. Such defects either simply ''heal up,'' or the corresponding energy transitions shift toward higher energies with further oxidation of the silicon and formation of SiO_2. They consequently cannot be excited by the 633-nm radiation used in this project, as is evidenced by the absence of appreciable PL for the SiO_2 samples used here.

Figure 2 shows the spectral dependences of the PA signal amplitude $I_{PA}(\lambda)$, recorded at the light-modulation frequency of 90 Hz. The significant difference in the PA signal amplitude for the powdered samples and the thin films of PS is explained by the mechanism of the PA effect. As a result, the main contribution to I_{PA} comes from the energy of the light absorbed at a depth approximately equal to the thermal diffusion length $\mu=[2k/(2\pi\nu\rho C)]^{1/2}$, where k is the thermal conductivity, C is the specific heat, ρ is the density of the test material, and ν is the modulation frequency. For the powdered materials, the thermal diffusion length at low modulation frequencies undoubtedly exceeds the absorption depth of the light, while the thickness of the sample, which here is determined by the thickness of the layer of powder in the measurement cell and was about 2 mm in our experiments, exceeds the thermal diffusion length. In the PS, the film thickness at the same frequencies is significantly less than thermal diffusion length, and this appreciably reduces the PA signal amplitude. For the same reason, the spectra of the PS (Fig. 2, curve *1*) contains two characteristic spectral features, one of which, in the region of 750 nm, corresponds

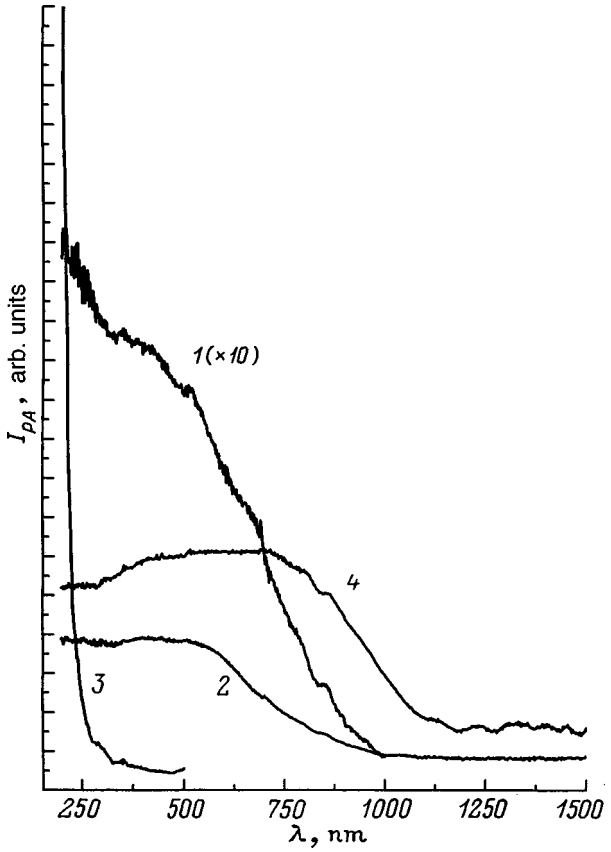

FIG. 3. Spectral dependences of the PA signal amplitude $I_{PA}(\lambda)$ for porous silicon (*1*) and the oxides SiO (*2*) and SiO_2 (*3*), as well as for powdered Si (*4*), recorded with the light modulated at 1.5 kHz.

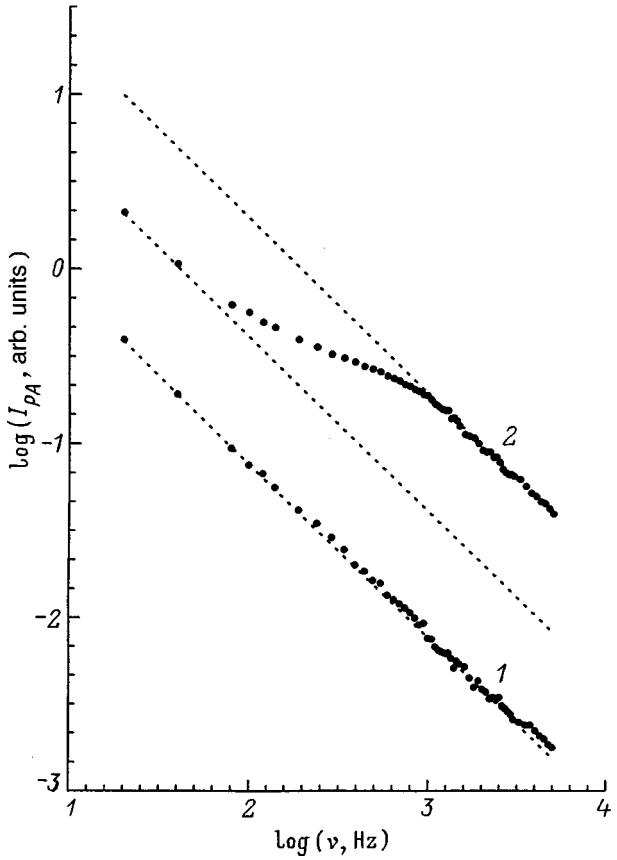

FIG. 4. Frequency dependence of the PA signal amplitude for porous silicon in log–log coordinates, excited by light with wavelength 900 nm (*1*) and 300 nm (*2*). The dotted lines show the dependence $I_{PA} \sim 1/\nu$.

to the edge of the absorption band in the porous layer, while the other, at about 1100 nm, corresponds to the fundamental absorption edge in single-crystal silicon.[7]

The spectral behavior of the $I_{PA}(\lambda)$ dependence for Si, SiO, and SiO_2 powders corresponds to the well-known absorption spectra of these materials,[10] with the exception of the appreciable reduction in amplitude of the PA signal for Si and SiO in the visible region as the wavelength decreases. This feature of the PA spectra can be caused by the significant scattering of light when it propagates in a powdered material. The efficiency of such scattering increases as the wavelength decreases, and also as a consequence of the increased specular reflectance from the faces of the individual powder particles, analogous to that in diamond powders.[8]

The above considerations are confirmed by the shape of the spectral dependences $I_{PA}(\lambda)$ obtained for the same materials at a higher modulation frequency (1500 Hz) (see Fig. 3). First, because the ratio of the PS film thickness to the thermal diffusion length changes, the relative amplitude of the PA signal increases. The spectral feature in the 1100-nm region caused by the single-crystal silicon substrate is absent in the PA spectrum for PS (curve *1*). This means that the thermal diffusion length does not exceed the thickness of the porous layer (15 μm). There is a similar explanation for the absence of an appreciable decrease of the PA signal amplitude for the Si and SiO powders in the short-wavelength region. For high frequencies, the thermal diffusion length is comparable to the size of the powder particles, and this reduces the number of faces through which the light passes and is then scattered.

A certain increase in the PA signal amplitude for PS in the UV region should be pointed out. This occurs apparently because the porous film contains oxides of the type of SiO_x, with $x \approx 2$. Such a possibility has been repeatedly noted in the literature (see, for example, Refs. 3–5). A comparison of the $I_{PA}(\lambda)$ spectra obtained for PS at different modulation frequencies suggests that the distribution of the various silicon oxides over the film thickness is inhomogeneous and that the film composition near the surface is closer to SiO_2.[10] Such a variation of the optical absorption over depth correlates with the PL properties of PS, for which direct measurements were used to establish a significant decrease of the quantum efficiency with distance from the outer surface of the PS film.[11]

The dependence of the PA signal on the modulation frequency mentioned above makes it possible to determine one of the most important physical parameters of PS films—the thermal conductivity k. We made a rough estimate of k in an earlier paper[7] on the basis of PA measurements. We studied[7] in more detail the frequency dependence of the PA signal for PS, the results of which are presented in Fig. 4 in log–log coordinates. For most cases encountered in practice, the PA signal amplitude is inversely proportional to the modulation frequency ν,[6,8] and this was recorded for all the powder

samples of Si, SiO, SiO_2 and for single-crystal silicon, regardless of the spectral content of the exciting light. The same inversely proportional dependence on frequency was obtained for PS samples when we used IR radiation (900 nm), which was transmitted through the porous layer and absorbed in the substrate curve *1* in Fig. 4). For shorter-wavelength radiation (300 nm), which is efficiently absorbed in the PS film (curve *2* in Fig. 4), a linear behavior of the $\log(I_{PA})$ dependence on $\log(\nu)$ is observed in the initial section (in the low-frequency region) and for ν greater than 1 kHz.

As pointed out above, the PA signal amplitude is determined by the amount of heat given off as a result of the absorption of light at a depth of the order of the thermal diffusion length μ. Most of the UV radiation is absorbed in a thin film of PS, but, at low modulation frequencies, the heat propagates into the depth of the crystal substrate, which has thermophysical parameters different from the PS and which determines the value of the PA signal in this case. As the modulation frequency increases, the thermal diffusion length gradually decreases and evidently becomes comparable with the thickness of the porous layer (15 μm) at a frequency of about 1 kHz. A further increase of the frequency produces the linear dependence of $\log(I_{PA})$ on $\log(\nu)$ characteristic of homogeneous materials. When IR radiation is used, the character of the frequency dependence is determined by the absorption depth of the light, for which the PS film is virtually transparent.

Starting from the known porosity of the PS of 80%, as well as from tabulated data for the density $\rho = 2.328\ \mathrm{g/cm^3}$ and the specific heat of silicon $C = 0.7\ \mathrm{J/(g \cdot K)}$, we find that, in accordance with the expression for the thermal diffusion length μ, the thermal conductivity of the porous silicon is about $k \approx 1.2\ \mathrm{W/(m \cdot K)}$, which is somewhat greater than the value we obtained in Ref. 7, because of the more accurate method. This estimate does not allow for the inhomogeneity of the PS in composition. The extremely low thermal conductivity is of interest from the viewpoint of the practical use of PS, as well as for the correct interpretation of the data of various studies involving methods that cause the porous layer to be heated, as is the case, for example, in studying Raman scattering.[12]

The data concerning optical absorption obtained by PA spectroscopy and the results of our study of PL in samples of PS and the oxides SiO and SiO_2 thus show that there is a definite correlation of the degree of oxidation of the silicon and the optical properties of the porous layer. It seems most likely that both the silicon matrix and the oxide components of the surface coating are responsible for forming the absorption spectrum of PS. The luminescence properties of PS depend on various defects in the nonstoichiometric oxide SiO_x.

One of the authors (A. N. Obraztsov) would like to express his appreciation to the International Matsumae Foundation for providing a stipend, because of which this work was possible. Another author (V. Yu. Timoshenko) wishes to thank the Russian State Scientific–Technical Program ''The physics of solid-state nanostructures'' for financial support of a part of this study.

[1] A. G. Gullis, L. T. Canham, and P. D. J. Calcott, J. Appl. Phys. **82**, 909 (1997).
[2] G. Bomchil, A. Halimaouri, and R. Herino, Appl. Surf. Sci. **41/42**, 604 (1989).
[3] N. E. Korsunskaya, T. V. Torchinskaya, B. R. Dzhumaev, B. M. Bulakh, O. D. Smiyan, A. L. Kapitanchuk, and S. O. Antonov, Fiz. Tekh. Poluprovodn. **30**, 1507 (1996) [Semiconductors **30**, 792 (1996)].
[4] W. E. Carlos and S. M. Prokes, J. Vac. Sci. Technol. B **13**, 1653 (1995).
[5] H. Tamura, M. Rückschloss, T. Wirschem, and S. Vepřek, Thin Solid Films **255**, 92 (1995).
[6] A. Rosencwaig, *Photoacoustics and Photoacoustic Spectroscopy* (Wiley & Sons, New York, 1980), p. 95.
[7] A. N. Obraztsov, H. Okushi, H. Watanabe, and V. Yu. Timoshenko, Fiz. Tekh. Poluprovodn. **31**, 629 (1997) [Semiconductors **31**, 531 (1997)].
[8] A. N. Obraztsov, I. Yu. Pavlovsky, T. Izumi, H. Okushi, and H. Watanabe, Appl. Phys. A: Mater. Sci. Process. **65**, 505 (1997).
[9] F. L. Gakeener and A. E. Geissberg, J. de Phys C9, **43**, 343 (1982).
[10] H. R. Philipp, J. Phys. Chem. Solids **32**, 1935 (1971).
[11] A. N. Obraztsov, V. A. Karavanskiĭ, H. Okushi, and H. Watanabe, Poverkhnost', No. 1, 64 (1998).
[12] V. A. Karavanskiĭ and A. N. Obraztsov, Fiz. Tekh. Poluprovodn. **29**, 582 (1995) [Semiconductors **29**, 302 (1995)].

Translated by W. J. Manthey

Photosensitive structures based on porous silicon

É. B. Kaganovich, É. G. Manoĭlov, and S. V. Svechnikov

Institute of Semiconductor Physics, National Academy of Sciences of Ukraine, 252650 Kiev, Ukraine
(Submitted June 15, 1998; accepted for publication July 1, 1998)
Fiz. Tekh. Poluprovodn. **33**, 327–331 (March 1999)

The electrical and photoelectric properties of two types of sandwich structures are discussed: Al/porous silicon/single-crystal silicon (c-Si)/Al with thin and thick layers of porous silicon, obtained by chemical coloration etching without applying an electric field. It is established that the properties of the structures with thin porous silicon layers are determined by the porous-silicon–c-Si heterojunction. Its properties are explained in terms of an energy-band diagram of an isotypic heterojunction with opposite directions of band bending on the two sides of the junction, caused by the appearance of local states at the boundary. The photosensitivity of the structures with a thick porous silicon layer is determined by the photoconductivity of the porous silicon. The maximum of the spectral dependence of the photoconductivity of the porous silicon layers is at 400–500 nm. These results are compared with those known for structures based on porous silicon obtained by anodization. © *1999 American Institute of Physics.*
[S1063-7826(99)01503-3]

INTRODUCTION

Porous silicon (PS) continues to attract attention because of its potential for creating visible radiation sources and for integrating photo- and microelectronics elements based on silicon technology. Despite intensive studies of PS, because of its complexity, even the mechanisms of visible photoluminescence (PL) have not been definitively explained. The photoelectric properties of PS have only begun to be studied.[1–23] Photoelectric phenomena are also an effective means of studying electronic processes and of establishing the energy-band diagrams of structures. In addition to the use of PS for radiation sources, there is also interest in using it for photodetectors.

Papers devoted to the study of the photoelectric properties of PS have discussed the photoconductivity (PC) of free layers of PS,[1] the PC of the PS layers in M/PS/c-Si/M structures (M=metal and c-Si=single-crystal silicon),[2–4] the frozen (residual) PC of PS layers,[5] the photodiode properties of M/PS/c-Si/M structures,[2,4,6–16] their photovoltaic properties,[17,18] the photoelectromotive force and photoinduced charge capture in PS,[18–21] and the position-sensitive photovoltaic effect.[22,23] Known photosensitive structures are usually sandwich-type M/PS/c-Si/M structures in which the PS layer, from several micrometers to about 100 μm thick, is formed by electrochemical etching of c-Si. Etching mechanisms for anodization without the application of a field are similar in principle, and PS layers obtained by these two methods possess similar visible PL at room temperature. However, chemical coloration etching is simpler, does not require the use of special apparatus, and is a less rough process, which makes it possible to obtain thin PS layers (less than 1 μm thick) that are more homogeneous in thickness and have a smoother surface.[24,25] In this paper we report the results of an experimental study of the properties of photosensitive Al/PS/p-Si/Al structures in which the PS layers are formed by coloration chemical etching without applying a field. Our goal was to study the electrical and photoelectric properties of such structures, to compare the results with those for known structures based on PS obtained by anodization, and to analyze them in terms of accepted energy-band diagrams of the structures.

SAMPLES AND EXPERIMENTAL TECHNIQUE

Photosensitive sandwich-type M/PS/c-Si/M structures can display the properties of the M/PS Schottky barrier, of the PS itself, and of the heterojunction (HJ) PS/c-Si. The approach that we used to overcome the complications associated with these properties in establishing the photosensitivity mechanism involved the use of a thin, low-resistance PS layer, in which the bias is predominantly applied to the HJ and its properties are determined by the properties of the structure, and the case of a thick, high-resistance PS layer, in which the external applied voltage predominantly falls on the PS and the properties of the structure are given by the PS layer.

Substrates of p-type (100) Si with a resistivity of $10\,\Omega\cdot$cm served as the starting samples. They were dipped into an $HF:HNO_3:H_2O=1:3:5$ (by volume) solution. The reagents used were 49% HF and 70% HNO_3. The etching time was as much as 10–15 min, while the layer thicknesses were less than 1 μm (thin PS layers). Thick PS layers were obtained by chemically etching p-Si subjected to preliminary modification by pulses from a YAG laser operating in the free-lasing regime (wavelength $\lambda=1.06\,\mu$m, energy per pulse $E_1=0.3$ J, pulse width $t_i=2\times10^{-4}$ sec).[26] The laser beam was focused by an SOK-1 optical unit and was displaced over the surface of the silicon wafer using a given pattern. Since the etching rates of the laser-recrystallized sili-

con exceeded those for unirradiated silicon, this allowed us to use not only a nonphotolithographic method to shape the topology of the PS layers, but also to obtain thick (more than 1 μm) PS layers. A comparison of the PS layers was monitored by additional processing, for example, dehydration, etc.

When they were excited with nitrogen laser radiation, the PS layers possessed visible PL with a maximum at 650–750 nm. The maximum of the PL excitation spectrum was at 300 nm. The PL relaxation spectra displayed fast, short-wavelength bands and slow, long-wavelength bands;[27] i.e., the PL properties of these layers are similar to those of PS obtained by anodization.

To form sandwich structures, an aluminum film was sputtered onto the PS surface, with a contact area of about 1 mm^2. An ohmic contact to the substrate was created by baking the aluminum into the *p*-Si.

Measurements were made of the static I–V characteristics in the dark and in the light and the dynamic I–V characteristics, as well as the spectral dependences of the sensitivity of the structure when a reverse bias was applied and in the open-circuit regime. The I–V characteristics were measured on an automatic apparatus based on a Poisk-1.02 computer. The voltage across the sample was supplied from a V5-47 dc source having digital control, and was monitored by a V5-34A digital voltmeter. The range of supplied voltages was 0–30 V, and the measured currents were 5×10^{-11}–1×10^{-2} A. The voltage was varied over a rising and falling stepwise dependence with a step of 0.1 V, with various step widths (0.1 and 10 sec) and an interval between them of 200 ns.

RESULTS AND DISCUSSION

In structures with a low-resistance PS layer, the I–V characteristics in the dark (Fig. 1a, curve *1*) have a rectifying character. The ratio of the currents in the forward and reverse directions for several volts of applied bias reaches about 10^5. The positive axis of the I–V characteristic (forward voltage) corresponds to positive bias applied to the *p*-Si. A distinctly expressed saturation is always observed on the reverse branch. An analysis of the forward branch reveals that the base resistance of the PS layer is several kΩ and the nonideality factor for moderate biases is $n=2-3$. Signs of a ''soft'' breakdown of the HJ appear on the forward branch in a number of samples: A small saturation section is followed by a section with a sharp increase of the current (see the inset in Fig. 1a).

Under illumination, the I–V characteristic (Fig. 1a, curve *2*) has a typical photodiode character. The ratio of the currents in the light (about 1×10^{-2} W/cm^2) and in the dark with a few volts of reverse bias is 2–3 orders of magnitude. As the reverse bias is increased, the photocurrent increases very slowly. The open-circuit voltage is 0.25–0.3 V, and its sign corresponds to depletion bending of the bands of *p*-Si.

On the dynamic I–V characteristics, the forward branches display hysteresis loops (see the inset in Fig. 1c). The I–V characteristics measured as the voltage was varied in an increasing direction lie lower than those recorded with the voltage decreasing, which indicates the appearance of

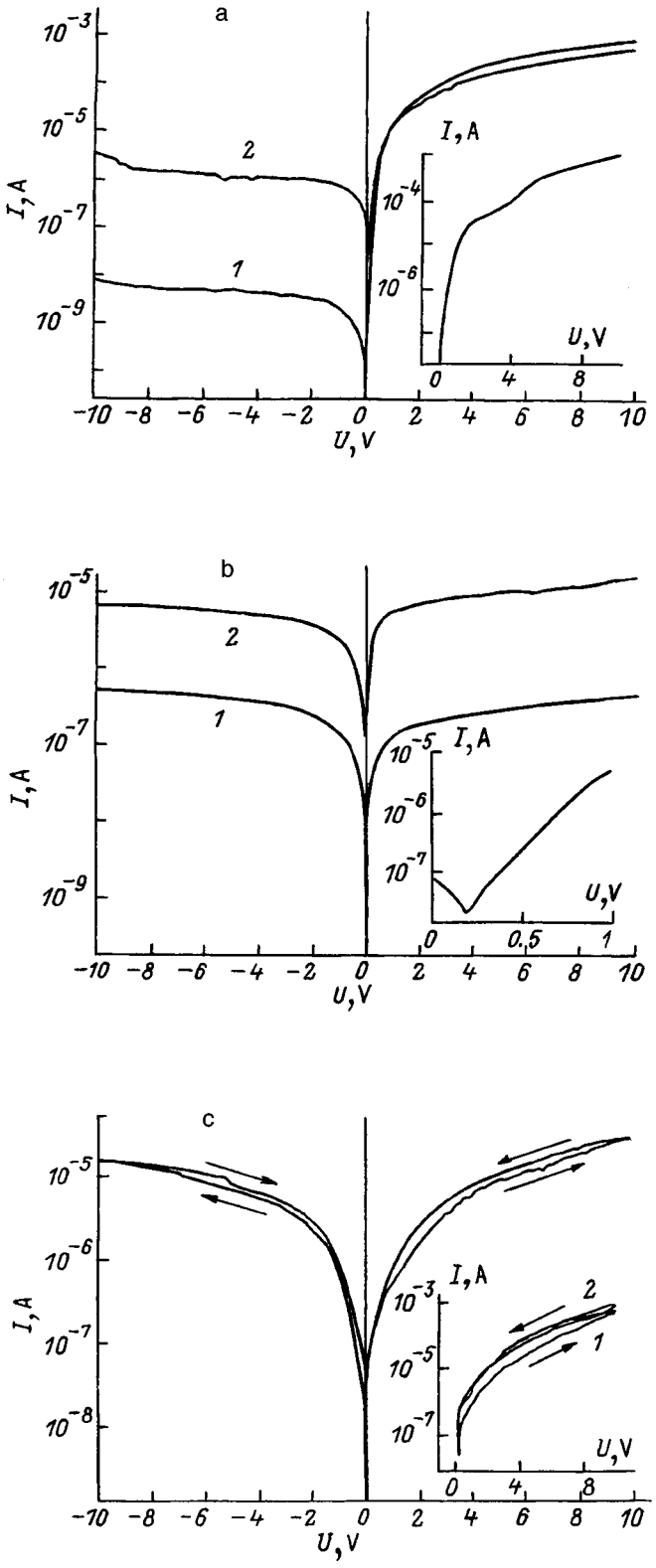

FIG. 1. The I–V characteristics of Al/PS/*c*-Si/Al structures: static (a) and (b), dynamic (c), with a thin PS layer (a) and a thick PS layer (b) and (c), in the dark (*1*) and in the light (*2*). The insets show the branch of the I–V characteristic in the dark with a section of the saturation and the region of ''soft'' breakdown (a), the branch of the I–V characteristic in the light with a section of the dip (b), and the dynamic I–V characteristics for a structure with a thin PS layer (c).

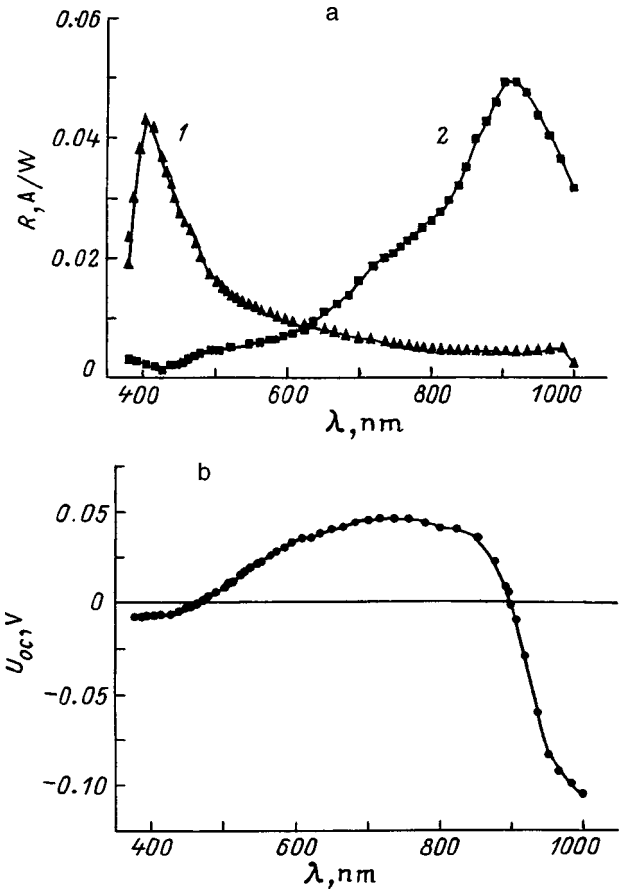

FIG. 2. (a) Spectral dependences of the sensitivity of Al/PS/*c*-Si/Al structures with a thick (*1*) and a thin (*2*) PS layer. (b) Photoresponse spectrum of a structure with a thin PS layer, measured in the open-circuit regime.

slow capture centers for holes. No hysteresis is observed on the reverse branches of the I–V characteristics.

The spectral sensitivity characteristic has a maximum at about 900 nm (Fig. 2a, curve *2*) and is similar to the spectral sensitivity of Si photodiodes. This is evidence that the radiation is predominantly absorbed in the *p*-Si. The sensitivity reaches about 0.1 A/W. As the transparency of the front aluminum contact increases, the quantum yield at the maximum sensitivity is high, approaching unity.

On the spectral sensitivity curves measured in the open-circuit regime, the photoresponse changes sign in the short-wavelength and long-wavelength regions (Fig. 2b).

In structures with a high-resistance PS layer, the I–V characteristic in the dark is symmetric and nonlinear (Fig. 1b). The ratio of the currents in the light (about 10^{-2} W/cm^2) and in the dark is one or two orders of magnitude and is independent of the polarity of the applied voltage. Several sections of the I–V characteristics in the light display dips, which are evidence of the appearance of a built-in electric field (see the inset in Fig. 1b). Hysteresis loops, which indicate hole capture in slow traps, are detected in the forward and the reverse branches of the dynamic I–V characteristics (Fig. 1c). The spectral dependence of the sensitivity is characterized by a maximum in the short-wavelength region at 400–500 nm (Fig. 2a, curve *1*).

We have analyzed the results in terms of a model which

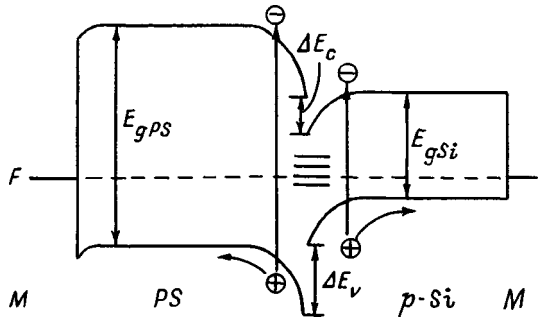

FIG. 3. Energy-band diagram of the *p*-PS/*p*-Si HJ.[11,32]

disregards the appearance of an Al/PS Schottky barrier. Preliminary measurements of the I–V characteristics of test structures with various metal films (Al, Cu, In, Au) deposited on the thick and the thin PS layers displayed no dependence of the parameters of the M/PS Schottky barrier on the type of metal. This occurs evidently because the Fermi level is pinned as a result of the high density of surface electronic states. A similar character of the M/PS boundary was observed in Ref. 15, where the sputtering of Ca, Mg, Sb, and Au revealed that only the series resistance depended on the type of metal, with this dependence showing up at high biases. The results of an analysis of the I–V characteristics and the voltage–capacitance characteristics of the structures allowed Peng *et al.*[16] to ignore the band bending of the PS at the M/PS boundary. When photosensitive Al/PS/*p*-Si/Al structures were studied in Refs. 11 and 12, it was thus considered possible to regard the Al/PS contact as slightly rectifying. However, rectifying properties of this contact were detected in many papers on the charge-carrier transport and electroluminescence of PS-based structures and in some on their photoelectric properties. For example, in analyzing the current-conduction mechanism in an Al/PS/*c*-Si/Al structure in Ref. 28, they considered a model that included two barriers: the Al/PS contact barrier and the HJ, which were connected facing each other, but for structures in which there was no saturation on the reverse branch of the I–V characteristic. In this study the reverse branch of the I–V characteristic was considered a Schottky barrier, and the conductivity of the structure had a bipolar character. We should note that the contact-injection phenomena in PS and their connections with the conditions under which the M/PS structures are obtained have only begun to be studied.

The results of the study of a structure with a thin PS layer presented above can be explained in terms of the energy-band diagram of the isotypic HJ between the broad-band PS (2–3 eV) and the *c*-Si (1.1 eV) with close-lying carrier concentrations, with allowance for the states at the interface (Fig. 3).[29,30] Such a diagram for a model of an HJ in the form of two Schottky barriers connected facing each other was proposed in Ref. 11 for the analysis of the sensitivity of photodiode structures based on the HJ *p*-PS/*p*-Si. Actually, such a model is characterized by saturation of the I–V characteristics in both directions (the saturation section in the forward direction can also be indistinct because of a ''soft'' breakdown of the barrier on the side of the broad-band semi-

conductor) and heteropolar photoresponses, as has been observed experimentally.

When the quantum energy of the incident radiation is greater than the band gap of the *p*-Si but less than that of the PS, the radiation is absorbed in the *p*-Si, and the sign of the photoresponse is determined by the charge of the holes moving according to the depletion band bending from the interface of the HJ to the ohmic contact (positive photoresponse, see Figs. 2b and 3). As the quantum energy of the incident radiation increases to values corresponding to the energy gap of the PS, holes are photogenerated in the PS. The negative photoresponse in the short-wavelength region, which is associated with the motion of these photoholes from the boundary of the HJ into the depth of the PS, correlates with the opposite sign of the Schottky barrier on the side of the PS. The negative photoresponse in the long-wavelength region can be associated with the photoexcitation of carriers from surface electron states caused by interface traps or with optical transitions from the valence band of the PS into the conduction band of the *c*-Si. Note that these surface electron states are fast traps for holes, whereas slow traps with a relaxation time of about 1 sec appear in the hysteresis loops of the dynamic I–V characteristics.

A similar hysteresis effect and heteropolar photoresponses were observed earlier[12] for Al/PS/*p*-Si/Al structures. However, the reverse current of the I–V characteristics increased linearly with increasing bias for these structures, while the forward current was extrapolated by an exponential dependence. Laptev *et al.*[12] interpreted the results in terms of a model of an isotypic HJ whose energy-band diagram contains peaks and dips.

In studying photoinduced charge capture in PS, Matveeva *et al.*[19] detected a component of the photoelectromotive force associated with the depletion region in *p*-Si at the boundary with the PS and established the presence of slow states on the surface of the voids.

The results of the study of structures with a thick PS layer show that their photosensitivity is determined by the PC of the PS. Taking into account the PL properties of the layers, these results make it possible to draw the energy-band diagram, which includes quantum-well *c*-Si nanocrystallites with local states in the quantum well and barrier layers of SiO_xH_y in which, depending on the conditions under which the PS is formed, there is a variation in the composition and accordingly in the height of the potential barriers. The radiation absorption is determined by optical transitions between local states of the *c*-Si nanocrystallites and between them and delocalized states of the barrier layers.

The carriers that participate in the PC drift; i.e., those that participate in geminal radiative recombination and in radiative recombination at the surface states of the crystallites are eliminated, and therefore the quantum yield of the PC is small. It thus follows that the requirements for increasing the PL and the PC intensities are opposite. To increase the PL intensity, it is necessary to restrict the flow of carriers out of the Si nanocrystallites; conversely, to increase the PC intensity, it is necessary to lower the potential barriers that restrict the current transfer. Since the charge-carrier mobilities are low in PS [they do not exceed 10^{-2}–10^{-3} $cm^2/(V \cdot sec)$; Ref. 31], and since the product of the drift mobilities by the charge-carrier lifetime is $\mu \cdot \tau \sim 10^{-10}$ cm^2/sec (Ref. 33), the drift length of the carriers is no more than 1 μm even for large electric fields. Therefore, thin PS layers should be used to increase the charge-carrier collection factor.

The key questions regarding the PC of the PS layers are as follows: through what region do the charge carriers flow, and what is their transport mechanism? Since PS is a nanocomposite that contains segments of quantum filaments and quantum dots of *c*-Si in a host of porous hydrated silicon oxide, the transport mechanism can involve charge-carrier tunneling through the barriers between the silicon nanocrystallites and the flow of carriers injected from the silicon nanocrystallites along the interface regions and the barrier layers. The regions of flow and the transport mechanisms depend not only on the conditions under which the layers are obtained and consequently their microstructure, but also on the conditions under which the PC is measured: the excitation levels, the temperature, and the electric field. The transport properties and the PC of PS layers have only begun to be studied.

In summary, we have investigated the I–V characteristics and the spectral characteristics of the photoresponses of Al/PS/*c*-Si/Al structures in which, in contrast with the previously reported studies, the PS layers are obtained by chemical etching without applying a field. It has been shown that not only PL properties but also electrical and photoelectric properties similar to those in structures based on PS formed by anodization can be obtained more simply in such structures. Attention has been focused on the effectiveness of designing electrical instruments that use structures based on thin PS layers (less than 1 μm thick) obtained simply by chemical etching, which are more homogeneous and have a smooth surface and lower leakage currents. It has been established that the photodiode properties of the structures are determined by the isotypic *p*-PS/*p*-Si HJ, taking into account the appearance of local states at the interface. The photosensitivity of the structures, in which the properties of the M/PS barriers and the PS/*c*-Si HJs do not manifest themselves, is determined by the PC of the PS, whose maximum spectral dependence lies in the range 400–500 nm. The appearance of slow traps in the PS layers has been detected from the hysteresis loops of the I–V characteristics.

[1] P. Hlimonaz, O. Klima, A. Hospodková, E. Hulicius, J. Oswald, E. Šipek, and J. Kočka, Appl. Phys. Lett. **64**, 3118 (1994).
[2] T. Ozaki, M. Araki, S. Yoshimura, H. Koyama, and N. Koshida, J. Appl. Phys. **76**, 1986 (1994).
[3] M. J. Heben and Y. S. Tsuo, MRS Symp. Proceedings 283 (1993).
[4] A. Dafinei, G. Cracium, C. Flueraru, C. Sargentis, and E. Niculescu, in CAS'97 Proceedings of the 1997 International Semiconductor Conference, Sinaia, Romania, 1997, p. 189.
[5] W. H. Lee, H. Lee, and C. Lee, J. Non-Cryst. Solids **164–166**, 965 (1993).
[6] J. P. Zheng, K. L. Jiao, W. P. Shen, W. A. Anderson, and H. S. Kwok, Appl. Phys. Lett. **61**, 459 (1992).
[7] H. Shi, Y. Zheng, Y. Wang, and R. Yuan, Appl. Phys. Lett. **63**, 770 (1993).
[8] L. V. Belyakov, D. N. Goryachev, O. M. Sreseli, and I. D. Yaroshetskiĭ, Fiz. Tekh. Poluprovodn. **27**, 1371 (1993) [Semiconductors **27**, 758 (1993)].
[9] L. Z. Yu and C. R. Wie, Sens. Actuators A **39**, 253 (1993).

[10] C. Tsai, K.-H. Li, J. C. Campbell, and A. Tasch, Appl. Phys. Lett. **62**, 2818 (1993).
[11] L. A. Balagurov, D. G. Yarkin, G. A. Petrovicheva, E. A. Petrova, A. F. Orlov, and S. Ya. Andryushin, J. Appl. Phys. **82**, 4647 (1997).
[12] A. N. Laptev, A. V. Prokaznikov, and N. A. Rud', Pis'ma Zh. Tekh. Fiz. **23**, 59 (1997) [Tech. Phys. Lett. **23**, 113 (1997)].
[13] E. V. Astrova, A. A. Lebedev, A. D. Remenyuk, V. Yu. Rud', and Yu. V. Rud', Fiz. Tekh. Poluprovodn. **31**, 159 (1997) [Semiconductors **31**, 121 (1997)].
[14] V. Yu. Rud' and Yu. V. Rud', Fiz. Tekh. Poluprovodn. **31**, 245 (1997) [Semiconductors **31**, 197 (1997)].
[15] N. J. Pulsford, G. L. J. A. Rikken, Y. A. R. R. Kessener, E. J. Lous, and A. H. J. Venhuizen, J. Lumin. **57**, 181 (1993).
[16] C. Peng, K. D. Hirschman, and P. M. Fauchet, J. Appl. Phys. **80**, 295 (1996).
[17] G. Smestad, M. Kunst, and C. Vial, Sol. Energy Mater. Sol. Cells **26**, 277 (1992).
[18] Yu. A. Vashptanov, Pis'ma Zh. Tekh. Fiz. **23**, 77 (1997) [Tech. Phys. Lett. **23**, 43 (1997)].
[19] A. B. Matveeva, E. A. Konstantinova, V. Yu. Timoshenko, and P. K. Kashkarov, Fiz. Tekh. Poluprovodn. **29**, 2180 (1995) [Semiconductors **29**, 1142 (1995)].
[20] P. K. Kashkarov, E. A. Konstantinova, A. V. Petrov, A. V. Petrukhin, and V. Yu. Timoshenko, Poverkhnost' Fiz. Khim. Mekh. **6**, 75 (1994).
[21] A. V. Petrov and A. V. Petrukhin, Fiz. Tekh. Poluprovodn. **28**, 82 (1994) [Semiconductors **28**, 49 (1994)].
[22] C. C. Yeh, K. Y. J. Hsu, L. K. Samanta, P. P. Chen, and H. L. Hwang, Appl. Phys. Lett. **62**, 1617 (1993).
[23] D. W. Boeringer and R. Tsu, Appl. Phys. Lett. **65**, 2332 (1994).
[24] R. W. Fathauer, T. George, A. Ksendzov, and R. P. Vasquez, Appl. Phys. Lett. **60**, 995 (1992).
[25] J. Sarathy, S. Shih, Kin Jung, C. Tsai, K.-H. Li, D.-L. Kwong, J. C. Campbell, Shueh-Li Yau, and A. J. Bard, Appl. Phys. Lett. **60**, 1532 (1992).
[26] S. V. Svechnikov, L. L. Fedorenko, E. B. Kaganovich, A. D. Sardarly, S. P. Dikiĭ, and S. V. Baranets', Ukr. Fiz. Zh. **39**, 704 (1994).
[27] L. L. Fedorenko, A. D. Sardarly, É. B. Kaganovich, S. V. Svechnikov, S. P. Dikiĭ, and S. V. Baranets, Fiz. Tekh. Poluprovodn. **31**, 6 (1997) [Semiconductors **31**, 4 (1997)].
[28] S. P. Zimin, V. S. Kuznetsov, N. V. Perch, and A. V. Prokaznikov, Pis'ma Zh. Tekh. Fiz. **20**, 22 (1994) [Tech. Phys. Lett. **20**, 99 (1994)].
[29] A. G. Milnes and D. L. Feucht, *Heterojunctions and Metal–Semiconductor Junctions* (Academic Press, New York, 1972; Mir, Moscow, 1975).
[30] B. L. Sharma and R. K. Purohit, *Semiconductor Heterojunctions* (Pergamon Press, Oxford, 1974; Sov. Radio, Moscow, 1979).
[31] L. L. Kazakova, A. A. Lebedev, and É. A. Lebedev, Fiz. Tekh. Poluprovodn. **31**, 7 (1997) [Semiconductors **31**, 12 (1997)].
[32] P. H. Hao, X. Y. Hou, F. L. Zhang, and Xun Wang, Appl. Phys. Lett. **64**, 3602 (1994).
[33] O. Klima, P. Hlinomaz, A. Hospodková, J. Oswald, and J. Kočka, J. Non-Cryst. Solids **164–166**, 961 (1993).

Translated by W. J. Manthey

Photoconductivity of amorphous hydrated silicon doped by ion implantation

A. G. Kazanskiĭ* and N. V. Ryzhkova

M. V. Lomonosov Moscow State University, 119899 Moscow, Russia

S. M. Pietruszko

Warsaw University of Technology, Institute of Microelectronics and Optoelectronics, IMiO PW, 00-662 Warsaw, Poland

(Submitted June 29, 1998; accepted for publication July 28, 1998)
Fiz. Tekh. Poluprovodn. **33**, 332–335 (March 1999)

The effect of the concentration of impurities (phosphorus and boron) on the photoconductivity of films of amorphous hydrated silicon, hydrated and doped by ion implantation has been studied. The results are compared with data for films doped from the vapor phase. A substantial difference in the dependences of the photoconductivity on the doping level for phosphorus and boron is detected. The photoconductivity of phosphorus-implanted films increases with the doping level and is an order of magnitude lower than the photoconductivity of films doped with phosphorus from the vapor phase. At the same time, the photoconductivity of boron-implanted films depends only slightly on the doping level and virtually coincides with that of films doped with boron from the vapor phase. These results are explained in terms of a recombination model that allows for the difference in charge transfer of the defect states in *n*- and *p*-type films. © *1999 American Institute of Physics.* [S1063-7826(99)01603-8]

Ion implantation is widely used to dope crystalline semiconductors. Films of amorphous hydrated semiconductors, in particular, amorphous hydrated silicon (*a*-Si : H), are most often doped during their production from the vapor phase by adding phosphine or diborane to the reaction chamber. The implantation of group-III and group-V elements to amorphous hydrated silicon also makes it possible to vary the conductivity of the given material within wide limits.[1–3] In contrast with doping from the vapor phase, the hydrogen concentration in the film is independent of the level of introduced impurity.[3] The electrical properties of *a*-Si : H films doped by ion implantation have been studied in detail in Refs. 1–9. The available data[1,4,10] indicate that, when ions are implanted into an amorphous material, additional defects consisting of nonradiative recombination centers must be introduced. At the same time, the photoelectric properties of *a*-Si : H doped by ion implantation have been studied to a considerably less extent.[1,4,9] In particular, there is virtually no systematic research on the photoconductivity of films doped with acceptor impurities.

In this paper we report the results of an experimental study of the effect of the ion implantation of elements of group-III (boron) and group-V (phosphorus) on the photoconductivity of *a*-Si : H films and compare their photoelectric properties with those of films doped from the vapor phase.

Films of *a*-Si : H (0.5 μm thick) for ion implantation were deposited using thermal decomposition of monosilane (SiH_4). Wafers of crystalline silicon with a layer of SiO_2 (1 μm thick) formed on the surface were used as substrates. The films were hydrated and doped with phosphorus or boron by ion implantation. The hydrogen concentration in the films was 12 at.%. After implantation, the films were annealed at a temperature of 400 °C. Aluminum contacts were formed on the film surface. Before the measurements were made, the films were annealed in vacuum at a temperature of 180 °C for 30 min. The measurements were made at room temperature. The photoconductivity was determined with the films illuminated by light with quantum energy 1.8 eV and intensity $10^{14}\,\mathrm{cm}^{-2}\,\mathrm{sec}^{-1}$.

Figure 1 shows the dependence of the conductivity σ_d of the test films on the concentration of implanted phosphorus and boron. This figure also shows the data obtained in Ref. 1, in which phosphorus and boron were implanted into *a*-Si : H films obtained by the decomposition of monosilane in an rf glow discharge. It can be seen from the figure that σ_d in the films that we studied, which were hydrated by ion implantation, varied by more than six orders of magnitude when phosphorus or boron was implanted. The character of the variation of σ_d is close to the data for films hydrated during their deposition in an rf glow-discharge plasma.[1] A certain difference is observed only for the transition region from *n*-type to *p*-type conductivity. The indicated transition is observed for the films that we studied when the introduced boron concentration is an order of magnitude less than for the films obtained in Ref. 1.

The dependence of the photoconductivity $\Delta\sigma_{\mathrm{ph}}$ of the test films on the position of the Fermi level E_f relative to the conduction band E_c (the valence band E_v) for *n*-type (*p*-type) films is shown in Fig. 2. The E_c-E_f and E_f-E_v values were determined from the conductivity, using the relationship $|E_{c,v}-E_f|=kT\ln(\sigma_0/\sigma_d)$, where $\sigma_0=150\,\Omega^{-1}\mathrm{cm}^{-1}$ (Ref. 11). The same figure shows the data for *a*-Si : H films, which were obtained by decomposing monosilane in an rf glow discharge and which were doped with phosphorus or boron from the vapor phase.

Let us consider the results obtained for phosphorus-

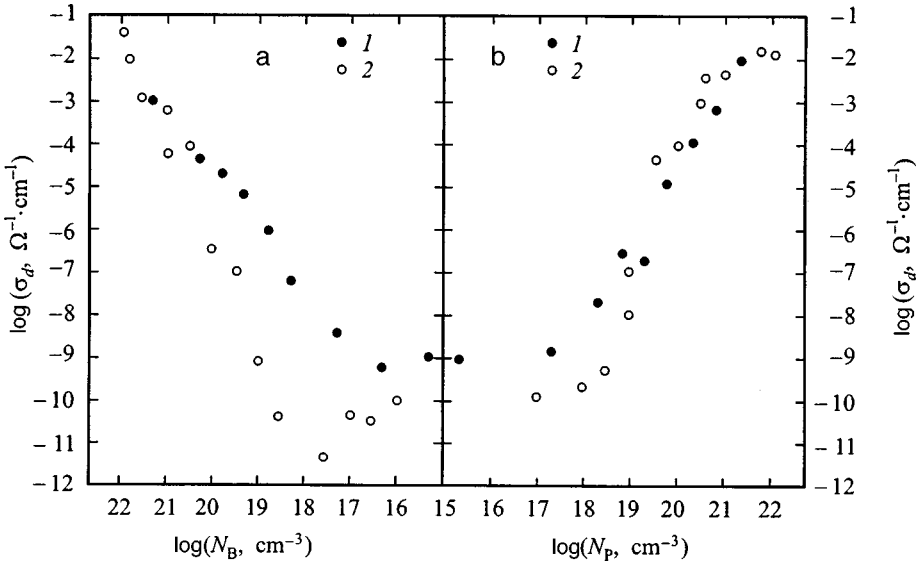

FIG. 1. Conductivity of *a*-Si : H films vs concentration of implanted boron (a) and phosphorus (b). Data of *1*—this paper, *2*—Ref. 1.

implanted films. It can be seen from Fig. 2b that $\Delta\sigma_{ph}$ of the phosphorus-implanted films is an order of magnitude less than $\Delta\sigma_{ph}$ for films doped from the vapor phase, consistent with the data of Ref. 1. In the opinion of Le Comber *et al.*,[1,4] this result is attributable to the introduction of additional recombination centers during ion implantation. This assumption agrees with the results of our comparative measurements by the constant-photocurrent method of the absorption α in the defect region of the spectrum (0.8–1.4 eV) for films doped with phosphorus by ion implantation and from the vapor phase with similar $E_c - E_f$ values. The $\alpha(1.2\,\text{eV})/\alpha(1.8\,\text{eV})$ value for the phosphorus-implanted films was an order of magnitude greater than for films doped from the vapor phase. This indicates a large density of states corresponding to defects at energies $E < E_f$ in the mobility gap of the phosphorus-implanted films.

As can be seen from Fig. 2b, as E_f shifts toward E_c, which occurs when the phosphorus concentration N_P increases, the $\Delta\sigma_{ph}$ value of the phosphorus-implanted films increases. If the implantation increases the concentration of dangling bonds, the observed increase of $\Delta\sigma_{ph}$ is associated with a reduced concentration of the principal recombination centers of nonequilibrium electrons—neutral dangling bonds, which become negatively charged when E_f shifts toward E_c.[12] Note that the total concentration of dangling bonds in neutral and negatively charged states increases with doping in this case.[2] At the same time, the nonradiative-recombination centers that appear during implantation are, in the opinion of Searle *et al.*,[10] not dangling bonds. In this case, the observed increase of $\Delta\sigma_{ph}$ of the phosphorus-implanted films as E_f shifts toward E_c indicates a reduced concentration of recombination centers which correspond to the introduced defects (possibly because they undergo charge transfer).

Let us consider the results obtained for boron-implanted *p*-type films (see Fig. 2a). It can be seen from the figure that, in contrast with phosphorus-implanted films, the $\Delta\sigma_{ph}$ values of films implanted with boron by ion implantation and from

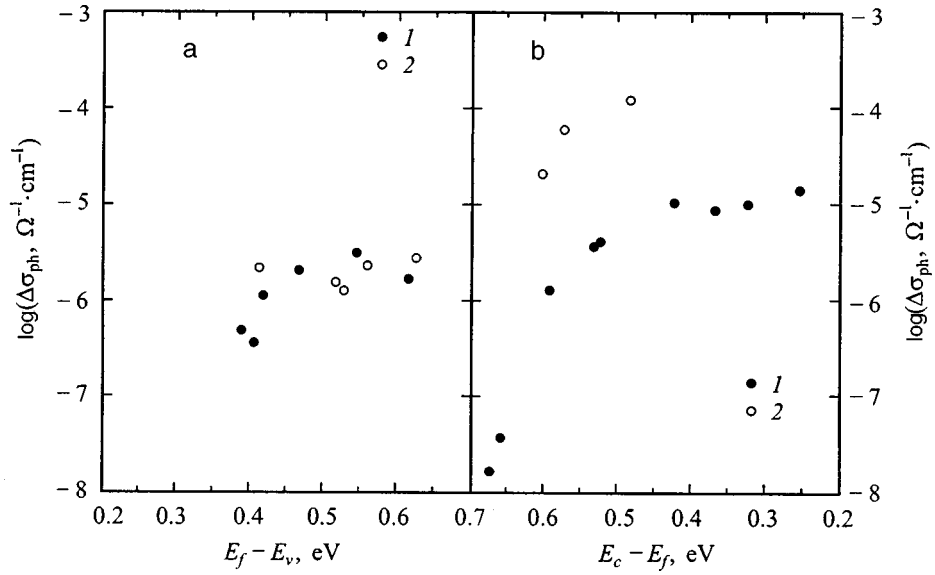

FIG. 2. Photoconductivity vs position of the Fermi level for *a*-Si : H films doped with boron (a) and phosphorus (b) by ion implantation (*1*) and from the vapor phase (*2*).

the vapor phase are close to each other. The measurements showed that the $\alpha(1.2\,\text{eV})/\alpha(1.8\,\text{eV})$ values for films with equal $E_f - E_v$ values are also close to each other. The latter result indicates that ion implantation does not substantially increase the density of states in the energy region $E > E_f$ in *p*-type *a*-Si : H films.

As can be seen from the figure, the increase in the concentration of implanted boron N_B and, accordingly, the shift of E_f toward E_v causes essentially no change in $\Delta\sigma_{ph}$. A certain reduction is seen only for the maximum concentrations of introduced boron. The weak dependence of $\Delta\sigma_{ph}$ on E_f in *p*-type films can be explained in terms of the model developed in Ref. 13. According to this model, the substantial difference in the length of the density-of-states tails close to E_v and E_c has the effect that, in *p*-type *a*-Si : H films, in contrast with *n*-type films, when optical excitation occurs, the concentration N^0 of the principal recombination centers—neutral dangling bonds—substantially differs from the equilibrium value N_0^0. In this case, N^0 is determined by the concentration of nonequilibrium holes trapped at the valence-band tail and, accordingly, depends on the density of states in the valence-band tail and is independent of N_0^0 and, accordingly, of the position of E_f. As a result, $\Delta\sigma_{ph}$ must be independent of E_f and N_0^0 and must decrease as the density of states in the valence-band tail increases.

The influence of interference in the *a*-Si : H / SiO_2 / *c*-Si test structures on the measured spectral dependences of α in the region of the exponential Urbach tail does not allow us to determine the slope of the Urbach tail and, accordingly, prevents us from evaluating how implantation affects the parameters of the density-of-states tail of the valence band.[14] If it is assumed that the valence-band tail does not change with small concentrations of implanted boron and increases because of the increase of disorder in the structure with large concentrations, then the model considered by us can be used to explain the similar values of $\Delta\sigma_{ph}$ for films doped with boron by ion implantation and those from the vapor phase, and also a certain reduction of $\Delta\sigma_{ph}$ at the maximum concentrations of the implanted boron.

In summary, our studies have shown that doping *a*-Si : H films with phosphorus by ion implantation results in larger values of the density of states in the mobility gap in the $E < E_f$ energy region and smaller values of $\Delta\sigma_{ph}$ in comparison with doping from the vapor phase. In the case of boron, implantation does not significantly increase the density of states in the mobility gap in the $E > E_f$ energy region, while the $\Delta\sigma_{ph}$ values are similar for films doped by the indicated methods.

This work was supported in part by the the program ''Universities of Russia—Fundamental Research.''

*E-mail: kazanskii@scon279.phys.msu.su; Fax: (095) 939 37 31

[1] P. G. Le Comber, W. E. Spear, G. Muller, and S. Kalbitzer, J. Non-Cryst. Solids **35–36**, 327 (1980).
[2] H. Mannsperger, S. Kalbitzer, and G. Muller, Appl. Phys. A: Solids Surf. **41**, 253 (1986).
[3] F. J. Demond, G. Muller, S. Kalbitzer, W. E. Spear, and P. G. Le Comber, Nucl. Instrum. Methods **191**, 59 (1981).
[4] G. Muller and P. G. Le Comber, Philos. Mag. B **43**, 419 (1981).
[5] W. E. Spear, P. G. Le Comber, S. Kalbitzer, and G. Muller, Philos. Mag. B **39**, 159 (1979).
[6] W. Beyer, D. Stritzker, and H. Wagner, J. Non-Cryst. Solids **35–36**, 321 (1980).
[7] H. Matsumura, N. Kuzuta, H. Ishiwara, and S. Furukawa, Radiat. Eff. **48**, 133 (1980).
[8] S. M. Pietruszko, J. Non-Cryst. Solids **164–166**, 255 (1993).
[9] K. Boringer, X. H. Liu, and S. Kalbitzer, J. Phys. C **16**, L1187 (1983).
[10] T. M. Searle, W. A. Jackson, and S. Kalbitzer, J. Non-Cryst. Solids **114**, 286 (1989).
[11] H. Overhof and P. Thomas, *Transport in Hydrogenated Amorphous Semiconductors* (Springer Tracts in Modern Physics, 1989), Vol. 114.
[12] W. E. Spear, H. L. Steemer, P. G. Le Comber, and R. A. Gibson, Philos. Mag. B **50**, L33 (1984).
[13] A. G. Kazanskiĭ and E. A. Shamonina, Fiz. Tekh. Poluprovodn. **27**, 1688 (1993) [Semiconductors **27**, 932 (1993)].
[14] R. Kuntz and J. Dziesiaty, Phys. Status Solidi A **124**, K149 (1991).

Translated by W. J. Manthey

Electronic properties and structure of *a*-Si:H films with higher photosensitivity

O. A. Golikova and M. M. Kazanin

A. F. Ioffe Physicotechnical Institute, Russian Academy of Sciences, 194021 St. Petersburg, Russia
(Submitted August 11, 1998; accepted for publication September 16, 1998)
Fiz. Tekh. Poluprovodn. **33**, 336–339 (March 1999)

The temperature dependences of the photoconductivity, the Urbach parameter, the optical modulation spectra, and the Raman spectra were studied in order to determine the cause of the increase in photosensitivity of *a*-Si:H films. It is shown that these films combine a low defect density with the existence of deep hole capture centers. These factors increase the value of σ_{ph} at $T=300$ K in comparison with the σ_{ph} of standard *a*-Si:H, with $\Delta E=$ const.
 [S1063-7826(99)01703-2]

INTRODUCTION

In our previous paper,[1] we presented the results of experimental studies of *a*-Si:H films in which the photosensitivity σ_{ph}/σ_d at room temperature was increased by as much as a factor of 100. The activation energy of the dark conductivity σ_d, $\Delta E=0.85-1.1$ eV, varied when changes were made in the conditions for depositing the films by rf glow discharge from 100% SiH_4 at a temperature $T_s=300\,^\circ$C. The photoconductivity σ_{ph} was measured when the films were illuminated by light with $h\nu=2$ eV and a flux $\Phi=10^{15}\,\mathrm{cm}^{-2}\,\mathrm{sec}^{-1}$, which corresponds to a photocarrier-generation rate $G=10^{19}\,\mathrm{cm}^{-3}\,\mathrm{sec}^{-1}$. The photoconductivity σ_{ph} reached values of 10^3 S/cm, even though we detected no radical reduction (by several orders of magnitude) of the defect density, which was determined by the constant-photocurrent method (CPM). A number of other anomalous properties of the films, which were studied in Ref. 1 and which were similar in many respects to the properties of the films described in Ref. 2, were also pointed out. The available data, however, were not sufficient to understand why the photoconductivity increased. In view of this circumstance, we obtained in our study some additional information on *a*-Si:H films with increased σ_{ph}/σ_d by studying the temperature dependences of the photoconductivity, the Urbach parameter (CPM), the optical modulation spectra, and the Raman spectra. Our goal in this study was to determine the electronic properties and the structure of the indicated films by comparing them with standard *a*-Si:H films.

EXPERIMENTAL RESULTS AND DISCUSSION

Figure 1 shows the temperature dependences of the photoconductivity. Curves *1* and *2* refer, respectively, to a film studied by us and to a standard *a*-Si:H film. The activation energy of σ_d was 1.05 eV in both films. It can be seen that the curves strongly differ from each other in shape: In the first case, a sharp temperature quenching of the photoconductivity (TQP) is observed, beginning with $T\cong 290-300$ K. At lower temperatures σ_{ph} exponentially increased with energy 0.02–0.03 eV. For the standard *a*-Si:H film, activation energies of σ_{ph} with a similar magnitude were observed in the entire temperature interval studied here; i.e., there is no TQP region (Fig. 1).

Let us now consider the temperature dependence of σ_{ph} for a film of intrinsic ($\Delta E=0.85$ eV) *a*-Si:H from the data of Ref. 2 under the condition that the incident light flux is $\Phi=10^{15}\,\mathrm{cm}^{-2}\,\mathrm{sec}^{-1}$. Since the measurements in Ref. 2 were made for $\Phi=10^{14}\,\mathrm{cm}^{-2}\,\mathrm{sec}^{-1}$, we used the linearity of the lux–ampere characteristic (LAC)[1] to recalculate the data of

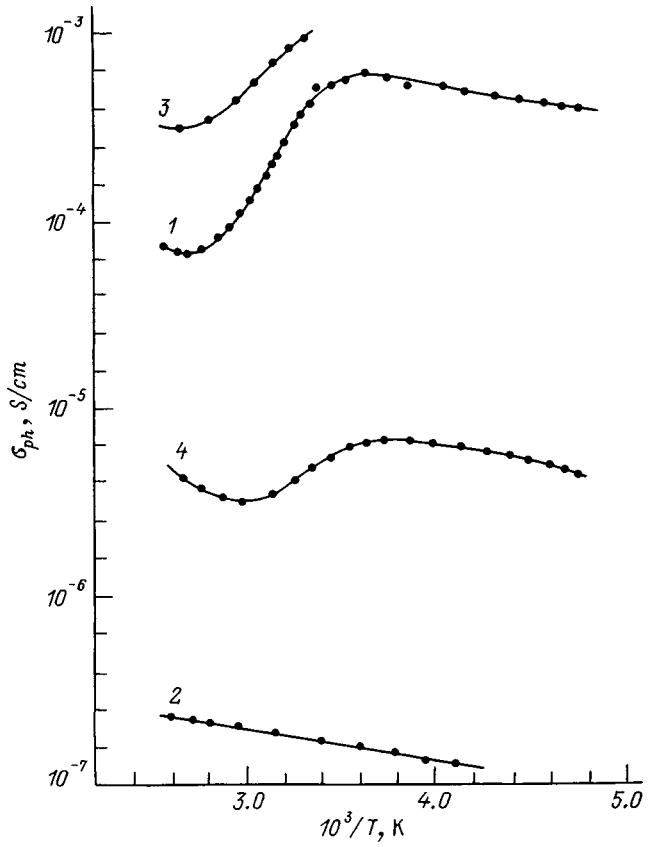

FIG. 1. Temperature dependences of the photoconductivity of *1*—*a*-Si:H with increased σ_{ph}/σ_d, *2*—standard *a*-Si:H (in both cases, $\Delta E=1.05$ eV), *3*—*a*-Si:H with increased σ_{ph}/σ_d (Ref. 2), *4*—standard *a*-Si:H (in both cases, $\Delta E=0.85$ eV).

Ref. 2 (Fig. 1, curve *3*). For comparison, Fig. 1 shows σ_{ph} for an intrinsic standard *a*-Si : H film (curve *4*). It can be seen that curves *3* and *4* differ significantly from each other: The TQP of a standard film, as has been established in other papers (see, for example, Ref. 3), occurs at significantly lower temperatures, and the change in this region is much weaker.

As shown by the results of studies of σ_{ph} and of our other films with increased σ_{ph}/σ_d, the high-temperature TQP regions are actually a characteristic property of such films; the maximum values of σ_{ph} are observed at temperatures close to room temperature.

There are various models of TQP in semiconductors, the best known of which is Rose's model.[4] This model assumes that the recombination channel changes at low temperatures. If recombination at high temperatures occurs through centers near the middle of E_g, for which $S_n = S_p$ (the capture cross section of electrons and holes), recombination at low temperatures goes through centers located close to the edge of the valence band, for which $S_n \ll S_p$. Because of this circumstance, σ_{ph} increases as the temperature is lowered. However, Rose's model implies superlinearity of the LAC, which is not observed in our case.[1] Conversely, the films with increased σ_{ph}/σ_d display an LAC whose exponent is close to unity, which is inherent to standard *a*-Si : H with a low defect density [the LAC was measured as the intensity of the light flux ($\lambda = 630$ nm) varied over three orders of magnitude at $T = 300$ K]. Therefore, in what follows, we shall start from the TQP model proposed for *a*-Si : H in Ref. 3. According to Ref. 3, recombination at high temperatures occurs from delocalized states through the states of dangling bonds—*D* centers. Electrons are quickly captured at neutral D^0 centers, transforming them into charged D^- centers. The recombination rate is determined by hole capture at the D^- centers. As a result, they are transformed back into D^0 centers, which capture new electrons, etc. However, as the temperature is lowered, a greater and greater part of the holes are captured at deep states of the valence-band tail. The hole flux toward the D^- centers decreases, and the number of D^0 centers that capture electrons accordingly decreases. Therefore, σ_{ph} increases with decreasing temperature (it falls as temperature rises; i.e., TQP occurs). Finally, as the temperature decreases further, the photocarriers trapped on the band-tail states undergo tunnelling recombination. Accordingly, σ_{ph} is determined by the thermal generation of electrons into the conduction band from its tail states and decreases with decreasing temperature (Fig. 1).

The existence of capture centers that efficiently capture holes thus raises the value of σ_{ph}, and the temperature at which this rise occurs increases as the depth of the position of the capture centers increases relative to the valence-band edge. There was interest in explaining the origin of these traps in the films that we studied, in which domains about 1 nm across apparently occur, as in the films described in Ref. 2. As regards to nanosize domains, Roca i Cabarrocas etal.[2] nevertheless leave the question of their structure unanswered. In other words, it is not clear whether these domains are silicon nanocrystals (*nc*).

Figure 2 shows the dependence of the Urbach parameter

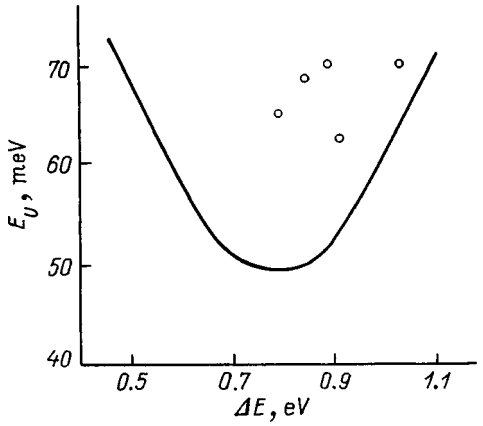

FIG. 2. The Urbach parameter plotted as a function of the activation energy of dark conductivity. The curve is for standard *a*-Si : H,[5] and the points are for *a*-Si : H with increased σ_{ph}/σ_d.

E_U on ΔE. It can be seen that, for $\Delta E = \text{const}$, the E_U of the films that we studied is substantially greater than the E_U of standard *a*-Si : H films. At the same time, as shown in Ref. 1, the opposite picture is observed for N_D. Thus, the interconnection between N_D and E_U usually observed[5] for *a*-Si : H is absent here.

In connection with what was said above, information was independently obtained concerning the defect density in the test films—by optical modulation spectroscopy (OMS), as in Ref. 6. Figure 3 shows the OMS spectra for three films: *1* (standard *a*-Si : H, $\Delta E = 0.8$ eV), *2* and *3* (*a*-Si : H with increased σ_{ph}/σ_d, $\Delta E = 0.92$ and 1.1 eV, respectively). It is well known[5] that, as ΔE varies in the interval 0.8–1.1 eV in standard *a*-Si : H, the value of N_D determined by the CPM increases by about an order of magnitude. However, a tendency is observed here to reduce the defect density as one goes from standard *a*-Si : H to *a*-Si : H with high photosensitivity, despite the increase of ΔE. Information on the defect density, as before,[6] was obtained by considering the region of the OMS spectrum close to 1 eV.

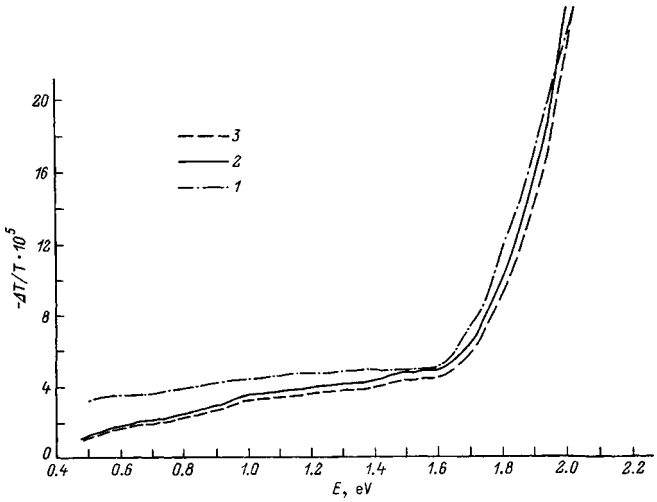

FIG. 3. OMS spectra for films of standard *a*-Si : H (*1*) and *a*-Si : H with increased σ_{ph}/σ_d (*2, 3*). The ΔE values are given in the text.

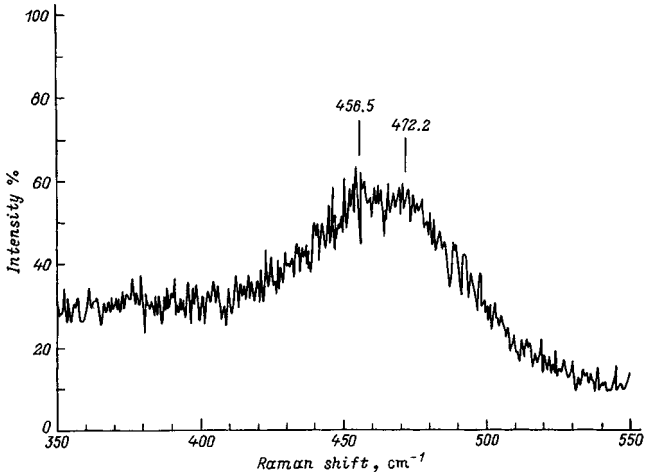

FIG. 4. Raman spectrum for an *a*-Si : H film with maximum $\sigma_{\rm ph}/\sigma_d$.

The sharp growth of $(-\Delta T/T)$, called thermomodulation, makes it possible to estimate E_g. [6] Earlier, E_g was determined independently by Tauts's method for films 1, 2, and 3: $E_g = 1.75$, 1.88, and 1.88 eV, respectively. Despite the difference in the values of E_g of film 1 from films 2 and 3, an increase of the OMS signal is observed for them, starting with $E = 1.6$ eV. This must be evidence that the valence-band tail is broadened for films with increased photosensitivity.

It is obvious that the data obtained by the CPM and OMS methods agree with each other. Thus, the films that we studied actually have lower values of N_D and at the same time deeper hole traps than standard *a*-Si : H films with ΔE = const. These two factors are responsible for the increased photoconductivity. We assume that inclusions of small (about 1 nm) domains (*ns* domains) result in the removal of local stresses in the *a*-Si : H host. This in turn reduces the number of dangling Si–Si bonds (*D* centers); i.e., the short-range order is improved. On the other hand, however, the presence of *ns* domains results in inhomogeneity of the structure beyond its limits and broadens the valence-band tail, as indicated by the increase of the Urbach parameter.

The structure of the *a*-Si : H matrix in the films studied here thus differs from that of standard *a*-Si : H. Based on the data of IR spectroscopy, certain differences regarding the hydrogen concentration in the films and the silicon–hydrogen bonds were pointed out earlier in Refs. 1 and 2. Here we show the Raman spectrum of one of our films which has the maximum photosensitivity (Fig. 4): It could be expected that the structural features of the Si subsystem show up most distinctly in this case.

As can be seen in Fig. 4, besides the standard *TO* band, the spectrum includes a band at 456 $\rm cm^{-1}$, whereas the one at 525 $\rm cm^{-1}$, characteristic of the crystalline phase, is absent. The latter can mean that the crystalline inclusions are too small[7] ($\leqslant 7$ nm) or that the *ns* domains are not nanocrystals of silicon. It is then possible to attempt to associate the origin of the band at 456 $\rm cm^{-1}$ with the presence of the *ns* inclusions in the films. We should point out that a *TO* band at frequencies close to 456 $\rm cm^{-1}$ was observed during studies of standard *a*-Si : H films[5] which have $\Delta E = 1.05$–1.10 eV and which contain about 16 at. % of hydrogen (twice as much as is contained in intrinsic *a*-Si : H deposited at the same temperature $T_s = 300\,^\circ$C). However, these were single-phase films: no other *TO* bands besides that indicated above were observed for them; they were distinguished by high defect density, low σ_d, and low $\sigma_{\rm ph}$. [1] Nevertheless, small inclusions of such a phase in the *a*-Si : H host possibly may have a positive effect on the electronic properties of the films.

Of course, the question of the nature of the inclusions that radically increase the photoconductivity of *a*-Si : H films can in no case be considered solved. In this connection, it should be recalled that Azuma et al.[8] reported the same photosensitivity in *a*-Si : H films that contain not *ns* domains but other ''inclusions,'' consisting of voids (2–4 vol %); here the hydrogen concentration in the films reached about 20 at. %. Clearly, the role of inclusions in increasing the photosensitivity actually reduces to a modification of the structure whose model, taking into account our data, is proposed by us in this paper. This model, in our view, explains the photoconductivity increase at room temperature in comparison with the photoconductivity of standard *a*-Si : H. As for the increase of σ_d with $\Delta E =$ const,[1] it most likely occurs because the temperature coefficient of the shift of the Fermi level in this case cannot be considered equal to zero, because the density of localized states is not symmetrically distributed relative to $E_g/2$. The nonsymmetry actually increases because of the significant broadening of the valence-band tail. If σ_d increases by a factor of 10, then, since $\sigma_d \sim \exp(-\gamma_F/k)$,[9] we obtain -2.8×10^{-4} eV/K for γ_F, and for the temperature coefficient of the $\varepsilon_c^* - \varepsilon_F$ gap, equal to $\gamma_c - \gamma_F$, we obtain 5.2×10^{-4} eV/K if $\gamma_c = 2.4\times10^{-4}$ eV/K.[9]

We should point out that the γ_F value that we determined is significantly lower than that determined by Ruff *et al.*:[10] 5.4×10^{-4} eV/K. However, they studied not *a*-Si : H with *ns* domains but microcrystalline silicon (μc-Si), for which the crystalline phase was recorded by Raman spectroscopy, while the value of $\sigma_{d(300\,\rm K)}$ reached 10^{-3} S/cm. In other words, it was very high in comparison with the σ_d of the samples that we studied ($\sigma_d = 10^{-8}$–10^{-10} S/cm). It therefore seems logical that the density of localized states in μc-Si undergoes significantly larger change in comparison with standard *a*-Si : H than the density of states in films with *ns* domains. The difference in the temperature coefficients of the Fermi level is attributable to this change.

CONCLUSION

The results which we obtained in this study, with allowance for the previous results,[1,2,8] have made it possible to explain the photosensitivity increase at $T = 300$ K in the *a*-Si : H films studied here in comparison with standard films. A necessary condition for this explanation is that the *a*-Si : H host must be modified by means of nanosize *ns* inclusions, which, on one hand, reduce the defect density by reducing the local stresses. On the other hand, the existence of such inclusions strongly broadens the valence-band tail, i.e., it creates very deep traps for holes which lowers the recombination rate through *D* centers at high temperatures.

We wish to thank Professor Guy J. Adriaenssens (K.U. Leuven) for providing the OMS data.

This work was supported by Grant INTAS N 931916.

[1] O. A. Golikova and M. M. Kazanin, Fiz. Tekh. Poluprovodn. **32**, 484 (1998) [Semiconductors **32**, 434 (1998)].
[2] P. Roca i Cabarrocas, S. Hamma, P. St'ahel, C. Longeaud, J. P. Kleider, R. Meaudre, and M. Meaudre, in *Proceedings of EPSEC-14*, Barcelona, July 1997, p. 5A20.
[3] Dersch, L. Schweitzer, and J. Stuke, Phys. Rev. B **28**, 4678 (1983).
[4] A. Rose, *Concepts in Photoconductivity and Allied Problems* (Interscience, New York, 1963; Mir, Moscow, 1966).
[5] O. A. Golikova and V. Kh. Kudoyarova, Fiz. Tekh. Poluprovodn. **29**, 1128 (1995) [Semiconductors **29**, 584 (1995)].
[6] G. J. Adriaenssens, O. A. Golikova, and W. Grevendonk, Fiz. Tekh. Poluprovodn. **32**, 123 (1998) [Semiconductors **32**, 109 (1998)].
[7] T. Okada, T. Twaki, K. Yamomoto, H. Kashara, and K. Abe, Solid State Commun. **49**, 809 (1984).
[8] M. Azuma, T. Yukoi, and I. Shimizu, in Abstracts of ICAS-16, Kobe, Sept. 1995, Mo-B03-2.
[9] J. Stuke, J. Non-Cryst. Solids **97/98**, 1 (1987).
[10] D. Ruff, H. Mell, L. Tolf, G. Huhn, I. Silber, and W. Fuhs, in Abstracts ICAMS-17, Budapest, August, 1997, ThP113/4.

Translated by W. J. Manthey

THE PHYSICS OF SEMICONDUCTOR DEVICES

Electrical and photoelectric characteristics of *n*-Si/porous silicon/Pd diode structures and the effect of gaseous hydrogen on them

S. V. Slobodchikov, D. N. Goryachev, Kh. M. Salikhov, and O. M. Sreseli

A. F. Ioffe Physicotechnical Institute, Russian Academy of Sciences, 194021 St. Petersburg, Russia
(Submitted June 22, 1998; accepted for publication June 25, 1998)
Fiz. Tekh. Poluprovodn. **33**, 340–343 (March 1999)

The current–voltage characteristics and the photovoltage of Pd/*por*-Si/*n*-Si diode structures in the temperature interval 106–300 K are investigated. The forward branch of the I–V characteristic at room temperature is exponential, with a nonideality factor $n \gtrsim 12$. The dependence of the current on the voltage at a low temperature and a high injection level is a power function with an exponent equal to 4.1. Amplification of the photocurrent is detected as the reverse bias increases; the gain reaches 10^3 at 106 K when the bias was more than 10 V. It is concluded that a double charge-carrier injection mechanism predominates during charge transfer through the porous layer. When gaseous hydrogen acts on the structure, the photovoltage decreases by three orders of magnitude, while the dark current decreases by an order of magnitude. The structures studied here are characterized by significant relaxation times of the increase of the currents and the recovery of the currents and the photovoltage after the action of hydrogen. The effect of hydrogen on the photoelectric characteristics is associated with the formation of an additional dipole layer at the Pd/*por*-Si boundary, which lowers the Schottky barrier.
 [S1063-7826(99)01803-7]

INTRODUCTION

Most of the attention of researchers studying porous silicon (*por*-Si) and diode structures based on it is devoted to the phenomena of photo- and electroluminescence, their dependence on production conditions, and the structure of the porous layers. Study of the electrical and photoelectric characteristics of such structures and, in particular, of metal/*por*-Si structures has received less attention. These studies, however, are of interest both with respect to the current-transport mechanism in such diode structures and in connection with possible practical applications. Kovalevskaya et al.[1] published the results of an experimental study of MOS structures with a palladium contact, based on single-crystal *p*- and *n*-type Si, and showed that high-sensitivity hydrogen detectors can be built.

In this article we present the results of measurements of the I–V characteristics, the photovoltage, and the photocurrent in Pd/*por*-Si/*n*-Si structures and the effect of gaseous hydrogen on them.

EXPERIMENTAL PROCEDURE

The *por*-Si layers were fabricated by anodizing an *n*-Si (100) surface with $\rho = 2\ \Omega \cdot$cm in a mixture of 48% hydrofluoric acid with ethanol (1:1) for 10 min with a current density of 10 mA/cm^2 through a platinum counterelectrode. An ohmic contact was previously created on the opposite side of the silicon wafer by fusing aluminum and then sputter-coating gold. During the electrolysis, the light of a 100-W incandescent lamp equipped with a filter transparent in the IR was focused onto the sample. Such a light intensity was sufficient to completely straighten the bands at the silicon surface.

The *por*-Si surface was metallized by cathode deposition of palladium from an aminochloride electrolyte $[Pd(NH_3)_4]Cl_2$ with a current density of 1 mA/cm^2 for 10 min. The calculated thickness of the palladium layer was 100 nm.

The electrical and photoelectric characteristics were measured by standard techniques, using an SPM-2 monochromator and a graphite radiation source. A pulsed H_2 supply was provided by the technique of Ref. 1.

ELECTRICAL CHARACTERISTICS

Figure 1 shows the forward branches (negative potential on the substrate) of the I–V characteristics, recorded at $T = 106$ and 300 K. The dependence $I \sim \exp(qV/nkT)$ with $n \gtrsim 12$ is typical at both temperatures in the current interval to $I \simeq 10^{-6}$ A. The exponential behavior is replaced by the power dependence $I \sim V^{4.1}$ at higher injection levels at $T = 106$ K.

High values of the nonideality factor *n* of the I–V characteristics are typical of Schottky barriers based on *por*-Si. While the *n* values do not exceed 10 in Al/*por*-Si/*p*-Si structures,[2] values of 55–60 for Au/*por*-Si/*p*-Si structures are given in Refs. 3 and 4. The parameters of the diodes are improved on *n*-type substrates and with electrochemical or chemical deposition of the metal contact, and the values obtained for *n* can therefore be regarded as normal for Schottky

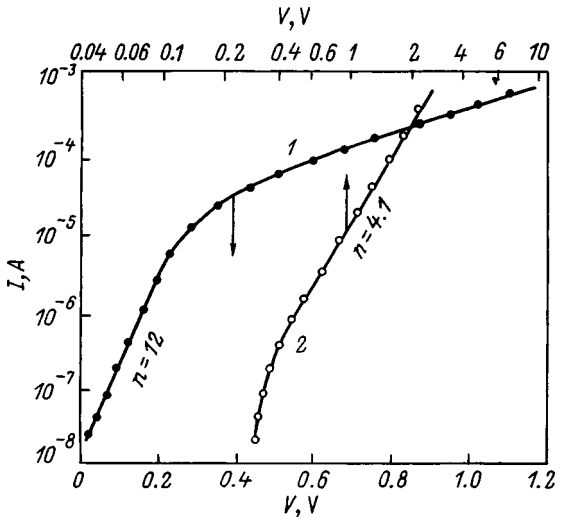

FIG. 1. The current–voltage characteristics (forward direction) of Pd/*por*-Si/*n*-Si structures. Temperature, K: *1*—300 (lower scale), *2*—106 (upper scale).

barriers made from noble metals. The transition to a power function of the current versus the voltage at high voltages and low temperatures,

$$I \sim V^m, \tag{1}$$

allows the current-transport mechanism to be explained by double injection of carriers into the porous layer—electrons are injected from the *n*-Si substrate through the Si/*por*-Si heterojunction and holes are injected through the Schottky barrier. It is evident that, with either polarity of the applied voltage, the injection coefficients of the electrons and holes will not be ideal; i.e., the ratios I_n/I and I_p/I will be less than unity. However, the forward direction of the current will be characterized by a higher injection coefficient of electrons into the porous layer in comparison with hole injection. For a monotonic distribution of the carriers injected into the *por*-Si and in the presence of active capture centers, the nonideality factor n is proportional to $\cosh(W/L)$, where W is the thickness of the porous layer and L is the diffusion length.[5] When $W \gg L$, the value of n can be large, as we have observed experimentally.

As the injection level increases, recombination increases in the skin layer of the *por*-Si at the boundary with Pd and at the heterojunction boundary with the substrate. The distribution of carriers injected into the *por*-Si layer becomes nonmonotonic, and this changes the form of the I–V characteristics from exponential to a power function [Eq. (1)]. When $W > L$ and the injection contacts are nonideal, the power m is 4 (Ref. 5), consistent with the experimental data.

The forward I–V characteristics are characterized by a long rise time of the forward current when the voltage is applied in steps (Fig. 2). The presence of steps on certain curves (Fig. 2, curve *2*) is evidence that several levels, with different characteristic times, participate in the capture and recombination processes. Estimating their depth from the thermal liberation time, we obtain the energy interval $E_{ti} \approx 0.80-0.90$ eV.

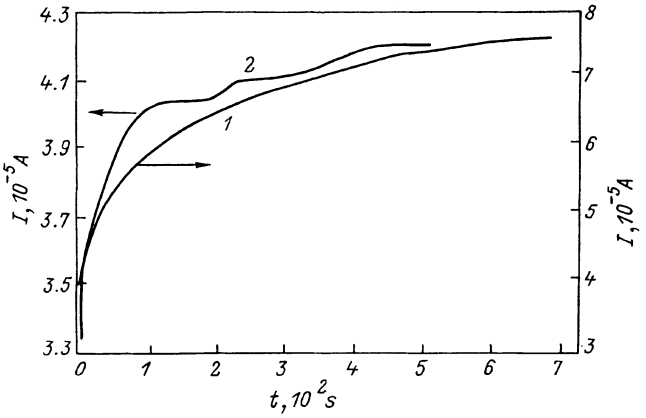

FIG. 2. Curves showing the increase of forward current with stepwise switching on of the voltage for Pd/*por*-Si/*n*-Si samples.

PHOTOELECTRIC CHARACTERISTICS

Analyzing the results of measurements of the photoelectric effect in these structures, we should first point out that the spectral characteristics of neither the photovoltage nor the photocurrent display any features in the short-wavelength part of the spectra corresponding to broad-band *por*-Si, as observed, for example, in Ref. 6. A Fowler tail corresponding to a barrier equal to 0.32 eV is observed on the long-wavelength section.

The dependence of the photocurrent on the reverse bias was studied with close-to-monochromatic illumination with $\lambda = 1.0\ \mu$m (Fig. 3). At large voltages, this dependence goes from sublinear to superlinear with a power m equal to 4.2. At $T = 106$ K, the gain for $V > 10$ V reaches values of 10^3. As the temperature is raised from 106 to 300 K, the gain falls by more than an order of magnitude.

In our view, the influence of two factors should be evaluated in analyzing the amplification mechanism: the tunneling of minority charge carriers through the Schottky barrier and the concentration variation of these carriers as a function of the injection level of electrons into the porous layer. The tunneling of carriers seems unlikely, since, on one

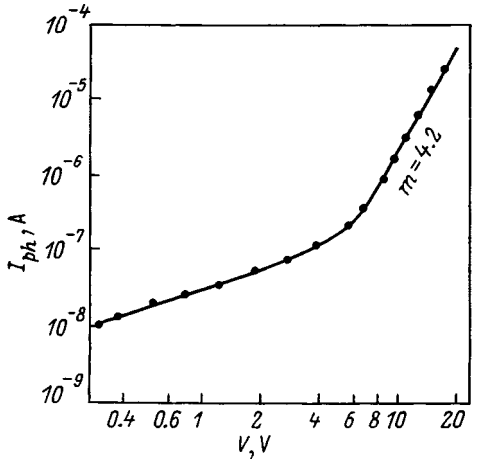

FIG. 3. Photocurrent I_{ph} vs reverse bias V at $T = 106$ K with monochromatic illumination ($\lambda = 1.0\ \mu$m).

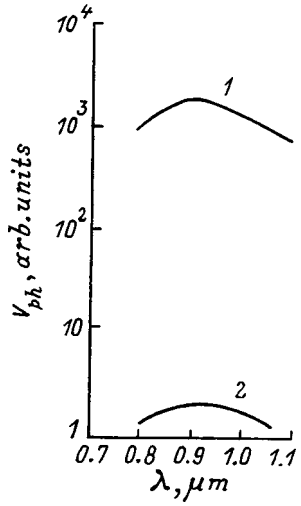

FIG. 4. Photovoltage spectra V_{ph} of a Pd/*por*-Si/*n*-Si structure: *1*—initial, *2*—in a H_2 atmosphere.

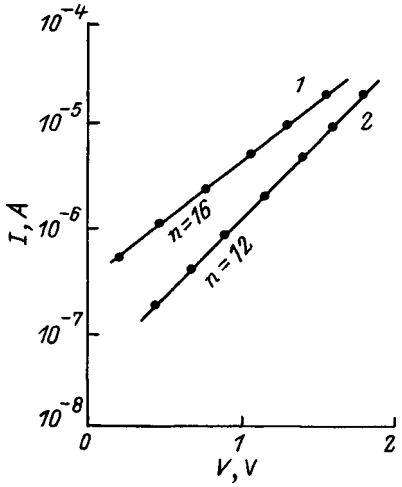

FIG. 5. Variation of the dark current (forward direction) with pulsed action of hydrogen: *1*—initial curve, *2*—in a H_2 atmosphere.

hand, the electric fields were not very large ($<10^6$ V/cm), and, on the other, a rather strong temperature dependence of the gain was observed, which cannot be expected with tunneling. It is hard to regard a porous silicon layer as an ordinary photoconductor with amplification determined by carrier transit, since *por*-Si is characterized by extremely low carrier mobility.[7] In addition, the experiments showed that the photocurrent depends on the polarity of the applied voltage: The photocurrent decreases with forward bias, dropping especially sharply as the bias voltage increases.

The photocurrent amplification in the test structures, in our view, is attributable to the increase of the lifetime and, accordingly, the diffusion length. The observed long-lived relaxation of the forward current, with a high electron-injection coefficient I_n/I, is evidence that the deep centers are electron-capture centers. With reverse bias at the Pd/*por*-Si boundary, there is a predominant filling of these centers, and this region broadens along the *por*-Si layer as the voltage increases. The photocarriers in this case have an ambipolar diffusion length that increases with increasing bias, and the number of electron–hole pairs separated by the Schottky barrier accordingly increases. The theoretical dependence for a nonuniform distribution of minority nonequilibrium carriers $\Delta p \sim I \sim V^4$ mentioned earlier approximately corresponds to the $I_{ph} \sim V^{4.2}$ dependence experimentally observed for the photocurrent at high reverse bias (Fig. 3). The temperature dependence of the photocurrent under reverse bias turned out to be fairly insignificant, as should be expected, since the population of deep levels does not vary much in the temperature interval considered here.

EFFECT OF HYDROGEN ON THE PHOTOELECTRIC AND ELECTRICAL CHARACTERISTICS

The effect of gaseous hydrogen on the region of maximum spectral sensitivity is shown in Fig. 4, while the variations of the forward branch of the I–V characteristic are shown in Fig. 5. The virtually inertialess decrease of the photovoltage in a hydrogen atmosphere is almost three orders of magnitude, while the forward current falls off by less than an order of magnitude. The reverse current varies in a similar way. When this is compared with the results obtained on single-crystal *n*-Si,[1] note that there is a sharply increasing relaxation of the photovoltage and the dark current after the hydrogen pulse is switched off (Fig. 6). Moreover, the dark currents decrease as a result of the introduction of hydrogen, whereas they increase in *n*-Si.[1] If the variation of the photovolage can be attributed, as before, to the lowering of the Schottky barrier, the variation of the dark currents can most likely be explained by the effect of hydrogen on the density and charge transfer of deep levels in the porous silicon layer.

The lowering of the Schottky barrier can be attributed to the ''temporary'' defects initiated by the hydrogen atoms, which create an additional dipole layer deposited on the dipole layer of the barrier. As a result, both the photocurrent and the internal differential resistance of the barrier fall off. The reduction of the forward and reverse dark currents, however, in these structures is determined not only by the properties of the Schottky barrier, but also by the current-

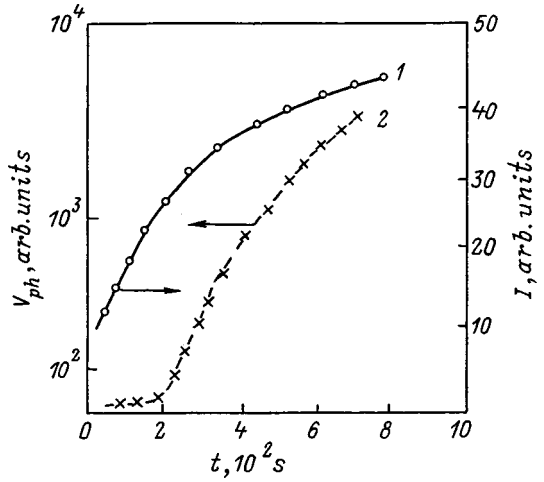

FIG. 6. Relaxation curves of the dark current in the reverse direction (points on curve *1*) and photovoltage (*2*) after switching off the pulse of H_2. Solid curve *1* shows the calculated values for $E_t = 0.8$ eV.

transport mechanism in the porous layer. The forward current falls off because additional capture centers form in a hydrogen atmosphere. This process must reduce the ideality coefficient n.[1] A falloff of n has actually been observed experimentally: $n=16$ without hydrogen and $n=12$ with hydrogen. The sharp lowering of the Schottky barrier in a hydrogen atmosphere causes the electron injection to increase under reverse bias, and the mechanism by which hydrogen affects the reverse current remains essentially the same as for the forward current. In contrast with the forward current, the relaxation of the reverse current is determined by the liberation of nonequilibrium minority carriers from the capture level $E_t=0.8$ eV (Fig. 6), which is apparently associated with a large concentration of these centers in the porous layer. The relaxation dependence of the photovoltage is more complex and involves the participation of a number of levels in the process.[5] The relaxation times of the photovoltage and the dark currents are long, about 12 min.

The resulting data on the effect of gaseous hydrogen on the photovoltage and the I–V characteristics of Pd/*por*-Si/*n*-Si structures show that the variations in these characteristics are comparable in magnitude with the corresponding variations in structures based on single-crystal silicon. However, the longer relaxation times of the parameters measured here make it less promising to use these structures to sense gaseous hydrogen.

D. N. Goryachev and O. M. Sreseli wish to thank the Russian Fund for Fundamental Research for supporting this work (Grant No. 96-02-17903).

[1] G. G. Kovalevskaya, M. M. Meredov, E. V. Russu, Kh. M. Salikhov, and S. V. Slobodchikov, Zh. Tekh. Fiz. **63**(2), 185 (1993) [Tech. Phys. **38**, 149 (1993).
[2] H. Shi, Y. Zheng, Y. Wang, and R. Yuan, Appl. Phys. Lett. , **63**, 770 (1993).
[3] N. Koshida and H. Koyama, Appl. Phys. Lett. **60**, 347 (1992).
[4] L. Pavesi, M. Ceschini, G. Mariotto, E. Zanghellini, O. Bisi, M. Anderie, L. Calliari, M. Fedrizzi, and L. Fedrizzi, J. Appl. Phys. **75**, 1118 (1994).
[5] É. I. Adirovich, P. M. Karageorgiĭ-Alkalaev, and A. Yu. Leĭderman, *Double-Injection Currents in Semiconductors* (Nauka, Moscow, 1978).
[6] L. V. Belyakov, D. N. Goryachev, O. M. Sreseli, and I. D. Yaroshetskiĭ, Fiz. Tekh. Poluprovodn. **27**, 1371 (1993) [Semiconductors **27**, 758 (1993)].
[7] C. Peng, K. D. Hirschman, and P. M. Fauchet, J. Appl. Phys. **80**, 295 (1996).

Translated by W. J. Manthey

Temperature dependence of the quantum efficiency of silicon $p-n$ photodiodes

Yu. A. Goldberg, V. V. Zabrodsky, O. I. Obolensky, T. V. Petelina, and V. L. Suhanov

A. F. Ioffe Physicotechnical Institute, Russian Academy of Sciences, 194021 St. Petersburg, Russia
(Submitted July 15, 1998; accepted for publication July 28, 1998)
Fiz. Tekh. Poluprovodn. **33**, 344–345 (March 1999)

The temperature dependence of the quantum efficiency of silicon $p-n$ photodiodes for photon energies of 1.1–5.2 eV is measured in the temperature range 77–300 K. It is shown that for photons with energies exceeding 1.4 eV the change in quantum efficiency is less than 0.01% per degree. The temperature dependences of the photoresponse of silicon photodiodes and of GaAs and GaP Schottky barrier photodiodes are compared. © *1999 American Institute of Physics.* [S1063-7826(99)01903-1]

1. Silicon $p-n$ structures and GaAs and GaP Schottky diodes are the most widespread ultraviolet semiconductor photodetectors.[1,2] These devices have the common shortcoming of a sharp drop in quantum efficiency at short wavelengths. An additional drawback of the GaAs and GaP devices is that they have a strong temperature dependence of the photocurrent, which increases severalfold as the temperature is raised from 100 to 300 K.[3,4]

We are unaware of any experimental papers in which the temperature dependence of the quantum efficiency of silicon $p-n$-structures has been studied in a wide range of temperatures. In this paper we report the results of such a study. Our experiments show that in the short-wavelength interval corresponding to 1.4–5.2 eV, the quantum efficiency is essentially independent of temperature. In the long-wavelength interval corresponding to 1.1–1.3 eV, there is a strong temperature dependence apparently due to the increased number of photons required for an indirect optical transition.

A model has been proposed[3,4] to explain the rapid rise in the photocurrent with temperature. According to this model, photocarriers are captured at traps located in the space charge region. This sort of trap presumably is capable of simultaneously capturing an electron and a hole, so that, at low temperatures, a large fraction of the photocarriers recombine at traps, while the remainder are ejected from the trap by thermal excitation. This fraction of the photocarriers also contributes to the photocurrent, which increases with temperature. The experimental results and their explanation given in Refs. 3 and 4 indicate that there is an extremely high concentration of traps in the space charge region. Estimates show that atomic traps should have a concentration on the order of 10^{19} cm^{-3}, so that probably these traps are two-dimensional, like dislocation loops.

The absence of an increase in the photocurrent with temperature in silicon $p-n$ structures is, we believe, of fundamental importance. It is evidence of a high technological and design perfection in the silicon structures and of the absence of any structural defects in their space charge regions.

2. The objects of study were silicon photodiodes prepared by local diffusion from the gaseous phase. An initial n-Si:P substrate with a [100] orientation and a specific resistance of 20 $\Omega\cdot$cm was oxidized in dry oxygen in the presence of chlorine-containing substances. After oxidation a 7×7 mm window was opened up and boron was diffused into it to a depth of $\leqslant 30$ nm. Here the impurity concentration in the layer near the surface was determined by Rutherford backscatter spectroscopy (RBS) to be $N_A(0) \approx 10^{22}$ cm^{-3}. An isotypic $n-n^+$ junction was created on the opposite side. Metal contacts were formed on the front using photolithographic techniques and etching of a vacuum-deposited aluminum film.

Figure 1 shows the spectral characteristic of a photodiode of this type. An analysis of the quantum efficiency spectrum of this photodiode along with the reflection spectrum of silicon[5] shows that the inner quantum efficiency of the detector is close to unity. This type of detector can operate in the ultraviolet.

A model of similar highly asymmetric silicon $p-n$ junctions with ultrashallow doping has been examined by Redfield.[6] A high electric field $E>10^4$ V/cm, which extends up to the outer surface of the doped region of the $p-n$ junction, ensures that the carriers generated in this region drift at a high velocity, close to the maximum saturation value of $\approx 10^7$ cm/s. The time over which a carrier generated near the surface reaches the $p-n$ junction is $t\leqslant 3$

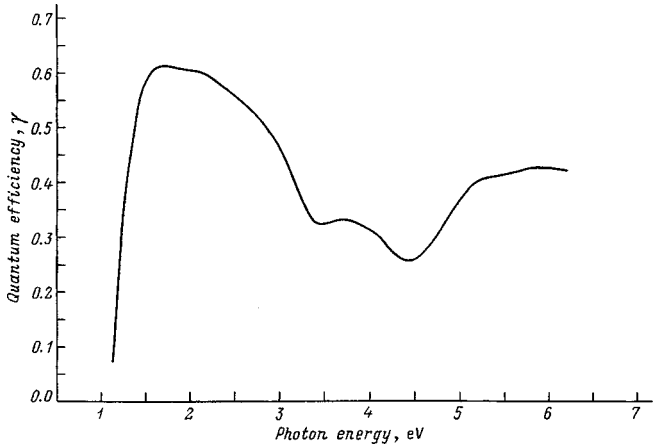

FIG. 1. The quantum efficiency of a silicon photodiode (in electrons per photon) as a function of photon energy at room temperature.

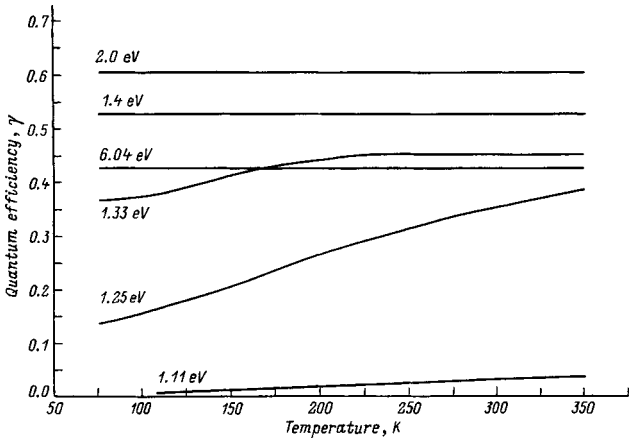

FIG. 2. Quantum efficiency of a silicon photodiode (in electrons per photon) as a function of temperature at several photon energies.

$\times 10^{-13}$ s. These short drift times explain the low level of recombination losses in the thin, highly doped region of the $p-n$ junction.

3. The results of the experiments are reflected in Fig. 2 and reduce to the following.

For photon energies of 1.1–1.3 eV, the quantum efficiency increases with rising temperature, and more rapidly for lower energy photons. We assume that this is related to an increase in the number of photons, since when the photon energy slightly exceeds the band gap, the indirect optical transitions mainly involve absorption of a photon.

For photon energies of 1.4–5.2 eV, the quantum efficiency is temperature independent. Since the error in the measurements was less than 1.5%, we may conclude that in this region of the spectrum the change in the quantum efficiency is less than 0.01%/°C.

We thank O. V. Konstantinov for a discussion of the results of this study.

[1] Hamamatsu Photonics Photodiodes Catalog, 1995.
[2] E. I. Ivanov, L. B. Lopatina, V. L. Sukhanov, V. V. Tuchkevich, and N. N. Shmidt, Fiz. Tekh. Poluprovodn. **15**, 1343 (1981) [Sov. Phys. Semicond. **15**, 775 (1981)].
[3] Yu. A. Goldberg, O. V. Konstantinov, O. I. Obolensky, E. A. Posse, and B. V. Tsarenkov, Fiz. Tekh. Poluprovodn. **31**, 563 (1997) [Semiconductors **31**, 473 (1997)].
[4] Yu. A. Goldberg, O. V. Konstantinov, E. A. Posse, and B. V. Tsarenkov, Fiz. Tekh. Poluprovodn. **29**, 219 (1995) [Semiconductors **291**, 108 (1995)].
[5] H. R. Philipp and E. A. Taft, Phys. Rev. **99**, 1151 (1955).
[6] D. Redfield, Appl. Phys. Lett. **35**, 182 (1979).

Translated by D. H. McNeill

Planar-doped gallium-arsenide structures for bulk potential barrier microwave diodes

N. A. Maleev, A. Yu. Egorov, A. E. Zhukov, A. R. Kovsh, and V. M. Ustinov

A. F. Ioffe Physicotechnical Institute, Russian Academy of Sciences, 194021 St. Petersburg, Russia

V. V. Volkov

Svetlana–Élektronpribor, Inc. 194156 St. Petersburg, Russia

M. F. Kokorev

St. Petersburg State Electrical Engineering University 197376 St. Petersburg, Russia

(Submitted July 23, 1998; accepted for publication July 28, 1998)
Fiz. Tekh. Poluprovodn. **33**, 346–350 (March 1999)

Diodes with a planar-doped potential barrier are devices with charge transfer by majority carriers for which the height of the potential barrier and the shape of the current–voltage characteristics can be controlled by means of a definite combination of layers during the growth of the epitaxial structures. These devices have emerged as potential replacements of Schottky-barrier diodes for a number of microwave applications. Some typical problems that arise when structures with a planar-doped potential barrier are grown by molecular-beam epitaxy are studied. A process for obtaining the structures, based on combining vapor-phase epitaxy with molecular-beam epitaxy, is proposed. Various methods are studied for forming ohmic contacts in structures with a planar-doped potential barrier. A process which provides low contact resistances ($<6\times10^{-7}\,\Omega\cdot\mathrm{cm}^2$) and a high percentage yield of serviceable diodes ($>95\%$) is developed. Microwave diodes fabricated with a planar-doped potential barrier are compared with Schottky diodes based on gallium arsenide. © *1999 American Institute of Physics.* [S1063-7826(99)02003-7]

Diodes with a bulk potential barrier formed in an epitaxial structure based on *n*-type gallium arsenide by introducing a thin *p*-type layer were proposed and experimentally implemented at the beginning of the 1980s.[1] They became possible because of the development of modern epitaxial technologies, most importantly, molecular-beam epitaxy (MBE).

There are two main varieties of such diode structures: so-called camel diodes, in which a doped *p* layer is located directly in a layer with *n*-type conductivity, and diodes with a planar-doped potential barrier (PDDs). Current is transported in a PDD by majority carriers (electrons) through the potential barrier formed by introducing a thin, p^+ layer into an undoped region (the *i*-region) located between two layers of *n*-type conductivity (Fig. 1). The thickness *t* and the doping level N_A of the p^+ layer in this case is such that it is completely depleted by the majority carriers (holes).[2,3]

It is possible to control the height of the potential barrier in planar-doped structures by varying the parameters of the epitaxial structures. In contrast, for Schottky-barrier diodes (SBDs) based on gallium arsenide, the barrier height Φ_b is about 0.7–0.8 eV for most of the metals that are used. This is important when creating the structures with low potential-barrier height needed for microwave (MW) detector diodes with zero bias and mixer diodes in systems with low heterodyne power. Such low-barrier SBDs are ordinarily based on Si,[4] InP,[5] or InGaAs.[6] PDDs have a number of important advantages over them. Since the potential-barrier region in a PDD is far from the surface, and since it is formed during the growth of the epitaxial structure, there are no problems associated with how the processing quality of the surface under the barrier contact affects the characteristics of the diodes,

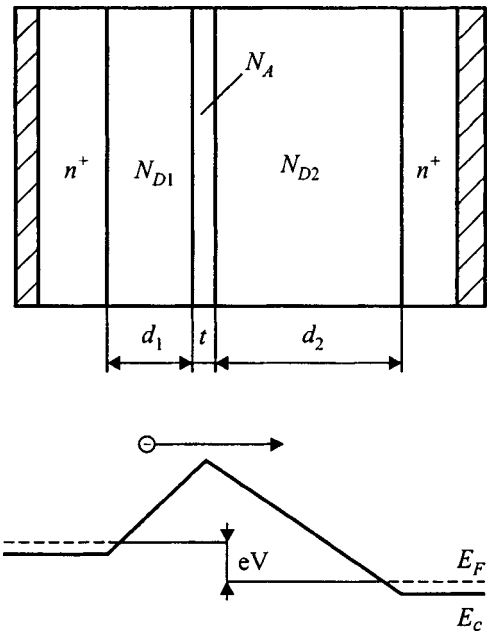

FIG. 1. Operating principle of a diode with a planar-doped potential barrier. The doping level of the p^+ layer is $N_A=(1-10)\times10^{17}\,\mathrm{cm}^{-3}$, the thickness is $t=5-10$ nm, the doping level of the *i* layers is N_{D1}, $N_{D2}<10^{15}\,\mathrm{cm}^{-3}$, and the thicknesses are d_1, $d_2=10-1000$ nm.

and the low-frequency noise caused by surface states is reduced.[7,8] The characteristics of PDDs have higher-temperature stability than do those of SBDs.[9] Finally, diodes with planar-doped barriers are more stable against pulse overloads.[10]

A key problem that needs to be solved to ensure the required characteristics of PDDs and their reproducibility is to monitor the charge and the spatial position of the thin p^+ layer. Another important aspect is to ensure a low background doping level and a given thickness of the i layers. The technological method that most fully satisfies these requirements is MBE.

The results noted above involving the creation of high-quality PDDs were achieved by using structures grown by MBE. Nevertheless, there are several technological and design problems associated with the need to perfect the characteristics of PDDs, to improve the reproducibility of the parameters, and to increase the output of serviceable diodes.

In this paper we report the results of an experimental study of various methods for forming ohmic contacts to planar-doped structures with a bulk potential barrier. We also optimize the design and technology of growing PDD structures by MBE and carry out a comparative study of the characteristics of MW PDDs and SBDs based on GaAs.

At the first stage of the study, a process was developed for obtaining PDD structures with given current–voltage characteristics and a given barrier capacitance. A series of test samples, which differ in the thicknesses of the undoped layers (d_1,d_2) and the position and doping level (N_A) of the p^+ layer, was fabricated. The planar-doped structures were grown by MBE on a Riber-32P apparatus. Silicon was used as a donor impurity, and Be as an acceptor. To check the quality of the epitaxial structures and the correspondence of their parameters to the calculated values, test diodes were fabricated in the form of mesa-structures 70 μm in diameter, with an upper ohmic contact 50 μm in diameter and an annular ohmic contact to the lower n^+ layer. AuGe / Ni / Au ohmic contacts were formed using a process optimized earlier for fabricating MW field-effect transistors.[11] A peroxide–ammonia etchant was used to etch the mesa structures.

In the total-depletion approximation (i.e., assuming sharp boundaries of the depletion regions) and with a sufficiently high potential barrier, the simple analytical model of Refs. 2 and 3 can be used to describe the I–V characteristics of the PDDs. In the indicated approximation, the potential-barrier height in the absence of external voltage is given by

$$\Phi_b = \frac{eN_A t}{\varepsilon\varepsilon_0}\,\frac{d_1 d_2}{d_1+d_2},$$

where e is the charge of the electron, ε_0 is the permittivity of free space, and $\varepsilon = 13.1$ is the relative permittivity of GaAs. If the voltage drop across the undoped layers is much greater than the thermal potential kT/e, the current through the barrier in both directions is determined in most cases by thermoelectron emission. This current density can be determined from

$$J = A^{**}T^2 \exp\left[-\frac{e(\Phi_b - E_F)}{kT}\right] \times\left\{\exp\left[\frac{eV}{n_2 kT}\right] - \exp\left[-\frac{eV}{n_1 kT}\right]\right\},$$

where $A^{**} = 4.4\times 10^4$ A/m^{2}K is the effective Richardson constant for GaAs, T is the absolute temperature, V is the applied voltage, and n_1 and n_2 are the ideality factors, defined by

$$n_1 = \frac{d_1+d_2}{d_1}, \quad n_2 = \frac{d_1+d_2}{d_2}.$$

The specific capacitance (per unit area) of a PDD is approximately constant and in the total-depletion approximation is given by

$$C = \frac{\varepsilon\varepsilon_0}{d_1+d_2}.$$

Table I shows the design parameters of some of the as-grown structures, as well as the calculated and experimental values of the parameters that characterize the I–V characteristics of the test PDDs. The observed systematic excess of the barrier height over the calculated value can be attributed to a certain excess of the actual Be concentration relative to the assumed value, since capacitance measurements confirm that the total thickness of the undoped region agrees well with the calculated value. The growth regimes of the planar-doped p^+ layer were corrected in accordance with the resulting data.

A crucial problem in PDD fabrication technology is reproducibility in creating the upper ohmic contact. The use of alloy contacts based on AuGe is possible for a sufficiently thick upper n^+ layer (no less than 0.3–0.4 μm), since local regions with a large penetration depth of the contact layer can be formed. Alternative versions are to use nonalloy ohmic contacts by brazing in a metallic contact coating at

TABLE I. Parameters of the PDD test structures.

					Ideality factor		Φ_b, mV	
Sample	d_1, nm	d_2, nm	t, nm	N_A, cm^{-3}	Calculation	Experiment	Calculation	Experiment
2-640	200	100	10	4×10^{17}	1.5	1.5	368	577
2-641	300	100	10	4×10^{17}	1.33	1.5	410	697
2-680	150	30	10	10^{18}	1.2	1.34	344	476

TABLE II. Comparison of methods of forming the upper ohmic contact.

Structure of the upper contact layer (thickness, doping level)	Contact metallization	Fusing (brazing) regime	Typical values of contact resistance ρ_c, $\Omega \cdot cm^2$	Yield of serviceable test diodes, % (diameter of mesa-structures 70 μm)
n^+-GaAs (400 nm, 3×10^{18} cm^{-3})	AuGe / Ni / Au	420 °C, 30 sec, H_2 atmosphere	$(1.95-3.4)\times10^{-7}$	74
n^+-GaAs (400 nm, 3×10^{18} cm^{-3})	AuGe / Ni / Au	300 °C, 30 min, H_2 atmosphere	$(2.1-3.2)\times10^{-7}$	89
n^+-$In_{0.5}Ga_{0.5}As$ (50 nm, 1×10^{19} cm^{-3}) / grad-$In_xGa_{1-x}As$	Ti / Pt / Au	300 °C, 5 min, H_2 atmosphere	$(4.9-5.6)\times10^{-7}$	94
(50 nm, 5×10^{18} cm^{-3}) / n^+-GaAs (50 nm, 3×10^{18} cm^{-3})				

temperatures below the eutectic point (a so-called diffusion contact) or by very strongly doping the skin layer of the original epitaxial structure.[2] We studied both possibilities. Diffusion contacts based on the metallization of AuGe / Ni /Au were formed by brazing at 300 °C for 30 min in a hydrogen atmosphere. This provided a higher percentage yield of serviceable test diode structures (to 90%) by comparison with alloy contacts. However, the technology developed for forming ohmic contacts based on the metallization of Ti / Au or Cr / Au seems more promising. Instead of an n^+-GaAs contact layer, layers of n^+-GaAs, n^+-$Ga_xIn_{1-x}As$ with variable composition, and n^+-$Ga_{0.5}In_{0.5}As$ were gradually grown. The total thickness of the contact layers was 0.15 μm. Various technologies for fabricating ohmic contacts are compared in Table II. A technology based on nonalloy contacts ensures a high yield of serviceable structures (more than 95%), reproducibility, and low contact resistance ($\rho_c < 5\times10^{-7}\ \Omega\cdot cm^2$).

As for GaAs-based SBDs, two main types of device structures are used when creating MW PDDs: those based on conductive (n^+-GaAs) substrates, and those based on semi-insulating (SI GaAs) substrates.[7,8] The latter version is more promising from the viewpoint of movement in the millimeter range, since structures based on a semi-insulating substrate make it possible to create diodes with beam leads having minimum stray parameters.[5] In addition, such structures are potentially suitable for monolithic integrated circuits. Relatively thick, buried n^+ layers (4–6 μm thick), which ensure a low series resistance, are ordinarily used in diodes based on semi-insulating substrates.[8] Since the characteristic growth rates of GaAs are about 1 μm/h for MBE, it takes much longer to grow such epitaxial structures. To reduce the duration of the MBE process, a combined process was developed. In this process structures with planar doping are grown on standard SAG-5 epitaxial structures (4–5 μm of n^+ GaAs on an SI GaAs substrate) obtained by vapor-phase epitaxy (VPE). To prevent a potential barrier from forming at the epitaxial-structure–substrate boundary, the growth process was begun with delta-doping of Si with a surface concentration of 5×10^{12} cm^{-2}.

The quality of epitaxial structures for PDDs and the homogeneity of their parameters are substantially affected by such factors as the features of the MBE apparatus that is used (most importantly, the homogeneity of the fluxes and the characteristic defect densities of the epitaxial layers), as well as the growth regime (in particular, whether or not the sub-

TABLE III. Comparison of technologies for fabricating PDDs.

Features of MBE	Type of substrate	Charge of p^+ layer, cm^{-2}	Lower contact layer; contact	Upper contact layer; contact	Φ_b, mV		Yield of serviceable diodes, %
					Calculation	Experiment	
A	n^+-GaAs	10^{12}	n^+-GaAs, 0.5 μm; AuGe / Ni / Au	n^+-GaAs, 0.4 μm; AuGe / Ni / Au	372	392±87	73
B	SI GaAs	4×10^{11}	n^+-GaAs, 4.5 μm; AuGe / Ni / Au	n^+-GaAs, 0.3 μm; AuGe / Ni / Au	414	527±41	86
C	SI GaAs	6.5×10^{11}	n^+-GaAs, 5.0 μm VPE +0.5 μm MBE; AuGe / Ni / Au	n^+-InGaAs / GaAs, 0.15 μm; Ti / Pt / Au	384	382±17	96

Note: For all the samples, the design value was $t = 10$ nm. *A* and *B* refer to the EP1203 apparatus with no sample rotation; *C* refers to the Riber 32P apparatus with sample rotation.

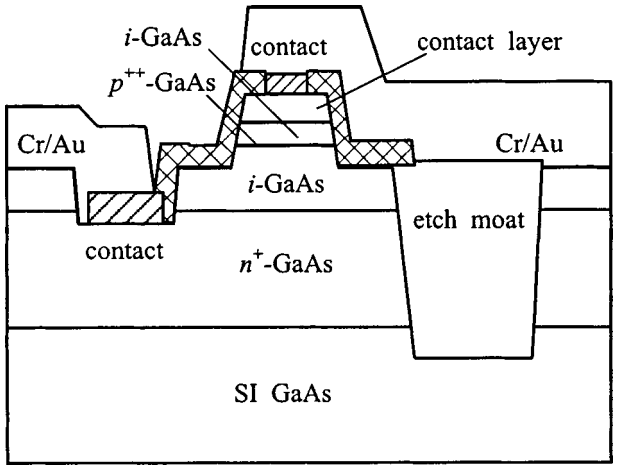

FIG. 2. Design of the diode.

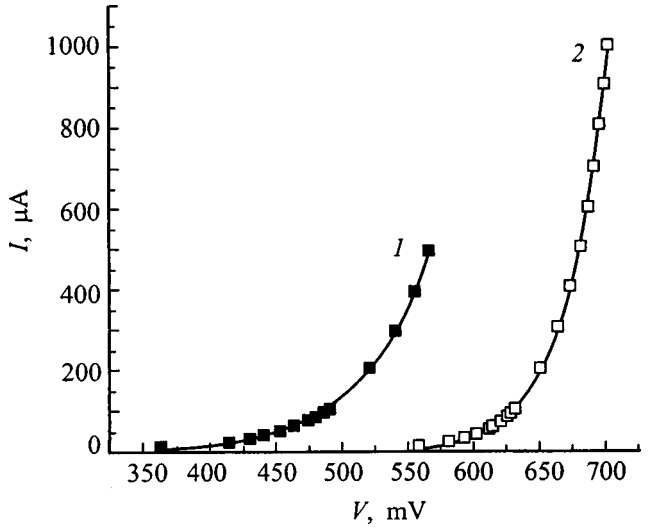

FIG. 3. The I–V characteristics of GaAs-based diodes: *1*—PDD, *2*—SBD.

strate rotates). The results of a comprehensive comparison of various methods of growing PDD structures is shown in Table III. It is evident that the last version (technology *C*) excels the first two (technologies *A* and *B*) in terms of the main parameters.

PDDs suitable for use in balance mixers of the 3-cm range were developed in the course of this study. Working devices have been implemented in the form of a monolithic diode pair (two diodes in one crystal). A planar design based on a semi-insulating substrate with insulation by air bridges is used in this case (Fig. 2), making it easy to keep the active regions small and minimizing the stray capacitance. The working epitaxial structure was grown on an AGChP-8 semi-insulating gallium arsenide (SI GaAs) substrate, using technology *C*, and consisted of the following layers: a buried n^+ layer 5 μm thick (grown by VPE), an n^+ layer 0.3 μm thick, an undoped layer 150 nm thick, a p^+ layer 10 nm thick doped with Be ($N_A = 7\times10^{17}\,\mathrm{cm}^{-3}$), an undoped layer 60 nm thick, and an upper contact layer with a total thickness of 0.15 μm. The diameter of the mesas was 15 μm, while that of the upper ohmic contact was 10 μm. Peroxide–sulfuric-acid and peroxide–ammonia etchants were used to fabricate the mesa structures. The devices were passivated by silicon dioxide obtained by plasmochemical deposition. The lower alloy ohmic contact was created by using AuGe / Ni / Au metallization, while the upper nonalloy contact used Ti / Pt / Au. The process of fabricating the device was completed by forming the second metallization based on Cr / Au, galvanically growing Au, etching the air bridges, and separating the crystals. The design and the diode-fabrication process described here are potentially suitable for millimeter-range devices (made in unpackaged form, with beam leads).

To adequately evaluate the characteristics of the PDDs, GaAs-based SBDs with an active layer 0.15 μm thick, a doping level of $(5–6)\times10^{16}\,\mathrm{cm}^{-3}$, and a barrier electrode 10 μm in diameter were fabricated using a similar technology. Figure 3 shows the I–V characteristics of the diodes, while Fig. 4 shows the dependences of the rectified current I on the MW signal power P_{in} with detection in the zero-bias regime (load resistance 100 Ω).

These studies show that the PDDs are characterized by a relatively weak dependence of the capacitance on the voltage and a low barrier height in comparison with the GaAs-based SBDs. The technology developed here ensures high uniformity of the parameters of the individual diodes, which is especially important in implementing balance mixers. The higher sensitivity of the PDDs at low signal powers makes it possible to use them in mixers with a low heterodyne signal level. A comparison of the Doppler noise of balance mixers fabricated using GaAs-based SBDs and PDDs showed that the PDDs reduce the low-frequency noise level by a factor of 1.5–2 and are as good as the best commercial Si-based SBDs in terms of this parameter. The mixers based on PDDs ensured that the given value of the conversion factor for heterodyne powers was a factor of 3–4 lower in this case than is required when GaAs-based SBDs are used.

In summary, a technology has been developed for fabricating structures based on gallium arsenide with planar-doped barriers by MBE, and a design and technology have

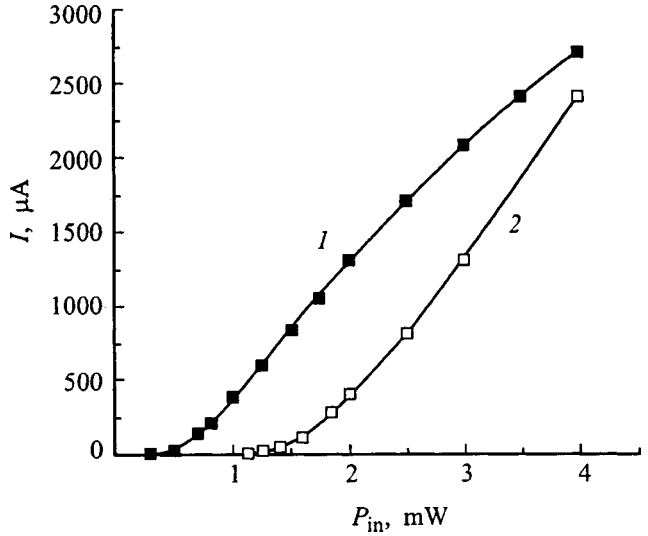

FIG. 4. Comparison of GaAs-based diodes operating in the zero-bias detector regime: *1*—PDD, *2*—SBD.

also been developed for fabricating MW diodes based on these structures. The proposed approach ensures that the parameters are reproducible, reduces the time of the epitaxial process, and makes it possible to create nonalloy ohmic contacts and to implement diodes of planar design. The advantages of PDDs in comparison with GaAs-based SBDs have been demonstrated.

[1] R. J. Malik, R. T. Aucoin, R. L. Ross, K. Board, C. E. C. Wood, and L. F. Eastman, Electron. Lett. **16**, 836 (1980).
[2] M. Shur, *GaAs Devices and Circuits* (Plenum Press, New York, 1987; Mir, Moscow, 1981).
[3] M. J. Kearney and I. Dale, GEC J. Res. **8**, 1 (1990).
[4] B. L. Sharma and S. C. Gupta, Semicond. Sci. Technol. **23**, 90 (1980).
[5] V. G. Bozhkov, V. V. Vilisova, K. I. Kurakan, O. Yu. Malakhovskiĭ, and T. M. Tabakeeva, Élektron. Prom. No. 9, 82 (1993).
[6] P. Marsh, D. Pavlidis, and K. Hong, IEEE Trans. Electron Devices **44**, 7 (1997).
[7] J. Dale, A. Condie, S. Neylon, and M. J. Kearney, IEEE MTT-S Digest (1989), p. 467.
[8] S. Hutchinson, M. Carr, R. Gwilliam, M. J. Kelly, and B. J. Sealy, Electron. Lett. **31**, 583 (1995).
[9] V. V. Tuyen and B. Szentpali, J. Appl. Phys. **68**, 2824 (1990).
[10] I. Dale, A. Condie, S. Neylon, and M. J. Kearney, in *Nineteenth European Microwave Conference Proceedings*, 1989, p. 237.
[11] V. M. Ustinov, A. Yu. Egorov, A. E. Zhukov, P. S. Kop'ev, V. A. Krasnik, and N. A. Maleev, Mikroelektronika **23**, 13 (1994).

Translated by W. J. Manthey

Suppression of Auger recombination in diode lasers utilizing InAsSb/InAsSbP and InAs/GaInAsSb type-II heterojunctions

G. G. Zegrya, M. P. Mikhaĭlova, T. N. Danilova, A. N. Imenkov, K. D. Moiseev, V. V. Sherstnev, and Yu. P. Yakovlev

A. F. Ioffe Physicotechnical Institute, Russian Academy of Sciences, 194021 St. Petersburg, Russia
(Submitted July 23, 1998; accepted for publication August 5, 1998)
Fiz. Tekh. Poluprovodn. **33**, 351–356 (March 1999)

The results of a comparative study of the temperature dependence of the threshold current, the differential quantum efficiency, and the polarization of light are reported for type-I and type-II InAsSb/InAsSbP heterostructures and for a tunneling injection laser utilizing a type-II GaInAsSb/InGaAsSb separate-confinement heterojunction. The theoretically predicted suppression of nonradiative Auger recombination in type-II InAsSb/InAsSbP lasers with a large ratio of band discontinuities at the interface $\Delta E_v/\Delta E_c = 3.4$ is verified experimentally. Weakening of the temperature dependence of the threshold current is established for both type-II laser configurations. The maximum working temperatures $T_{\lim} = 203$ and 195 K and the characteristic temperatures $T_0 = 40$ and 47 K are attained for (respectively) a conventional type-II InAsSb/InAsSbP laser and a type-II *p*-GaInAsSb/*n*-InGaAsSb tunneling injection laser.
 [S1063-7826(99)02103-1]

In recent years there has been growing interest in the design and study of long-wavelength lasers utilizing III-V compounds for the spectral range $\lambda = 2-5\ \mu$m, which have a promising potential for high-current laser diode spectroscopy and ecological monitoring.[1,2] So far, however, long-wavelength lasers ($\lambda > 3\ \mu$m) operating on interband transitions at room temperature are nonexistent. Projects on the design of long-wavelength lasers operating at high temperatures are currently in progress at several leading science centers.[2–7] Infrared lasers constructed on the basis of InAsSb/InAs, GaInAsSb/InAs, and AlGaAsSb/InAsSb double heterostructures grown by liquid-phase epitaxy, molecular-beam epitaxy, and vapor-phase epitaxy from organometallic compounds have been operating to date in the continuous-wave regime up to a temperature $T = 120$ K and in the pulsed regime up to $T = 255$ K. Consequently, the design of mid-IR lasers operating close to room temperature poses an important problem.

Several physical factors are responsible for limiting the operation of long-wavelength lasers at high temperatures. The main factors affecting the maximum operating temperature of a laser are: a) Auger recombination; b) intraband absorption of radiation; c) carrier heating processes. Auger recombination exerts the most powerful influence on the temperature dependence of the threshold current. This process is predominant over radiative recombination in bulk narrow-gap semiconductors of the type InAs, GaSb, and their solid solutions with a ''resonant'' band structure, where the width of the band gap E_g is close in energy to the spin-orbit (SO) splitting of the valence band Δ_{so} (Ref. 8). Several physical approaches have been proposed in recent years to suppress Auger recombination processes in narrow-gap heterostructures and to improve the temperature characteristics of long-wavelength lasers. These approaches include the application of strained-layer structures, type-II superlattices, and the fabrication of quantum-cascade lasers operating on intersubband transitions.[5–7] At present, two types of lasers — conventional bipolar and quantum-cascade unipolar — are on a par in terms of their optical power parameters and threshold currents. The major advantage of bipolar lasers utilizing double heterostructures is the relative simplicity of their structure and fabrication technology, which is of utmost importance for the practical application of such devices. With a decrease in the width of the band gap, however, nonradiative Auger processes begin to prevail in conventional interband-transition laser structures utilizing narrow-gap III-V compounds.[8]

In this study we confirmed experimentally a theoretical prediction of the suppression of Auger recombination in long-wavelength, type-II heterojunction laser structures. We also conducted a comparative study of type-I and type-II laser heterostructures and a comparative analysis of their Auger recombination rates.

THEORETICAL ANALYSIS

We consider the schematic band diagram of a type-II heterostructure with quantum wells (Fig. 1). Two Auger recombination processes are dominant in type-II heterojunctions: 1) the CHHS Auger process involving an electron and a hole with transition of the hole into a SO-split-off band; 2) the CHCC process involving the transition of a hot electron into the conduction band. The CHCC process prevails over the CHHS process if the following condition is satisfied:

$$(E_g - \Delta_{so})/E_g > m_c/m_{so},$$

where Δ_{so} is the magnitude of the SO splitting of the valence band, E_g is the effective width of the band gap, and m_c and m_{so} are the effective masses of the electron and the hole in the SO-split off band, respectively.

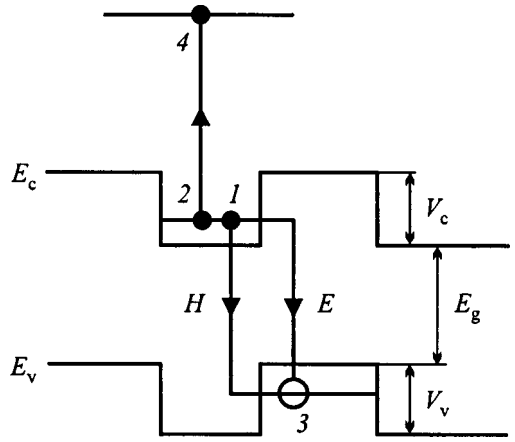

FIG. 1. Band energy diagram of a type-II heterostructure with quantum wells: (*1, 2*) initial states of particles in recombination; (*3, 4*) final states; *H* and *E* are the two possible channels of electron-hole recombination.

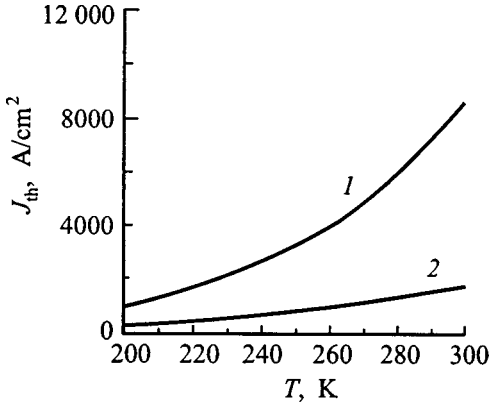

FIG. 3. Calculated temperature dependence of the threshold current density J_{th} of a type II heterojunction laser structure for $V_v = V_c$ (*1*) and $V_v = 3V_c$ (*2*). The calculations have been carried out for a square quantum well with well and barrier dimensions $a = b = 80$ Å.

In type-II heterostructures, where the band discontinuities have the same sign, nonequilibrium electrons and holes are spatially separated, existing on opposite sides of the heterojunction. Consequently, the radiative recombination of nonequilibrium electrons and holes becomes possible when they tunnel through the heterojunction. This means that two recombination channels can exist in such structures: the *E* channel, where a tunneling electron recombines with a hole in a quantum well, and the *H* channel, where a tunneling hole recombines with an electron in a quantum well. As a result, as shown in Ref. 9, the amplitudes of the two channels introduce a destructive contribution in the Coulomb interaction matrix element and, hence, in the Auger recombination rate. Here the Auger recombination rate becomes a nonmonotonic function of the heights of the heterojunctions for electrons (V_c) and holes (V_v). For a specific ratio between V_c and V_v the Auger recombination rate has a minimum, as demonstrated by the theoretical curve in Fig. 2. For real heterostructures the minimum shifts toward smaller ratios V_v/V_c. Since the radiative recombination rate R depends weakly on V_v/V_c, the ratio of the radiative and nonradiative recombination rates R/G has a maximum at the value of V_v/V_c where G passes through a minimum.

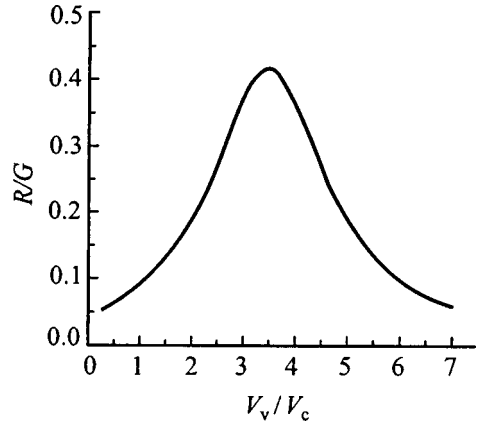

FIG. 2. Dependence of the ratio of radiative (R) and nonradiative (G) recombination rates on the ratio of the barrier heights in the valence and conduction bands at the heterojunction V_v/V_c. The calculations have been carried out for a square quantum well with well and barrier dimensions $a = b = 80$ Å, $T = 250$ K.

It has been shown[10] that the contributions to the Auger transition matrix element (M) from the two recombination channels E and H are of the same order of magnitude because of the mutual conversion of light holes and heavy holes when they interact with the heterojunction. These contributions to M have opposite signs and cancel each other. As a result, the matrix element M of the Auger recombination process in type-II heterojunctions has an additional smallness of the order of $[Tm_h/V_c m_c]^{3/2} < 1$, where T is the lattice temperature, and m_h is the effective hole mass. Since the two recombination channels interfere destructively, the end result is a reduction in the Auger recombination rate in type-II heterostructures. This conclusion is corroborated by the deep minimum for the Auger recombination rate in the dependence of G on V_v/V_c (Fig. 2). It is important to compare the Auger recombination rate in type-II heterostructures at the minimum ($G^{\min}$) with the same rate in a type-I heterostructure (G_I):

$$\frac{G^{\min}}{G_I} \sim \left(\frac{T}{V_c}\frac{m_h}{m_c}\right)^3 \frac{V_c}{E_g} \ll 1.$$

In contrast with type-I heterostructures, therefore, appreciable suppression of the Auger recombination process is possible in type-II heterostructures. On the other hand, the radiative recombination rates are comparable for type-I and type-II heterojunctions: $R_{II}/R_I \sim 1$.

Consequently, our theoretical analysis shows that the ratio of the radiative recombination rate (R_{II}) to the nonradiative Auger recombination rate in type-II heterostructures can have a sharp maximum, which, in turn, depends on the ratio of the barrier heights V_c and V_v at the heterojunction. We can therefore lower the Auger recombination rate significantly by a suitable choice of parameters for the type-II heterostructure. Accordingly, the temperature dependence of the internal quantum efficiency (η) and the threshold current density (J_{th}) also depend strongly on the ratio V_v/V_c, as shown in Figs. 3 and 4 (Ref. 11). We have verified the sup-

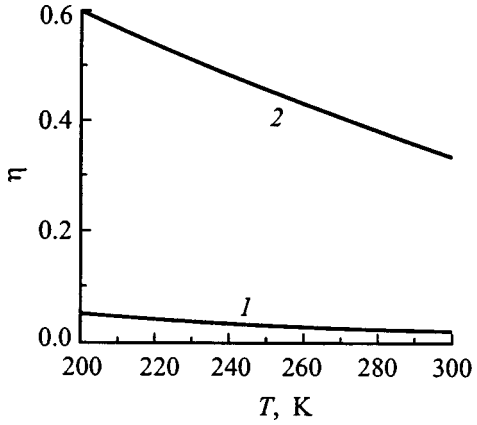

FIG. 4. Calculated temperature dependence of the internal quantum efficiency η for $V_v = V_c$ (*1*) and $V_v = 3V_c$ (*2*). The calculations have been carried out for a square quantum well with well and barrier dimensions $a = b = 80$ Å.

pression of Auger recombination experimentally in the example of long-wavelength InAs(Sb)/InAsSbP laser heterostructures with type-I and type-II heterojunctions between the active layer and the cladding layers, along with type II GaInAsSb/InGaAsSb heterostructures.

EXPERIMENT

Two types of InAsSb/InAsSbP heterostructure lasers with separate electron and optical confinement were grown by liquid-phase epitaxy on InAs(100) substrates (Fig. 5). In one of the structures the active layer formed a type-II heterojunction with cladding layers (Fig. 5a); the second structure had a type-I heterojunction (Fig. 5b). Electron confinement was provided by InAs layers in the first case and by $InAs_{0.84}Sb_{0.06}P_{0.1}$ layers in the second case. The composition of the active region and the optical confinement layers were identical for both structures ($InAs_{0.95}Sb_{0.05}$ and $InAs_{0.5}Sb_{0.16}P_{0.34}$, respectively). The band discontinuities (ΔE_c and ΔE_v) at the heterojunctions between the active region and the cladding layers in the type-II lasers were set equal to $\Delta E_c \sim 15$ meV and $\Delta E_v \sim 52$ meV, i.e., their ratio was $\Delta E_v / \Delta E_c = 3.4$, which should correspond to the minimum Auger recombination rate G^A (Fig. 2).

In addition, two types of tunneling injection lasers incorporating a type-II GaInAsSb/InGaAsSb heterojunction in the

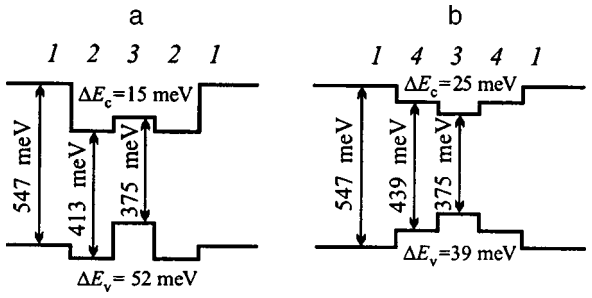

FIG. 5. InAsSb/InAsSbP laser structures: (a) with a type-II heterojunction at the interface with the active region; (b) with a typ-I heterojunction at the interface with the active region; (*1*) layer of solid solution $InAs_{0.52}Sb_{0.18}P_{0.3}$; (*2*) InAs; (*3*) $InAs_{0.95}Sb_{0.05}$; (*4*) $InAs_{0.84}Sb_{0.06}P_{0.1}$.

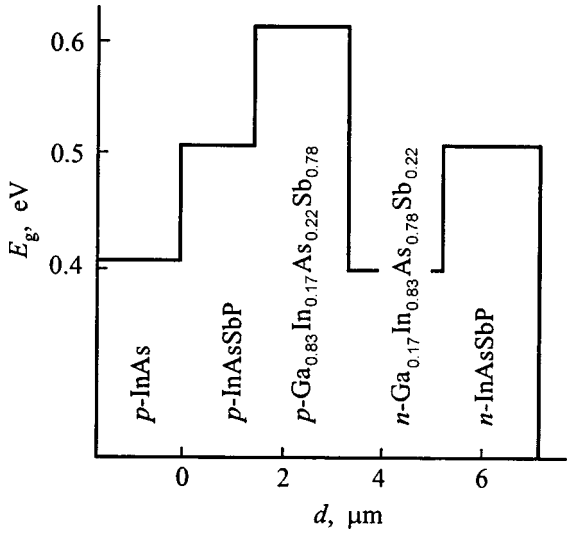

FIG. 6. Schematic diagram of the structure of a tunneling injection laser with a *p*-GaInAsSb/*n*-InGaAsSb separate-confinement type-II heterojunction in the active region.

active region were grown by liquid-phase epitaxy on InAs(100) substrates.[12] The active region of these lasers consisted of two quaternary solid solutions $Ga_{1-x}In_xAs_ySb_{1-y}$, one wide-gap ($x = 0.17$, $y = 0.22$) and the other narrow-gap ($x = 0.83$, $y = 0.78$), which formed a separate-confinement type-II heterojunction (Fig. 6). The layers of the solid solution $InA_{0.62}Sb_{0.12}P_{0.26}$ were used to improve the optical confinement. This structure was invested with good electron confinement by high barriers at the heterojunction ($\Delta E_c = 640$ meV and $\Delta E_v = 420$ meV).

Mesa stripe lasers were fabricated by standard lithography with a stripe width of 15 μm and a cavity length of the order of 350 μm. All the types of laser structures were investigated in the pulsed regime with a pulse length of 100–500 ns and a repetition rate of 10^5 Hz in the temperature range $T = 77 - 200$ K. The temperature dependence of the threshold current, the differential quantum efficiency, and the polarization of radiation in the spontaneous and coherent regimes were investigated.

RESULTS AND DISCUSSION

Type-I and Type-II Heterostructures Based on an InAsSb/InAsSbP Heterojunction

We have set ourselves the objective of investigating the characteristics of laser structures with various ratios $\Delta E_v / \Delta E_c$. It has been shown[10] that the maximum suppression of nonradiative Auger recombination is attainable for a ratio $\Delta E_v / \Delta E_c \sim 3 - 4$. In addition, increasing ΔE_v has a positive effect on the localization of holes in the active region of the laser structure, an important asset in relation to lasing near room temperature. We have investigated the temperature dependence of the threshold current (Fig. 7) and the differential quantum efficiency (Fig. 8) on the structures shown in Fig. 5. While a characteristic temperature $T_0 = 35 - 40$ K and limiting working temperature $T_{\lim} = 203$ K are attained for the type-II InAsSb/InAsSbP heterojunction laser (Fig. 7, curve *2*), the same characteristics for the laser struc-

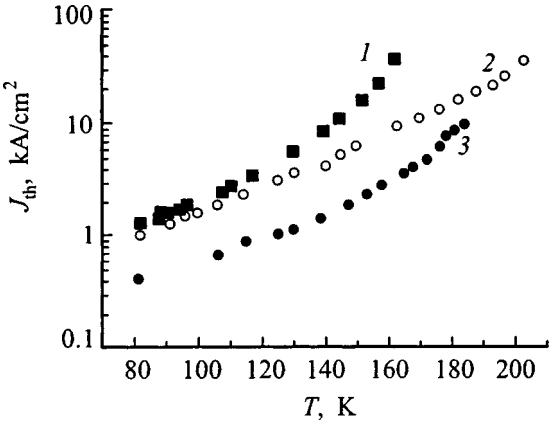

FIG. 7. Temperature dependence of the threshold current J_{th} for three types of laser structures: (*1*) InAsSb/InAsSbP laser with a type-I heterojunction ($T_0=25$ K, $T_{lim}=160$ K); (*2*) type-II InAsSb/InAsSbP heterojunction laser ($T_0=40$ K, $T_{lim}=203$ K) with a type-II heterojunction; (*3*) GaInAsSb/InGaAsSb laser with a type-II heterojunction in the active region ($T_0=47$ K, $T_{lim}=195$ K).

ture utilizing a type-I heterojunction are $T_0=25-28$ K and $T_{lim}=145$ K (Fig. 7, curve *3*). It is important to note that the absolute values of the threshold current J_{th} and the quantum efficiency η for both types of laser structures are close at $T=77$ K, but their temperature dependences differ markedly. A significant difference for the two investigated types of structure is observed in the temperature dependence of the differential quantum efficiency (Fig. 8). While $\eta\sim 20\%$ for both types of structures at a low temperature (77 K), for type-I heterojunction lasers it drops more steeply with the temperature, indicating a sizable contribution from the nonradiative Auger process. For example, when the working temperature is raised to 120 K, the quantum efficiency in the type-II heterojunction structures is four times its value for type-I heterojunction lasers. A comparison of the two types of laser structures having an active region based on a type-II heterojunction with different ratios $\Delta E_v/\Delta E_c$ reveals substantial weakening of the temperature dependence of the threshold current and the attainment of a higher working

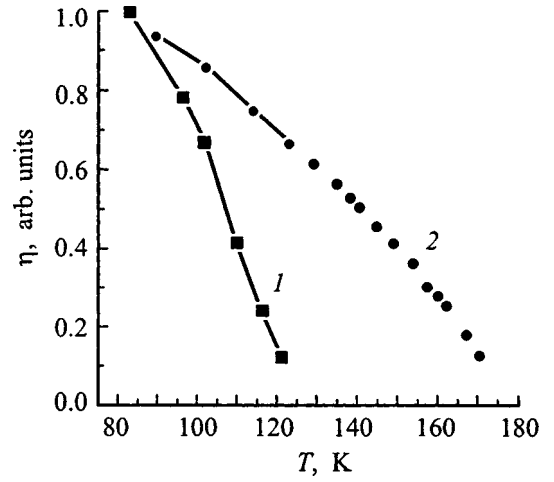

FIG. 8. Temperature dependence of the differential quantum efficiency for the two laser structures shown in Fig. 5: (*1*) type-I heterostructure; (*2*) type-II heterostructure.

temperature for type-II heterojunction lasers with $\Delta E_v/\Delta E_c\sim 3$. This experimental result is, in our view, direct confirmation of the theoretically predicted[9–11] mechanism underlying the suppression of Auger recombination at a type-II heterojunction.

To compare the roles of type-I and type-II heterointerfaces in radiative recombination processes, we have investigated the polarization of the laser beam. We have uncovered an appreciable TM-polarization contribution in both types of laser structures (the vector **E** is perpendicular to the plane of the *p-n* junction). The degree of polarization α is determined from the standard relation

$$\alpha=\frac{P_{TM}-P_{TE}}{P_{TM}+P_{TE}},$$

where P_{TM} and P_{TE} are the radiation intensities for TM- and TE-polarized light, respectively. The maximum values of α are 80% and 73% (at a current $J\sim 1.5J_{th}$) for type II and type I heterostructures, respectively. It has been shown[12] that TM polarization is typical of indirect radiative transitions associated with carrier-heterojunction interaction.

We can conclude, therefore, that interface recombination is predominant in the temperature interval 77–120 K in lasers with an type-II InAsSb/InAsSbP heterojunction between the active region and the cladding layers.

We have estimated the Auger recombination coefficients of type-I and type-II laser heterostructures by comparing the theoretical results with the experimental data. The threshold current J_{th} can be specified in a form that takes into account the contributions of radiative (J_{ph}) and nonradiative (J_A) recombination:

$$J_{th}\sim e(R_{ph}+G_A)=J_{ph}+J_A,$$

where R_{ph} and G_A are the two-dimensional radiative and Auger recombination rates, respectively. At high temperatures ($T>150$ K), where the main contribution to the current is from the Auger process, the threshold current is

$$J_{th}\sim J_A=eC_A(n_{th})^3,$$

where C_A is the Auger coefficient, and n_{th} is the two-dimensional concentration at the lasing threshold. The characteristic temperature T_0 is now determined from the relation

$$1/T_0=d(\ln J_{th})/dT.$$

Using the experimentally determined threshold currents in type-I and type-II heterostructures, we have estimated the values of the two-dimensional Auger recombination coefficients at $T=160$ K:

$$C_A^{I}\sim 2\times 10^{-15}\,\text{cm}^4/\text{s} \quad \text{and} \quad C_A^{II}\sim 4.6\times 10^{-16}\,\text{cm}^4/\text{s}.$$

Thus, Auger recombination is suppressed by the factor $C_A^{I}/C_A^{II}\sim 4.4$ in type-II heterostructures. This reduction is further corroborated by an increase in the quantum efficiency and a decrease in the threshold current by approximately the same ratio.

Laser Utilizing a Separate-Confinement Type-II 1-GaInAsSb/InGaAsSb Heterojunction with an Improved Temperature Characteristic

As mentioned in the description of the experiment, we have fabricated a tunneling injection laser structure using a separate-confinement type-II *p-n* heterojunction in the system of solid solutions p-$Ga_{0.83}In_{0.17}As_{0.22}Sb_{0.78}$/$n$-$In_{0.83}Ga_{0.17}As_{0.78}Sb_{0.22}$ (Fig. 6). We first described the concept and initial implementation of this type of laser in Ref. 13. As expected, the asymmetric structure of the band discontinuities and the large heights of the cutoffs in the conduction and valence bands at the heterojunction ($\Delta E_c \sim 640$ meV and $\Delta E_v \sim 420$ meV) endow such a structure simultaneously with good electron and hole confinement. Since the principal mechanism of radiative recombination in the structure is tunneling radiative recombination through quantum states at the type-II heterojunction, we expected to see the suppression of Auger recombination and a weaker temperature dependence of the threshold current in comparison with the results of Ref. 12, in which a like-carrier (*p-p*), separate-confinement type-II heterojunction was used in the active region, and strong leakage of holes across the heterojunction created a high threshold current. Indeed, it is evident from Fig. 7 that the threshold current in the investigated structure utilizing a type-II *p-n* heterojunction is four times smaller than in the previous type-II *p-p* heterojunction laser structure described in Ref. 12. The temperature dependence of the threshold current is weaker than in InAsSb/InAsSbP lasers operating in the same spectral interval of $3.2-3.4\ \mu$m at $T=77$ K. The GaInAsSb/InGaAsSb laser operates in the pulsed regime up to 200 K, with a characteristic temperature $T_0=47$ K. When the temperature is raised above 150 K, the threshold current increases considerably ($T_0=30$ K). This behavior can be attributed to the threshold current contribution from the Auger process associated with the transition of a hot hole into the SO-split-off band (CHHS) and to the absorption of radiation by free carriers inside the valence zone.

An investigation of the polarization of light in the spontaneous and coherent regimes for this laser structure have also demonstrated the predominant role of TM polarization with an increase in the current. This result corroborates the tunneling origin of optical radiative transitions through the type-II heterojunction.

To further improve the characteristics of long-wavelength lasers and to elevate their working temperature to room temperature, the design of the laser structure will have to be improved and other processes (carrier leakage across the heterojunctions, intraband absorption, and carrier heating) will have to be taken into account. We note that the suppression of Auger recombination has also been observed in quantum-well laser structures utilizing type-II heterojunctions.[13–15]

CONCLUSIONS

We have carried out comparative studies of laser heterostructures utilizing type-I and type-II heterojunctions in the systems of solid solutions InAsSb/InAsSbP and GaInAsSb/InGaAsSb. We have observed experimentally the theoretically predicted suppression of Auger recombination in laser with a type-II heterointerface. The suppression of Auger recombination produces a substantial increase in the quantum efficiency and raises the working temperature of laser structures based on a type-II GaInAsSb/InGaAsSb heterojunction. We have estimated the Auger recombination rate constants in type-I and type-II heterostructures. We have shown that nonradiative Auger recombination can be controlled within reasonable limits by the right choice of heterostructure parameters (relative heights of the barriers at the heterojunction boundary ΔE_c and ΔE_v). The working temperature limit of long-wavelength lasers can be raised to room temperature or higher by further optimizing the laser structure with allowance for other processes (carrier leakage across the heterojunctions, intraband absorption, and carrier heating).

This work has received partial support from the Russian Fund for Fundamental Research, Projects No. 96-17841a and No. 98-07-90336, and from the Ministry of Science Program ''Physics of Solid State Nanostructures,'' Projects No. 96-1010 and No. 97-0003.

[1] A. I. Nadezhdinski and A. M. Prokhorov, Proc. SPIE **1724**, 2 (1992).
[2] A. Popov, A. Baranov, V. Sherstnev, Yu. Yakovlev, B. Scheumann, R. Mucke, and P. Werle, in *Program and Abstracts of the Fourth International Symposium on Ionization Phenomena* (Freiburg, 1994).
[3] A. N. Baranov, A. N. Imenkov, V. V. Sherstnev, and Yu. P. Yakovlev, Appl. Phys. Lett. **64**, 2480 (1994).
[4] M. Aidaraliev, N. V. Zotova, B. A. Matveev, N. M. Stus', and G. N. Talalakin, Semicond. Sci. Technol. **2**, 1575 (1993).
[5] H. K. Choi, G. W. Turner, S. J. Eglash, and Z. L. Liau, Appl. Phys. Lett. **65**, 2251 (1994).
[6] J. H. Zhang, Appl. Phys. Lett. **66**, 118 (1995).
[7] J. Faist, F. Capasso, D. L. Sivko, C. Sirtori, A. L. Hutchinson, and A. J. Cho, Science **264**, 553 (1994).
[8] B. L. Gel'mont, Z. N. Sokolova, and I. N. Yassievich, Fiz. Tekh. Poluprovodn. **16**, 592 (1982) [Sov. Phys. Semicond. **16**, 382 (1982)].
[9] G. G. Zegrya and A. D. Andreev, Appl. Phys. Lett. **67**, 2681 (1995).
[10] G. G. Zegrya and A. D. Andreev, Zh. Éksp. Teor. Fiz. **109**, 615 (1996) [JETP **75**, 328 (1996)].
[11] N. S. Averkiev, A. N. Baranov, A. N. Imenkov, A. A. Rogachev, and Yu. P. Yakovlev, Pis'ma Zh. Tekh. Fiz. **13**, 332 (1987) [Sov. Tech. Phys. Lett. **13**, 135 (1987)].
[12] K. D. Moiseev, M. P. Mikhaĭlova, O. G. Ershov, and Yu. P. Yakovlev, Pis'ma Zh. Tekh. Fiz. **21**(12), 83 (1995) [Tech. Phys. Lett. **21**, 482 (1995)].
[13] J. R. Meyer, C. A. Hoffman, and F. J. Bartoli, Appl. Phys. Lett. **67**, 757 (1995).
[14] C. L. Felix, J. R. Meyer, I. Vurgaftman, C.-H. Lin, S. J. Murry, D. Zhang, and S.-S. Pei, IEEE Photonics Technol. Lett. **PTL-9**, 734 (1997).
[15] T. Hasenberg, R. H. Miles, A. R. Kost, and L. West, IEEE J. Quant. Electron. **QE-33**, 1403 (1997).

Translated by James S. Wood

Bistability of electroluminescence in a type-II AlGaAsSb/InGaAsSb double heterostructure

B. E. Zhurtanov, K. D. Moiseev, M. P. Mikhaĭlova, T. I. Voronina, N. D. Stoyanov, and Yu. P. Yakovlev

A. F. Ioffe Physicotechnical Institute, Russian Academy of Sciences, 194021 St. Petersburg, Russia
(Submitted August 5, 1998; accepted for publication August 6, 1998)
Fiz. Tekh. Poluprovodn. **33**, 357–361 (March 1999)

Electroluminescence bistability is observed in a typ-II *P*-AlGaAsSb/*p*-InGaAsSb/*N*-AlGaAsSbheterostructure with lightly doped cladding layers and a narrow-gap active region (the width of the band gap is $E_g = 326$ meV at the temperature $T = 77$ K). A current-controlled negative differential resistance is observed in the forward branch of the current-voltage characteristic. Strong narrowband electroluminescence (half-width $\sim 7-10$ meV) is observed at the end of the negative differential resistance interval, where the photon energy at the radiation maximum exceeds the width of the band gap of the narrow-gap material by 50 meV. This phenomenon is attributed to the tunneling injection and indirect radiative recombination of carriers localized at the AlGaAsSb/InGaAsSb heterojunction. As the voltage is increased, radiative transitions in the bulk of the active region begin to provide the main contribution, and the radiation maximum jumps to the long-wavelength end. Tunneling injection structures of this kind can be used to construct highly efficient current-controlled light-emitting diodes. © *1999 American Institute of Physics.* [S1063-7826(99)02203-6]

Type-II heterostructures made from In(Ga)AsSb solid solutions, which are isoperiodic with InAs and GaSb substrates, and InAs/Ga(In)Sb quantum-well structures have been vigorously studied in recent years as promising structures for the design of lasers operating in the spectral range $\lambda = 3-5\ \mu$m (Refs. 1–4). This range contains absorption bands of many industrial gases, so that the design of such light sources has important bearing on gas analysis and ecological monitoring problems. A new type of tunneling injection laser utilizing separate-confinement type II heterojunctions has been proposed recently. In such a laser carriers are injected into the active region by the resonant tunneling of electrons across the heterojunction, thereby obviating the need for additional electron confinement.[5] I has also been predicted theoretically[6,7] that nonradiative Auger recombination can be suppressed at a type-II heterojunction. All these considerations focus close attention on the study of type-II heterojunctions.

In this paper we give the results of a detailed investigation of the bistability of injection electroluminescence in double heterostructure lasers utilizing type-II $Al_xGa_{1-x}AsSb/In_{1-x}Ga_xAsSb$ heterojunctions with a narrow-gap active region and asymmetric band discontinuities at the heterojunction.

The investigated $Al_xGa_{1-x}AsSb/InGaAsSb$ laser structures with a high Al content in the cladding layers ($x = 0.63$) were grown by liquid-phase epitaxy on a *p*-GaSbn(100) substrate (Fig. 1a). A layer of the narrow-gap solid solution $In_{0.93}Ga_{0.07}As_{0.82}Sb_{0.18}$ (width of the band gap $E_g = 0.326$ meV at $T = 77$ K) was chosen as the active region; it was placed between two layers of the wide-gap solid solution $Al_{0.63}Ga_{0.37}AsSb$ ($E_g = 1.47$ meV at $T = 77$ K). Either the *P*-AlGaAsSb cladding layers were intentionally left undoped, or they were lightly doped with a Zn impurity from the fluxed melt during growth, so that the density of carriers in them did not exceed $p = 1 \times 10^{17}\ \text{cm}^{-3}$. The carrier density in the Te-doped *N*-AlGaAsSb cladding layers was of the order of $n = 4 \times 10^{17}\ \text{cm}^{-3}$. The *p*-type active region was doped with Zn during growth to a carrier density $p = 2 \times 10^{17}\ \text{cm}^{-3}$. The band energy diagram of the AlGaAsSb/InGaAsSb heterostructure is a stepped type-II heterojunction with asymmetric band discontinuities at the heterojunction $\Delta E_c = 1.35$ eV (conduction band) and $\Delta E_v = 0.2$ eV (valence band), as established in Ref. 8 (Fig. 1b).

Mesa-stripe laser structures with a cavity length of $350\ \mu$m and a stripe width of $11\ \mu$m were constructed by standard photolithography. The electroluminescence was investigated in the quasi-steady-state regime driven by current pulses of duration 2.5 ms with an off-duty factor equal to 2. The electroluminescence spectra were recorded by an MDR-4 grating monochromator with a 150-line grating. The infrared signal receiver was a liquid-nitrogen-cooled InSb photoresistance.

The current-voltage (*I-V*) characteristics and electroluminescence of forward-biased typ-II *P*-AlGaAsSb/*p*-InGaAsSb/*N*-AlGaAsSb double heterostructures were investigated at $T = 77$ K.

Strong bistability of the current *J* from the applied voltage *U* is observed in the forward branch of the *I-V* characteristic of the investigated structure, and the *I-V* characteristic is S-shaped with a negative differential resistance (NDR) interval and a turn-on voltage $U_{on} = 3.6$ V (Fig. 2). We note that such a behavior of the *I-V* characteristic has been observed previously in InAs/AlGaSb resonant-tunneling double heterostructures.[9]

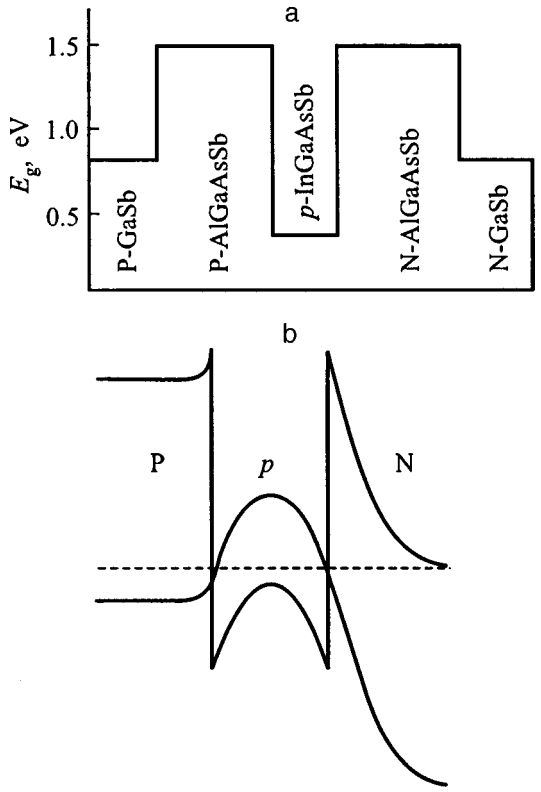

FIG. 1. Layered profile of the band gap of the laser structure (a) and band energy diagram of a type-II *P*-AlGaAsSb/*p*-InGaAsSb/*N*-AlGaAsSb double heterostructure in thermodynamic equilibrium (b).

On the first part of the forward branch of the *I-V* characteristic the total current through the structure increases slowly and does not exceed 60 mA at the turn-on voltage. Faint electroluminescence begins to appear immediately after turn-on (the beginning of the NDR interval, $U=3.47$ V). The emission spectrum (Fig. 3) contains a single band with a photon energy at the maximum $h\nu_m \simeq 370$ eV ($\lambda_m \simeq 3.34\,\mu$m) and a half-width of the order of 30 meV. As the control current is increased, the voltage on the structure is observed to drop abruptly to 1.1 V (Fig. 2), and strong electroluminescence sets in with a threshold be-

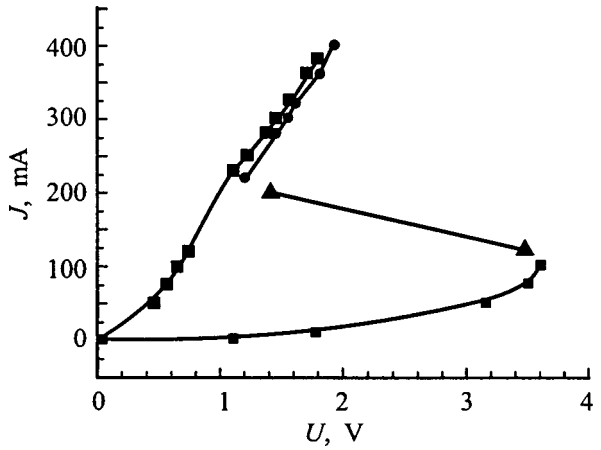

FIG. 2. Current-voltage curve of a forward-biased type-II *P*-AlGaAsSb/*p*-InGaAsSb/*N*-AlGaAsSb double heterostructure.

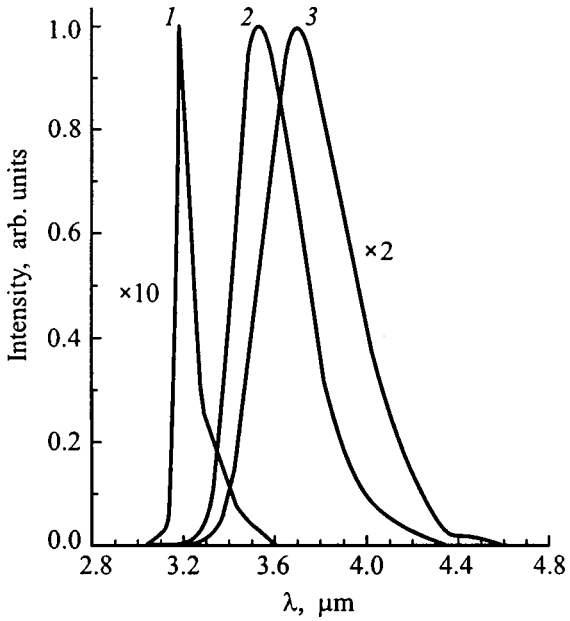

FIG. 3. Electroluminescence spectra for various bias voltages: (*1*) $U=1.1$ V; (*2*) $U=1.4$ V; (*3*) $U=1.8$ V, $T=77$ K.

havior at the end of the NDR interval. Now a single band having an asymmetric shape with a half-width of 7–10 meV and a sharp short-wavelength edge is observed in the spectrum (Fig. 3). The maximum of the band occurs at a wavelength $\lambda_m=3.3\,\mu$m, which corresponds to a photon energy $h\nu_m=376$ eV. It is important to note that this band is shifted almost 50 meV along the energy scale in comparison with the width of the band gap of the active region of the laser structure ($E_g=0.326$ meV). The intensity of the observed superluminescence for the given band is comparable with the emission intensity of a diode laser at the lasing threshold.

The asymmetric shape of the emission band, its high intensity, and the ''blue'' shift of the photon energy at the maximum of the emission spectrum mandated a more detailed investigation of the electroluminescence characteristics of such heterostructures with a view toward determining the possible mechanisms of radiative recombination in laser double heterostructures utilizing AlGaAsSb/InGaAsSb type-II heterojunctions with asymmetric band discontinuities at the heterojunction.

We note that the total voltage is distributed nonuniformly in the structure. In the investigated laser structures the narrow-gap *p*-InGaAsSb active layer is bounded by wide-gap *P*-type and *N*-type AlGaAsSb emitter layers. Based on data from a scanning electron microscope examination of chips of the investigated heterostructures in the induced current regime, it has been established that a very large space-charge region is situated in the *N*-AlGaAsSb cladding layer, i.e., a strong built-in electric field exists near the *p*-InGaAsSb/*N*-AlGaAsSb heterojunction. Consequently, an external bias voltage applied in the structure drops mostly (about 2.0 V, based on our estimates) near the *N*-AlGaAsSb/*p*-InGaAsSb heterojunction, and a comparatively small fraction of it drops at the *P*-AlGaAsSb/*p*-InGaAsSb heterojunction.

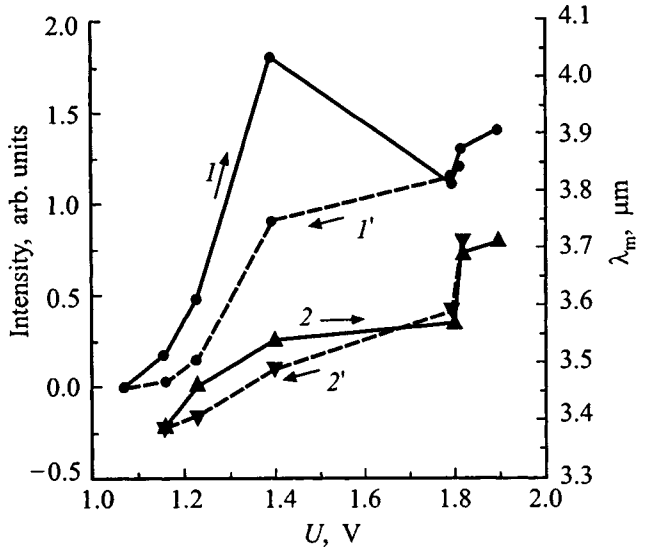

FIG. 4. Dependences of the electroluminescence intensity (*1*, *1′*) and emission wavelength λ_m (*2*, *2′*) on the applied voltage *U*.

Figure 4 shows the dependences of the emission wavelength λ_m (curves *2* and *2′*) and intensities (curves *1* and *1′*) on the applied external bias *U* corresponding to the voltage interval on the part of the *I-V* characteristic after transition through the NDR interval (Fig. 5). Three characteristic intervals are also discerned on these curves. The emission intensity increases sublinearly as the external bias is increased in the voltage interval 1.1–1.4 V. The maximum of the emission band shifts toward the long-wavelength end to $\lambda_m \simeq 3.5\ \mu$m, and the electroluminescence band broadens to 20 meV. However, the shape of the band remains asymmetric with a steep short-wavelength edge. The current through the structure increases superlinearly in this voltage interval.

A further increase of the external bias in the voltage interval $U = 1.4 - 1.8$ V causes the emission voltage to suddenly drop by one half, while the wavelength corresponding to the maximum of the emission band remains constant ($\lambda_m = 3.5\ \mu$m). It should be emphasized that the current through the structure increases in this voltage interval, gradually approaching saturation.

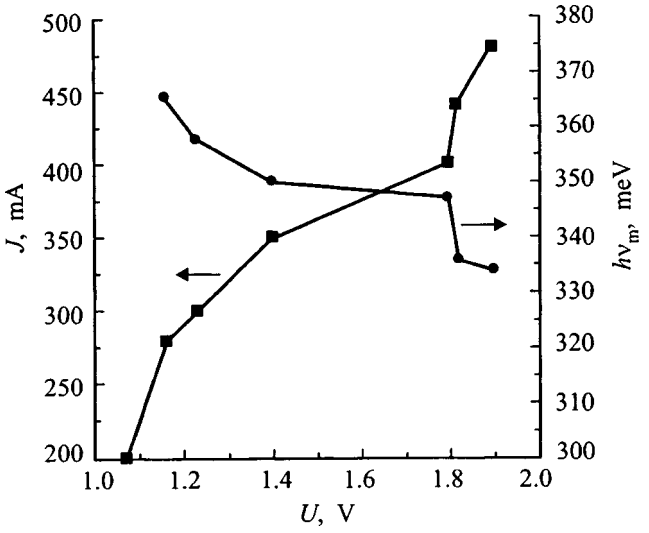

FIG. 5. Current-voltage characteristic and dependence of the emission energy on the voltage for a type-II *P*-AlGaAsSb/*p*-InGaAsSb/*N*-AlGaAsSb double heterostructure after traversal of the negative differential resistance interval.

It is interesting to note that the behavior of all three graphs representing the voltage dependences of the current, emission wavelength, and emission intensity exhibits an abrupt change at an external bias voltage $U \simeq 1.8$ V. A linear dependence of the current on the voltage is observed at an external bias above 1.8 V, its slope corresponding to a residual series resistance $R_s = 1\ \Omega$. In this case the emission intensity in the voltage interval 1.8–2.0 V increases slightly, approaching saturation at $U > 2.0$ V. The maximum of the emission band, in turn, suddenly shifts in the long-wavelength direction to $\lambda_m \simeq 3.8\ \mu$m, which corresponds to the characteristic wavelength for interband radiative recombination in the bulk of the narrow-gap solid solution $In_{0.94}Ga_{0.06}As_{0.82}Sb_{0.18}$. The shape of the observed emission band is nearly symmetric (Gaussian) with a half-width of 30 meV, which is also characteristic of interband transitions.

It is evident from Fig. 4 that the plot of the intensity versus voltage has hysteresis. When the external bias is lowered from 2.0 V to 1.05 V (reverse path, curves *1′* and *2′*), the behavior of the electroluminescence intensity and emission wavelength curves repeats the behavior of these curves when the external bias is increased (forward path, curves *1* and *2*) in the voltage intervals 1.1–1.4 V and 1.8–2.0 V. In the voltage interval 1.4–1.8 V, however, the electroluminescence intensity decreases monotonically as the external bias is either increased or decreased.

Thus, it is evident from the experimental data that the electroluminescence spectrum of an AlGaAsSb/InGaAsSb/AlGaAsSb depends strongly on the applied external bias. At the instant of onset of superluminescence the maximum of the emission band shifts upward 50 meV along the energy scale in comparison with the width of the band gap of the narrow-gap layer; now the band has a highly asymmetric profile, and its half-width is close to *kT*. As the voltage on the structure is increased (to 2 V), this narrow emission band gradually transforms into a longer-wavelength band ($h\nu_m \simeq 326$ meV) with a symmetric profile of half-width of 30 meV, which is typical of interband radiative transitions. We should add that we have previously observed such a ''blue'' shift of the electroluminescence due to the strong pileup of electrons at a type-II heterojunction in an AlGaAsSb/InGaAsSb double laser heterostructure with cladding layers containing 34% Al (Ref. 10), in quantum-well structures,[11] and in GaAs/GaAlAs superlattices.[12]

To analyze the possible mechanism of radiative recombination and current flow through the structure, we consider the band energy diagram of a forward-biased type II *P*-AlGaAsSb/*p*-InGaAsSb/*N*-AlGaAsSb heterostructure (Fig. 6). An electron channel exists at the type II *P*-AlGaAsSb/*p*-InGaAsSb heterojunction in thermodynamic equilibrium.[13] In the given situation a two-dimensional electron gas accumulates in the quantum well near the heterojunction on the side of the narrow-gap semiconductor, as a result of the resonant transition of electrons from the deep acceptor level E_A

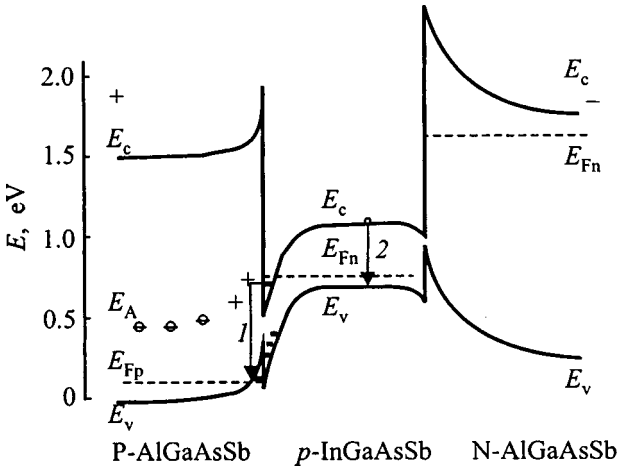

FIG. 6. Band diagram of a forward-biased type-II *P*-AlGaAsSb/*p*-InGaAsSb/*N*-AlGaAsSbdouble heterostructure. The arrows indicate radiative transitions: (*1*) at the *P*-*p* heterojunction; (*2*) in the *p*-InGaAsSb layer. E_{Fn} and E_{Fp} are the Fermi quasi-levels of electrons and holes.

situated in the lightly doped wide-gap solution *P*-AlGaAsSb ($E_A = 400$ meV, native V_{Al} defect[14]) into the conduction band of the narrow-gap *p*-InGaAsSb solid solution.

When an external bias is applied to the laser structure, the band bends at the *P*-AlGaAsSb/*p*-InGaAsSb heterojunction increase: The top of the valence band E_v of the *P*-AlGaAsSbsolid solution drops down, while the bottom of the conduction band E_c of the *p*-InGaAsSb solid solution moves upward. Consequently, the depth of the self-consistent quantum wells at the *P*-*p* heterojunction increases, and their width, in turn, decreases. In this case the quantum-well levels of electrons and holes are squeezed out of the quantum wells, and the energy spacing between them increases. The direction of the external electric field in the presence of bias coincides with the direction of the internal field of the type-II *P*-AlGaAsSb/*p*-InGaAsSb heterojunction. In our opinion, an increase in the voltage on the structure strengthens the localization of carriers near the *P*-*p* heterojunction and raises the densities of electrons and holes at the quantum-well levels. The strong electroluminescence generated as a result of indirect (tunneling) optical transitions of localized electrons and holes across the *P*-*p* heterojunction leads to suppression of the narrow, short-wavelength emission band.[3]

We note that the filling of an electron level in a quantum well on the side of the narrow-gap InGaAsSb solid solution in our case is a resonance process induced by injection from the wide-gap *N*-AlGaAsSb solid solution across the type-II *N*-AlGaAsSb/*p*-InGaAsSbheterojunction in the presence of a forward bias. The high potential barrier created by the asymmetry of the band discontinuities at the *P*-AlGaAsSb/*p*-InGaAsSb heterojunction prevents any further movement of electrons and forces them to pile up at the *P*-*p* heterojunction on the side of the InGaAsSb layer. We assume that the observed strong electroluminescence in our case represents the superposition of radiation from two recombination channels: interface (tunneling) recombination through localized states at the *P*-AlGaAsSb/*p*-InGaAsSb heterojunction and bulk recombination due to interband transitions in the narrow-gap *p*-InGaAsSb layer. The interface radiative recombination channel is dominant in the voltage interval 1.1–1.4 V, whereas in the presence of an external bias higher than 1.8 V we observe a pattern where the main electroluminescence contribution is from bulk radiative recombination. We therefore have an interface-to-bulk recombination switching mechanism in the voltage interval 1.4–1.8 V.

Thus, electroluminescence bistability associated with two distinct radiative recombination mechanisms in the active region is observed in *P*-AlGaAsSb/*p*-InGaAsSb/*N*-AlGaAsSbdouble laser heterostructures with lightly doped cladding layers. When an external bias voltage is applied, the electroluminescence is initially governed by tunneling carrier injection and indirect (interface) radiative recombination, across the heterjunction, of electrons from a quantum well on the side of the narrow-gap layer of the InGaAsSb solid solution with holes localized in the wide-gap AlGaAsSb solid solution. When high voltages are applied to the structure, radiative transitions in the bulk of the active region begin to provide the main contribution. Such tunneling injection structures can be used to construct highly efficient current-controlled IR light-emitting diodes.

This work has received partial support under the auspices of the Ministry of Sciences Project ''Physics of Solid State Nanostructures'' No. 96-1010.

[1] A. N. Baranov, A. N. Imenkov, V. V. Sherstnev, and Yu. P. Yakovlev, Appl. Phys. Lett. **64**, 2480 (1994).
[2] M. P. Mikhaĭlova, I. A. Andreev, T. I. Voronina, T. S. Lagunova, D. D. Moiseev, and Yu. P. Yakovlev, Fiz. Tekh. Poluprovodn. **29**, 678 (1995) [Semiconductors **29**, 353 (1995)].
[3] M. P. Mikhailova, K. D. Moiseev, G. G. Zegrya, and Yu. P. Yakovlev, Solid-State Electron. **40**, 673 (1996).
[4] H. K. Choi, C. W. Turner, S. J. Eglash, and Z. I. Liau, Appl. Phys. Lett. **65**, 2251 (1994).
[5] K. D. Moiseev, M. P. Mikhaĭlova, O. G. Ershov, and Yu. P. Yakovlev, Fiz. Tekh. Poluprovodn. **30**, 399 (1996) [Semiconductors **30**, 223 (1996)].
[6] G. G. Zegrya and A. D. Andreev, Appl. Phys. Lett. **67**, 2681 (1995).
[7] J. R. Meyer, C. A. Hoffman, and F. J. Bartoli, Appl. Phys. Lett. **67**, 757 (1995).
[8] M. P. Mikhailova, B. E. Zhurtanov, K. D. Moiseev, A. N. Imenkov, O. G. Ershov, and Yu. P. Yakovlev, in *Proceedings of the Materials Research Society 1997 Fall Meeting*, Vol. 484 (MRS, Boston, 1997), p. 101.
[9] D. H. Chow and J. N. Schulman, Appl. Phys. Lett. **64**, 76 (1994).
[10] K. D. Moiseev, M. P. Mikhaĭlova, O. V. Andreĭchuk, B. E. Samorukov, and Yu. P. Yakovlev, Pis'ma Zh. Tekh. Fiz. **23**(9), 68 (1997) [Tech. Phys. Lett. **23**, 364 (1997)].
[11] R. Q. Yang, C.-H. Lin, S. J. Murry, S. S. Pei, H. C. Liu, M. Buchanan, and E. Dupont, Appl. Phys. Lett. **70**, 2013 (1997).
[12] S. M. Cao, M. Willander, A. A. Toropov, T. V. Shubina, B. Ya. Mel'tser, P. S. Kop'ev, T. Lundström, P. O. Holtz, J. P. Bergman, and B. Monemar, Appl. Phys. Lett. **72**, 347 (1998).
[13] R. I. Voronina, T. S. Lagunova, M. P. Mikhaĭlova, K. D. Moiseev, and Yu. P. Yakovlev, Fiz. Tekh. Poluprovodn. **30**, 223 (1996) [Semiconductors **30**, 523 (1996)].
[14] F. Fuchs, J. Schmitz, H. Obloh, J. D. Ralston, and P. Koidl, Appl. Phys. Lett. **64**, 1665 (1994).

Translated by James S. Wood

Effect of heat treatment on the photoelectric properties of Si(Zn) photodetectors

E. V. Astrova, V. B. Voronkov, A. A. Lebedev, A. N. Lodygin, and A. D. Remenyuk

A. F. Ioffe Physicotechnical Institute, Russian Academy of Sciences, 194021 St. Petersburg, Russia
(Submitted August 30, 1998; accepted for publication September 7, 1998)
Fiz. Tekh. Poluprovodn. **33**, 362–369 (March 1999)

It is established that the heat treatment of *p*-type silicon doped with zinc at a high concentration ($N_{Zn} \approx 2\times10^{16}$ cm^3) in the temperature range 450–650 °C induces inhomogeneities of the electrical conductivity, which are detrimental to the stable operation of an ionization image converter. Their formation leads to a marked increase (as much as 10^2-fold) in the photoconductivity, a variation of its spectral curve, the onset of slow relaxation of the photocurrent and a persistent conductivity, and current filamentation. The observed phenomena can be explained by a model based on the spatial separation of carriers, where the recombination of nonequilibrium holes with negative charged zinc centers is prevented by potential barriers formed by these inhomogeneities. It is postulated that the inhomogeneities of the potential in *p*-type Si(Zn) are the result of a redistribution of zinc centers in the crystal with the formation of *i*-type inclusions in the *p*-matrix. © *1999 American Institute of Physics.* [S1063-7826(99)02303-0]

INTRODUCTION

It has been established that a zinc atom occupying a lattice site in silicon exhibits the properties of a deep, doubly charged acceptor, producing E_{Zn1} ($E_v+0.3$ eV) and E_{Zn2} ($E_v+0.6$ eV) levels in the band gap.[1] The phenomenon of low-temperature ($T\leqslant100$ K) impurity photoconductivity involving the E_{Zn1} level has found applications in the design of highly sensitive near-infrared photodetectors.[2,3] In the same category are ionization image converters capable of transforming thermal radiation from an object into visible light.[4,5] The operating principle and capabilities of this type of thermographic system are described in Ref. 6.

The converter is a gas-discharge device with two electrodes (one a zinc-doped silicon plate, and the other a glass plate with a transparent conducting layer), to which a high dc voltage is applied. The discharge gap of thickness $\sim100\,\mu$m is filled with a gas at below-atmospheric pressure. The photosensitive silicon electrode determines the local current density and luminance of the gas discharge. The luminance in the visible part of the spectrum is proportional to the local variation of the conductivity of silicon. In the presence of a high electric field $\mathcal{E}\approx5\times10^3$ V/cm the semiconductor must operate as a linear resistive electrode and be extremely homogeneous. When zinc-doped silicon Si(Zn) is used, unstable burning of the discharge with the formation of current filaments in the form of bright luminescent dots is observed in the ionization system in a number of cases,[7] together with a long afterglow. It has been shown[7] that the discharge zone merely has a passive role in the formation of the current filaments, and the observed instabilities are caused by inhomogeneity of the semiconductor. Our objective in this study was to investigate the conditions and causes of the onset of the inhomogeneities and time lags, which deter the utilization of Si(Zn) semiconductors in ionization image converters.

SAMPLE PREPARATION

Silicon prepared by the floating-zone method and doped with phosphorus, with a resistivity $\rho=300\,\Omega\cdot$cm (phosphorus concentration $N_P=1.7\times10^{13}$ cm^{-3}), was used for the zinc doping operation. Zinc was diffused into wafers of diameter 30 mm in an evacuated cell at a temperature $T=1180$ °C and zinc vapor pressure of 2 atm. The cooldown rate to ~700 °C was ~8 deg/s. During the diffusion period ($\geqslant29$ h) the wafer, having a thickness of 1 mm, was uniformly saturated with zinc[8] at a concentration $\sim2\times10^{16}$ cm^{-3}, which is close to the maximum solubility. The conductivity changed to *p*-type, the silicon acquiring a low resistivity at room temperature ($\rho=12-18\,\Omega\cdot$cm at $T=300$ K) and a high resistivity at a low temperature ($\rho\geqslant10^{12}\,\Omega\cdot$cm at $T=77$ K). We refer to this material from now on as *p*-type Si(Zn). To form a transparent ohmic contact, boron B^+ ions were implanted in one of the surfaces of the wafer before and after Zn diffusion. In the first case the boron was activated during diffusion annealing, and in the second case the sample was subjected to an additional 20-s pulsed photon anneal at $T\approx1050$ °C. The metal ring used to attach the photodetector to the voltage source in the gas-discharge cell was brazed at a temperature of 450–650 °C.

The functional readiness and main parameters of the photodetector were determined by placing it in a gas-discharge chamber (Fig. 1). Light from an incandescent lamp was focused onto the silicon plate from the side of the p^+-contact, and a uniform illumination was created, its intensity regulated by means of neutral filters. The photodetector was cooled down to $T=85$ K, and a voltage $V_c\leqslant1000$ V was applied between the electrodes. The operating regime of the system was such as to maintain the burning of a Townsend discharge with a constant voltage drop ~300 V across the gas-discharge gap. The criteria of functional readiness of the photodetector were uniform luminescing of the

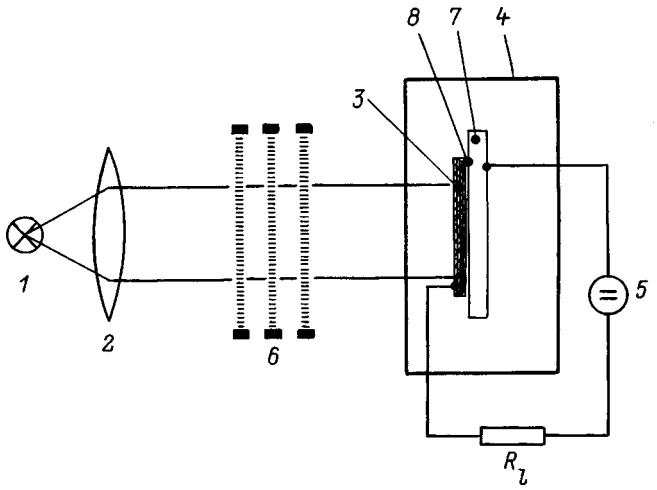

FIG. 1. Schematic representation of the ionization image converter: (*1*) incandescent lamp; (*2*) lens; (*3*) *p*-Si(Zn) electrode; (*4*) gas-discharge chamber; (*5*) power supply; (*6*) mesh filters; (*7*) transparent electrode; (*8*) gas-discharge gap; R_l is the load resistance.

discharge over the entire area and linearity of the current-voltage (*I-V*) curve and the current-illuminance curve (CIC). The power-current sensitivity R of the detector was determined from the slope of the CIC at an interelectrode voltage $V_c = 800$ V (i.e., 500 V on the Si wafer). The dark current, more accurately called the background current by virtue of the high sensitivity of Si(Zn) to room-temperature thermal radiation, was determined at the same voltage with the light source turned off. The dark current density j_b nonetheless served as a useful parameter for characterizing the photodetectors in the presence of identical background illumination.

EXPERIMENTAL RESULTS

It has been established that the ''dark'' current density j_b and the photosensitivity R increase as a result of the heat treatment of a Si(Zn) photodetector during preparation of the contacts. Table I shows data obtained for wafers from eight batches of photodetectors before and after heat treatment, one wafer from each batch. Despite the scatter of the parameters from one batch to the next, the general pattern is constant. Photodetectors having a high photosensitivity $R \geqslant 2$ A/W ($V = 500$ V) exhibit slow growth and decay of the photocurrent with characteristic times of the order of several tens of seconds, along with a persistent conductivity after the light is turned off; the behavior of such photodetectors is different in different spectral regions. For example, while the ''dark'' current (at $V = 500$ V) has the value $j_{b0} = 2.7 \times 10^{-6}$ A/cm^2 before illumination, after exposure to light of intensity $\sim 10^{-3}$ W/cm^2 through a Si filter it increases to $j_{br} = 1.1 \times 10^{-5}$ A/cm^2; i.e., by a factor ~ 4, and remains constant until the sample warms up (persistent conductivity). When a Ge filter is used, the postillumination ''dark'' current returns to its initial value.

The increase in R and j_b after heat treatment is accompanied by the onset of inhomogeneities of the resistivity of the material. The luminescence of the gas discharge provides a means for recording this inhomogeneity. It should be noted that a luminescent dot of diameter ~ 1 mm, which is evidence of current filamentation, not only occurs when a certain threshold voltage is applied, as described in Ref. 7, but also shows up in many cases upon increasing the light intensity at a constant interelectrode voltage. Subsequent annealing in the temperature range $T_a = 450$–650 °C causes R and j_b to increase smoothly at first and then to rise sharply.

Consequently, heat treatment of the *p*-type Si(Zn) photodetector produces the following changes:

- The dark current density and the photosensitivity increase.
- In the transparency range of the Si filter the photoresponse rises slowly and decays even more slowly.
- Instability emerges in the form of inhomogeneity of the current through the photodetector.

The sensitivity of a photoresistor in the impurity region of the spectrum is determined by the density of light-generated free charge carriers, which are free holes (p) in our case. For the simple model in which a single acceptor level E_{Zn1} and a compensating donor level E_D, completely ionized at the given temperature, exist in the band gap, the hole density for the lowest excitation level is[9]

$$p = \left(\frac{N_{Zn1}}{N_D} - 1 \right) \left[\frac{\kappa_p^0 I}{v_p \sigma_p^-} + N_v \exp\left(- \frac{E_{Zn1}}{kT} \right) \right], \qquad (1)$$

where κ_p^0 is the photoionization cross section of the Zn^0 center, σ_p^- is the hole capture cross section of Zn^-, v_p is the hole thermal velocity, N_v is the density of states in the valence band, $E_{Zn1} = 0.3$ eV is the ionization energy of a $Zn^{0/-}$ center, and I is the extrinsic light intensity. The first term in

TABLE I. Effect of heat treatment on the parameters of *p*-type Si(Zn) photodetectors.

Plate No.	After Zn diffusion		After photon anneal (1050 °C, 20 s)		After metallization (450–650 °C, 20–30 min)	
	j_b, 10^{-6} A/cm^2	R, A/W	j_b, 10^{-6} A/cm^2	R, A/W	j_b, 10^{-6} A/cm^2	R, A/W
7-10	0.9	0.33	2.1	0.6	5.6	3.0
8-2	0.15	0.08	0.92	0.37	1.8	1.0
9-1	0.16	0.77	2.1	0.91	500	reject
62-8	1.6	0.31	0.44	0.10	2.4	2.4
10-1	0.18	0.12	0.52	0.29	3.8	2.0
11-1	0.18	0.14	0.7	0.26	6.0	3.1
13-1	0.16	0.07	0.56	0.15	1.3	0.9
14-11	0.13	0.02	0.64	0.15	4	2.7

the brackets gives the hole density due to competing photoexcitation and reverse trapping by negatively charged centers. The number of the latter depends on the degree of compensation of the material, i.e., the density of donors. The second term characterizes thermally ionized holes. Estimates show that the density of the latter is small ($\sim 10^2\,\mathrm{cm}^{-3}$) at $T=85\,\mathrm{K}$ and can be disregarded. Since $N_{Zn1} \gg N_D$, from Eq. (1) we obtain

$$p=\frac{N_{Zn1}}{N_D}\,\frac{\kappa_p^0 I}{v_p \sigma_p^-}=N_{Zn1}\kappa_p^0 I\tau_p, \tag{2}$$

where $\tau_p=(v_p\sigma_p^- N_D)^{-1}$ is the hole lifetime, i.e., all other conditions being equal, the photosensitivity is determined by the ratio of the number densities N_{Zn1}/N_D rather than by their absolute values. Subjecting the supersaturated solid solution of zinc in silicon to additional anneals, ostensibly one might expect the concentration of electrically active zinc to decrease and, accordingly, the photosensitivity and dark current to decrease as well. However, the opposite pattern is observed, leaving no choice but to assume that the degree of compensation by annealing decreases.

ADDITIONAL EXPERIMENTS

To find the cause of the observed phenomena, we have conducted further experiments to: measure the capacitance-voltage (C-V) curves of Si(Zn,B) Schottky diodes initially doped with boron ($\rho=10\,\Omega\cdot\mathrm{cm}$ and $40\,\Omega\cdot\mathrm{cm}$) and saturated with zinc in the same technological process as the photodetector wafers; investigate the photoconductivity spectra, its kinetics, and the impurity photoconductivity extinction spectra in intrinsic light.

To measure the photoconductivity spectra, samples with dimensions $10\times4\times1$ mm were cut from Si(Zn) wafers and were then etched in SR-4 and treated in HF to lower the surface conductivity. Ohmic contacts were prepared by rubbing the metal with Ga-Al pencil. The measurements were performed in the longitudinal photoconductivity regime, i.e., with the light and the current in the same direction. The light intensity did not exceed $10^{15}\,\mathrm{phot/cm^2\cdot s}$. The measurement temperature was $T=77\,\mathrm{K}$. The photocurrent was determined as the difference between the current in the illuminated and nonilluminated sample with a voltage of 100 V applied to the latter, corresponding to a field $\mathcal{E}=10^3\,\mathrm{V/cm}$; the difference was normalized to a constant number of incident photons.

These studies have shown that the spectrum of energy levels in Si(Zn) is far more complicated than in the model discussed above. In addition to zinc acceptors, donor centers D_x are formed in the material after heat treatment; their density, determined from the C-V curves, is $N_{D_x}=5.8\times10^{14}\,\mathrm{cm}^{-3}$. It is evident that the density of the generated donors greatly exceeds the phosphorous doping level of the original material.

One of the most abundant unmanageable impurities in Si is iron, which produces a deep donor level $E_v+0.4\,\mathrm{eV}$ in the band gap.[1] To test whether the donors observed in Si(Zn) are iron centers, the silicon was heat-treated and hardened under the same conditions as when doped with zinc. Compensation

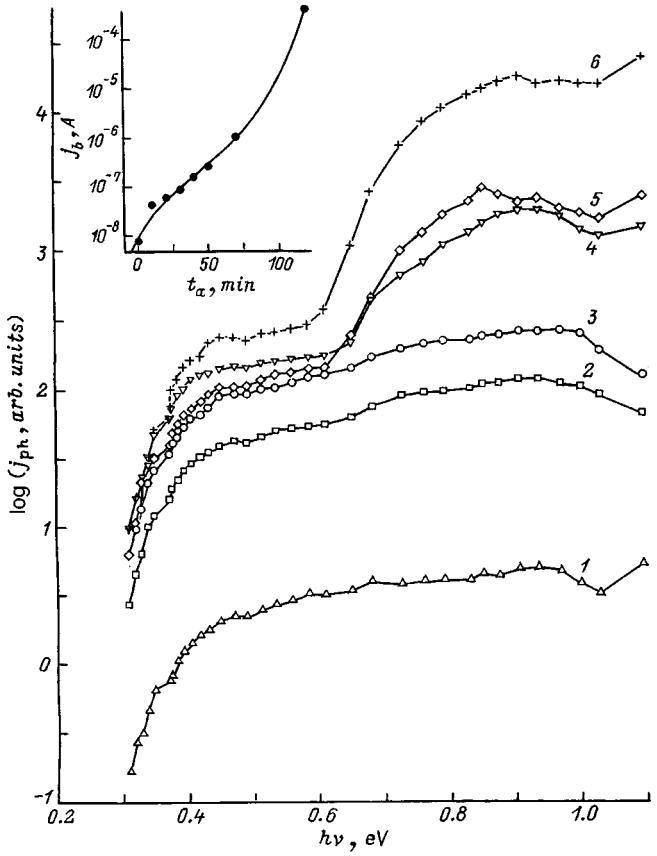

FIG. 2. Spectral dependence of the photocurrent in a p-Si(Zn) sample without annealing (*1*) and after annealing at $T_a=600\,^\circ\mathrm{C}$ for various anneal times: (*2*) $t_a=20$ min; (*3*) 30 min; (*4*) 50 min; (*5*) 60 min; (*6*) 70 min. $T=77$ K, $\mathcal{E}=10^3$ V/cm Inset: variation of the ''dark'' current during annealing of the same sample.

took place in silicon samples with a boron concentration $<2\times10^{15}\,\mathrm{cm}^{-3}$, and they acquired a high resistivity. Compensation was reduced by annealing at just $T_a=400\,^\circ\mathrm{C}$, as is typical of iron with its low thermal stability, whereas the donors in the Si(Zn) samples exhibited stability under heat treatment up to $T_a=800\,^\circ\mathrm{C}$. The detection of zinc donors in Si(Zn,B) has been reported previously and was attributed to the level $E_c-0.11\,\mathrm{eV}$ (Ref. 10). A level with energy $E_c-(0.41-0.49)\,\mathrm{eV}$ has also been observed in several studies[11–14] and can be attributed to interstitial zinc. Boltaks *et al.*[15] have detected two zinc donor levels $E_c-0.1\,\mathrm{eV}$ and $E_c-0.4\,\mathrm{eV}$ formed by the decay of a zinc-silicon solid solution at 900 °C. It is also known that zinc tends to form donor-acceptor pairs with transition metals.[16] The donor center D_x could well be an iron-zinc complex.

Besides the donor levels, a new deep level with an energy of 0.6 eV appears in p-type Si(Zn) after heat treatment. Figure 2 shows how the spectrum of the photocurrent j_{ph} of a sample vacuum-annealed at $T_a=600\,^\circ\mathrm{C}$ varies as the anneal time t_a is gradually increased, and the inset in the figure shows the corresponding values of the dark current j_b. Clearly, the original spectrum has one step at a photon energy $h\nu=0.3\,\mathrm{eV}$ corresponding to photoionization of the $\mathrm{Zn}^{0/-}$ level, consistent with a wealth of data on the photoconductivity of p-type Si(Zn) (see, e.g., Refs. 17 and 18). An increase in the anneal time causes the photocurrent to in-

crease over the entire spectral range $h\nu = 0.3-1.1$ eV. Beginning with an anneal time of 50 min, the spectrum acquires a very pronounced second step at $h\nu = 0.6$ eV, signaling the onset of yet another level. As annealing progresses, the photosensitivity in the short-wavelength region increases at a higher rate than in the region $h\nu < 0.6$ eV, attaining 10^4 times the initial value for an anneal time of 120 min. The ''dark'' current increases by five orders of magnitude in this case. A test has shown that not only the background current, but also the dark current measured with total shielding against background radiation increases enormously as a result of anneals, while the hole density differs from the calculated value by several orders of magnitude ($p = 10^5 - 10^9\ \mathrm{cm}^{-3}$). These data indicate that the zinc E_{Zn1} level (with an activation energy of 0.3 eV) is joined in the band gap by the onset of shallower acceptor levels. The $E_v + 0.23$ eV and $E_v + 0.33$ eV levels have in fact been recorded in Si(Zn,B) by deep-level transient spectroscopy (DLTS).[14,19] Their concentration undergoes significant changes during heat treatment: The number of centers with activation energy 0.23 eV increases during anneals at $T_a < 500\,^\circ$C and decreases at $T_a > 500\,^\circ$C, while the $E_v + 0.33$ eV level vanishes after heat treatment at $T_a > 400\,^\circ$C (Ref. 20).

We call attention to the fact that the rise and decay kinetics of the photocurrent in the samples after prolonged heat treatment differs in the two spectral ranges $h\nu > 0.6$ eV and $h\nu < 0.6$ eV. The process is slow in the short-wavelength range, with a characteristic time of tens to hundreds of seconds (see Figs. 3 and 4), and it is fast in the long-wavelength range. The increase in the photocurrent in the short-wavelength range once the light is turned on is well described by an exponential law, and its decrease after removal of the light more nearly fits a hyperbolic law, as is typical of quadratic recombination.[21] The rate of increase of the photocurrent at $h\nu > 0.6$ eV increases with the light intensity, whereas the rate of decay is independent of the level of illumination. Despite the low excitation level in both spectral ranges, the CIC in the short-wavelength region is sublinear, but remains linear in the long-wavelength region (Fig. 5). In addition to the slow relaxation of the photoconductivity in the range $h\nu > 0.6$ eV, we see a persistent dark conductivity which exceeds the preillumination ''dark'' conductivity by a factor ~ 20; i.e., a whole set of phenomena emerges, fully consistent with everything disclosed in our analysis of the operation of photodetectors in a gas-discharge chamber.

The onset of a second step in the photoconductivity spectrum indicates the initiation of a photoactive deep level; a good candidate for this role is the second zinc $\mathrm{Zn}^{-/2-}$ level. The electron capture cross section of Zn^- at $T = 77 - 90$ K is very small, $\sigma_n^- = 5\times10^{-21}\ \mathrm{cm}^2$ (Ref. 22), whereas the hole cross section of a Zn^{2-} center is $\sigma_p^{2-} = 2\times10^{-14} - 2\times10^{-15}\ \mathrm{cm}^2$ (Refs. 11 and 19), so that in intrinsic light it becomes an activation center, increasing the electron lifetime by a factor of 10^4 (Ref. 13). In the photoconductivity spectrum, however, the E_{Zn2} level can appear only in highly compensated *n*-Si(Zn), where $N_{\mathrm{Zn}} < N_D < 2N_{\mathrm{Zn}}$. The photoelectric properties of this kind of high-resistivity *n*-Si(Zn) has intrigued many researchers. A slow persistence of the photoresponse has been observed in the material,[10] along with IR extinction of the intrinsic steady-state photoconductivity.[13,23]

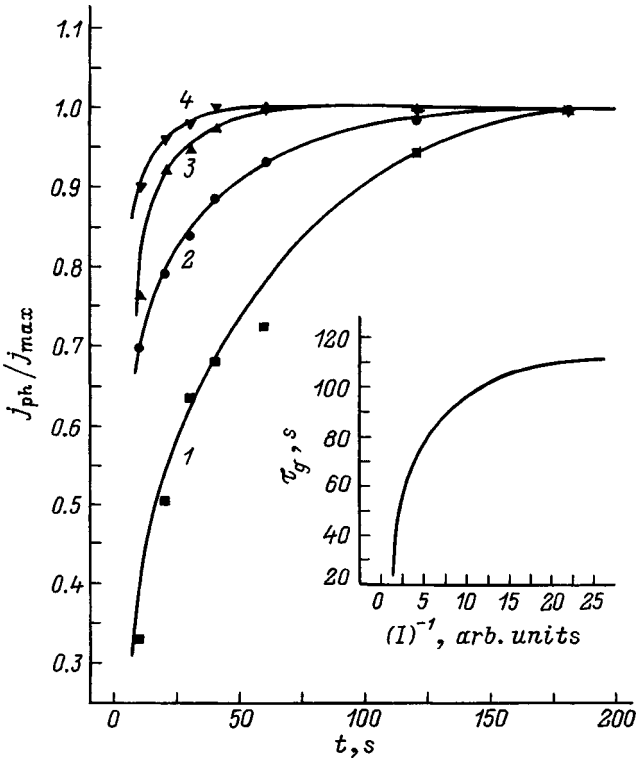

FIG. 3. Rise kinetics of the photocurrent in a *p*-Si(Zn) sample after annealing at $T_a = 600\,^\circ$C for $t_a = 70$ min and various light intensities, $h\nu = 0.79$ eV. The photocurrent is normalized to its steady-state value $j_{\max}$ for each intensity *I*: (*1*) I_0; (*2*) $4I_0$; (*3*) $9I_0$; (*4*) $16I_0$. Inset: dependence of the photocurrent rise time τ_g on the reciprocal light intensity I^{-1}, $T = 77$ K.

We have also investigated such highly compensated *n*-type Si(Zn). An *n*-silicon sample with an initial resistivity $\rho = 0.2\ \Omega\cdot$cm ($N_{\mathrm{P}} = 2.5\times10^{16}\ \mathrm{cm}^{-3}$) was placed in the Zn

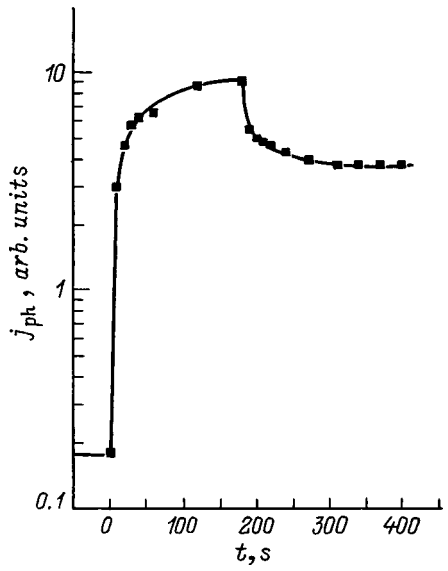

FIG. 4. Decay kinetics of the photocurrent in an annealed *p*-Si(Zn) sample after the removal of light with $h\nu = 0.79$ eV. The current before illumination is $j_{b0} = 0.18$ μA, and the residual ''dark'' current after illumination is $j_{br} = 3.8$ μA.

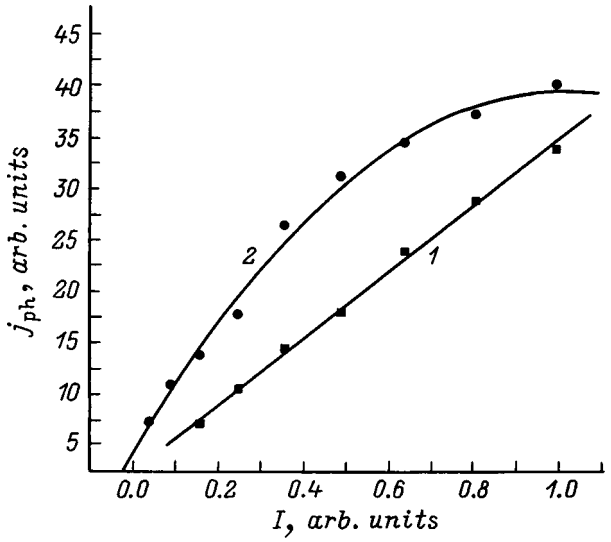

FIG. 5. Current-illuminance curves of an annealed *p*-Si(Zn) sample in different spectral ranges: (*1*) 0.51; (*2*) 0.79.

diffusion cell; after zinc diffusion the sample acquired a high resistivity even at room temperature ($\rho \geqslant 2$ k$\Omega \cdot$cm). Its photoconductivity spectrum at $T=77$ K has a long-wavelength edge at $h\nu \approx 0.5$ eV, and under the combined influence of intrinsic and extrinsic light, extinction of the photocurrent was observed in it. Moreover, this sample exhibits a slow rise and decay of the photocurrent, similar to the behavior in annealed *p*-Si(Zn). The photocurrent extinction spectra in both samples are shown in Fig. 6.

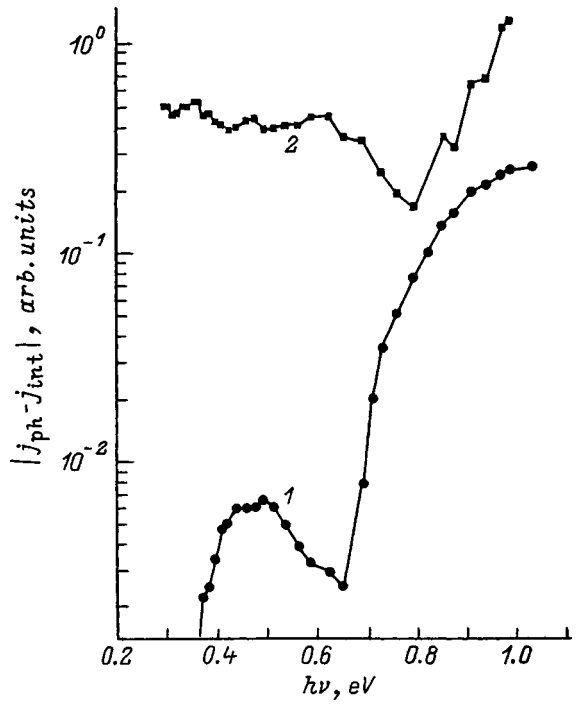

FIG. 6. Infrared extinction spectra of the intrinsic photoconductivity in annealed *p*-Si(Zn) (*1*) and *n*-Si(Zn) (*2*) samples, $T=77$ K, $\mathcal{E}=100$ V/cm. The energy of intrinsic illumination photons is $h\nu=1.55$ eV.

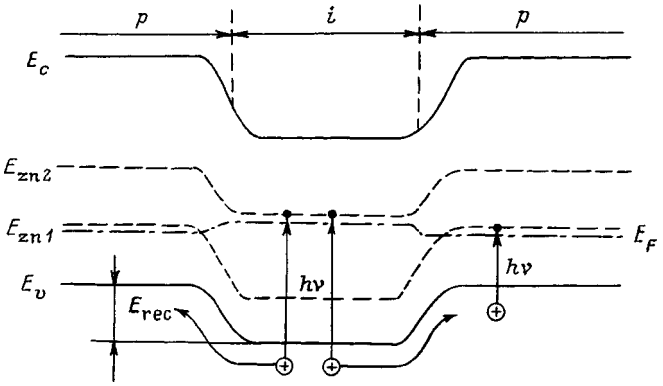

FIG. 7. Potential barrier around an *i*-type conductivity inclusion in the *p*-matrix of Si(Zn) and, at the barrier, spatial separation of holes excited by extrinsic light.

DISCUSSION OF THE RESULTS

We now attempt to interpret the above-described experimental facts. We consider the influence of a low-temperature ($T_a=450-650\,^\circ$C) anneal on *p*-Si(Zn). The increases in the dark current and the photosensitivity suggest that the ratio N_{Zn1}/N_D increases in accordance with Eq. (2). Measurements of the *C-V* curves show that the decrease in the concentration of electrically active zinc as a result of such anneals is rather slight (by a factor <1.5), i.e., it must be assumed that the main cause of such an abrupt increase in the photoresponse is a decrease in the donor density N_{Dx}. On the other hand, the new step in the photoconductivity spectrum at $h\nu=0.6$ eV indicates the emergence of photoelectric transitions at the second zinc E_{Zn2} level. This event is possible if all the E_{Zn1} levels are filled with electrons, i.e., if the Fermi level (E_F) is close to the middle of the band gap: $E_{Zn1}<E_F \leqslant E_{Zn2}$. But then the opposite must be assumed, that the compensation by heat treatment increases, i.e., the donor density increases.

This contradiction can be resolved only if we assume that spatial inhomogeneities are created in the bulk of the Si by a redistribution of impurity atoms. Examples of the latter process are the enrichment of both regions with zinc at the expense of depletion of other elements (precipitation at lattice defects, the formation of an impurity atmosphere around dislocations, etc.) and the formation of clusters of donors D_x when they are ''purged'' from the rest of the crystal. In either case we witness the emergence of local regions separated from the remaining matrix by potential barriers and surrounded by a space-charge layer (see Fig. 7). The proposed model is supported by experimental data, which can be conditionally segregated into three groups:

1) the direct observation of anneal-induced inhomogeneities of the electrical conductivity;

2) the presence of phenomena which are typical of a photoconductor with inhomogeneities and which are associated with an anomalously long free-carrier lifetime (see the review article in Ref. 24 and the references to earlier papers cited there);

3) the identification of the level with energy 0.6 eV as

the second zinc E_{Zn2} level, which indicates the formation of high-resistivity regions.

The current structures of Si(Zn) in the system {semiconductor/gas-discharge gap} has been investigated in detail.[7] The inhomogeneities of ρ were seen as bright luminescent dots against the uniform background luminescence of the gas discharge. The main focus of attention here was the dark *I-V* characteristic, and IR radiation with a broad spectrum was used to illuminate the photodetector. It follows from our measurements that the behavior of the system differs considerably for the two spectral ranges $h\nu < 0.6$ eV and $h\nu > 0.6$ eV; i.e., all phenomena associated with inhomogeneities occur only in the short-wavelength part of the spectrum.

We now examine the second group of experimental data in greater detail. According to the barrier model,[24] the long-time relaxation and persistent conductivity are linked to the presence in the material of collective (macroscopic) potential barriers associated with inhomogeneities. The electric fields of these barriers instigate the spatial separation of light-excited carriers. For example, holes excited from the E_{Zn2} level in the high-resistivity region of *p*-Si(Zn) (Fig. 7) flow over into the lower-resistivity matrix and contribute to the photocurrent. To recombine with electrons at centers left in the *i*-region, they must overcome a recombination barrier of height E_{rec}, so that holes excited by light with $h\nu > 0.6$ eV have an anomalously long lifetime. The high persistent conductivity in *p*-type Si(Zn) after heat treatment indicates that the *i*-regions occupy a substantial portion of the total volume of the photoresistor.

Since the electric fields generated by carrier separation partially compensate for the potential well of the inhomogeneities, E_{rec} decreases as the density of photocarriers increases, and the CIC of the sample becomes sublinear. Indeed, if we compare the CIC of such a sample for the two spectral regions (Fig. 5), it is clearly evident that diagram is linear for $h\nu = 0.51$ eV and is sublinear for $h\nu = 0.79$ eV. Inhomogeneous semiconductors are also characterized by shortening of the photocurrent rise time τ_g with increasing illumination intensity I at a rate slower than the I^{-1} law (Ref. 24). The functional dependence $\tau_g = f(I^{-1})$ obtained by us from the photocurrent rise curves in Fig. 3 and shown in the inset in the figure is in fact sublinear.

The rate of decay of the photocurrent in annealed *p*-Si(Zn) samples does not change as the intensity of light with $h\nu > 0.6$ eV is increased, and it has a fast interval followed by a very slow decay, which is perceived as a persistent conductivity (Fig. 4); these effects are also typical of inhomogeneous materials with potential barriers.[23]

We now turn to the third data group. To show that the 0.6-eV deep level observed in our photodetectors is associated with the photoexcitation of holes at the E_{Zn2} level in the newly formed *i*-regions, we draw on a characteristic property of this kind of material: IR extinction of the intrinsic photoconductivity. The long electron lifetime observed in intrinsic light in high-resistivity *n*-Si(Zn) ($\tau_n = 100$ ms) (Ref. 13) is explained by the facile trapping of holes and the poor trapping of electrons by Zn^{-2} activation centers. As a result, holes trapped by them are eliminated from recombination through other centers, τ_n increases, and the conductivity becomes essentially monopolar. If the sample is simultaneously exposed to a combination of extrinsic and intrinsic light with a certain intensity ratio so that the rate of liberation of holes by IR radiation from a Zn^{2-} center is greater than its rate of trapping of electrons, $\kappa_p^- I > n v_n \sigma_n^-$, where n is the density of free electrons, which depends on the intrinsic light intensity, and κ_p^- is the photoionization cross section of Zn^-, the electron lifetime drops, and the photocurrent decreases, i.e., IR extinction is observed. Figure 6 shows spectra obtained in combined exposure of the samples to intrinsic light with $h\nu = 1.55$ eV and extrinsic light with a different wavelength. The photocurrent $|j_{\text{ph}} - j_{\text{int}}|$, plotted along the vertical axis, is the absolute value of the difference between the photocurrent j_{ph} and the intrinsic photocurrent j_{int}. The intensity ratios of the intrinsic and extrinsic light are such that this difference is positive for *p*-Si(Zn) and negative for *n*-Si(Zn). Our extinction spectrum observed in the *n*-Si(Zn) sample agrees with the long-wavelength edge at $h\nu = 0.6$ eV in Refs. 13 and 23. A similar pattern is observed in an annealed *p*-Si(Zn) sample. IR extinction is not observed in unannealed *p*-Si(Zn) samples. The onset of a step at $h\nu = 0.6$ eV in the intrinsic photoconductivity spectra justifies the identification of this level as corresponding to transition from the Zn^- charge state to the Zn^{2-} state.

Consequently, all the investigated properties of photodetectors after heat treatment corroborate the conclusion that inhomogeneities are formed in them. It is still not clear just which centers form clusters in heat treatment. Exactly the same result, specifically a local increase in the degree of compensation, can be achieved either by enrichment with donor centers (high-resistivity regions with a reduced ratio N_{Zn}/N_D) or by the depletion of zinc acceptors occupying lattice sites from these same regions. An attempt to detect zinc precipitates by x-ray diffraction topography proved unsuccessful, so that the microscopic pattern of events requires special investigation.

The increase in the photosensitivity at $h\nu > 0.6$ eV after anneals is associated with an increase in τ_p due to the spatial separation of holes and negatively charged Zn^{2-} centers. On the other hand, in the range $h\nu < 0.6$ eV the time constant τ_p more likely increases on account of a decrease in the degree of compensation in the *p*-type matrix, because the CIC remains linear. The mechanism based on the dual injection effect to account for the formation of current filaments[7] could probably admit some reexamination in light of the model proposed here.

CONCLUSIONS

From the results of our investigation we have established that the resistivity inhomogeneities occurring in *p*-Si(Zn) are formed during heat treatment at $T_a = 450 - 650\,^\circ$C. The amplitude of these inhomogeneities increases as the anneal time is increased. The formation of spatial inhomogeneities is attributed to a redistribution of impurity centers in the material and the resulting formation of highly compensated, high-resistivity regions. The Fermi level in these regions shifts toward the middle of the band gap, and it becomes possible

for holes to undergo photoelectric transitions from the E_{Zn2} level into the valence band. The impurity redistribution in the bulk of the Si causes the photosensitivity to increase significantly as a result of the increase in τ_p. The anomalously long lifetime of holes in the spectral range $0.6\,\text{eV} < h\nu < 1.1\,\text{eV}$ is attributable to the spatial separation of carriers and recombination centers by potential barriers around the inhomogeneities. This phenomenon has the effect of diminishing the response time of photodetectors, inducing a persistent conductivity, and generating multiple current filaments.

We are indebted to D. V. Tarkhin, V. V. Chaldyshev, Yu. A. Astrov, L. M. Portsel', V. V. Emtsev, and I. L. Shul'pina for a discussion and helpful consultations.

This investigation has been initiated by work under a contract with Münster University in Germany and has been carried out thanks to support from grants of the Ministry of Science under the program ''Physics of Nanostructures,'' Projects No. 96-1012 and 97-1039.

[1] A. G. Milnes, *Deep Impurities in Semiconductors* (Wiley, New York, 1973; Mir, Moscow, 1977).
[2] N. Sclar, Infrared Phys. **17**, 71 (1977).
[3] *Charge-Coupled Devices*, edited by D. F. Barbe (Springer-Verlag, Berlin/New York, 1980; Mir, Moscow, 1982).
[4] Sh. S. Kasymov, L. G. Paritskiĭ, and S. M. Ryvkin, manuscript deposited at the All-Union Institute of Scientific and Technical Information [in Russian], VINITI Deposit No. 2693, 29 (1974).
[5] Yu. A. Astrov, Sh. S. Kasymov, and S. M. Ryvkin, manuscript deposited at the All-Union Institute of Scientific and Technical Information [in Russian], VINITI Deposit No. 1032, 35 (1975).
[6] H. Willebrand, Yu. Astrov, L. Potsel, S. Teperik, and T. Gauselmann, Infrared Phys. Technol. **36**, 809 (1995).
[7] Yu. A. Astrov, Fiz. Tekh. Poluprovodn. **27**, 1973 (1993) [Semiconductors **27**, 1084 (1993)].
[8] H. Bracht, N. A. Stolwijk, and H. Mehrer, Phys. Rev. B **52**, 16542 (1995).
[9] A. Lebedev and E. V. Astrova, Preprint No. 1165 (FTI, A. F. Ioffe Physicotechnical Institute, Leningrad, 1987).
[10] Yu. I. Zavadskiĭ and B. V. Kornilov, Fiz. Tekh. Poluprovodn. **1**, 1326 (1967) [Sov. Phys. Semicond. **1**, 1103 (1967)].
[11] A. A. Lebedev, N. A. Sultanov, and W. Ecke, Fiz. Tekh. Poluprovodn. **21**, 18 (1987) [Sov. Phys. Semicond. **21**, 10 (1987)].
[12] A. A. Lebedev, N. A. Sultanov, and W. Ecke, Fiz. Tekh. Poluprovodn. **21**, 321 (1987) [Sov. Phys. Semicond. **21**, 193 (1987)].
[13] A. F. Sklensky and R. H. Bube, Phys. Rev. B **6**, 1328 (1972).
[14] S. Weiss, R. Beckmann, and R. Kassing, Appl. Phys. A: Solids Surf. **50**, 151 (1990).
[15] B. I. Boltaks, M. K. Bakhadyrkhanov, G. S. Kulikov, and É. M. Pedyash, Fiz. Tekh. Poluprovodn. **4**, 873 (1970) [Sov. Phys. Semicond. **4**, (1970)].
[16] C. A. J. Ammerlan and H. E. Altink, Solid State Phenom. **19-20**, 639 (1991).
[17] R. O. Carlson, Phys. Rev. **108**, 1390 (1957).
[18] N. Sclar, Solid-State Electron. **24**, 203 (1981).
[19] P. Stolz, G. Pensl, D. Gruenebaum, and N. Stolwijk, Mater. Sci. Eng., B **4**, 31 (1989).
[20] P. Stolz, Ph.D. Thesis (Erlangen–Nuremberg University, 1990).
[21] S. M. Ryvkin, *Photoelectric Effects in Semiconductors* (Consultants Bureau, New York, 1964; Fizmatgiz, Leningrad, 1963).
[22] A. C. Wang, L. S. Lee, and C. T. Sah, Phys. Rev. B **30**, 5896 (1984).
[23] A. A. Lebedev and A. T. Mamadalimov, Fiz. Tekh. Poluprovodn. **7**, 1470 (1973) [Sov. Phys. Semicond. **7**, 986 (1973)].
[24] M. K. Sheĭnkman and A. Ya. Shik, Fiz. Tekh. Poluprovodn. **10**, 209 (1976) [Sov. Phys. Semicond. **10**, 128 (1976)].

Translated by W. J. Manthey

Vertical double-collector, strain-sensitive transistor with accelerating electric fields in the base and in the emitter

G. G. Babichev, S. I. Kozlovskiĭ, and V. A. Romanov

Institute of Semiconductor Physics, National Academy of Sciences of Ukraine, 252028 Kiev, Ukraine
(Submitted February 23, 1998; accepted for publication August 25, 1998)
Fiz. Tekh. Poluprovodn. **33**, 370–377 (March 1999)

The characteristics of a bipolar vertical double-collector, strain-sensitive transistor with accelerating electric fields in the base and in the emitter are investigated theoretically. The structure and operating principle of the transistor are described, and the topology of the device is optimized. It is shown that the output signal is associated with two effects: transverse deflection of nonequilibrium carriers in the base and injection modulation by a transverse potential difference in the emitter. © *1999 American Institute of Physics.* [S1063-7826(99)02403-5]

INTRODUCTION

In general, the directions of the current and the electric field are known to differ in crystals endowed with anisotropy of the electrical conductivity.[1] This means that as the charge carriers move between electrodes, they come under the influence of forces transverse to the direction of the current. The magnitude of the force in the presence of anisotropy induced by external directional perturbations (uniaxial elastic strain, magnetic field, or light) is proportional to the magnitude of the perturbation (strength of the magnetic field, stress, or light intensity).

Consequently, the creation of an artificial anisotropy of the conductivity affords a possible means for the wide-range control of carrier transport phenomena. The practical application of this possibility has provided a basis for the development of a number of semiconductor devices: silicon integrated multicollector strain transistors,[2,3] which are sensitive to uniaxial stresses, and magnetotransistors,[4] which are sensitive to magnetic fields.

For a sufficiently high pulling (accelerating) electric field, even a slight anisotropy of the conductivity can produce a strong concentration effect (i.e., a transverse redistribution of carriers). In practice, therefore, the pulling field in the zone where the anisotropy is localized is chosen so that the drift (field) component of the current will exceed the diffusion component.

We have previously investigated horizontally structured, bipolar *n-p-n* and *p-n-p* double-collector, strain-sensitive transistors with an accelerating electric field in the base.[2,3] The measure of external mechanical perturbation in strain transistors is the collector current unbalance induced by injection deflection (or modulation) effects. In either case, the anisotropy induced by uniaxial elastic strain alters the transverse carrier distribution in the base of the strain transistor. In this case the influence of the induced anisotropy of the conductivity on carrier transport processes directly in the emitter is negligible because of the low electric field in the emitter, since essentially the entire emitter-base voltage is across the emitter *p-n* junction.

In this paper we investigate a vertically structured silicon integrated double-collector, strain-sensitive transistor with accelerating electric fields both in the base and in the emitter. In the investigated structures the unbalance of the collector currents is attributable to the simultaneous onset of two effects: 1) modulation of the injection of the base-emitter *p-n* junction due to the emergence of a transverse field in the emitter; 2) transverse carrier deflection in the base. The calculation of the main characteristics of the strain transistor is followed by a comparative analysis of how they are influenced by the indicated effects.

OPERATING PRINCIPLE OF THE STRAIN-SENSITIVE TRANSISTOR

We assume that a strain-sensitive transistor on a silicon diaphragm converts a uniformly distributed load over its surface into uniaxial compressive (tensile) elastic strain of the base and emitter of the strain transistor. As a result of strain, the hole mobility μ_p — holes being majority carriers in the emitter and minority carriers in the base — becomes anisotropic in the *xy* plane with nonzero off-diagonal components μ_{pxy}.

Figure 1 shows the topology of the strain transistor, including the *p*-emitter and *n*-base with two pairs of ohmic contacts in the form of p^+-p-type and n^+-n-type strips situated at the edges of the emitter and the base, respectively, plus two collector p^+-n junctions. Also shown in the figure is the orientation of elements of the strain transistor relative to the crystallographic axes.

The wiring schematic of the strain transistor and the longitudinal (along the *x* axis) distributions of the electric potentials in the base $\varphi_b(x)$ and in the emitter $\varphi_e(x)$ are shown in Fig. 2. The electric fields in the base and the emitter and the potential difference across the emitter-base *p-n* junction

$$\varphi_{eb}(x,y)=\varphi_e(x,y)-\varphi_b(x) \tag{1}$$

are given by the external sources V_{be}, V_{bb}, and V_e. According to Eq. (1), the forward-biased emitter-base *p-n* junction region is dictated by the values of x $(0<x<x_0)$, for which $\varphi_{eb}(x,y)>0$.

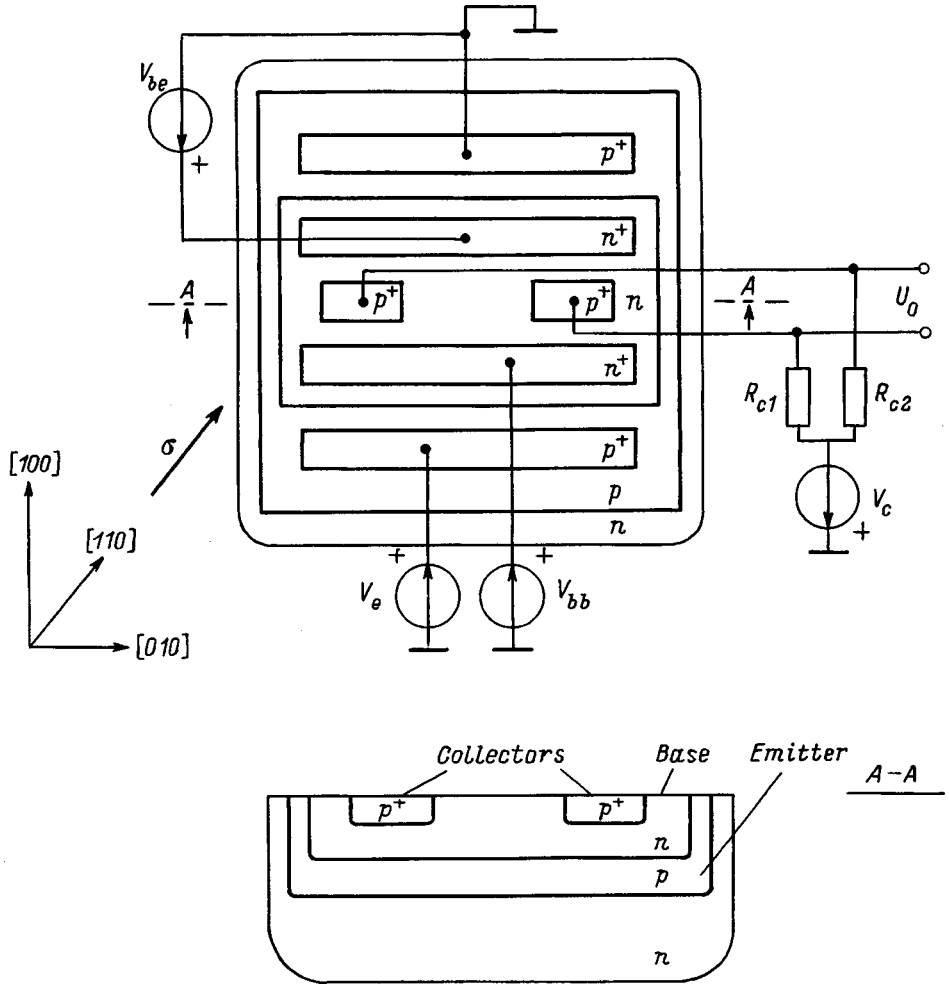

FIG. 1. Topology, wiring diagram, and crystallographic orientation of the strain-sensitive transistor.

Carriers injected into the base region drift in the longitudinal pulling field and diffuse in the z-direction, eventually reaching the collector junctions. At zero strain the collector currents, which are determined by the diffusion flow of carriers in the z-direction, are equal, and the output signal recorded from the load resistances, R_{c1} and R_{c2}, is close to zero (under the condition $R_{c1}=R_{c2}$). We assume from now on that $R_{c1}=R_{c2}=R_c$.

When a distributed mechanical load is applied to the diaphragm at the site of the strain transistor, a uniaxial compressive (tensile) strain is generated in the [110] direction, imparting anisotropy to the hole mobility both in the base and in the emitter of the strain transistor. The anisotropy of the hole mobility in the emitter, where holes are majority carriers, induces a transverse potential difference. The induced potential difference modulates the injection of the emitter-base p-n junction, shifting one of the edges of this junction (at $y=0$ or $y=l_y$, depending on the sign of the strain) in the forward direction and shifting the other edge in the reverse direction. Holes injected into the base region of the strain transistor in this way drift in the pulling field of the base (in the x-direction), are deflected in the transverse (y-) direction by virtue of the induced anisotropy, diffuse in the z-direction, and attain the collector junctions. The modulation of the injection of the emitter-base p-n junction and the onset in the base of a transverse flux of pairs generated by the anisotropy of the mobility produces a sharp unbalance of the collector currents, and an output signal appears.

Strictly speaking, the electron mobility μ_n also becomes anisotropic in this situation, but it can be ignored for the given orientation of the strain transistor elements relative to the crystallographic axes and for the given direction of uniaxial strain. The anisotropy parameter a can then be written in the form

$$a=\frac{\mu_{nxy}}{\mu_{nyy}}-\frac{\mu_{pxy}}{\mu_{pyy}}\approx-\frac{\mu_{pxy}}{\mu_{pyy}}. \tag{2}$$

Here $\mu_n\cong\mu_{nyy}$ and $\mu_p\cong\mu_{pyy}$.

It is important to note that the operating principle of the strain-sensitive transistor discussed here is formally equivalent to the operating principle of an analogously structured magnetotransistor,[5] which is sensitive to a transverse magnetic field, where the anisotropy parameter is equal to the sum of the Hall angles for electrons and holes.

By analogy with magnetotransistors,[2] we assume the main characteristics of the strain transistor to be the absolute sensitivity S_A and the relative sensitivity S_R, which are defined as the corresponding derivatives of the stress σ, evaluated at zero stress:

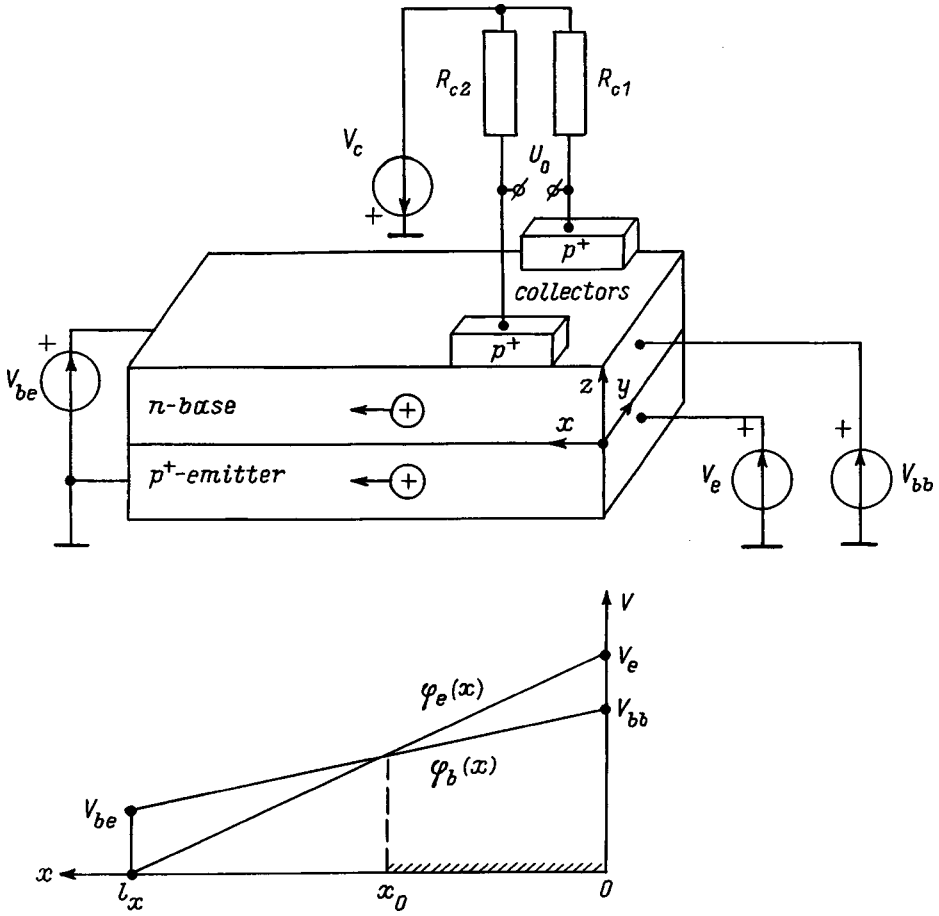

FIG. 2. Main elements of the structure of the strain transistor and longitudinal distributions of the electric potential in the base and emitter.

$$S_A \equiv \left| \frac{\partial U_0}{\partial \sigma} \right|_{\sigma=0}, \tag{3}$$

$$S_R \equiv U_0^{-1} \left| \frac{\partial U_0}{\partial \sigma} \right|_{\sigma=0}, \tag{4}$$

where U_0 is the difference in the voltage drops across the resistances R_{c1} and R_{c2} in the rows of collectors.

We can then assume that the output resistance r_c of the collectors of the strain transistor is high, i.e., $r_c \ll R_c$. We can therefore replace Eqs. (3) and (4) by the expressions

$$S_A = R_c \left| \frac{\partial (I_{c1} - I_{c2})}{\partial \sigma} \right|_{\sigma=0}, \tag{5}$$

$$S_R = (I_{c1} + I_{c2})^{-1} \left| \frac{\partial (I_{c1} - I_{c2})}{\partial \sigma} \right|_{\sigma=0}. \tag{6}$$

Here I_{c1} and I_{c2} are the collector currents.

RESULTS OF THE CALCULATIONS AND DISCUSSION

The following assumptions are used in the theoretical analysis of the operation of the strain-sensitive transistor:

a) a weak injection level, so that the density of minority carriers is much lower than the density of majority carriers at any point of the base and the emitter;

b) weak strains, so that the anisotropy parameter a is sufficiently small:

$$|a| \ll 1.$$

The base and the emitter of the strain transistor are bounded by the respective coordinates

$$(0 \leqslant x \leqslant l_x, \quad 0 \leqslant y \leqslant l_y, \quad 0 \leqslant z \leqslant l_z);$$

$$(0 \leqslant x' \leqslant l_x, \quad 0 \leqslant y' \leqslant l_y, \quad 0 \leqslant z' \leqslant l_z).$$

Under the stated approximations and simplification the spatial distribution of the nonequilibrium carrier density $p(x, y, z)$ in the base of the strain transistor is determined from the solution of the bipolar transport equation

$$D_p \left[\frac{\partial^2 p}{\partial x^2} + \frac{\partial^2 p}{\partial y^2} + \frac{\partial^2 p}{\partial z^2} + 2\alpha_x \frac{\partial p}{\partial x} + 2\alpha_y \frac{\partial p}{\partial y} \right] - \frac{p - p_0}{\tau} = -\rho(x', y')\,\delta(x - x')\,\delta(y - y')\,\delta(z - z') \tag{7}$$

subject to the boundary conditions

$$p(0,y,z) = p(l_x,y,z) = p(x,0,z) = p(x,l_y,z) = p(x,y,l_z) = p_0, \tag{8}$$

where D_p, τ, and p_0 are the diffusion coefficient, lifetime, and equilibrium density of holes in the base, respectively, and $\delta(x - x')$ is the Dirac delta function. The function $\rho(x', y')$ describes the density of sources of nonequilibrium carriers. The quantities α_x and α_y are related to the pulling field E_x in the base of the strain transistor by the equations

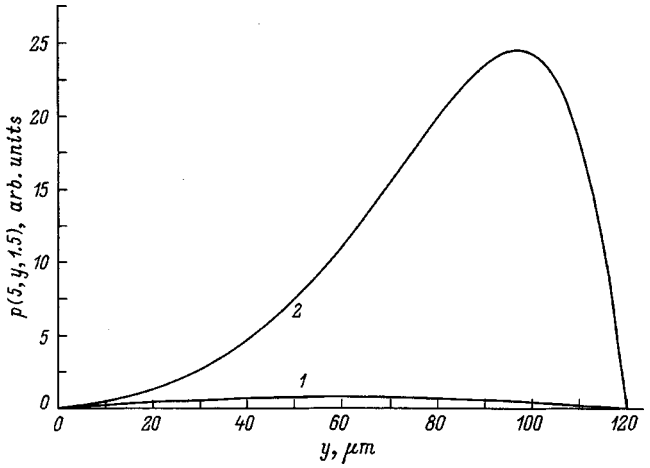

FIG. 3. Transverse distributions of nonequilibrium carriers in the base of the strain transistor for different values of the anisotropy parameter: (*1*) $\alpha=0$; (*2*) $\alpha=0.055$.

$$\alpha_x=\frac{eE_x}{2k_BT}, \quad \alpha_y=a\alpha_x, \tag{9}$$

where e is the electron charge, k_B is the Boltzmann constant, and T is the temperature.

The Green's function for Eq. (7) is

$$p(x,y,z,x',y',z')=\frac{4l_x}{D_pl_yl_z}\exp[\alpha_x(x-x')+\alpha_y(y-y')]\times\sum_{m,k=1}^{\infty}\frac{\sinh\left[\beta_{mk}\left(1-\frac{x}{l_x}\right)\right]}{\beta_{mk}\sinh(\beta_{mk})}\times\sinh\left(\frac{\beta_{mk}x'}{l_x}\right)\sin q_kz\sin q_my\sin q_my'\times\sin q_kz', \tag{10}$$

$$q_m=\pi\frac{m}{l_y}, \quad q_k=\pi\frac{k}{l_z},$$

$$\beta_{mk}^2=l_x^2(q_m^2+q_k^2+\alpha_x^2+\alpha_y^2+L^{-2}), \quad L=\sqrt{D_p\tau}.$$

The Green's function gives the nonequilibrium carrier density created at the point of the base with coordinates (x, y, z) by a source of unit strength at the point with coordinates (x', y', z') (Ref. 6).

In our case nonequilibrium carriers are injected by the forward-biased part of the emitter-base *p-n* junction ($0\leqslant x'\leqslant x_0$, $0\leqslant y'\leqslant l_y$, $0\leqslant z'\leqslant l_{ze}$ with the density of sources $\rho(x', y')$:

$$\rho(x',y')=\frac{p_0}{\tau}\{\exp[\varphi_{eb}(x',y')/k_BT]-1\}, \tag{11}$$

where the potential difference $\varphi_{eb}(x', y')$ is described by the expression

$$\varphi_{eb}(x',y')=V_e\left[1-\frac{x'}{l_x}+a\Phi(x',y')\right]-V_{be}\frac{x'}{l_x}-V_{bb}\left(1-\frac{x'}{l_x}\right). \tag{12}$$

Here $V_ea\Phi(x', y')$ describes the variation of the spatial distribution of the potential in the emitter due to the onset of anisotropy of the majority-carrier (hole) conductivity:[7]

$$\Phi(x',y')=\frac{2}{\pi^2}\sum_{n=1}^{\infty}\frac{\sin\left(\frac{\pi nx'}{l_x}\right)}{n^2}\times[(-1)^n-1]\frac{\sinh\left[\frac{\pi n}{l_x}\left(y'-\frac{l_y}{2}\right)\right]}{\cosh\left(\frac{\pi nl_y}{2l_x}\right)}. \tag{13}$$

In light of the foregoing considerations, the nonequilibrium carrier distribution in the base of the strain transistor can be found by integration:

$$p(x,y,z)=\int_0^{x_0}dx'\int_0^{l_y}dy'\int_0^{l_{ze}}dz'\rho(x',y')\times p(x,y,z,x',y',z'). \tag{14}$$

The evaluation of the integral (14) is simplified considerably if the series (13) is replaced by the function

$$\Psi(x_0,y')=\langle\Phi(x',0)\rangle_{x_0}\left(1-2\frac{y'}{l_y}\right), \tag{15}$$

where the symbol $\langle\ldots\rangle_{x_0}$ denotes averaging over the interval $0\leqslant x'\leqslant x_0$, and

$$\langle\Phi(x',0)\rangle_{x_0}=\frac{2}{\pi^3}\frac{l_x}{x_0}\times\sum_{n=1}^{\infty}\left[\cos\left(\frac{\pi nx}{l_x}\right)-1\right]\frac{(-1)^n-1}{n^3}\times\tanh\left(\pi n\frac{l_y}{2l_x}\right). \tag{16}$$

We determine the value of x_0 from the condition $\varphi_{eb}(x_0, l_y/2)=0$:

$$x_0=\frac{V_e-V_{bb}}{V_e-V_{bb}+V_{be}}l_x. \tag{17}$$

For the ensuing discussion we specify the dimensions: base $l_x\times l_y\times l_z=30\times120\times3$ μm; emitter $l_x'\times l_y'\times l_z'=30\times120\times2$ μm; $L=30$ μm. The collector *p-n* junctions are situated at the depth $z=l_z$. The supply voltages are $V_e=1.4$ V, $V_{be}=0.1$ V, and $V_{bb}=1.2$ V.

The value of the anisotropy parameter is related to the uniaxial stress σ by

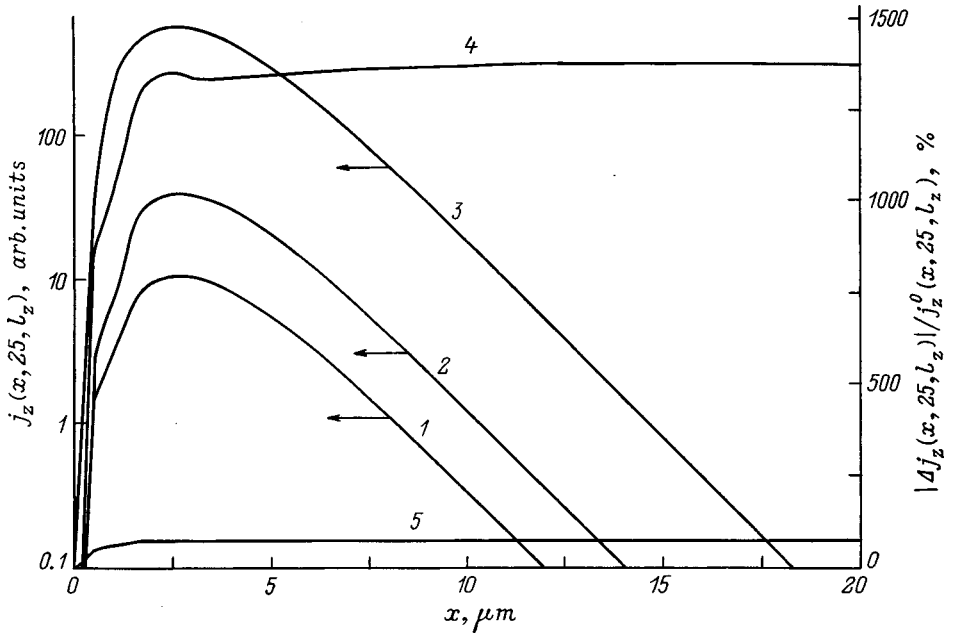

FIG. 4. Longitudinal distributions of the vertical component of the current density in the base of the strain transistor in the presence of strain (*1*, *3*) and without strain (*2*) and the relative strain-induced variations of this component (*4*, *5*) for various values of the anisotropy constant: (*2*) $a=0$; (*3*, *4*) $a=0.055$; (*1*, *5*) $a=-0.055$.

$$a \cong -\Pi_{44}^{p}\frac{\sigma}{2}, \tag{18}$$

where Π_{44}^{p} is the shear piezoelectric resistance for *p*-type Si. In our calculations the anisotropy parameter is assigned the value $a=0.055$, which corresponds to a uniaxial stress $\sigma=800\ \mathrm{kgf/cm^2}$.

Figure 3 shows the transverse distributions of the nonequilibrium carrier density in the base of the strain transistor along the line with coordinates $(5,y,1.5$, in μm). Clearly, for zero strain the distribution is mirror-symmetric about the middle plane $(x, l_y/2, z)$ (curve *1*). In the presence of a finite stress σ the distribution becomes asymmetric, the gradient of the nonequilibrium hole density increasing significantly at one collector and decreasing at the other. In addition, the total number of nonequilibrium carriers in the base increases as well, as is inferred directly from a comparison of the areas under curves *1* and *2*. This strain-induced change of the spatial distribution of holes in the base is a direct consequence of the onset of modulation of injection of the emitter-base *p-n* junction, when a transverse potential difference is formed in the emitter under the influence of the longitudinal pulling field and the induced anisotropy of the conductivity. This potential difference shifts one of the edges of the emitter-base *p-n* junction in the forward direction and the other edge in the reverse direction, depending on the sign of the stress.

The longitudinal distributions of the current densities $j_z(x)$ along the line described by the coordinates $(x, 25, l_z)$ with and without strain are shown in Fig. 4. Also shown are plots of the relative strain-induced variation of the current

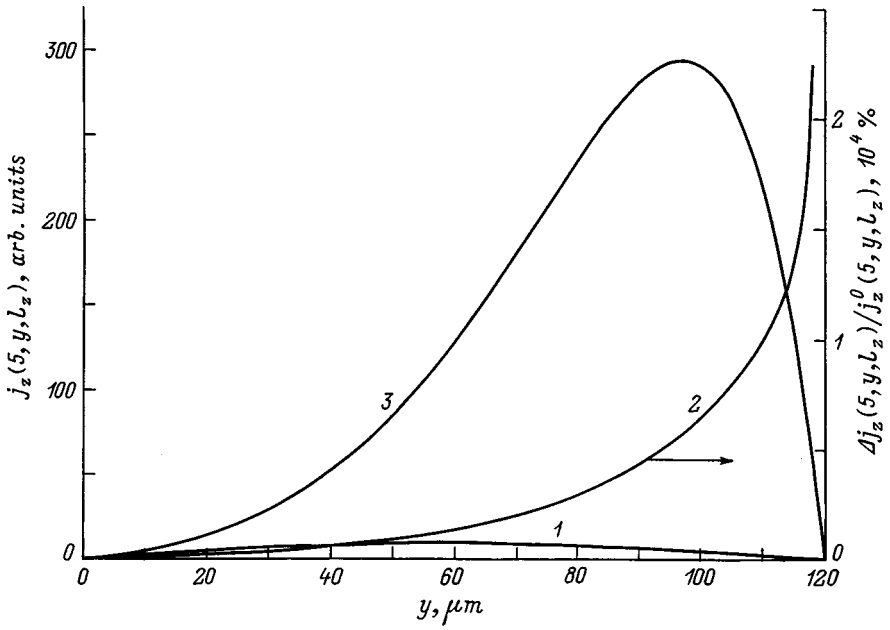

FIG. 5. Transverse distributions of the vertical component of the current density in the base of the strain transistor in the presence of strain (*3*) and without strain (*1*) and the relative strain-induced variations of this component (*2*) for various values of the anisotropy constant: (*1*) $a=0$; (*2*, *3*) $a=0.055$.

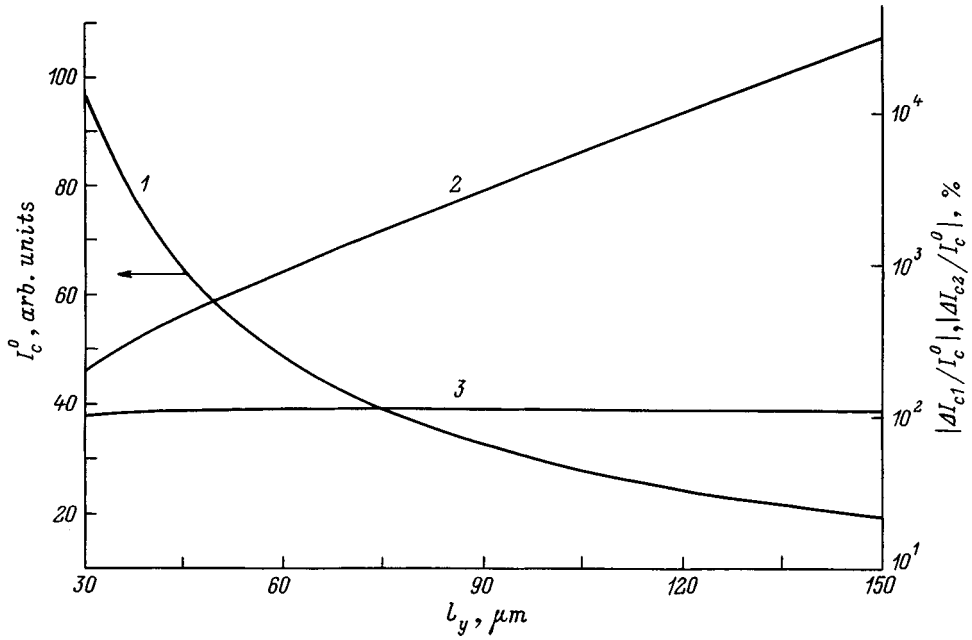

FIG. 6. Collector currents (*1*) and their relative strain-induced variations (*2, 3*) versus widths of the base and emitter of the strain transistor for various values of the anisotropy constant: (*1*) $a=0$; (*2, 3*) $a=0.055$.

densities: $\Delta j_z(x)/j_z^0(x)$, where $\Delta j_z(x)=|j_z(x)-j_z^0(x)|$, and $j_z(x)$ and $j_z^0(x)$ are the current densities at zero stress and in the presence of a deforming stress σ.

Figure 5 shows analogous plots for the transverse distributions of the current densities $j_z^0(y)$ and $j_z(y)$, along with their relative strain-induced variations $\Delta j_z(y)$.

The graphs in Figs. 4 and 5 can be used to optimize the positions, lengths, and widths of the collectors. In particular, for the investigated situation the collector junctions can be bounded by the coordinates $4\leqslant x_{c1,c2}\leqslant 9$, $15\leqslant y_{c1}\leqslant 35$, and $85\leqslant y_{c2}\leqslant 105$.

Figure 6 shows the collector currents $I_{c1}^0=I_{c2}^0=I_c^0$ and their relative strain-induced variations $|\Delta I_{c1c2}/I_c^0|$ as functions of the width of the base and the emitter l_y. It is evident from the figure that a threefold increase in l_y produces a 50-fold increase in the relative variation of the collector current with the collector operating in the nonequilibrium carrier enrichment regime, where I_c^0 is reduced by one half. Consequently, increasing l_y is an effective means of enhancing the relative sensitivity S_R.

Figure 7 shows the dependence of the relative variations of the collector currents on the anisotropy parameter. For small values of the latter ($|a|\leqslant 0.03$) the current increases in one of the collectors and decreases in the other (see the inset to Fig. 7). As the absolute value of the parameter a increases (for $|a|>0.03$), the currents in both collectors are observed to increase. This behavior can be attributed to the fact that for large values of $|a|$ nonequilibrium carriers injected by the forward-biased part of the emitter-base *p-n* junction reach both collectors. Consequently, the injection modulation is much larger than the deflection. This conclusion is supported by the graphs in Fig. 8 showing the collector currents as

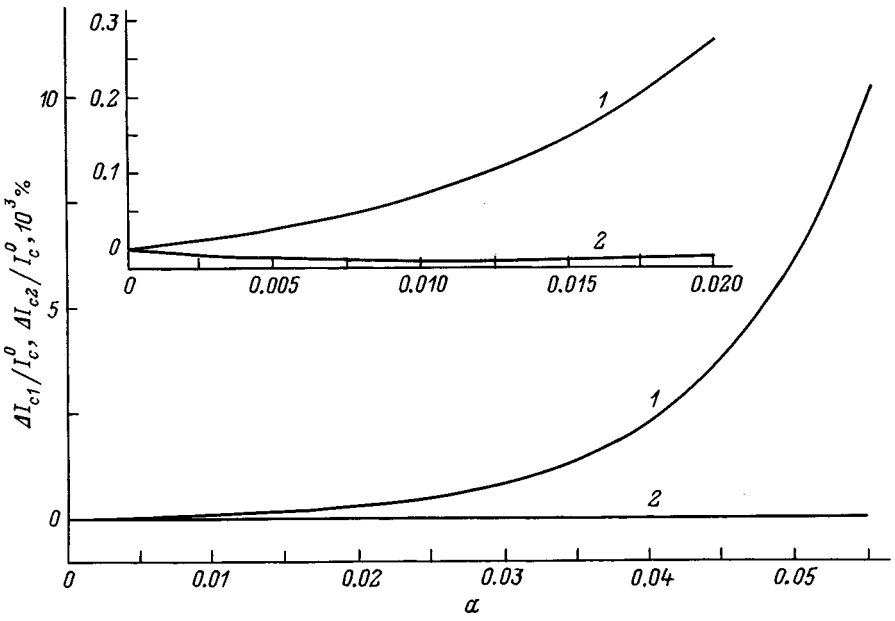

FIG. 7. Variations of the collector currents $\Delta I_{c1}/I_c^0$ (*1*) and $\Delta I_{c2}/I_c^0$ (*2*) versus anisotropy parameter a. Inset: the same for small values of a.

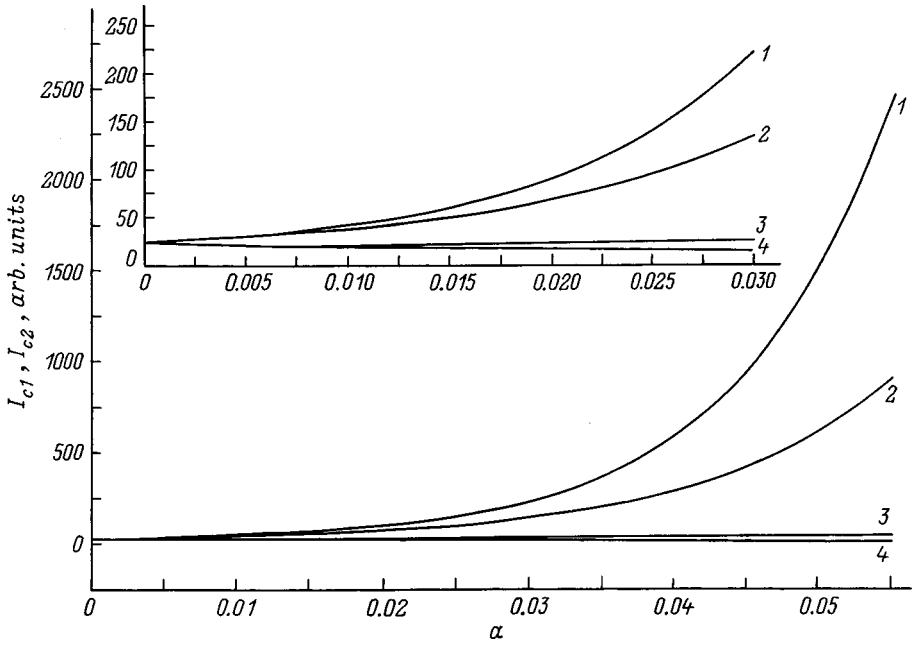

FIG. 8. Collector currents I_{c1} and I_{c2} versus anisotropy parameters: $(1, 4)$ under the influence of the deflection and injection modulation effects; $(2, 3)$ under the influence of the deflection effect. Inset: the same for small values of a.

functions of the anisotropy parameter with and without $[\Phi(x', y')=0]$ injection modulation. It follows from the plots of $I_{c1}(a)$ and $I_{c2}(a)$ in Fig. 8 that for small values of the anisotropy constant the variations of the collector currents are mainly attributable to the deflection effect, and for large values of $|a|$ ($|a|>0.03$) the injection modulation effect causes the current of one collector to more than double (Fig. 8, curves *1* and *3*).

We conclude with estimates of S_A and S_R. For the typical parameters $R_c=2\ \mathrm{k\Omega}$ and $I_c^0=1\ \mathrm{mA}$ we obtain $S_A=6\ \mathrm{mV\cdot cm^2/kgf}$ and $S_R=3.0\times10^{-3}\ \mathrm{cm^2/kgf}$, which are approximately twice the corresponding values for an *n-p-n* strain-sensitive transistor,[4] all other conditions being equal.

[1] I. I. Boĭko and V. A. Romanov, Fiz. Tekh. Poluprovodn. **11**, 817 (1977) [Sov. Phys. Semicond. **11**, 481 (1977)].
[2] H. P. Baltes and R. S. Popovic, Proc. SPIE **34**, 1107 (1986).
[3] G. G. Babichev, V. N. Guz', I. P. Zhad'ko, S. I. Kozlovskiĭ, and V. A. Romanov, Fiz. Tekh. Poluprovodn. **26**, 1244 (1992) [Sov. Phys. Semicond. **26**, 694 (1992)].
[4] S. I. Kozlovskiĭ, Fiz. Tekh. Poluprovodn. **29**, 1783 (1995) [Semiconductors **29**, 930 (1995)].
[5] F. F. Fang and D. D. Tang, ''Double carrier deflection high sensitivity magnetic sensor,'' U.S. Patent No. 4,939,536 (1990).
[6] D. D. Ivanenko and A. Sokolov, *Classical Field Theory* [in Russian], GITTL, Moscow-Leningrad, 1949, p. 432.
[7] I. I. Boĭko, I. P. Zhad'ko, S. I. Kozlovskiĭ, and V. A. Romanov, Optoélektron. Poluprovodn. Tekh. **27**, 94 (1993).

Translated by James S. Wood

Announcement: Fourth Russian Conference on the Physics of Semiconductors (SEMICONDUCTORS 99)

The Fourth Russian Conference on the Physics of Semiconductors (SEMICONDUCTORS 99) furthers the traditions established by past conferences held biennially in Nizhny Novgorod, St. Petersburg (Zelenogorsk), and Moscow.

Organizers:

General Physics and Astronomy Branch, Russian Academy of Sciences
Scientific Council of the Russian Academy of Sciences on Project ''Physics of Semiconductors''
Institute of Semiconductor Physics, Siberian Branch of the Russian Academy of Sciences
Novosibirsk State Technical University
Tomsk State University

Time and Place:

The Fourth Russian Conference on the Physics of Semiconductors will be held October 25–29, 1999, in the city of Novosibirsk.

Important Dates:

— Abstracts of the papers should be submitted before April 10, 1999.
— Second announcement will be made in June, 1999.

Main Topics of the Conference (Classification of Papers):

1. Electronic and optical properties of bulk semiconductors: relaxation of carriers, ultrafast phenomena, excitons, phonons, phase transitions, ordering.
2. Films and layers: epitaxy, atomic and electronic surface structure, adsorption and surface reactions, processes of formation (self-organization) of nanoclusters, scanning tunneling and atomic-force microscopy, near-field optical microscopy.
3. Heterostructures and superlattices: structural properties, optics, electron transport, microcavities.
4. Two-dimensional systems: structural, electronic, and magnetic properties, tunneling, localization, phonons, plasmons, rf transport, quantum Hall effect, correlation effects.
5. One-dimensional and zero-dimensional systems: energy spectrum, electron transport, optical properties, localization, interaction effects.
6. Defects and impurities (bulk semiconductors and quantum-well structures): impurities with shallow levels and deep levels, magnetic impurities, structural defects.
7. Wide-gap materials (SiC, GaN, II-VI, etc.): growth, optical and electronic properties.
8. Technology, instruments, and methods of research: electronic and optical instruments, devices, and lasers.

Submission of Abstracts:

Abstracts of papers should be sent in:

— electronic form (on diskette or by electronic mail in Word 6 or Word 7 editor, coded in uuencode, to the address: L. A. Il'ina, Institute of Semiconductor Physics, Siberian Branch of the Russian Academy of Sciences, pr. ak. Lavrent'eva, 17, 630090 Novosibirsk, Russia (E-mail: ilina@isp.nsc.ru).
— hard copy, one original and six copies of the abstracts of papers, to the address:
I. P. Akimchenko, P. N. Lebedev Physics Institute, Russian Academy of Sciences, Leninskiĭ Prospect, 53, Moscow 117924, Russia
(E-mail: akim@gpad.ac.ru).

Format of Abstracts:

The length of the abstract should not exceed one page, including figures. The text of the abstract should be ready for publication, viz.: printed on a laser or inkjet printer in Times New Roman Cyr font using Word 6 or Word 7 editor, on format A4 white paper. The type style should be normal size, Roman 12-point, spacing 1.5 for the body of the text, 14-point boldface for headings, and 12-point boldface for author's names. The authors' affiliations are required, including e-mail and postal

addresses, telephone number, and fax number all in 12-point type style; the last name of the author designated for correspondence must be underlined. This information is followed by a triple space and the body of the text. Margins: top 20 mm, left 30 mm, and right 20 mm.

Figures should be executed on a computer and incorporated into the text. Literature references in the text are indicated by numbers in brackets, [1], [2], etc. The list of references is separated from the text by a double space without any heading (''Literature'' or the like) and in the form: 1. Sidorov O.P. Pis'ma ZhTF, **58**, 108 (1993). The classification number under ''Main Topics of the Conference'' should be marked in pencil in the upper right-hand corner of each copy.

Abstracts of papers that do not conform to these instructions will not be considered.

Organ izing Committee:

Chairman of the Organizing Committee:

K. K. Svitashev	IFP SO RAN, Novosibirsk

Cochairmen:

A. L. Aseev	IFP SO RAN, Novosibirsk
I. G. Neizvestnyĭ	IFP SO RAN, Novosibirsk

Vice-Chairman:

A. V. Dvurechenskiĭ	IFP SO RAN, Novosibirsk
Tel. (3832) 33-24-66	
dvurech@isp.nsc.ru	

Scientific Secretary:

L. A. Il'ina	IFP SO RAN, Novosibirsk
Tel: (3832) 33-32-60	
Fax (3832) 33-27-71	ilina@isp.nsc.ru

I. P. Akimchenko	OOFA RAN, Moscow
V. N. Brudnyĭ	TGU, Tomsk
V. A. Gridchin	NGTU, Novosibirsk
M. D. Efremov	IFP SO RAN, Novosibirsk
A. G. Zabrodskiĭ	FTI im. A. F. Ioffe, St. Petersburg
V. V. Kalilin	IFP SO RAN, Novosibirsk
Z. D. Kvon	IFP SO RAN, Novosibirsk
Z. F. Krasil'nik	IFM RAN, Nizhny Novgorod
G. L. Kuryshev	IFP SO RAN, Novosibirsk
A. V. Latyshev	IFP SO RAN, Novosibirsk
S. D. Luchinin	IFP SO RAN, Novosibirsk
V. P. Migal'	IFP SO RAN, Novosibirsk
V. N. Ovsyuk	KTI PM SO RAN, Novosibirsk
V. Ya. Prints	IFP SO RAN, Novosibirsk
O. P. Pchelyakov	IFP SO RAN, Novosibirsk
N. N. Sibel'din	FIAN, Moscow
E. V. Skubnevskiĭ	IFP SO RAN, Novosibirsk
A. I. Toporov	IFP SO RAN, Novosibirsk

Program Committee:

V. B. Timofeev	IFTT RAN, Chernogolovka (Chairman)
I. P. Akimchenko	OOFA RAN, Moscow (Scientific Secretary)
Zh. I. Alferov	FTI im. A. F. Ioffe, St. Petersburg
A. L. Aseev	IFP SO RAN, Novosibirsk
A. A. Gippius	FIAN, Moscow
A. A. Gorbatsevich	MIÉG, Zelenograd
V. S. Dneprovskiĭ	MGU, Moscow
A. V. Dvurechenskiĭ	IFP SO RAN, Novosibirsk
A. G. Zabrodskiĭ	FTI im. A. F. Ioffe, St. Petersburg
B. P. Zakharchenya	FTI im. A. F. Ioffe, St. Petersburg
M. S. Kagan	IRÉ RAN, Moscow
L. V. Keldysh	FIAN, Moscow
Yu. V. Kopeav	FIAN, Moscow
P. S. Kop'ev	FTI im. A. F. Ioffe, St. Petersburg
I. V. Kukushkin	IFTT RAN, Chernogolovka
V. D. Kulakovskiĭ	IFTT RAN, Chernogolovka
M. G. Mil'dvidskiĭ	GIREDMET, Moscow
I. G. Neizvestnyĭ	IFP SO RAN, Novosibirsk
V. I. Perel'	FTI im. A. F. Ioffe, St. Petersburg
Ya. E. Pokrovskiĭ	IRÉ RAN, Moscow
V. M. Pudalov	FIAN, Moscow
N. N. Sibel'din	FIAN, Moscow
R. A. Suris	FTI im. A. F. Ioffe, St. Petersburg
A. S. Terekhov	IFP SO RAN, Novosibirsk
A. V. Chaplik	IFP SO RAN, Novosibirsk
V. I. Shashkin	IFM RAN, Nizhny Novgorod

Format of Abstracts:

FIAN	P. N. Lebedev Physics Institute, Russian Academy of Sciences
FTI im. A. F. Ioffe	A. F. Ioffe Physicotechnical Institute
GIREDMET	State Scientific-Research and Design Institute of the Rare Metal Industry
IRÉ RAN	Institute of Radio Engineering and Electronics, Russian Academy of Sciences
IFM RAN	Institute of Physics of Microstructures, Russian Academy of Sciences
IFP SO RAN	Institute of Semiconductor Physics, Siberian Branch of the Russian Academy of Sciences
IFTT RAN	Institute of Solid-State Physics, Russian Academy of Sciences
KTI PM SO RAN	Design-Technological Institute of Applied Microelectronics, Siberian Branch of the Russian Academy of Sciences
MGU	Moscow State University
MIÉT	Moscow Institute of Electronic Technology
NGTU	Moscow State Technical College
OOFA RAN	General Physics and Astronomy Division, Russian Academy of Sciences

Web site:

http://isp.nsc/ru/∼semi99